Ph.D. thesis

Theoretical studies on extended Higgs sectors towards future precision measurements

Masashi Aiko

Department of Physics, Osaka University

Abstract

We investigate the extended Higgs models especially focusing on the following three topics, the physics of the discovered Higgs boson, that of additional Higgs bosons, and the global symmetry of the Higgs sector. The discovered Higgs boson is a probe of new physics, and detailed studies of its nature are one of the central interests of current and future high energy physics. The Higgs strahlung process from an electron-positron collision is the dominant production process at the early stage of the future lepton colliders such as the International Linear Collider (ILC), and the production cross section will be measured with a few percent accuracies. We study the higher-order corrections for the Higgs strahlung process in various extended Higgs models. We find that the extended Higgs models can be classified by measuring the pattern of deviations from the standard model (SM) prediction in the cross section times decay branching ratio. The direct search of additional Higgs bosons is also the key program especially at the current Large Hadron Collider (LHC) experiment and its luminosity upgraded operation (HL-LHC). We find that indirect and direct studies play a complementary role. If the couplings of the discovered Higgs boson are slightly different from those in the SM, the decay modes into the discovered Higgs boson are quite useful to search additional Higgs bosons at the HL-LHC. On the other hand, theoretical arguments such as perturbative unitarity and vacuum stability put an upper bound for the typical mass scale of additional Higgs bosons if deviations are measured at the ILC. Thus, the synergy between indirect and direct searches enables us to explore the wide range of the parameter space of the extended Higgs models. The decay patterns of additional Higgs bosons are drastically changed depending on the size of deviations in the discovered Higgs boson couplings. We find that the Higgs-to-Higgs decays are sensitive to the radiative corrections. Therefore, it is important to include the higher-order corrections for the direct searches of additional Higgs bosons. Finally, we propose a new scenario, where the current experimental data are explained as a consequence of the global symmetry of the Higgs potential at a high energy scale. We find that there are characteristic predictions on the mass spectrum of the additional Higgs bosons and on the coupling constants of the discovered Higgs boson. These features can be tested at the collider experiments such as the HL-LHC and the ILC.

Acknowledgements

I would like to express my sincere gratitude to my supervisor, Prof. Shinya Kanemura for providing me with a lot of instruction to the research of particle physics. I am much obliged to Prof. Kentarou Mawatari, Prof. Kei Yagyu, Prof. Mariko Kikuchi, Dr. Kodai Sakurai for the fruitful collaborations. I would like to appreciate Prof. Tetsuya Onogi, Prof. Masaharu Aoki, Prof. Satoshi Yamaguchi for the careful reading of my thesis. I am also grateful to faculty members of the Particle Physics Theory group of Osaka University, Prof. Ryosuke Sato, Prof. Minoru Tanaka, Prof. Norihiro Iizuka, Prof. Hidenori Fukaya, and Prof. Yutaka Hosotani. I also thank colleagues of the laboratory for providing me with a good environment during my Ph.D. program. Finally, I would like to express my gratitude to my family, in particular my parents, for their kindful support and encouragement.

Contents

Chapter 1

Introduction and summary

1.1 Introduction

The standard model (SM) of particle physics successfully describes the nature of fundamental particles. The way of the three known interactions, strong, weak and electromagnetic interactions, are determined by a gauge principle [1, 2], which imposes the invariance of the theory under local gauge transformations. The strong interaction is described by Quantum Chromodynamics (QCD) [3–6], while the Glashow-Weinberg-Salam (GWS) model [7–9] of the electroweak interactions provides a unified description for the weak and electromagnetic interactions. The masses of fundamental particles, especially of gauge bosons, are prohibited by the gauge symmetry, while the observed particles are massive. The Higgs mechanism [10–14] successfully provides the masses of particles based on the spontaneous breaking down of the gauge symmetry triggered by a fundamental scalar field.

The SM has been tested in detail especially at the collider experiments. The large electron-positron (LEP) collider [15] revealed the non-abelian structure of the weak interaction. It also tested the quantum corrections of the top quark and the Higgs boson even before their discoveries through the precision study of weak gauge bosons. The hadron collider such as the Tevatron and the Large Hadron Collider (LHC) discovered the top quark [16, 17] and the Higgs boson [18, 19] with the masses consistent with the results of the electroweak precision tests at the LEP. Since the discovery of the Higgs boson, it has turned out that its properties are in agreement with those in the SM within theoretical and experimental uncertainties [20, 21].

Despite the success of the SM, we are convinced that the SM is not a fundamental theory because of the following reasons. First of all, the SM does not contain gravity. Second, there are phenomena that cannot be explained within the SM, such as the existence of dark matter [22], baryon asymmetry of the universe [22,23] and tiny but non-zero neutrino masses [24–26]. Third, there are conceptual problems in the SM such as the hierarchy problem [27–29], the strong CP problem [30], no unified description for the gauge group [31] and the flavor structure [32] and so on. Therefore, the SM must be replaced by a more fundamental theory.

In seeking a more fundamental theory, one may realize that the structure of the Higgs sector, which determines the concrete realization of the Higgs mechanism, is still a mystery while the Higgs boson was found. There is no theoretical principle to insist on the minimal structure of the Higgs sector as introduced in the SM. We can construct models with extended Higgs sectors, that are consistent with current experimental data. In addition, new physics models with non-minimal Higgs sectors can solve the above-mentioned problems in the SM. Determination of the structure of the Higgs sector is one of the central interests of current and future high-energy physics. By unraveling the nature of the Higgs sector, we can narrow down

the scenario of new physics.

The clear evidence of extended Higgs sectors is a discovery of additional Higgs bosons. Its properties such as the mass, the electric charge and the parity give important information about the Higgs sector. Various efforts have been devoted to discovering such new particles in a wide variety of search channels. Although no observation of such new particles has been reported, leading to constraints on parameters of extended Higgs models, there are various scenarios that have not been explored yet. Therefore, the direct search of new particles is one of the key programs especially at the LHC as well as at its luminosity upgraded operation (HL-LHC).

In addition to the direct search, we can indirectly explore the extended Higgs sector. Even before the discoveries of the top quark and the Higgs boson, we had a rough estimation for their masses by studying their indirect effects on the electroweak observables. In addition, even before the discovery of the SM-like Higgs boson, the extended Higgs sector is also constrained by electroweak precision measurements and various flavor measurements. The electroweak precision measurements, especially the measurement of the electroweak rho parameter, tell us the information about the multiplet structure of the Higgs fields. On the other hand, flavor measurements, especially the suppression of the flavor-changing neutral current (FCNC), give information about the structure of the Yukawa interactions. Thus, the indirect study of new particles is a powerful way to explore new physics models.

The discovery of the SM-like Higgs boson has opened a new window. The evidence of extended Higgs sectors indirectly appears in the properties of the SM-like Higgs boson, since they might be changed from that in the SM. Thus, the studies of the various Higgs observables such as the decay branching ratios, total width and production cross sections tell us important hints for extended Higgs sectors. If the deviations from the SM predictions are observed, one can theoretically deduce an upper limit on the typical mass scale of additional Higgs bosons, and this would set the next target of the energy scale at hadron colliders. Therefore, the discovered Higgs boson is a probe of new physics. The detailed studies of the SM-like Higgs boson are also one of the key programs at current and future collider experiments.

At the LHC, the Higgs boson couplings have been measured with typically order ten percent accuracy [20, 21], and they have been in agreement with those in the SM up to now. This leads us to study the so-called *Higgs alignment* scenario [33] in extended Higgs models, where SM-like Higgs boson couplings take their SM values. In most of the extended Higgs models, such SM-like scenario can be realized by following two ways. The first one is the alignment due to the decoupling of additional Higgs bosons. In the decoupling scenario, a new scale introduced in extended Higgs models is much larger than the TeV scale, and their indirect effects decouple from observables at the electroweak scale [34]. The second one is the alignment of the SM-like Higgs boson couplings without decoupling. In this scenario, inner parameters of extended Higgs models, especially mixing among the SM-like Higgs boson and additional Higgs bosons, take the values so that the SM-like Higgs boson couplings take their SM values.

The accuracy of Higgs measurements will be improved at the HL-LHC and further significantly at future lepton colliders such as the International Linear Collider (ILC) [35–38], the Future Circular Collider (FCC-ee) [39] and the Circular Electron Positron Collider (CEPC) [40]. Since a few percent accuracies are typically expected in these future experiments, theoretical predictions at the lowest order of perturbation are not enough, and inclusion of the higher-order corrections due to the quantum effects is important. In addition, the current SM-like situation makes the study of the higher-order corrections further important because these corrections would give different predictions from the SM even if the SM-like Higgs boson couplings are aligned at the lowest order.

It should be emphasized that there is a complementarity between direct and indirect searches,

and it enables us to study the extended Higgs sector in detail at future collider experiments. The direct search of additional Higgs bosons gives a lower bound for the mass scale of the additional Higgs bosons. On the other hand, if the couplings of the SM-like Higgs boson slightly deviate from those in the SM, the indirect search gives an upper bound for the mass scale of the additional Higgs bosons. As we discuss in this thesis, decays of additional Higgs bosons into the SM-like Higgs boson can be a dominant decay process in the approximate alignment scenario, and such Higgs-to-Higgs decays are quite useful for the direct search of additional Higgs bosons. Thus, we can explore the extended Higgs sector, especially in the approximately SM-like scenario by utilizing the synergy between the direct search of Higgs-to-Higgs decay at future hadron colliders and the indirect search at future lepton colliders.

In this thesis, we show that higher-order corrections play an important role not only in the physics of the discovered Higgs boson but also in that of additional Higgs bosons. In order to open the Higgs-to-Higgs decay modes, the SM-like Higgs boson couplings should deviate from their SM value at the lowest order. Therefore, the Higgs-to-Higgs decays are suppressed at the tree level in the alignment scenario. Since the size of the lowest-order contribution is relatively small, the size of higher-order corrections might be the same magnitude. Thus, the inclusion of the higher-order corrections is important, especially for the Higgs-to-Higgs decays in the approximate alignment scenario.

From a theoretical viewpoint, it is important to investigate the origin of Higgs alignment. The Higgs alignment would indicate the nature of the Higgs sector, as the electroweak rho parameter and suppression of the FCNCs shed light on the structure of the extended Higgs sector. Global symmetry is one of the promising ways to naturally understand these observations. In this thesis, we propose a new scenario where both the electroweak rho parameter and the Higgs alignment by a global symmetry of the Higgs potential at a higher scale. We have the characteristic predictions on the mass spectrum of the additional Higgs bosons and the SM-like Higgs boson couplings, and this scenario can be tested at future collider experiments. Since the structure of the Higgs potential would be determined by the dynamics of more fundamental theory, we can shed light on the nature of new physics by reconstructing the shape of the Higgs potential.

1.2 Summary of the author's work

We present the following results in this thesis.

(I) **Cross section for the Higgs strahlung process from electron-positron collisions including the full next-to-leading order electroweak corrections in various extended Higgs models.** [in Chapter 6]

We evaluate the production cross section for $e^+e^- \to hZ$ process with arbitrary sets of electron and Z boson polarization including the full next-to-leading order electroweak corrections in various extended Higgs models, such as the Higgs singlet model (HSM), the inert doublet model (IDM) and the two Higgs doublet model (2HDM). We find that the various extended Higgs models can be discriminated by precisely analyzing the deviation in the cross section times branching ratio.

(II) **The synergy between direct searches for additional Higgs bosons at the hadron colliders and precision measurements of the SM-like Higgs boson properties at future electron-positron colliders.** [in Chapter 7]

In the 2HDM, we concretely show that most of the parameter space can be explored by the direct searches of the additional Higgs bosons and also by the theoretical constraints if the future collider experiments measure the deviations in the coupling constants of the SM-like Higgs boson.

(III) **Decay branching ratios of charged Higgs bosons including NLO EW corrections, as well as QCD corrections.** [in Chapter 8]

We evaluate the decay branching ratios of charged Higgs bosons including NLO EW corrections, as well as QCD corrections in the 2HDMs.

(IV) **Decay branching ratios of CP-odd Higgs boson including NLO EW corrections, as well as QCD corrections.** [in Chapter 9]

We evaluate the decay branching ratios of CP-odd Higgs boson including NLO EW corrections, as well as QCD corrections in the 2HDMs.

(V) **New scenario for the SM-like Higgs couplings originated from the global symmetry of the Higgs potential at a high energy scale.** [in Chapter 10]

We propose a new scenario of the 2HDM, where the current experimental data for the electroweak rho parameter and those for the Higgs boson couplings can be simultaneously explained. We find that there are characteristic predictions on the mass spectrum of the additional Higgs bosons and on the couplings of the SM-like Higgs boson, which make it possible to test this scenario at the current and future collider experiments.

These results are based on the following author's work in collaboration with Prof. Shinya Kanemura, Prof. Kentarou Mawatari, Prof. Kei Yagyu, Prof. Mariko Kikuchi and Dr. Kodai Sakurai.

[**41**] M. Aiko, S. Kanemura and K. Mawatari. "Next-to-leading-order corrections to the Higgs strahlung process from electron-positron collisions in extended Higgs models", Eur. Phys. J. C, Vol. 81, No. 11, p. 1000, 2021.

[**42**] M. Aiko, S. Kanemura, M. Kikuchi, K. Mawatari, K. Sakurai and K. Yagyu, "Probing extended Higgs sectors by the synergy between direct searches at the LHC and precision tests at future lepton colliders", Nucl. Phys. B, Vol. 966, p. 115375, 2021.

[**43**] M. Aiko, S. Kanemura and K. Sakurai, "Radiative corrections to decays of charged Higgs bosons in two Higgs doublet models", Nucl. Phys. B, Vol. 973, p. 115581, 2021.

[**44**] M. Aiko and S. Kanemura, "New scenario for aligned Higgs couplings originated from the twisted custodial symmetry at high energies", JHEP, Vol. 02, p. 046, 2021.

1.3 Organization

This thesis is organized as follows. In Chapter 2 and 3, we review the SM and the extended Higgs models. In Chapter 4, we review the gauge independent renormalization of the SM and the extended Higgs models. In Chapter 5, we review the decays of the discovered Higgs boson including the higher-order corrections. In Chapter 6, we study the Higgs strahlung production process at electron-proton colliders including the quantum corrections. In Chapter 7, we study the synergy between direct searches for additional Higgs bosons at the hadron colliders

and precision measurements of the SM-like Higgs boson properties at future electron-positron colliders. In Chapter 8 and 9, we study the radiative corrections for the decays of additional Higgs bosons and discuss their impacts motivated by the study in Chapter 7. In Chapter 10, we propose the scenario where the current experimental constraints are explained as a consequence of the global symmetry structure of the Higgs potential. We conclude this thesis in Chapter 11.

Part I

Review of the Higgs physics

Chapter 2

Review of the standard model

In this chapter, we review the SM. The SM is based on the two pillars. The first one is the gauge principle [1] which determines the structure of the gauge interactions. The second one is the Higgs mechanism [10–14] by which the SM particles acquire their mass through the spontaneous breaking down of the gauge symmetry.

We follow the sign notation in `H-COUP` program [45, 46] which corresponds to $\eta = \eta' = \eta_e = -1,\ \eta_Z = \eta_\theta = \eta_Y = +1$ and $\eta_G = +1$ in Ref. [47].

2.1 Particle contents

In this section, we list the particle contents of the SM and their representation under the gauge group $G = SU(3)_c \times SU(2)_L \times U(1)_Y$.

2.1.1 Quarks and Leptons

	$SU(3)_C$	$SU(2)_L$	$U(1)_Y$
Q^i	**3**	**2**	$1/6$
u^i_R	**3**	**1**	$2/3$
d^i_R	**3**	**1**	$-1/3$
L^i	**1**	**2**	$-1/2$
ℓ^i_R	**1**	**1**	-1

Table 2.1: Representation of fermion fields under the SM gauge symmetry. Index i represents the generation of quarks and leptons. **3** and **2** are fundamental representation of $SU(3)_c$ and $SU(2)_L$, respectively. Index R represents the right-handed fermions, while Q and L corresponds to left-handed quarks and leptons, respectively.

There are six flavors of quarks and leptons in the SM. Based on the $SU(2)_L$ multiplet structure, we classify the quarks and leptons into three generations. The transformation properties of fermion multiplets are summarized in Table. 2.1.

The left-handed quarks $Q^i = (u^i, d'^i)^T_L$ are the fundamental representation of $SU(3)_c$ and $SU(2)_L$ gauge symmetry.

$$Q^1 = \begin{pmatrix} u \\ d' \end{pmatrix}_L, \quad Q^2 = \begin{pmatrix} c \\ s' \end{pmatrix}_L, \quad Q^3 = \begin{pmatrix} t \\ b' \end{pmatrix}_L. \tag{2.1}$$

The right-handed quarks u_R^i and d_R^i are also the fundamental representation of $SU(3)_c$ but singlet of $SU(2)_L$.

All of the leptons are singlet under the $SU(3)_c$. The left-handed leptons $L^i = (\nu_\ell^i, \ell^i)_L^T$ are the fundamental representation of $SU(2)_L$

$$L^1 = \begin{pmatrix} \nu_e \\ e \end{pmatrix}_L, \quad L^2 = \begin{pmatrix} \nu_\mu \\ \mu \end{pmatrix}_L, \quad L^3 = \begin{pmatrix} \nu_\tau \\ \tau \end{pmatrix}_L, \tag{2.2}$$

while right-handed leptons ℓ_R^i are singlet.

2.1.2 Gauge bosons

	$SU(3)_C$	$SU(2)_L$	$U(1)_Y$
G_μ^a	**8**	**1**	0
W_μ^i	**1**	**3**	0
B_μ	**1**	**1**	0

Table 2.2: Representation of gauge fields under the SM gauge symmetry. $SU(3)_c$ index $a = 1, 2, \cdots 8$, and $SU(2)_L$ index $i = 1, 2, 3$. **8** and **3** are adjoint representation of $SU(3)_c$ and $SU(2)_L$ respectively.

There are three kinds of gauge fields in the SM. The transformation properties of gauge fields are summarized in Table. 2.2.

2.1.3 Higgs boson

	$SU(3)_C$	$SU(2)_L$	$U(1)_Y$
Φ	**1**	**2**	$1/2$
Φ^c	**1**	**2**	$-1/2$

Table 2.3: Representation of Higgs fields under the SM gauge symmetry. Φ^c is charge conjugation of Φ.

There is one Higgs doublet field in the SM. The transformation properties of Higgs fields are summarized in Table. 2.3. The charge conjugation of Higgs field Φ^c is defined as

$$\Phi^c = i\sigma_2 \Phi^*. \tag{2.3}$$

Φ^c behaves as a doublet under the $SU(2)_L$ transformation, while it has opposite hypercharge as Φ.

2.2 Classical Lagrangian of the SM

The classical Lagrangian of the standard model is given by

$$\begin{aligned}\mathcal{L}_{\rm SM} = &-\frac{1}{4}\sum_{a=1}^{8} G^a_{\mu\nu}G^{a\mu\nu} - \frac{1}{4}\sum_{a=1}^{3} W^a_{\mu\nu}W^{a\mu\nu} - \frac{1}{4}B_{\mu\nu}B^{\mu\nu} \\ &+ \overline{Q}^i(i\not{D})Q^i + \overline{u}^i_R(i\not{D})u^i_R + \overline{d}^i_R(i\not{D})d^i_R + \overline{L}^i(i\not{D})L^i + \overline{\ell}^i_R(i\not{D})\ell^i_R \\ &+ (D_\mu\Phi)^\dagger D^\mu\Phi + \mu^2\Phi^\dagger\Phi - \frac{\lambda}{2}(\Phi^\dagger\Phi)^2 \\ &- \Big[Y^{ij}_u\overline{Q}^i u^j_R\Phi^c + Y^{ij}_d\overline{Q}^i d^j_R\Phi + Y^{ij}_e\overline{L}^i\ell^j_R\Phi + \text{h.c.}\Big]. \end{aligned} \tag{2.4}$$

The field strength tensors $G^a_{\mu\nu}, W^a_{\mu\nu}, B_{\mu\nu}$ are defined as

$$G^a_{\mu\nu} = \partial_\mu G^a_\nu - \partial_\nu G^a_\mu + g_s f^{abc} G^b_\mu G^c_\nu, \tag{2.5}$$
$$W^a_{\mu\nu} = \partial_\mu W^a_\nu - \partial_\nu W^a_\mu + g\epsilon^{abc} W^b_\mu W^c_\nu, \tag{2.6}$$
$$B^a_{\mu\nu} = \partial_\mu B^a_\nu - \partial_\nu B^a_\mu, \tag{2.7}$$

where f^{abc} and ϵ^{abc} are the structure constants of $SU(3)_c$ and $SU(2)_L$, respectively. The covariant derivative is defined as

$$D_\mu = \partial_\mu - ig_s T^a G^a_\mu - ig\tau^a W^a_\mu - ig' Y B_\mu, \tag{2.8}$$

where $T^a = \lambda^a/2$ are $SU(3)_c$ generators with the Gell-Mann matrices λ^a, while $\tau^i = \sigma^i/2$ are $SU(2)_L$ generators with the Pauli matrices σ^i.

2.2.1 Higgs mechanism

In the SM, the Higgs potential is given by

$$V(\Phi) = -\mu^2\Phi^\dagger\Phi + \frac{\lambda}{2}(\Phi^\dagger\Phi)^2, \tag{2.9}$$

where μ^2 and λ are real parameter, and λ is positive due to the stability of the Higgs potential.

If μ^2 is positive, the Higgs potential has a non-trivial minimum, and $SU(2)_L \times U(1)_Y$ gauge symmetry spontaneously breaks down into $U(1)_{\rm em}$. We parametrize Φ as

$$\Phi = \begin{pmatrix} G^+ \\ \frac{1}{\sqrt{2}}(v + h + iG^0) \end{pmatrix}, \tag{2.10}$$

where v is vacuum expectation value (VEV), and $G^\pm$ and G^0 are the Nambu-Goldstone (NG) bosons [48, 49]. The stationary condition, $\partial V(\Phi)/\partial h|_0 = 0$, leads to

$$\mu^2 = \frac{1}{2}\lambda v^2, \tag{2.11}$$

and the mass of the Higgs boson h is given by

$$m_h^2 = \lambda v^2. \tag{2.12}$$

We obtain the mass terms of the gauge bosons from the kinetic term of the Higgs field

$$\mathcal{L}_{\text{Higgs}} \supset \left(\frac{gv}{2}\right)^2 W_\mu^+ W^{-\mu} + \frac{v^2}{8}\begin{pmatrix} W_\mu^3 & B_\mu \end{pmatrix}\begin{pmatrix} g^2 & gg' \\ gg' & g'^2 \end{pmatrix}\begin{pmatrix} W^{3\mu} \\ B^\mu \end{pmatrix}, \tag{2.13}$$

where we have defined charged weak bosons $W^\pm$ as

$$W_\mu^\pm \equiv \frac{1}{\sqrt{2}}\left(W_\mu^1 \mp i W_\mu^2\right). \tag{2.14}$$

We define mass eigenstates Z_μ and A_μ as

$$\begin{pmatrix} Z_\mu \\ A_\mu \end{pmatrix} \equiv \begin{pmatrix} c_W & -s_W \\ s_W & c_W \end{pmatrix}\begin{pmatrix} W_\mu^3 \\ B_\mu \end{pmatrix}, \tag{2.15}$$

with the shorthand notation for the trigonometric functions as $s_W = \sin\theta_W$ and $c_W = \cos\theta_W$. The weak mixing angle θ_W is defined by $\tan\theta_W \equiv g'/g$. The masses of the gauge bosons are given by

$$m_W = \frac{1}{2}gv, \quad m_Z = \frac{1}{2}g_Z v, \quad m_\gamma = 0, \tag{2.16}$$

with $g_Z \equiv g/c_W$.

We obtain the mass terms of the quarks and leptons from the Yukawa interaction terms

$$\mathcal{L}_{\text{Yukawa}} \supset -\sum_{f=u,d,e} \overline{f}^i_L \left(\frac{1}{\sqrt{2}} Y_f^{ij} v\right) f_R^j + \text{h.c.} \tag{2.17}$$

Since any n-dimensional square complex matrix can be diagonalized by a bi-unitary transformation, we can define the mass eigenstate of the quarks and leptons as,

$$u_L^i = U_L^{ij} u_L^{(m)j}, \quad u_R^i = U_R^{ij} u_R^{(m)j}, \tag{2.18}$$
$$d_L^i = D_L^{ij} d_L^{(m)j}, \quad d_R^i = D_R^{ij} d_R^{(m)j}, \tag{2.19}$$
$$e_L^i = E_L^{ij} e_L^{(m)j}, \quad e_R^i = E_R^{ij} e_R^{(m)j}, \tag{2.20}$$

such that

$$\text{diag}(m_u, m_c, m_t) = \frac{v}{\sqrt{2}}(U_L^\dagger)^{ik} Y_u^{k\ell} U_R^{\ell j}, \tag{2.21}$$
$$\text{diag}(m_d, m_s, m_b) = \frac{v}{\sqrt{2}}(D_L^\dagger)^{ik} Y_d^{k\ell} D_R^{\ell j}, \tag{2.22}$$
$$\text{diag}(m_e, m_\mu, m_\tau) = \frac{v}{\sqrt{2}}(E_L^\dagger)^{ik} Y_e^{k\ell} E_R^{\ell j}. \tag{2.23}$$

2.2.2 Weak and electromagnetic currents

We obtain the fermion's electromagnetic, weak-charged and weak-neutral currents from the kinetic terms of the fermions. In the mass eigenstate, they are given by

$$\mathcal{L} \supset e J_{\text{em}}^\mu A_\mu + \frac{g}{\sqrt{2}}\left[J_+^\mu W_\mu^+ + h.c.\right] + g_Z J_Z^\mu Z_\mu, \tag{2.24}$$

with $e \equiv g s_W = g' c_W$. The electromagnetic current is given by

$$J^\mu_{\rm em} = \delta_{ij} \sum_{f=u,d,e} Q_f \overline{f}^{(m)i} \gamma^\mu f^{(m)j}, \tag{2.25}$$

where the electromagnetic charge Q_f is determined by the Nishijima-Gell-Mann's formula [50–52],

$$Q_f \equiv \tau^3_f + Y_f. \tag{2.26}$$

The weak-charged current is defined by

$$J^\mu_+ = V^{ij}_{\rm CKM} \overline{u}^{(m)i} \gamma^\mu P_L d^{(m)j} + \delta_{ij} \overline{\nu}^i \gamma^\mu P_L e^{(m)j}, \tag{2.27}$$

with Cabibbo-Kobayashi-Maskawa (CKM) matrix [53, 54]

$$V^{ij}_{\rm CKM} = (U^\dagger_L)^{ik} D^{kj}_L. \tag{2.28}$$

Since there is no mass term for the neutrinos, we have rotated the left-handed neutrinos so that the leptonic charged current becomes flavor diagonal. The weak-neutral current is given by

$$J^\mu_Z = \delta_{ij} \sum_{f=u,d,e} \overline{f}^{(m)i} \gamma^\mu (v_f - a_f \gamma^5) f^{(m)j}, \tag{2.29}$$

with

$$v_f = \frac{1}{2}\tau^3_f - Q_f s^2_W, \quad a_f = \frac{1}{2}\tau^3_f. \tag{2.30}$$

Since the weak-neutral current is flavor diagonal, it conserves all quark flavors in the SM [55].

2.2.3 Higgs boson couplings

The interaction terms of the Higgs boson and the weak gauge bosons are given by

$$\mathcal{L} \supset \frac{m^2_W}{v} g^{\mu\nu} h W^+_\mu W^-_\mu + \frac{m^2_Z}{2v} g^{\mu\nu} h Z_\mu Z_\mu. \tag{2.31}$$

Since the Higgs boson is neutral under the $SU(3)_c$ color and the $U(1)_{\rm em}$ charge, there is no tree-level interaction with the gluon and the photon. The interaction terms of the Higgs boson and the fermions are given by

$$\mathcal{L}_{\rm Yukawa} \supset - \sum_{f=u,d,e} \frac{m_f}{v} \overline{f} f h. \tag{2.32}$$

Since the mass matrices and the Yukawa interaction terms are diagonalized simultaneously, the interactions of the Higgs boson and fermions conserve the quark flavors in the SM.

The Higgs boson couplings to gauge bosons and fermions are proportional to their mass. Thus, its couplings to the weak gauge bosons, top and bottom quark, and tau lepton are relevant for the Higgs physics.

2.3 Quantization of the standard model

2.3.1 Gauge fixing in the R_ξ gauge

We need to make the gauge fixing following the Faddeev-Popov prescription [56] in order to quantize the standard model. In the R_ξ gauge [57], the gauge fixing terms are given by

$$\mathcal{L}_{\rm GF} = -\frac{1}{2}F_G^2 - F_+F_- - \frac{1}{2}F_Z^2 - \frac{1}{2}F_A^2, \tag{2.33}$$

where

$$F_G^a = (\xi_G)^{-1/2}\partial^\mu G_\mu^a, \tag{2.34}$$
$$F_\pm = (\xi_W)^{-1/2}\partial^\mu W_\mu^\pm \mp i(\xi_W)^{1/2} m_W G^\pm, \tag{2.35}$$
$$F_Z = (\xi_Z)^{-1/2}\partial^\mu Z_\mu - (\xi_Z)^{1/2} m_Z G, \tag{2.36}$$
$$F_A = (\xi_A)^{-1/2}\partial^\mu A_\mu. \tag{2.37}$$

In the R_ξ gauge, the mixing terms between the gauge bosons and the NG bosons cancel out. We choose the gauge parameters as

$$\xi_G = \xi_W = \xi_Z = \xi_A = \xi, \tag{2.38}$$

and adopt the 't Hooft-Feynman gauge [58] where $\xi = 1$.

2.3.2 Fadeev-Popov Ghost

In order to restore the unitarity, the Fadeev-Popov ghosts [56] must be introduced as

$$\begin{aligned}\mathcal{L}_{\rm ghost} = &\sum_{a,b=1}^{8} \bar\omega^a \frac{\partial(\delta F_G^a)}{\partial\beta^b}\omega^b \\ &+ \sum_{i=\pm,Z,A}\left[\bar c_+\frac{\partial(\delta F_+)}{\partial\alpha^i} + \bar c_-\frac{\partial(\delta F_-)}{\partial\alpha^i} + \bar c_Z\frac{\partial(\delta F_Z)}{\partial\alpha^i} + \bar c_A\frac{\partial(\delta F_A)}{\partial\alpha^i}\right]c^i,\end{aligned} \tag{2.39}$$

where ω^a denote the $SU(3)_c$ ghosts, and $c_\pm, c_Z$ and c_A are electroweak ghosts. We have defined the gauge parameters β^a by the $SU(3)_c$ transformation

$$U_c = \exp(-ig_s T^a \beta^a). \tag{2.40}$$

In addition, We have defined the gauge parameters $\alpha^\pm, \alpha^Z, \alpha^A$ as

$$\alpha^\pm = \frac{1}{\sqrt{2}}(\alpha^1 \mp i\alpha^2), \tag{2.41}$$
$$\alpha_Z = \alpha^3 c_W - \alpha^4 s_W, \tag{2.42}$$
$$\alpha_A = \alpha^3 s_W + \alpha^4 c_W. \tag{2.43}$$

by the $SU(2)_L$ and $U(1)_Y$ transformation

$$U_L = \exp\bigl(-ig\tau^i\alpha^i\bigr), \quad i = 1,2,3, \tag{2.44}$$
$$U_Y = \exp\bigl(-ig'Y\alpha^4\bigr). \tag{2.45}$$

2.4 Higgs sector in the SM

In this section, we discuss theoretical and experimental features of the Higgs sector in the SM.

2.4.1 Custodial symmetry

The Higgs potential in the SM given in Eq. (2.9) respects not only the local $SU(2)_L \times U(1)_Y$ gauge symmetry but also global $O(4)$ symmetry. In the symmetric phase, we parametrize Φ as

$$\Phi = \frac{1}{\sqrt{2}} \begin{pmatrix} \phi_1 + i\phi_2 \\ \phi_3 + i\phi_4 \end{pmatrix}. \tag{2.46}$$

Since the Higgs potential consists of $|\Phi|^2 = \sum_i \phi_i^2/2$, this is invariant under the global $SO(4)$ transformation of ϕ_i

$$\phi_i \to O_{ij}\phi_j, \quad O_{ij}O_{ik} = \delta_{ik}. \tag{2.47}$$

In the broken phase, the VEV of ϕ_3 breaks the global $SO(4)$ symmetry into $SO(3)$ symmetry leading to three NG bosons.

The $SO(4)$ and $SO(3)$ groups are homomorphic to $SU(2) \times SU(2)$ and $SU(2)$ groups, respectively. Therefore, we can regard the breaking pattern of the global symmetry as $SU(2) \times SU(2)$ symmetry into $SU(2)$ symmetry. We call the unbroken $SO(4) \sim SU(2)_L \times SU(2)_R$ symmetry as *custodial symmetry*, while this terminology is originally introduced for the residual $SU(2)_V$ symmetry [59]. One can study this global symmetry structure by introducing a bi-doublet field,

$$M = (\Phi^c, \Phi). \tag{2.48}$$

The bi-doublet field transforms under the $SU(2)_L \times U(1)_Y$ transformation as,

$$SU(2)_L \ : \ M \to e^{ig\alpha_a(x)\tau_a} M, \tag{2.49}$$

$$U(1)_Y \ : \ M \to M e^{-ig'Y\alpha_4(x)\sigma_3}, \tag{2.50}$$

and $\mathrm{Tr}\big(M^\dagger M\big) = 2|\Phi|^2$ is gauge invariant. The Higgs potential is written by

$$V(\Phi) = -\frac{\mu^2}{2}\,\mathrm{Tr}\big(M^\dagger M\big) + \frac{\lambda}{8}\,\mathrm{Tr}^2(M^\dagger M), \tag{2.51}$$

and it is invariant under the global $SU(2)_L \times SU(2)_R$ transformation of the bi-doublet field,

$$M \to U_L M U_R^\dagger. \tag{2.52}$$

From Eq. (2.50), we can see that global $U(1)_Y$ is a subgroup of global $SU(2)_R$.

In the broken phase, the bi-doublet field becomes,

$$\langle M \rangle = \frac{v}{\sqrt{2}} \begin{pmatrix} 1 & 0 \\ 0 & 1 \end{pmatrix}, \tag{2.53}$$

and this breaks both $SU(2)_L$ and $SU(2)_R$,

$$U_L \langle M \rangle \neq \langle M \rangle, \quad \langle M \rangle U_R^\dagger \neq \langle M \rangle. \tag{2.54}$$

However, $\langle M \rangle$ leaves the unbroken subgroup $SU(2)_V$, which is corresponding to simultaneous transformation of $SU(2)_L$ and $SU(2)_R$ with U_V

$$U_V \langle M \rangle U_V^\dagger = \langle M \rangle . \tag{2.55}$$

Thus the VEV of the bi-doublet filed breaks global $SU(2)_L \times SU(2)_R$ symmetry into $SU(2)_V$.

The custodial symmetry is not the global symmetry of the whole SM Lagrangian. The covariant derivative of the bi-doublet field is written by

$$D_\mu M = \partial_\mu M - igW_\mu \tau^a M + ig' Y B_\mu M \sigma_3. \tag{2.56}$$

Since $U_R^\dagger$ does not commute with σ_3, the hypercharge interaction breaks the custodial symmetry. In order to study the Yukawa interaction terms, we introduce the left-handed doublet $Q_L^i = Q^i$ and the right-handed doublet $Q_R^i = (u^i, d'^i)_R^T$. The Yukawa interaction terms for quarks are written by

$$\mathcal{L}_{\text{Yuk}} \supset -\frac{1}{2}(Y_u^{ij} + Y_d^{ij})\overline{Q}_L^i M Q_R^j - \frac{1}{2}(Y_u^{ij} - Y_d^{ij})\overline{Q}_L^i M \sigma_3 Q_R^j. \tag{2.57}$$

Thus, the custodial symmetry is broken by the second term, which is proportional to the mass difference between up and down-type quarks after the symmetry breaking. Since there is no right-handed neutrino, the Yukawa interaction terms for leptons maximally break the custodial symmetry.

2.4.2 Perturbative unitarity

The perturbative unitarity bound [60,61] gives the upper limit on the mass of the Higgs boson in the SM. From Eq. (2.12), we can see that a heavier Higgs boson leads to a larger Higgs quartic coupling. This indicates that there is an upper bound for the mass of the Higgs boson above which the perturbative expansion for the Higgs quartic coupling is not verified.

Unitarity condition

The breakdown of the perturbative expansion violates the unitarity of the S matrix, $S^\dagger S = 1$. In order to isolate the interaction, we parametrize the S matrix as $S = 1 + iT$ and obtain

$$T^\dagger T = -i(T - T^\dagger). \tag{2.58}$$

For the initial state $|i\rangle = |k_1, k_2, \cdots\rangle$ and the final state $|f\rangle = |p_1, p_2, \cdots\rangle$, the scattering amplitude satisfies the unitarity condition,

$$-i\{\mathcal{M}(i \to f) - \mathcal{M}^*(f \to i)\} = \sum_X \int \mathrm{d}\Pi_X \mathcal{M}^*(f \to X)\mathcal{M}(i \to X), \tag{2.59}$$

where we used the completeness relationship

$$1 = \sum_X \left(\prod_{i=1}^X \int \frac{\mathrm{d}^3 q_i}{(2\pi)^3} \frac{1}{2E_i} \right) |X\rangle \langle X| \tag{2.60}$$

with an intermediate state $|X\rangle = |q_1, q_2, \cdots\rangle$. The scattering amplitude is defined by

$$\langle f | iT | i \rangle = (2\pi)^4 \delta^4 \Big(\sum k_i - \sum p_i \Big) i\mathcal{M}(i \to f), \tag{2.61}$$

and the phase space integral is defined by

$$\int \mathrm{d}\Pi_X = \left(\prod_{i=1}^{X} \int \frac{\mathrm{d}^3 q_i}{(2\pi)^3} \frac{1}{2E_i}\right) (2\pi)^4 \delta^4\Big(\sum k_i - \sum q_i\Big). \tag{2.62}$$

For the two-body to two-body scattering, we can define the partial wave amplitude a_J as

$$\mathcal{M}(i \to f) = 16\pi \sum_{j=0}^{\infty} (2J+1) a_J P_J(\cos\theta), \tag{2.63}$$

with the Legendre polynomials $P_J(\cos\theta)$. This gives the unitarity bound for the partial wave amplitude

$$\left| a_J^{2\to 2} - \frac{1}{2} \right|^2 + \sum_{n>2} \left| a_J^{2\to n} \right|^2 = \frac{1}{4}, \tag{2.64}$$

in a reprisentation where the elastic scattering amplitudes are diagonal. Thus, the two-body elastic scattering amplitudes lie on a circle of radius $\eta_j/2$ cenreted at $(0, 1/2)$ in the complex plane, with

$$\eta_j = \left(1 - 4 \sum_{n>2} \left| a_J^{2\to n} \right|^2\right)^{1/2}. \tag{2.65}$$

Lee-Quigg-Thacker bound

The high-energy region where $\sqrt{s} \gg m_V$, the longitudinal polarization vector of massive gauge boson V behaves as

$$\epsilon_L^\mu = \frac{p^\mu}{m_V} + \mathcal{O}\left(\frac{m_W}{\sqrt{s}}\right). \tag{2.66}$$

Therefore, it is expected that the amplitudes of four longitudinal gauge bosons scattering behave as

$$\mathcal{M} = A\left(\frac{E}{m_V}\right)^4 + B\left(\frac{E}{m_V}\right)^2 + C. \tag{2.67}$$

Therefore, they potentially break the unitarity bound at a high-energy limit. However, one can show that the coefficients A and B become zero after summing over the relevant Feynman diagrams. Thus, the unitarity bound constrains the magnitude of C, and it gives the upper bound for the mass of the Higgs boson, which is the so-called *Lee-Quigg-Thacker bound* [60,61].

Instead of evaluating the scattering amplitudes of longitudinal gauge bosons, we use the equivalence theorem. This theorem states that the longitudinal gauge bosons can be replaced by the corresponding NG bosons in the high-energy limit,

$$\mathcal{M}(W_L^\pm, Z_L) \simeq \mathcal{M}(G^\pm, G^0) + \mathcal{O}\left(\frac{m_W}{\sqrt{s}}\right). \tag{2.68}$$

In the high-energy limit with $s \gg m_h$, contact interaction diagrams are only relevant. The partial wave amplitudes are given by

$$a_0 = -\frac{G_F m_h^2}{8\pi\sqrt{2}} \begin{pmatrix} 3 & 0 & 0 & 0 \\ 0 & 1 & 0 & 0 \\ 0 & 0 & 1 & 0 \\ 0 & 0 & 0 & 1 \end{pmatrix} \begin{matrix} \frac{1}{\sqrt{2}} \left| G^+G^- + \frac{1}{2}(hh + G^0G^0) \right\rangle \\ \frac{1}{\sqrt{2}} \left| G^+G^- - \frac{1}{2}(hh + G^0G^0) \right\rangle \\ \frac{1}{2} \left| hh - G^0G^0 \right\rangle \\ \left| hG^0 \right\rangle \end{matrix}. \tag{2.69}$$

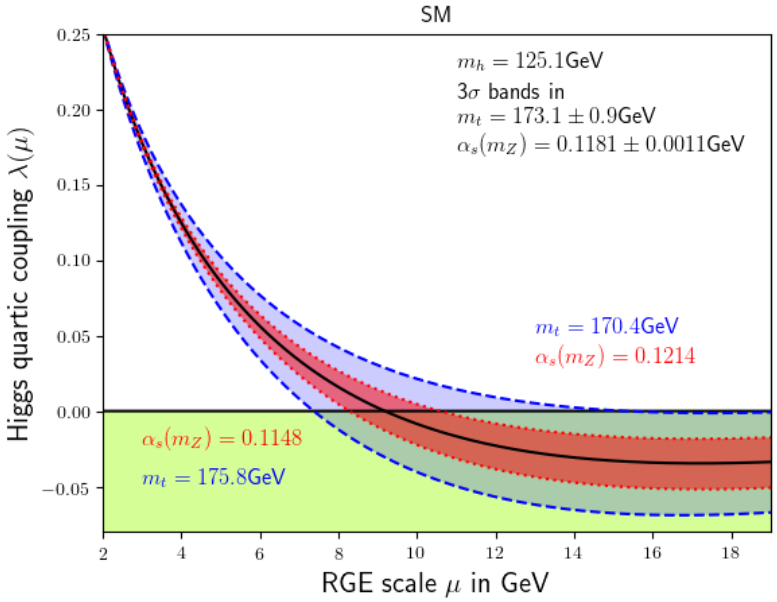

Figure 2.1: RG evolution of λ coupling varying m_t and α_s. We have reproduced Fig.1 in Ref. [62].

Form the largest eigenvalue, we obtain the upper bound for the mass of the Higgs boson as

$$m_h \leq \sqrt{\frac{4\pi\sqrt{2}}{3G_F}} \sim 500\,\text{GeV}. \tag{2.70}$$

The observed Higgs boson mass $m_h \simeq 125\,\text{GeV}$ satisfies the Lee-Quigg-Thacker bound, and we can verify the perturbative calculation within the SM.

2.4.3 Vacuum stability

At LO, the parameters of the Higgs potential in the SM should satisfy the following conditions,

$$\mu^2 > 0, \quad \lambda > 0. \tag{2.71}$$

The first condition is necessary to make the origin of the potential to be unstable and to occur the spontaneous breaking down of the gauge symmetry. The second condition guarantees that the Higgs potential is bounded from below with large field values.

However, the value of the coupling constant is scale-dependent. Therefore, one needs to study the scale dependence of the parameters of the Higgs potential by using the renormalization equation in order to investigate the potential structure at a large energy scale. Fig. 2.1 shows the scale dependence of $\lambda(\mu)$. We have reproduced Fig. 1 in Ref. [62] by using the one-loop beta functions and obtained consistent results. We vary the value of the input parameters m_t and α_s between the $\pm 3\sigma$. Black line in both Fig.2.1 shows the evolution of the λ for central value of m_t and α_s. The blue and red band show 3σ width of m_t and α_s respectively. The value of λ close to zero and breaks vacuum stability around 10^{10} GeV when we use central value of m_t and α_s. However, the value of the vacuum stability breaking scale is highly dependent on the value of the input parameter m_t, and it can be varied between 10^8 and 10^{16} GeV.

2.4.4 Flavor changing neutral current and GIM mechanism

As we have discussed in Subsecs. 2.2.2 and 2.2.3, both of the weak-neutral current and the Yukawa interaction conserve the quark flavors in the SM. Therefore, there is no flavor-changing neutral current (FCNC) in the SM.

FCNC processes such as $K^0 - \bar{K}^0$ mixing occur through the charged-current loop diagram. However, one-loop amplitudes are suppressed not only by the loop factor $1/4\pi$ but also by the mass-squared differences among the virtual quarks such as $(m_c^2 - m_u^2)/v^2$. This is because the mass differences of quarks are the only sources for the flavor violation in the SM since the weak-charged current also conserves the quark flavor if the masses of the quarks are degenerate. Thus, FCNC processes in the SM are highly suppressed as a consequence of the quark flavor structure, and this is the so-called *GIM mechanism* [55].

2.4.5 Electroweak precision test

The electroweak S, T and U parameters [63,64] parametrize the radiative corrections appearing in the two-point functions of weak gauge bosons. Since these parameters are independent of external particles in the process, they are so-called oblique parameters. These parameters are useful to study new particles because they can capture the non-decoupling effects of new particles.

The two-point functions of gauge bosons are composed of the transverse and longitudinal parts,

$$\Pi_{\mu\nu}^{AB}(q) = \left(-g_{\mu\nu} + \frac{q_\mu q_\nu}{q^2}\right)\Pi_T^{AB}(q^2) + \frac{q_\mu q_\nu}{q^2}\Pi_L^{AB}(q^2), \tag{2.72}$$

where $AB = \gamma\gamma,\ Z\gamma,\ ZZ,\ WW$. The transverse part can be parametrized as

$$\Pi_T^{\gamma\gamma}(q^2) = e^2\Pi_T^{QQ}(q^2), \tag{2.73}$$

$$\Pi_T^{Z\gamma}(q^2) = eg_Z\Big[\Pi_T^{3Q}(q^2) - s_W^2\Pi_T^{QQ}(q^2)\Big], \tag{2.74}$$

$$\Pi_T^{ZZ}(q^2) = g_Z^2\Big[\Pi_T^{33}(q^2) - 2s_W^2\Pi_T^{3Q}(q^2) + s_W^4\Pi_T^{QQ}(q^2)\Big], \tag{2.75}$$

$$\Pi_T^{WW}(q^2) = g^2\Pi_T^{11}(q^2). \tag{2.76}$$

The S, T and U parameters are defined by

$$S = 16\pi\,\mathrm{Re}\left[\Pi_{T,\gamma}^{3Q}(m_Z^2) - \Pi_{T,Z}^{33}(0)\right], \tag{2.77}$$

$$T = \frac{4\sqrt{2}G_F}{\alpha_{\mathrm{em}}}\,\mathrm{Re}\left[\Pi_T^{33}(0) - \Pi_T^{11}(0)\right], \tag{2.78}$$

$$U = 16\pi\,\mathrm{Re}\left[\Pi_{T,Z}^{33}(0) - \Pi_{T,W}^{11}(0)\right], \tag{2.79}$$

with

$$\Pi_{T,V}^{AB}(q^2) = \frac{\Pi_T^{AB}(q^2) - \Pi_T^{AB}(m_V^2)}{q^2 - m_V^2}. \tag{2.80}$$

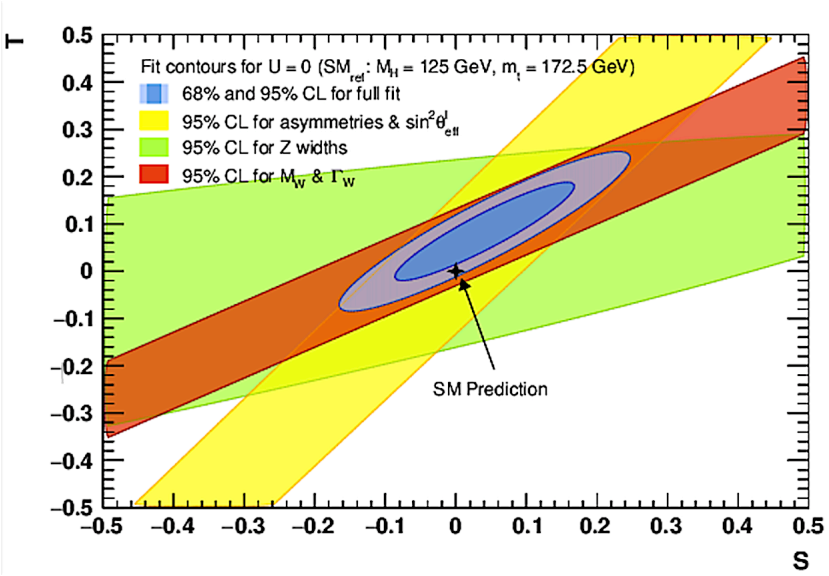

Figure 2.2: Constraints in the oblique parameters S and T fixing $U = 0$ (blue contour). The masses of Higgs boson and top quark are $m_h = 125$ GeV and $m_t = 172.5$ GeV, respectively. Individual constraints are also shown from the asymmetry and direct $\sin^2\theta^\ell_{\rm eff}$ measurements (yellow), the Z partial and total widths (green) and W mass and width (red). This figure is taken from Ref. [65].

In terms of the two-point functions of γ, Z and W bosons, S, T and U parameters are given by

$$\frac{\alpha}{4s_W^2 c_W^2} S = -\,\mathrm{Re}\left[\frac{\Pi_T^{ZZ}(m_Z^2) - \Pi_T^{ZZ}(0)}{m_Z^2} - \frac{c_W^2 - s_W^2}{c_W s_W}\frac{\Pi_T^{Z\gamma}(m_Z^2)}{m_Z^2} - \frac{\Pi_T^{\gamma\gamma}(m_Z^2)}{m_Z^2}\right], \tag{2.81}$$

$$\alpha T = -\,\mathrm{Re}\left[\frac{\Pi_T^{WW}(0)}{m_W^2} - \frac{\Pi_T^{ZZ}(0)}{m_Z^2}\right], \tag{2.82}$$

$$\frac{\alpha}{4s_W^2} U = -\,\mathrm{Re}\left[\frac{\Pi_T^{WW}(m_W^2) - \Pi_T^{WW}(0)}{m_W^2} - c_W^2\frac{\Pi_T^{ZZ}(m_Z^2) - \Pi_T^{ZZ}(0)}{m_Z^2} - 2s_W c_W\frac{\Pi_T^{Z\gamma}(m_Z^2)}{m_Z^2} - s_W^2\frac{\Pi_T^{\gamma\gamma}(m_Z^2)}{m_Z^2}\right]. \tag{2.83}$$

These parameters have been studied by the electroweak precision tests at LEP/SLC experiments, and they provided the information of masses of top quark and Higgs boson even before their discovery. Fig. 2.2 taken from Ref. [65] shows that the global fit for S and $T$the parameter. We can see that the SM predictions for S and T parameter with observed Higgs boson and top quark masses, $m_h = 125$ GeV and $m_t = 172.5$ GeV, are consistent with the current experimental data at 95% CL.

2.4.6 Decay of Higgs boson

The Higgs couplings to gauge bosons and fermions are proportional to their masses. Therefore, the Higgs boson tends to decay into heavy particles if such decay modes are kinematically allowed. We here qualitatively discuss the decay property of the Higgs boson, while the theoretical calculations including the higher-order corrections are discussed in Chapter 5.

The theoretical predictions for the Higgs branching ratio including the electroweak and QCD higher-order corrections have been performed [67]. We quote the recommended value

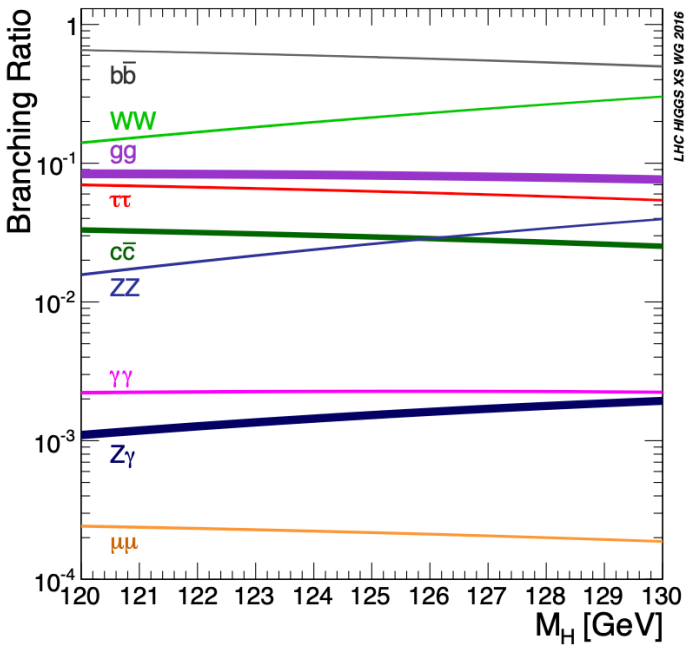

Figure 2.3: The theoretical predictions for the Higgs branching ratio including the electroweak and QCD higher-order corrections. This figure is taken from Ref. [66].

$b\bar{b}$	$\tau\bar{\tau}$	$\mu\bar{\mu}$	$c\bar{c}$	gg	$\gamma\gamma$	$Z\gamma$	WW	ZZ
58.2%	6.27%	0.0218%	2.89%	8.19%	0.227%	0.153%	21.4%	2.62%

Table 2.4: The theoretical predictions for the branching ratios of the Higgs boson with $m_h = 125$ GeV. The predicted total width is 4.09 MeV. These values are taken from Ref. [66]. We omit the estimated errors for simplicity.

for the Higgs branching ratio provided by the LHC Higgs Cross section Working Group [67]. These results have been evaluated by using the programs `HDECAY` [68, 69] and `PROPHECY4F` [70]. `HDECAY` evaluates the partial decay width for the Higgs two-body decays into a pair of fermions $h \to f\bar{f}$ and on-shell gauge boson pair $h \to VV$, as well as the loop-induced processes $h \to \gamma\gamma$, $Z\gamma$, gg. On the other hand, `PROPHECY4F` evaluates those for the Higgs off-shell four-body decays $h \to V^*V^* \to 4f$.

Fig. 2.3 taken from Ref. [66] shows the theoretical predictions for the branching ratio of the Higgs boson including the higher-order corrections as a function of its mass. The bands for each line show the respective uncertainties estimated by considering both the theoretical and the parametric uncertainties. The former comes from the experimental error for input parameters, while the latter comes from missing the higher-order corrections. The detail of the higher-order calculations and estimation of uncertainties are explained in Ref. [67]. We also list the predicted values for the Higgs branching ratio with the discovered mass $m_h = 125$ GeV in Table 2.4. These values are taken from Ref. [66].

Chapter 3

Review of the extended Higgs models

In this chapter, we review extended Higgs models. Before moving on to the descriptions of each extended Higgs model, we give the motivations for studying the extended Higgs sectors. We also discuss the electroweak rho parameter in the extended Higgs models and introduce the HSM, the 2HDM and the IDM.

Unraveling the structure of the Higgs sector is one of the promising ways to approach a more fundamental theory. While the SM-like Higgs boson was found, the structure of the Higgs sector is still a mystery. There is no theoretical principle to insist on the minimal structure of the Higgs sector as introduced in the SM. In addition, non-minimal Higgs sectors are often introduced in various new physics models, which can solve problems beyond the SM. Therefore, the determination of the Higgs sector is one of the important tasks to narrow down a scenario of new physics.

Although there are various ways to extend the Higgs sector in general, the electroweak rho parameter constrains the possible multiplet structure of the extended Higgs models. The rho parameter is defined by

$$\rho = \frac{m_W^2}{m_Z^2 \cos^2 \theta_W}. \tag{3.1}$$

It is unity at the tree level in the SM. On the other hand, it deviates from unity in extended Higgs models in general. The rho parameter at the tree level is given by

$$\rho_{\text{tree}} = \frac{\sum_i [T_i(T_i+1) - Y_i^2] v_i^2}{2\sum_i Y_i^2 v_i^2}, \tag{3.2}$$

in the model with an arbitrary number of scalar fields ϕ_i with a hypercharge Y_i, an isospin T_i and a VEV v_i. Since the observed value of the rho parameter is close to unity, the extended Higgs models in which the rho parameter becomes unity at the tree level are promising.

There are two ways to make the rho parameter unity at the tree level. The first way is introducing the Higgs multiplets which satisfy

$$T_i(T_i+1) - 3Y_i^2 = 0. \tag{3.3}$$

In such models, the rho parameter becomes unity independently of the value of Higgs VEVs. The HSM and 2HDM belong to this class. The second way is assuming an alignment among the Higgs VEVs. The Georgi-Machacek (GM) model [71], in which we introduce the additional real and complex triplet fields with $Y_i = 0$ and $Y_i = 1$, belongs to this class. We note that the rho parameter does not change if additional Higgs multiplets do not develop the VEVs, such as the IDM.

In this thesis, we study the HSM, the 2HDM and the IDM in detail as a representative of the extended Higgs models.

3.1 Higgs singlet model

In the HSM, we have one isospin doublet scalar field Φ with the hypercharge $Y = 1/2$ and one real singlet field S with $Y = 0$. The Lagrangian of the HSM is given by

$$\mathcal{L}_{\rm HSM} = \mathcal{L}_{\rm SM} + (\partial_\mu S)^2 - V_{\rm HSM}(\Phi, S), \tag{3.4}$$

where $\mathcal{L}_{\rm SM}$ is the Lagrangian of the SM without the Higgs potential. The most general Higgs potential is given by

$$\begin{aligned} V_{\rm HSM}(\Phi, S) = {} & m_\Phi^2|\Phi|^2 + \lambda|\Phi|^4 + \mu_{\Phi S}|\Phi|^2 S + \lambda_{\Phi S}|\Phi|^2 S^2 \\ & + t_S S + m_S^2 S^2 + \mu_S S^3 + \lambda_S S^4, \end{aligned} \tag{3.5}$$

where all the parameters are real.

We parametrize these scalar fields as

$$\Phi = \begin{pmatrix} G^+ \\ \frac{1}{\sqrt{2}}(v + \phi + iG^0) \end{pmatrix}, \quad S = v_S + s. \tag{3.6}$$

where v is the VEV of the doublet field which is related to the Fermi constant by $v = (\sqrt{2}G_F)^{-1/2}$, while v_S is the VEV of the singlet field. The component fields $G^\pm$ and G^0 in the doublet field correspond to the NG bosons. We can take any value of v_S without changing physical results [72].

The tadpole terms for ϕ and s are given by

$$T_\phi = v\big[m_\Phi^2 + \lambda v^2 + v_S(\lambda_{\Phi S} v_S + \mu_{\Phi S})\big], \tag{3.7}$$

$$T_S = t_s + \frac{1}{2}\mu_{\Phi S} v^2 + v_S\big[\lambda_{\Phi S} v^2 + 2m_S^2 + 3\mu_S v_S + 4\lambda_S v_S^2\big]. \tag{3.8}$$

By imposing the stational conditions $T_\Phi = T_S = 0$, m_Φ^2 and t_S are written as,

$$m_\Phi^2 = -\lambda v^2 - v_S(\lambda_{\Phi S} v_S + \mu_{\Phi S}), \tag{3.9}$$

$$t_S = -\frac{1}{2}\mu_{\Phi S} v^2 - v_S\big[\lambda_{\Phi S} v^2 + 2m_S^2 + 3\mu_S v_S + 4\lambda_S v_S^2\big]. \tag{3.10}$$

After solving the tadpole conditions, the mass matrix of the neutral scalar fields are given by

$$\mathcal{L} \supset -\frac{1}{2}(s, \phi)\begin{pmatrix} M_{11}^2 & M_{12}^2 \\ M_{12}^2 & M_{22}^2 \end{pmatrix}\begin{pmatrix} s \\ \phi \end{pmatrix}, \tag{3.11}$$

where

$$M_{11}^2 = M^2 + \lambda_{\Phi S} v^2, \quad M_{22}^2 = 2\lambda v^2, \quad M_{12}^2 = (2\lambda_{\Phi S} v_S + \mu_{\Phi S})v, \tag{3.12}$$

with

$$M^2 = 2m_S^2 + v_S(6\mu_S + 12\lambda_S v_S). \tag{3.13}$$

The mass eigenstates of the neutral scalar fields are defined by introducing the mixing angle α as

$$\begin{pmatrix} s \\ \phi \end{pmatrix} = R(\alpha)\begin{pmatrix} H \\ h \end{pmatrix} \quad \text{with} \quad R(\theta) = \begin{pmatrix} c_\theta & -s_\theta \\ s_\theta & c_\theta \end{pmatrix}. \tag{3.14}$$

We define the domain of α as $-\pi/2 \leq \alpha \leq \pi/2$. The squared masses of neutral Higgs bosons and mixing angle are given by

$$m_H^2 = M_{11}^2 c_\alpha^2 + M_{22}^2 s_\alpha^2 + M_{12}^2 s_{2\alpha}, \tag{3.15}$$

$$m_h^2 = M_{11}^2 s_\alpha^2 + M_{22}^2 c_\alpha^2 - M_{12}^2 s_{2\alpha}, \tag{3.16}$$

$$\tan 2\alpha = \frac{2M_{12}^2}{M_{11}^2 - M_{22}^2}, \tag{3.17}$$

We identify h as the discovered Higgs boson with a mass of 125 GeV.

We can replace the parameters λ, m_S^2 and $\mu_{\Phi S}$ with m_H^2, m_h^2 and α by using Eqs. (3.15)-(3.17) as

$$\lambda = \frac{1}{2}(m_h^2 c_\alpha^2 + m_H^2 s_\alpha^2), \tag{3.18}$$

$$m_S^2 = \frac{m_H^2 c_\alpha^2}{2} + \frac{m_h^2 s_\alpha^2}{2} - \frac{1}{2}\lambda_{\Phi S} v^2 - 3 v_S(\mu_S + 2\lambda_S v_S), \tag{3.19}$$

$$\mu_{\Phi S} = \frac{(m_H^2 - m_h^2) s_{2\alpha}}{2v} - 2\lambda_{\Phi S} v_S. \tag{3.20}$$

We choose the following five parameters to be the free input parameters in the HSM:

$$m_H, \quad \lambda_{\Phi S}, \quad \mu_S, \quad \lambda_S, \quad c_\alpha, \tag{3.21}$$

and the two parameters m_h and v are fixed by experiments. If the Higgs potential respects an exact discrete Z_2 symmetry, the t_S, μ_S and $\mu_{\Phi S}$ terms are forbidden. This corresponds to the case with $\alpha \to 0$ and $\mu_S \to 0$.

The kinetic terms of scalar fields are given by

$$\mathcal{L}_{\rm kin}^{\rm HSM} = |D_\mu \Phi|^2 + \frac{1}{2}(\partial_\mu S)^2, \tag{3.22}$$

where D_μ is the covariant derivative for the Higgs doublet. The gauge-gauge-scalar type interaction terms are given by

$$\mathcal{L}_{\rm kin}^{\rm HSM} \supset g m_W (c_\alpha W_\mu^+ W^{-\mu} h + s_\alpha W_\mu^+ W^{-\mu} H) + \frac{g_Z m_Z}{2}(c_\alpha Z_\mu Z^\mu h + s_\alpha Z_\mu Z^\mu H). \tag{3.23}$$

The Yukawa interaction terms are the same as those in the SM and given by

$$\mathcal{L}_{\rm Y}^{\rm HSM} = -Y_u \overline{Q}_L \widetilde{\Phi} u_R - Y_d \overline{Q}_L \Phi d_R - Y_e \overline{L}_L \Phi e_R + \text{h.c.}. \tag{3.24}$$

The interaction terms for h and H with fermions are given by

$$\mathcal{L}_{\rm Y}^{\rm HSM} \supset -\sum_{f=u,d,e} \frac{m_f}{v}(c_\alpha \bar{f} f h + s_\alpha \bar{f} f H). \tag{3.25}$$

We note that the SM-like Higgs boson couplings with the SM particles are universally suppressed by c_α as compared to those SM values.

The parameters in the Higgs potential are constrained by perturbative unitarity, vacuum stability and the conditions to avoid wrong vacua. For the perturbative unitarity bound, there are four independent eigenvalues given in Refs. [73, 74].

$$a_{1,\pm}^0 = \frac{1}{16\pi}\left(3\lambda + 6\lambda_S \pm \sqrt{(3\lambda - 6\lambda_S)^2 + 4\lambda_{\Phi S}^2}\right), \tag{3.26}$$

$$a_2^0 = \frac{1}{8\pi}\lambda, \tag{3.27}$$

$$a_3^0 = \frac{1}{8\pi}\lambda_{\Phi S}. \tag{3.28}$$

The necessary and sufficient conditions to satisfy vacuum stability are given by [75]

$$\lambda_\Phi > 0, \quad \lambda_S > 0, \quad 2\sqrt{\lambda_\Phi \lambda_S} + \lambda_{\Phi S} > 0. \tag{3.29}$$

For the conditions to avoid wrong vacua can be found in Refs. [72, 76, 77].

3.2 Two Higgs doublet model

In the 2HDM, we have two isospin doublet scalar fields Φ_1 and Φ_2 with the hypercharge $Y = 1/2$. The Lagrangian of the 2HDM is given by

$$\mathcal{L}_{\rm 2HDM} = \mathcal{L}_{\rm SM} + \mathcal{L}^{\rm 2HDM}_{\rm kin}(\Phi_1, \Phi_2) + \mathcal{L}^{\rm 2HDM}_{\rm Y}(\Phi_1, \Phi_2) - V_{\rm 2HDM}(\Phi_1, \Phi_2), \tag{3.30}$$

where $\mathcal{L}_{\rm SM}$ is the Lagrangian of the SM without the Higgs fields.

In the most general 2HDM, flavor-changing neutral currents (FCNCs) appear at tree level, and it is severely constrained by experiments. In order to avoid such FCNCs, we introduce a discrete Z_2 symmetry, where two doublets transform as $\Phi_1 \to \Phi_1$ and $\Phi_2 \to -\Phi_2$ [78, 79]. One can introduce the soft breaking term of the Z_2 symmetry in the Higgs potential without spoiling the desirable property of the flavor sector.

The most general Higgs potential under the softly-broken Z_2 symmetry is given by

$$\begin{aligned} V_{\rm 2HDM}(\Phi_1, \Phi_2) = {} & m_1^2 |\Phi_1|^2 + m_2^2 |\Phi_2|^2 - m_3^2 \Big(\Phi_1^\dagger \Phi_2 + \text{h.c.} \Big) \\ & + \frac{1}{2}\lambda_1 |\Phi_1|^4 + \frac{1}{2}\lambda_2 |\Phi_2|^4 + \lambda_3 |\Phi_1|^2 |\Phi_2|^2 + \lambda_4 \Big| \Phi_1^\dagger \Phi_2 \Big|^2 \\ & + \frac{1}{2}\lambda_5 \left[\Big(\Phi_1^\dagger \Phi_2 \Big)^2 + \text{h.c.} \right]. \end{aligned} \tag{3.31}$$

Although m_3^2 and λ_5 are generally complex, we take them to be real and consider the CP-conserving case for simplicity.

We parametrize the doublet fields as

$$\Phi_i = \begin{pmatrix} \omega_i^+ \\ \frac{1}{\sqrt{2}}(v_i + h_i + i z_i) \end{pmatrix}, \quad (i = 1, 2), \tag{3.32}$$

where v_1 and v_2 are the VEVs of two doublets with $v = \sqrt{v_1^2 + v_2^2}$. We define the ration of VEVs as $\tan\beta = v_2/v_1$.

The tadpole terms for h_1 and h_2 are given by

$$T_1 = v c_\beta \left[-m_1^2 + M^2 s_\beta^2 - \frac{v^2}{2}(\lambda_1 c_\beta^2 + \lambda_{345} s_\beta^2) \right], \tag{3.33}$$

$$T_2 = v s_\beta \left[-m_2^2 + M^2 c_\beta^2 - \frac{v^2}{2}(\lambda_2 s_\beta^2 + \lambda_{345} c_\beta^2) \right], \tag{3.34}$$

where $\lambda_{345} = \lambda_3 + \lambda_4 + \lambda_5$. The dimensionful parameter $M^2 = m_3^2/(s_\beta c_\beta)$ describes the softly-breaking scale of the Z_2 symmetry. Since we are considering the charge-conserving vacuum, there are no terms linear in the charged fields ω_i^+. In addition, there are no terms linear in the CP-odd fields z_i due to the CP-conservation in the Higgs potential. By imposing the stationary conditions $T_1 = T_2 = 0$, m_1^2 and m_2^2 are written as,

$$m_1^2 = M^2 s_\beta^2 - \frac{v^2}{2}(\lambda_1 c_\beta^2 + \lambda_{345} s_\beta^2), \tag{3.35}$$

$$m_2^2 = M^2 c_\beta^2 - \frac{v^2}{2}(\lambda_2 s_\beta^2 + \lambda_{345} c_\beta^2). \tag{3.36}$$

After solving the stationary conditions, the mass matrices of the Higgs fields are given by

$$V_{\rm 2HDM} \supset \frac{1}{2}\begin{pmatrix} h_1 & h_2 \end{pmatrix} M_h^2 \begin{pmatrix} h_1 \\ h_2 \end{pmatrix} + \frac{1}{2}\begin{pmatrix} z_1 & z_2 \end{pmatrix} M_z^2 \begin{pmatrix} z_1 \\ z_2 \end{pmatrix} + \begin{pmatrix} \omega_1^- & \omega_2^- \end{pmatrix} M_\omega^2 \begin{pmatrix} \omega_1^+ \\ \omega_2^+ \end{pmatrix}, \tag{3.37}$$

where

$$M_h^2 = \begin{pmatrix} m_{12}^2 \frac{v_2}{v_1} + \lambda_1 v_1^2 & -m_{12}^2 + \lambda_{345} v_1 v_2 \\ -m_{12}^2 + \lambda_{345} v_1 v_2 & m_{12}^2 \frac{v_1}{v_2} + \lambda_2 v_2^2 \end{pmatrix} + \begin{pmatrix} T_1/v_1 & 0 \\ 0 & T_2/v_2 \end{pmatrix}, \tag{3.38}$$

$$M_z^2 = \left(\frac{m_{12}^2}{v_1 v_2} - \lambda_5 \right) \begin{pmatrix} v_2^2 & -v_1 v_2 \\ -v_1 v_2 & v_1^2 \end{pmatrix} + \begin{pmatrix} T_1/v_1 & 0 \\ 0 & T_2/v_2 \end{pmatrix}, \tag{3.39}$$

$$M_\omega^2 = \frac{1}{2}\left(\frac{m_{12}^2}{v_1 v_2} - \frac{\lambda_4 + \lambda_5}{2} \right) \begin{pmatrix} v_2^2 & -v_1 v_2 \\ -v_1 v_2 & v_1^2 \end{pmatrix} + \frac{1}{2}\begin{pmatrix} T_1/v_1 & 0 \\ 0 & T_2/v_2 \end{pmatrix}, \tag{3.40}$$

Since M_z and M_ω have the same structure, we can diagonalize them by using the same angle β, while we need to introduce another angle α to diagonalize CP even states. The mass eigenstates of the Higgs fields are defined as

$$\begin{pmatrix} \omega_1^\pm \\ \omega_2^\pm \end{pmatrix} = R(\beta) \begin{pmatrix} G^\pm \\ H^\pm \end{pmatrix}, \quad \begin{pmatrix} z_1 \\ z_2 \end{pmatrix} = R(\beta) \begin{pmatrix} G^0 \\ A \end{pmatrix}, \quad \begin{pmatrix} h_1 \\ h_2 \end{pmatrix} = R(\alpha) \begin{pmatrix} H \\ h \end{pmatrix}, \tag{3.41}$$

where $H^\pm$ and A are the charged and CP-odd Higgs bosons respectively, while H and h are the CP-even Higgs bosons. We define the domain of β to be $0 \leq \beta \leq \pi/2$. We identify h as the discovered Higgs boson with a mass of 125 GeV. The squared masses of the charged and CP-odd Higgs bosons are given by

$$m_{H^\pm}^2 = M^2 - \frac{1}{2}(\lambda_4 + \lambda_5)v^2, \quad m_A^2 = M^2 - \lambda_5 v^2. \tag{3.42}$$

The squared masses of the neutral Higgs bosons and the mixing angle $\beta - \alpha$ are given by

$$m_H^2 = M_{11}^2 c_{\beta-\alpha}^2 + M_{22}^2 s_{\beta-\alpha}^2 - M_{12}^2 s_{2(\beta-\alpha)}, \tag{3.43}$$

$$m_h^2 = M_{11}^2 s_{\beta-\alpha}^2 + M_{22}^2 c_{\beta-\alpha}^2 + M_{12}^2 s_{2(\beta-\alpha)}, \tag{3.44}$$

$$\tan 2(\beta - \alpha) = -\frac{2M_{12}^2}{M_{11}^2 - M_{22}^2}, \tag{3.45}$$

where M_{ij}^2 $(i, j = 1, 2)$ are the squared mass matrix elements for the CP-even scalar states in the Higgs basis [80] $(h_1, h_2)R(\beta)$:

$$M_{11}^2 = (\lambda_1 c_\beta^4 + \lambda_2 s_\beta^4)v^2 + \frac{1}{2}\lambda_{345} v^2 s_{2\beta}^2, \tag{3.46}$$

$$M_{22}^2 = M^2 + \frac{1}{4}(\lambda_1 + \lambda_2 - 2\lambda_{345})v^2 s_{2\beta}^2, \tag{3.47}$$

$$M_{12}^2 = -\frac{1}{2}(\lambda_1 c_\beta^2 - \lambda_2 s_\beta^2 - \lambda_{345} c_{2\beta})v^2 s_{2\beta}. \tag{3.48}$$

We define the domain of $\beta - \alpha$ to be $0 \leq \beta - \alpha \leq \pi$ so that $s_{\beta-\alpha}$ is always positive and $c_{\beta-\alpha}$ has the opposite sign from M_{12}^2 [81]. The eight parameters in the Higgs potential are expressed by the following six input parameters:

$$m_H, \quad m_A, \quad m_{H^\pm}, \quad M^2, \quad \tan\beta, \quad s_{\beta-\alpha}, \tag{3.49}$$

	Z_2 charge							Mixing factor		
	Φ_1	Φ_2	Q_L	L_L	u_R	d_R	e_R	ζ_u	ζ_d	ζ_e
Type-I	+	−	+	+	−	−	−	$\cot\beta$	$\cot\beta$	$\cot\beta$
Type-II	+	−	+	+	−	+	+	$\cot\beta$	$-\tan\beta$	$-\tan\beta$
Type-X (lepton specific)	+	−	+	+	−	−	+	$\cot\beta$	$\cot\beta$	$-\tan\beta$
Type-Y (flipped)	+	−	+	+	−	+	−	$\cot\beta$	$-\tan\beta$	$\cot\beta$

Table 3.1: Charge assignment of the softly-broken Z_2 symmetry and the mixing factors in Yukawa interactions.

and the two parameters m_h and v are fixed by experiments. In addition, we have a degree of freedom of the sign of $c_{\beta-\alpha}$.

The kinetic terms of the Higgs doublets are given by

$$\mathcal{L}_{\rm kin}^{\rm 2HDM} = |D_\mu \Phi_1|^2 + |D_\mu \Phi_2|^2. \tag{3.50}$$

In the mass eigenbasis of the Higgs bosons, the gauge-gauge-scalar type interaction terms are given by

$$\mathcal{L}_{\rm kin}^{\rm 2HDM} \supset g m_W (s_{\beta-\alpha} W_\mu^+ W^{-\mu} h + c_{\beta-\alpha} W_\mu^+ W^{-\mu} H) + \frac{g_Z m_Z}{2}(s_{\beta-\alpha} Z_\mu Z^\mu h + c_{\beta-\alpha} Z_\mu Z^\mu H). \tag{3.51}$$

The Yukawa interaction terms under the Z_2 symmetry are given by

$$\mathcal{L}_{\rm Y}^{\rm 2HDM} = -Y_u \overline{Q}_L \widetilde{\Phi}_u u_R - Y_d \overline{Q}_L \Phi_d d_R - Y_e \overline{L}_L \Phi_e e_R + \text{h.c.}, \tag{3.52}$$

where $\Phi_{u,d,e}$ are either Φ_1 or Φ_2. As in Table 3.1, there are four types of Yukawa interactions according to the Z_2 charge assignment [82, 83]. The interaction terms for the physical Higgs bosons with the fermions are given by

$$\begin{aligned}\mathcal{L}_{\rm Y}^{\rm 2HDM} \supset & -\sum_{f=u,d,e} \frac{m_f}{v}\big[(s_{\beta-\alpha}+\zeta_f c_{\beta-\alpha})\bar{f}fh + (c_{\beta-\alpha}-\zeta_f s_{\beta-\alpha})\bar{f}fH - 2iI_f\zeta_f \bar{f}\gamma_5 f A\big] \\ & + \frac{\sqrt{2}}{v}\big[V_{ud}\bar{u}(m_u\zeta_u P_L - m_d\zeta_d P_R)dH^+ - m_e\zeta_e\bar{\nu}P_R e H^+ + \text{h.c.}\big],\end{aligned} \tag{3.53}$$

with $I_f = 1/2$ $(-1/2)$ for $f = u$ (d, e) and V_{ud} is the Cabbibo–Kobayashi–Maskawa matrix element.

The parameters in the Higgs potential are constrained by perturbative unitarity, vacuum stability and the condition to avoid wrong vacua. For the perturbative unitarity bound, there are twelve independent eigenvalues of the s-wave amplitude matrix [84–87].

$$a_{1,\pm}^0 = \frac{1}{32\pi}\Big[3(\lambda_1+\lambda_2) \pm \sqrt{9(\lambda_1-\lambda_2)^2 + 4(2\lambda_3+\lambda_4)^2}\Big], \tag{3.54}$$

$$a_{2,\pm}^0 = \frac{1}{32\pi}\Big[(\lambda_1+\lambda_2) \pm \sqrt{(\lambda_1-\lambda_2)^2 + 4\lambda_4^2}\Big], \tag{3.55}$$

$$a_{3,\pm}^0 = \frac{1}{32\pi}\Big[(\lambda_1+\lambda_2) \pm \sqrt{(\lambda_1-\lambda_2)^2 + 4\lambda_5^2}\Big], \tag{3.56}$$

$$a_{4,\pm}^0 = \frac{1}{16\pi}(\lambda_3 + 2\lambda_4 \pm 3\lambda_5), \tag{3.57}$$

$$a_{5,\pm}^0 = \frac{1}{16\pi}(\lambda_3 \pm \lambda_4), \tag{3.58}$$

$$a_{6,\pm}^0 = \frac{1}{16\pi}(\lambda_3 \pm \lambda_5). \tag{3.59}$$

The vacuum stability bound is sufficiently and necessarily satisfied by imposing the following conditions [88–92]

$$\lambda_1 > 0, \quad \lambda_2 > 0, \quad \sqrt{\lambda_1\lambda_2} + \lambda_3 + \mathrm{MIN}(0,\ \lambda_4+\lambda_5,\ \lambda_4-\lambda_5) > 0. \tag{3.60}$$

In addition, the wrong vacua can be avoided by taking $M^2 \geq 0$ [93]. We thus only take the positive value of M^2 in the following discussion.

3.3 Inert doublet model

The contents of the Higgs bosons in the IDM are the same as those in the 2HDM. In the IDM, we assume an exact Z_2 symmetry and prohibit the m_3^2 term in the Higgs potential which softly breaks the Z_2 symmetry in the 2HDM. We also assume that the second Higgs doublet Φ_2 does not develop the VEV to avoid the spontaneous breaking down of the Z_2 symmetry.

We parametrize the doublets as

$$\Phi_1 = \begin{pmatrix} G^+ \\ \frac{1}{\sqrt{2}}(v+h+iG^0) \end{pmatrix}, \quad \Phi_2 = \begin{pmatrix} H^+ \\ \frac{1}{\sqrt{2}}(H+iA) \end{pmatrix}. \tag{3.61}$$

The squared masses of the Higgs bosons are given by

$$m_h^2 = \lambda_1 v^2, \tag{3.62}$$

$$m_H^2 = M^2 + \frac{1}{2}(\lambda_3+\lambda_4+\lambda_5)v^2, \tag{3.63}$$

$$m_A^2 = M^2 + \frac{1}{2}(\lambda_3+\lambda_4-\lambda_5)v^2, \tag{3.64}$$

$$m_{H^\pm}^2 = M^2 + \frac{1}{2}\lambda_3 v^2, \tag{3.65}$$

where $M^2 \equiv m_2^2$. We note that in addition to the absence of the m_3^2 term, there is no tadpole condition for H. Therefore, the mass formulae for the scalar bosons are different from those in the 2HDM. We choose the following five parameters to be the free input parameters in the IDM:

$$m_H, \quad m_A, \quad m_{H^\pm}, \quad M^2, \quad \lambda_2, \tag{3.66}$$

and the two parameters m_h and v are fixed by experiments.

The parameters in the Higgs potential are constrained by perturbative unitarity, vacuum stability and the condition to guarantee the inert vacuum. The same conditions for perturbative unitarity and vacuum stability in the 2HDM can be applied to the IDM, because these bounds are given in terms of the scalar quartic couplings. In addition, there is the condition to guarantee the inert vacuum with $(\langle\Phi_1^0\rangle\ ,\ \langle\Phi_2^0\rangle) = (v/\sqrt{2}, 0)$ [94],

$$\frac{m_1^2}{\sqrt{\lambda_1}} < \frac{M^2}{\sqrt{\lambda_2}}. \tag{3.67}$$

Since the tadpole condition makes m_1^2 negative, and the vacuum stability condition constraints λ_1 and λ_2 to be positive, the condition given in Eq. (3.67) is satisfied by taking $M^2 > 0$. We refer to this condition as the one to avoid wrong vacua, according to the other two models discussed above.

Finally, we summarize the scaling factors for the SM-like Higgs boson couplings to the weak bosons κ_V and the fermions κ_f in Table 3.2.

	HSM	2HDMs	IDM
κ_V	c_α	$s_{\beta-\alpha}$	1
κ_f	c_α	$s_{\beta-\alpha} + \zeta_f c_{\beta-\alpha}$	1

Table 3.2: Scaling factors for the SM-like Higgs boson couplings in the extended Higgs models.

Chapter 4

Renormalization

In this chapter, we review the renormalization of the ultraviolet (UV) divergences in higher-order calculations.

Before moving to the detail of the renormalization scheme, we give a qualitative discussion here. We separate the parameters in the bare Lagrangian into the renormalized parameters and counterterms

$$g_B = Z_g g = g + \delta g. \tag{4.1}$$

The finite renormalized parameters are fixed by a set of renormalization conditions, and counterterms absorb the UV divergences in higher-order corrections. In addition, we redefine the bare fields in terms of the renormalized fields.

$$\phi_0 = Z_\phi^{1/2} \phi. \tag{4.2}$$

Expanding the renormalization constant as

$$Z_i = 1 + \delta Z_i, \tag{4.3}$$

the Lagrangian is split into a renomalized and counterterm part

$$\mathcal{L}(\phi_0, g_0) = \mathcal{L}(\phi, g) + \delta\mathcal{L}(\phi, g, \delta Z_\phi, \delta g), \tag{4.4}$$

which results for all Green functions to be finite at a given order.

4.1 Renormalization of the standard model

In this section, we review the renormalization scheme for the EWSM which has been developed in Refs. [95, 96]. We choose the particle masses and the fine-structure constant as the physical parameters. The weak-mixing angle θ_W is defined in terms of the masses of the weak gauge bosons

$$s^2_{\theta_W} = 1 - \frac{m_W^2}{m_Z^2}. \tag{4.5}$$

We separate the bare parameters in the symmetric Lagrangian into the physical parameters and the counterterms. For gauge sector,

$$W^a_{\mu,B} = (Z_W)^{1/2} W^a_\mu, \quad B_{\mu,B} = (Z_B)^{1/2} B_\mu, \tag{4.6}$$

$$g_B = Z_g (Z_W)^{-3/2} g, \quad g'_B = Z_{g'} (Z_B)^{-3/2} g'. \tag{4.7}$$

For matter sector

$$\psi^L_{i,B} = (Z^i_L)^{1/2}\psi^L_i, \tag{4.8}$$
$$\psi^R_{i\sigma,B} = (Z^{i\sigma}_R)^{1/2}\psi^R_{i\sigma}, \quad (\sigma = +,-) \tag{4.9}$$
$$y_{i\sigma,B} = (Z_\Phi)^{-1/2} Z^{i\sigma} y_{i\sigma}. \tag{4.10}$$

For Higgs sector

$$\Phi_B = (Z_\Phi)^{1/2}\Phi, \quad v_B = (Z_\Phi)^{1/2}(v - \delta v), \tag{4.11}$$
$$\mu^2_B = (Z_\Phi)^{-1}(\mu^2 - \delta\mu^2), \quad \lambda_B = (Z_\Phi)^{-2} Z_\lambda \lambda. \tag{4.12}$$

4.1.1 Gauge sector

The counterterms of mass eigenstates of gauge bosons are given by

$$W^\pm_{\mu 0} = \left(1 + \frac{1}{2}\delta Z_W\right) W^\pm_\mu, \tag{4.13}$$
$$\begin{pmatrix} Z_{\mu 0} \\ A_{\mu 0} \end{pmatrix} = \begin{pmatrix} 1 + \frac{1}{2}\delta Z_Z & \frac{1}{2}\left(\delta Z_{Z\gamma} - \frac{\delta s^2_W}{c_W s_W}\right) \\ \frac{1}{2}\left(\delta Z_{\gamma Z} + \frac{\delta s^2_W}{c_W s_W}\right) & 1 + \frac{1}{2}\delta Z_\gamma \end{pmatrix} \begin{pmatrix} Z_\mu \\ A_\mu \end{pmatrix}, \tag{4.14}$$

where

$$\begin{pmatrix} \delta Z_Z \\ \delta Z_\gamma \end{pmatrix} = \begin{pmatrix} c^2_W & s^2_W \\ s^2_W & c^2_W \end{pmatrix} \begin{pmatrix} \delta Z_W \\ \delta Z_B \end{pmatrix}, \tag{4.15}$$
$$\delta Z_{Z\gamma} = \delta Z_{\gamma Z} = \frac{c_W s_W}{c^2_W - s^2_W}(\delta Z_Z - \delta Z_\gamma) = s_W c_W (\delta Z_W - \delta Z_B), \tag{4.16}$$
$$\delta Z_{gg'} = s_W c_W (\delta Z_g - \delta Z_{g'}), \tag{4.17}$$
$$\delta Z_Z = \delta Z_\gamma + \frac{c^2_W - s^2_W}{c_W s_W}\delta Z_{\gamma Z}, \tag{4.18}$$
$$\delta Z_W = \delta Z_\gamma + \frac{c_W}{s_W}\delta Z_{\gamma Z}, \tag{4.19}$$
$$\frac{\delta s^2_W}{c_W s_W} = \frac{c_W}{s_W}\left(\frac{\delta m^2_Z}{m^2_Z} - \frac{\delta m^2_W}{m^2_W}\right) = 3\delta Z_{Z\gamma} - 2\delta Z_{gg'}. \tag{4.20}$$

Two point function of gauge bosons are expressed by the sum of longitudinal polarization part and transverse polarization part:

$$\Pi^{\mu\nu}_{VV}(q^2) = \left(-g^{\mu\nu} + \frac{q^\mu q^\nu}{q^2}\right)\Pi^T_{VV}(q^2) + \frac{q^\mu q^\nu}{q^2}\Pi^L_{VV}(q^2). \tag{4.21}$$

At the tree level, in 't Hooft-Feynman gauge, Π^T_{VV} and Π^L_{VV} are given by

$$\Pi^T_{VV} = \frac{i}{q^2 - m^2_V}, \quad \Pi^L_{VV} = \frac{-i}{q^2 - m^2_V}, \tag{4.22}$$

At the one-loop level, the vector boson propagators $\Pi^{\mu\nu}$ $(V = \gamma, Z, W)$ are given by

$$\Pi^{\mu\nu}_{VV}(q^2) = \frac{-ig^{\mu\nu}}{q^2 - m^2_V + \widehat{\Pi}_{VV}(q^2)}, \tag{4.23}$$
$$\Pi^{\mu\nu}_{Z\gamma}(q^2) = -ig^{\mu\nu}\left[\frac{1}{q^2}(-\widehat{\Pi}_{Z\gamma})\frac{1}{q^2 - m_Z}\right], \tag{4.24}$$

where the renormalized two point functions $\widehat{\Pi}_{VV}$ are written as

$$\begin{aligned}
\widehat{\Pi}_{WW}(q^2) &= \Pi^{\rm 1PI}_{WW}(q^2) - \delta m_W^2 + \delta Z_W(q^2 - m_W^2),\\
\widehat{\Pi}_{ZZ}(q^2) &= \Pi^{\rm 1PI}_{ZZ}(q^2) - \delta m_Z^2 + \delta Z_Z(q^2 - m_Z^2),\\
\widehat{\Pi}_{\gamma\gamma}(q^2) &= \Pi^{\rm 1PI}_{\gamma\gamma}(q^2) + \delta Z_\gamma q^2,\\
\widehat{\Pi}_{Z\gamma}(q^2) &= \Pi^{\rm 1PI}_{Z\gamma}(q^2) - \delta Z_{Z\gamma}\left(q^2 - \frac{1}{2}m_Z^2\right) - m_Z^2\frac{\delta s_W^2}{2 s_W c_W}.
\end{aligned}$$

We impose the following five renormalization conditions,

$$\mathrm{Re}\widehat{\Pi}_{WW}(m_W^2) = 0, \quad \mathrm{Re}\widehat{\Pi}_{ZZ}(m_Z^2) = 0, \tag{4.25}$$

$$\frac{d}{dq^2}\widehat{\Pi}_{\gamma\gamma}(q^2)\bigg|_{q^2=0} = 0, \quad \widehat{\Pi}_{\gamma Z}(0) = 0, \tag{4.26}$$

$$\widehat{\Gamma}^{\mu}_{ee\gamma}(q^2 = 0, \not{p}_1 = \not{p}_2 = m_e) = ie\gamma^\mu, \tag{4.27}$$

where $\widehat{\Gamma}^{\mu}_{ee\gamma}$ is the renormalized photon-electron-positron vertex. By these renormalization condition, five independent counter terms, $\delta m_W^2, \delta m_Z^2, \delta Z_\gamma, \delta Z_{\gamma Z}, \delta\alpha_{em}$, are fixed as

$$\delta m_W^2 = \mathrm{Re}\Pi^{\rm 1PI}_{WW}(m_W^2), \quad \delta m_Z^2 = \mathrm{Re}\Pi^{\rm 1PI}_{ZZ}(m_Z^2), \tag{4.28}$$

$$\delta Z_\gamma = -\frac{d}{dq^2}\widehat{\Pi}^{\rm 1PI}_{\gamma\gamma}(q^2)\bigg|_{q^2=0}, \quad \delta Z_{\gamma Z} = -\frac{2}{m_Z^2}\Pi^{\rm 1PI}_{\gamma Z}(0) + \frac{\delta s_W^2}{s_W c_W}, \tag{4.29}$$

$$\frac{\delta e}{e} = \frac{1}{2}\frac{d}{dq^2}\widehat{\Pi}^{\rm 1PI}_{\gamma\gamma}(q^2)\bigg|_{q^2=0} - \frac{s_W}{c_W}\frac{\Pi^{\rm 1PI}_{\gamma Z}(0)}{m_Z^2}. \tag{4.30}$$

The other counterterms are determined as

$$\frac{\delta s_W^2}{c_W s_W} = \frac{c_W}{s_W}\left[\frac{\mathrm{Re}\Pi^{\rm 1PI}_{ZZ}(m_Z)}{m_Z^2} - \frac{\mathrm{Re}\Pi^{\rm 1PI}_{WW}(m_W)}{m_W^2}\right], \tag{4.31}$$

$$\delta Z_Z = -\frac{d}{dq^2}\widehat{\Pi}^{\rm 1PI}_{\gamma\gamma}(q^2)\bigg|_{q^2=0} - \frac{2(c_W^2 - s_W^2)}{c_W s_W}\frac{\Pi^{\rm 1PI}_{\gamma Z}(0)}{m_Z^2} + \frac{c_W^2 - s_W^2}{c_W s_W}\frac{\delta s_W^2}{s_W c_W}, \tag{4.32}$$

$$\delta Z_W = -\frac{d}{dq^2}\widehat{\Pi}^{\rm 1PI}_{\gamma\gamma}(q^2)\bigg|_{q^2=0} - \frac{2c_W}{s_W}\frac{\Pi^{\rm 1PI}_{\gamma Z}(0)}{m_Z^2} + \frac{c_W}{s_W}\frac{\delta s_W^2}{s_W c_W}. \tag{4.33}$$

By the tree-level relation,

$$v_0^2 = \frac{m_{W0}^2 s_{W0}^2}{\pi\alpha_{em0}}, \tag{4.34}$$

we obtain the counterterm δv as

$$\frac{\delta v}{v} = \frac{1}{2}\left[\frac{s_W^2 - c_W^2}{s_W^2}\frac{\mathrm{Re}\Pi^{\rm 1PI}_{WW}(m_W^2)}{m_W^2} + \frac{c_W^2}{s_W^2}\frac{\mathrm{Re}\Pi^{\rm 1PI}_{ZZ}(m_W^2)}{m_Z^2} - \frac{\mathrm{d}\widehat{\Pi}^{\rm 1PI}_{\gamma\gamma}(q^2)}{\mathrm{d}q^2}\bigg|_{q^2=0} + \frac{2s_W}{c_W}\frac{\Pi^{\rm 1PI}_{\gamma Z}(0)}{m_Z^2}\right]. \tag{4.35}$$

In this renormalization scheme, the residue of the gauge boson two-point function is not unity. Therefore, we need to add the extra term $\mathrm{d}\widehat{\Pi}_{VV}(q^2)\big/\mathrm{d}q^2\,\big|_{q^2=m_V^2}$ to the each external $W^\pm$ and Z boson.

4.1.2 Fermion sector

The counterterms of the fermions in the mass eigenstate are given by,

$$m_{f0} = m_f + \delta m_f, \quad \psi_{0L} = \psi_L + \frac{1}{2}\delta Z_L^f \psi_L, \quad \psi_{0R} = \psi_R + \frac{1}{2}\delta Z_R^f \psi_R, \tag{4.36}$$

and for $\psi = \psi_L + \psi_R$,

$$\psi_0 = \psi + \frac{1}{2}\Big(\delta Z_V^f - \delta Z_A^f \gamma_5\Big)\psi, \tag{4.37}$$

with

$$\delta Z_V^f = \frac{1}{2}(\delta Z_L^f + \delta Z_R^f), \quad \delta Z_A^f = \frac{1}{2}(\delta Z_L^f - \delta Z_R^f). \tag{4.38}$$

Two point functions of fermion fields are composed of vector, axial and scalar parts,

$$\Pi_{ff}^{\rm 1PI}(p^2) = \not{p}\Pi_{ff,V}^{\rm 1PI} - \not{p}\gamma_5 \Pi_{ff,A}^{\rm 1PI} + m_f \Pi_{ff,S}^{\rm 1PI}. \tag{4.39}$$

At the one loop level, self energies $\Pi_{ff,V}^{1PI}, \Pi_{ff,A}^{1PI}$ and $\Pi_{ff,S}^{1PI}$ enter the fermion fields propagator S_F^f as follows,

$$S_F^f(p) = \frac{i}{\not{p} - m_f}\left[1 + i(\widehat{\Pi}_{ff,V} + \widehat{\Pi}_{ff,A})\frac{i}{\not{p} - m_f}\right], \tag{4.40}$$

where the renormalized self energies of fermions are given by

$$\widehat{\Pi}_{ff,V} = \not{p}\left(\Pi_{ff,V}^{\rm 1PI}(p^2) + \delta Z_V^f\right) + m_f\left(\Pi_{ff,S}^{1PI}(p^2) - \delta Z_V^f - \frac{\delta m_f}{m_f}\right), \tag{4.41}$$

$$\widehat{\Pi}_{ff,A} = -\not{p}\gamma_5\left(\Pi_{ff,A}^{\rm 1PI}(p^2) + \delta Z_A^f\right). \tag{4.42}$$

We impose the following renormalization conditions,

$$\widehat{\Pi}_{ff,V}(m_f^2) = 0, \quad \frac{d}{d\not{p}}\widehat{\Pi}_{ff,V}(p^2)\Big|_{p^2=m_f^2} = 0, \quad \frac{d}{d\not{p}}\widehat{\Pi}_{ff,A}(p^2)\Big|_{p^2=m_f^2} = 0. \tag{4.43}$$

By these renormalization conditions, three independent counterterms, $\delta m_f, \delta Z_V^f$ and δZ_A^f are determined as

$$\delta m_f = m_f\big[\Pi_{ff,V}^{\rm 1PI}(m_f^2) + \Pi_{ff,S}^{\rm 1PI}(m_f^2)\big], \tag{4.44}$$

$$\delta Z_V^f = -\Pi_{ff,V}^{\rm 1PI}(m_f^2) - 2m_f^2\left[\frac{d}{dp^2}\Pi_{ff,V}^{\rm 1PI}(p^2)\Big|_{p^2=m_f^2} + \frac{d}{dp^2}\Pi_{ff,S}^{\rm 1PI}(p^2)\Big|_{p^2=m_f^2}\right], \tag{4.45}$$

$$\delta Z_A^f = -\Pi_{ff,A}^{\rm 1PI}(m_f^2) + 2m_f^2\,\frac{d}{dp^2}\Pi_{ff,A}^{\rm 1PI}(p^2)\Big|_{p^2=m_f^2}. \tag{4.46}$$

4.1.3 Higgs sector

We shift bare Higgs mass, bare Higgs field and tadpole parameter as follows.

$$m_{h0}^2 = m_h^2 + \delta m_h^2, , \quad h_0 = h + \frac{1}{2}\delta Z_h, , \quad T_{h0} = T_h + \delta T_h. \tag{4.47}$$

At the one-loop level, the tadpole term is

$$i\widehat{T}_h = iT_h + i(T_h^{\rm 1PI} + \delta T_h). \tag{4.48}$$

We renormalize bare parameters such that the tadpole vanishes order by order,

$$T_h = 0, \quad T_h^{\rm 1PI} + \delta T_h = 0. \tag{4.49}$$

The renormalized self energy is defined by

$$\widehat{\Pi}_{hh}(p^2) = \Pi_{hh}^{\rm 1PI}(p^2) + (p^2 - m_h^2)\delta Z_h - \delta m_h^2 + \frac{\delta T_h}{v}. \tag{4.50}$$

We impose the following renormalization conditions,

$$\text{Re }\ \widehat{\Pi}_{hh}(m_h^2) = 0, \quad \left.\frac{{\rm d}\widehat{\Pi}_{hh}(p^2)}{{\rm d}p^2}\right|_{p^2=m_h^2} = 0. \tag{4.51}$$

By these renormalization conditions, two independent counter terms δm_h^2 and δZ_h are fixed as

$$\delta m_h^2 = \Pi_{hh}^{\rm 1PI}(m_h^2) + \frac{\delta T_h}{v}, \quad \delta Z_h = -\left.\frac{{\rm d}\widehat{\Pi}_{hh}^{\rm 1PI}(p^2)}{{\rm d}p^2}\right|_{p^2=m_h^2} \tag{4.52}$$

4.2 Renormalization of the extended Higgs models

4.2.1 Higgs singlet models

In the Higgs singlet model, we have the seven free parameters. We shift the bare parameters as

$$\begin{aligned} &m_{h0}^2 = m_h^2 + \delta m_h^2, \quad m_{H0}^2 = m_H^2 + \delta m_H^2, \quad \alpha_0 = \alpha + \delta\alpha, \\ &\lambda_{\Phi S0} = \lambda_{\Phi S} + \delta\lambda_{\Phi S}, \quad \lambda_{S0} = \lambda_S + \delta\lambda_S, \quad \mu_{S0} = \mu_S + \delta\mu_S. \end{aligned} \tag{4.53}$$

The CP-even scalar fields are shifted as

$$\begin{pmatrix} H_0 \\ h_0 \end{pmatrix} = \begin{pmatrix} 1 + \frac{1}{2}\delta Z_H & \delta C_{hH} + \delta\alpha \\ \delta C_{Hh} - \delta\alpha & 1 + \frac{1}{2}\delta Z_h \end{pmatrix} \begin{pmatrix} H \\ h \end{pmatrix}, \tag{4.54}$$

where $\delta C_{hH} = \delta C_{Hh}$. The tadpole terms are shifted as

$$T_{h0} = T_h + \delta T_h, \quad T_{H0} = T_H + \delta T_H, \tag{4.55}$$

where T_h and T_H are given by

$$\begin{pmatrix} T_s \\ T_\phi \end{pmatrix} = R(\alpha) \begin{pmatrix} T_H \\ T_h \end{pmatrix}. \tag{4.56}$$

At the one-loop level, the renormalized one-point functions are

$$\widehat{T}_h = T_h + T_h^{\rm 1PI} + \delta T_h, \quad \widehat{T}_H = T_H + T_H^{\rm 1PI} + \delta T_H. \tag{4.57}$$

We determine the counterterms such that the tadpole vanishes order by order,

$$T_h = 0, \quad T_h^{\rm 1PI} + \delta T_h = 0, \tag{4.58}$$
$$T_H = 0, \quad T_H^{\rm 1PI} + \delta T_H = 0. \tag{4.59}$$

At the one-loop level, the renormalized two-point functions are given by

$$\widehat{\Pi}_{hh}(p^2) = (p^2 - m_h^2)(1 + \delta Z_h) - \delta m_h^2 + \frac{c_\alpha^2}{v}\delta T_\phi + \Pi_{hh}^{\rm 1PI}(p^2), \tag{4.60}$$
$$\widehat{\Pi}_{hH}(p^2) = (p^2 - m_h^2)\delta C_{Hh} + (p^2 - m_H^2)\delta C_{hH} + (m_h^2 - m_H^2)\delta\alpha + \frac{c_\alpha s_\alpha}{v}\delta T_\phi + \Pi_{hH}^{\rm 1PI}(p^2), \tag{4.61}$$
$$\widehat{\Pi}_{HH}(p^2) = (p^2 - m_H^2)(1 + \delta Z_H) - \delta m_H^2 + \frac{s_\alpha^2}{v}\delta T_\phi + \Pi_{HH}^{\rm 1PI}(p^2). \tag{4.62}$$

We impose the following renormalization conditions,

$$\widehat{\Pi}_{hh}(m_h^2) = 0, \quad \widehat{\Pi}_{HH}(m_H^2) = 0, \tag{4.63}$$
$$\widehat{\Pi}_{hH}(m_h^2) = 0, \quad \widehat{\Pi}_{hH}(m_H^2) = 0, \tag{4.64}$$
$$\left.\frac{{\rm d}\widehat{\Pi}_{hh}(p^2)}{{\rm d}p^2}\right|_{p^2=m_h^2} = 0, \quad \left.\frac{{\rm d}\widehat{\Pi}_{HH}(p^2)}{{\rm d}p^2}\right|_{p^2=m_H^2} = 0 \tag{4.65}$$

By these renormalization conditions, the counterterms are determined as

$$\delta m_h^2 = \frac{c_\alpha^2}{v}\delta T_\phi + \Pi_{hh}^{\rm 1PI}(m_h^2), \quad \delta m_H^2 = \frac{s_\alpha^2}{v}\delta T_\phi + \Pi_{HH}^{\rm 1PI}(m_h^2), \tag{4.66}$$
$$\delta C_{hH} = \delta C_{Hh} = \frac{1}{2(m_H^2 - m_h^2)}\left[\Pi_{hH}^{\rm 1PI}(m_h^2) - \Pi_{hH}^{\rm 1PI}(m_H^2)\right], \tag{4.67}$$
$$\delta\alpha = \frac{1}{2(m_H^2 - m_h^2)}\left[\frac{2s_\alpha c_\alpha}{v}T_\phi + \Pi_{hH}^{\rm 1PI}(m_h^2) + \Pi_{hH}^{\rm 1PI}(m_H^2)\right], \tag{4.68}$$
$$\delta Z_h = -\left.\frac{{\rm d}\widehat{\Pi}_{hh}^{\rm 1PI}(p^2)}{{\rm d}p^2}\right|_{p^2=m_h^2}, \quad \delta Z_H = -\left.\frac{{\rm d}\widehat{\Pi}_{HH}^{\rm 1PI}(p^2)}{{\rm d}p^2}\right|_{p^2=m_H^2}. \tag{4.69}$$

We cannot determine the $\delta\mu_S$ and $\delta\lambda_{\Phi S}$ in terms of the one- and two-point functions. They are determined such that the UV divergences in the renormalized hhh and Hhh vertices disappear. The counterterms for the renormalized hhh and Hhh vertices are given by

$$\delta\Gamma_{hhh} = s_\alpha^3\delta\mu_S - v c_\alpha s_\alpha^2\delta\lambda_{\Phi S}, \tag{4.70}$$
$$\delta\Gamma_{Hhh} = -3c_\alpha s_\alpha^2\delta\mu_S - \frac{v}{4}(s_\alpha - 3s_{3\alpha})\delta\lambda_{\Phi S}. \tag{4.71}$$

They are determined as

$$\delta\Gamma_{hhh} = -\frac{s_\alpha^2}{16\pi^2}\Bigg[\sum_f \frac{2N_c^f m_f^2}{v}\lambda_{\Phi S}c_\alpha - \frac{2c_\alpha^3}{v^3}(2m_W^4+m_Z^4) - \frac{3}{v}\lambda_{\Phi S}c_\alpha(2m_W^2+m_Z^2) + \frac{m_h^2}{4v}\lambda_{\Phi S}(11c_\alpha+c_{3\alpha}) + \frac{m_H^2}{v}\lambda_{\Phi S}c_\alpha s_\alpha^2 + 4v\lambda_{\Phi S}(3\lambda_S+\lambda_{\Phi S})c_\alpha - 36\mu_S\lambda_S s_\alpha\Bigg]\Delta_{\rm div}, \tag{4.72}$$

$$\delta\Gamma_{Hhh} = \frac{s_\alpha}{16\pi^2}\Bigg[\sum_f \frac{N_c^f m_f^2}{v}\lambda_{\Phi S}(1+3c_{2\alpha}) - \frac{c_\alpha^2(c_{2\alpha}-3)}{v^3}(2m_W^4+m_Z^4) - \frac{3}{2v}\lambda_{\Phi S}(1+3c_{2\alpha})(2m_W^2+m_Z^2) + \frac{3m_h^2}{2v}\lambda_{\Phi S}c_\alpha^2(3+c_{2\alpha}) - \frac{3m_H^2}{v}\lambda_{\Phi S}s_\alpha^4 + 2v\lambda_{\Phi S}(3\lambda_S+\lambda_{\Phi S})(1+3c_{2\alpha}) - 108\mu_S\lambda_S c_\alpha s_\alpha\Bigg]\Delta_{\rm div}. \tag{4.73}$$

4.2.2 Two-Higgs doublet model

In the 2HDM, we have the seven free parameters. We shift the bare parameters as

$$m_{\phi 0}^2 = m_\phi^2 + \delta m_\phi^2, \quad \alpha_0 = \alpha + \delta\alpha, \quad \beta_0 = \beta + \delta\beta, \quad M_0^2 = M^2 + \delta M^2, \tag{4.74}$$

where $\phi = h, H, A, H^\pm$. The scalar fields are shifted as

$$\begin{pmatrix} H_0 \\ h_0 \end{pmatrix} = \begin{pmatrix} 1+\frac{1}{2}\delta Z_H & \delta C_h + \delta\alpha \\ \delta C_h - \delta\alpha & 1+\frac{1}{2}\delta Z_h \end{pmatrix}\begin{pmatrix} H \\ h \end{pmatrix}, \tag{4.75}$$

$$\begin{pmatrix} G_0^0 \\ A_0 \end{pmatrix} = \begin{pmatrix} 1+\frac{1}{2}\delta Z_{G^0} & \delta C_A + \delta\beta \\ \delta C_A - \delta\beta & 1+\frac{1}{2}\delta Z_A \end{pmatrix}\begin{pmatrix} G^0 \\ A \end{pmatrix}, \tag{4.76}$$

$$\begin{pmatrix} G_0^\pm \\ H_0^\pm \end{pmatrix} = \begin{pmatrix} 1+\frac{1}{2}\delta Z_{G^\pm} & \delta C_{H^\pm} + \delta\beta \\ \delta C_{H^\pm} - \delta\beta & 1+\frac{1}{2}\delta Z_{H^\pm} \end{pmatrix}\begin{pmatrix} G^\pm \\ H^\pm \end{pmatrix}. \tag{4.77}$$

The tadpole terms are shifted as

$$T_{h0} = T_h + \delta T_h, \quad T_{H0} = T_H + \delta T_H, \tag{4.78}$$

where T_h and T_H are given by

$$\begin{pmatrix} T_1 \\ T_2 \end{pmatrix} = R(\alpha)\begin{pmatrix} T_H \\ T_h \end{pmatrix}. \tag{4.79}$$

At the one-loop level, the renormalized one-point functions are

$$\widehat{T}_h = T_h + T_h^{\rm 1PI} + \delta T_h, \quad \widehat{T}_H = T_H + T_H^{\rm 1PI} + \delta T_H. \tag{4.80}$$

We determine the counterterms such that the tadpole vanishes order by order,

$$T_h = 0, \quad T_h^{\rm 1PI} + \delta T_h = 0, \tag{4.81}$$

$$T_H = 0, \quad T_H^{\rm 1PI} + \delta T_H = 0. \tag{4.82}$$

At the one-loop level, the renormalized two-point functions are given by

$$\widehat{\Pi}_{hh}(p^2) = (p^2 - m_h^2)(1 + \delta Z_h) - \delta m_h^2 + \tilde{\Pi}^{\rm 1PI}_{hh}(p^2), \tag{4.83}$$

$$\widehat{\Pi}_{HH}(p^2) = (p^2 - m_H^2)(1 + \delta Z_H) - \delta m_H^2 + \tilde{\Pi}^{\rm 1PI}_{HH}(p^2), \tag{4.84}$$

$$\widehat{\Pi}_{AA}(p^2) = (p^2 - m_A^2)(1 + \delta Z_A) - \delta m_A^2 + \tilde{\Pi}^{\rm 1PI}_{AA}(p^2), \tag{4.85}$$

$$\widehat{\Pi}_{H^+H^-}(p^2) = (p^2 - m_H^2)(1 + \delta Z_{H^\pm}) - \delta m_{H^\pm}^2 + \tilde{\Pi}^{\rm 1PI}_{H^+H^-}(p^2), \tag{4.86}$$

where

$$\tilde{\Pi}^{\rm 1PI}_{hh}(p^2) = \Pi^{\rm 1PI}_{hh}(p^2) + \frac{s_\alpha^2}{c_\beta}\frac{\delta T_1}{v} + \frac{c_\alpha^2}{s_\beta}\frac{\delta T_2}{v}, \tag{4.87}$$

$$\tilde{\Pi}^{\rm 1PI}_{HH}(p^2) = \Pi^{\rm 1PI}_{HH}(p^2) + \frac{c_\alpha^2}{c_\beta}\frac{\delta T_1}{v} + \frac{s_\alpha^2}{s_\beta}\frac{\delta T_2}{v}, \tag{4.88}$$

$$\tilde{\Pi}^{\rm 1PI}_{AA}(p^2) = \Pi^{\rm 1PI}_{AA}(p^2) + \frac{s_\beta^2}{c_\beta}\frac{\delta T_1}{v} + \frac{c_\beta^2}{s_\beta}\frac{\delta T_2}{v}, \tag{4.89}$$

$$\tilde{\Pi}^{\rm 1PI}_{H^+H^-}(p^2) = \Pi^{\rm 1PI}_{H^+H^-}(p^2) + \frac{s_\beta^2}{c_\beta}\frac{\delta T_1}{v} + \frac{c_\beta^2}{s_\beta}\frac{\delta T_2}{v}. \tag{4.90}$$

Those for the scalar mixings are given by

$$\widehat{\Pi}_{hH}(p^2) = \tilde{\Pi}^{\rm 1PI}_{hH}(p^2) + 2p^2\delta C_h + m_h^2(\delta\alpha - \delta C_h) - m_H^2(\delta\alpha + \delta C_h), \tag{4.91}$$

$$\widehat{\Pi}_{AG^0}(p^2) = \tilde{\Pi}^{\rm 1PI}_{AG^0}(p^2) + 2p^2\delta C_A + m_A^2(\delta\beta - \delta C_A), \tag{4.92}$$

$$\widehat{\Pi}_{H^+H^-}(p^2) = \tilde{\Pi}^{\rm 1PI}_{H^+G^-}(p^2) + 2p^2\delta C_{H^\pm} + m_{H^\pm}^2(\delta\beta - \delta C_{H^\pm}), \tag{4.93}$$

where

$$\tilde{\Pi}^{\rm 1PI}_{Hh}(p^2) = \Pi^{\rm 1PI}_{Hh}(p^2) - s_\alpha c_\alpha\left(\frac{\delta T_1}{c_\beta v} - \frac{\delta T_2}{s_\beta v}\right), \tag{4.94}$$

$$\tilde{\Pi}^{\rm 1PI}_{AG^0}(p^2) = \Pi^{\rm 1PI}_{AG^0}(p^2) + \frac{1}{v}(s_{\beta-\alpha}T_H - c_{\beta-\alpha}T_h), \tag{4.95}$$

$$\tilde{\Pi}^{\rm 1PI}_{H^+G^-}(p^2) = \Pi^{\rm 1PI}_{H^+G^-}(p^2) + \frac{1}{v}(s_{\beta-\alpha}T_H - c_{\beta-\alpha}T_h). \tag{4.96}$$

We impose the following renormalization conditions,

$$\widehat{\Pi}_{\phi\phi}(m_\phi^2) = 0, \quad \left.\frac{{\rm d}\widehat{\Pi}_{\phi\phi}(p^2)}{{\rm d}p^2}\right|_{p^2=m_\phi^2} = 0, \quad \text{for} \quad \phi = h, H, A, H^\pm \tag{4.97}$$

By these renormalization conditions, the counterterms are determined as

$$\delta m_\phi^2 = \tilde{\Pi}^{\rm 1PI}_{\phi\phi}(m_\phi^2), \tag{4.98}$$

$$\delta Z_\phi = -\left.\frac{{\rm d}\widehat{\Pi}^{\rm 1PI}_{\phi\phi}(p^2)}{{\rm d}p^2}\right|_{p^2=m_\phi^2}. \tag{4.99}$$

For the mixing between the CP-even scalars, we impose the following renormalization conditions,

$$\widehat{\Pi}_{Hh}(m_h^2) = \widehat{\Pi}_{Hh}(m_H^2) = 0. \tag{4.100}$$

The counterterms $\delta\alpha$ and δC_h are determined as

$$\delta\alpha = \frac{1}{2(m_H^2 - m_h^2)}\left[\Pi_{Hh}^{\rm 1PI}(m_h^2) + \Pi_{Hh}^{\rm 1PI}(m_H^2) - 2s_\alpha c_\alpha\left(\frac{\delta T_1}{c_\beta v} - \frac{\delta T_2}{s_\beta v}\right)\right], \tag{4.101}$$

$$\delta C_h = \frac{1}{2(m_H^2 - m_h^2)}\left[\Pi_{Hh}^{\rm 1PI}(m_h^2) - \Pi_{Hh}^{\rm 1PI}(m_H^2)\right]. \tag{4.102}$$

For the mixing between the CP-odd scalars, we impose the following renormalization conditions,

$$\widehat{\Pi}_{AG^0}(0) = \widehat{\Pi}_{AG^0}(m_A^2) = 0. \tag{4.103}$$

The counterterms $\delta\beta$ and δC_A are determined as

$$\delta\beta = -\frac{1}{2m_A^2}\left[\tilde{\Pi}_{AG^0}^{\rm 1PI}(m_A^2) + \tilde{\Pi}_{AG^0}^{\rm 1PI}(0)\right], \tag{4.104}$$

$$\delta C_A = -\frac{1}{2m_A^2}\left[\tilde{\Pi}_{AG^0}^{\rm 1PI}(m_A^2) - \tilde{\Pi}_{AG^0}^{\rm 1PI}(0)\right]. \tag{4.105}$$

For the mixing between the charged scalars, we impose the following renormalization condition,

$$\widehat{\Pi}_{H^+G^-}(0) = 0. \tag{4.106}$$

The counterterm $\delta C_{H^\pm}$ is determined as

$$\delta C_{H^\pm} = \delta\beta + \frac{1}{m_{H^\pm}^2}\tilde{\Pi}_{H^+G^-}^{\rm 1PI}(0). \tag{4.107}$$

Since $\delta\beta$ has already been fixed, we cannot fix the mixing between the charged scalars so that it disappears with $p^2 = m_{H^\pm}^2$. Therefore, we need to take into account the finite contribution of $\widehat{\Pi}_{H^+G^-}(m_{H^\pm})$.

We cannot determine the δM^2 in terms of the one- and two-point functions. We determine it so that the UV divergences in the renormalized hhh vertex disappear.

$$\frac{\delta M^2}{M^2} = \frac{1}{16\pi^2}\left[\sum_f \frac{2N_c^f m_f^2 \zeta_f^2}{v^2} + \frac{4M^2 - 2m_{H^\pm}^2 - m_A^2}{v^2} + \frac{s_{2\alpha}}{s_{2\beta}}\frac{m_H^2 - m_h^2}{v^2} - 3\frac{2m_W^2 + m_Z^2}{v^2}\right]\Delta_{\rm div}. \tag{4.108}$$

4.2.3 Inert doublet model

We shift the bare parameters as

$$m_{\phi 0}^2 = m_\phi^2 + \delta m_\phi^2, \quad M_0^2 = M^2 + \delta M^2, \quad \lambda_{20} = \lambda_2 + \delta\lambda_2, \tag{4.109}$$

where $\phi = h, H, A, H^\pm$. Since the Z_2 symmetry prohibits the scalar mixings, the scalar fields are shifted as

$$\phi_0 = \left(1 + \frac{1}{2}\delta Z_\phi\right)\phi. \tag{4.110}$$

The tadpole term is shifted as

$$T_{h0} = T_h + \delta T_h. \tag{4.111}$$

At the one-loop level, the renormalized one-point functions are

$$\widehat{T}_h = T_h + T_h^{\rm 1PI} + \delta T_h. \tag{4.112}$$

We determine the counterterms such that the tadpole vanishes order by order,

$$T_h = 0, \quad T_h^{\rm 1PI} + \delta T_h = 0. \tag{4.113}$$

At the one-loop level, the renormalized two-point functions are given by

$$\widehat{\Pi}_{\phi\phi}(p^2) = (p^2 - m_\phi^2)(1 + \delta Z_\phi) - \delta m_\phi^2 + \Pi_{\phi\phi}^{\rm 1PI}(p^2) \tag{4.114}$$

We impose the following renormalization conditions,

$$\widehat{\Pi}_{\phi\phi}(m_\phi^2) = 0, \quad \left.\frac{{\rm d}\widehat{\Pi}_{\phi\phi}(p^2)}{{\rm d}p^2}\right|_{p^2=m_\phi^2} = 0. \tag{4.115}$$

By these renormalization conditions, the counterterms are determined as

$$\delta m_\phi^2 = \tilde{\Pi}_{\phi\phi}^{\rm 1PI}(m_\phi^2), \tag{4.116}$$

$$\delta Z_\phi = -\left.\frac{{\rm d}\widehat{\Pi}_{\phi\phi}^{\rm 1PI}(p^2)}{{\rm d}p^2}\right|_{p^2=m_\phi^2}. \tag{4.117}$$

We cannot determine the δM^2 and $\delta\lambda_2$ in terms of the one- and two-point functions. We determine them so that the UV divergences in the renormalized hAA and $hhHH$ vertices disappear, respectively.

Chapter 5

One-loop calculations for decays of the SM-like Higgs boson

In this chapter, we review the decay rates of the SM-like Higgs boson for various decay modes. In Sec. 5.1, we list the analytic expressions of the form factors for vertex functions of the SM-like Higgs boson. The decay rates including NLO EW corrections, as well as QCD corrections up to NNLO, are given in terms of the form factors. In Sec. 5.2, the numerical evaluations are shown for the decay branching ratios of the SM-like Higgs boson obtained by using the `H-COUP` program [45, 46]. This chapter is the review of Refs. [97, 98].

5.1 Decay rates with higher order corrections

In this section, we discuss the decay rates with NLO EW corrections for the decays of the SM-like Higgs boson. For the decay into a pair of quarks $h \to q\bar{q}$, the QCD corrections up to NNLO are presented. For the loop-induced decay processes $h \to gg, \gamma\gamma, Z\gamma$, the QCD corrections up to NLO are presented.

5.1.1 Form factors for vertex functions

We define renormalized vertex functions that are relevant for the decays of the SM-like Higgs boson. NLO EW corrections are expressed in terms of the form factors of the vertex functions.

$hf\bar{f}$ vertex

The renormalized $hf\bar{f}$ vertex can be decomposed as [99]

$$\begin{aligned}\widehat{\Gamma}_{hf\bar{f}}(p_1^2, p_2^2, q^2) = \widehat{\Gamma}^S_{hf\bar{f}} + \gamma_5\widehat{\Gamma}^P_{hf\bar{f}} + \not{p}_1\widehat{\Gamma}^{V_1}_{hf\bar{f}} + \not{p}_2\widehat{\Gamma}^{V_2}_{hf\bar{f}} \\ + \not{p}_1\gamma_5\widehat{\Gamma}^{A_1}_{hf\bar{f}} + \not{p}_2\gamma_5\widehat{\Gamma}^{A_2}_{hf\bar{f}} + \not{p}_1\not{p}_2\widehat{\Gamma}^T_{hf\bar{f}} + \not{p}_1\not{p}_2\gamma_5\widehat{\Gamma}^{PT}_{hf\bar{f}},\end{aligned} \tag{5.1}$$

where $p_1(p_2)$ denotes the incoming four-momentum of the fermion (anti-fermion), and q is the outgoing four-momentum of the SM-like Higgs boson (see Fig. 5.1). The following relations hold for the on-shell fermions; i.e., $p_1^2 = p_2^2 = m_f^2$,

$$\widehat{\Gamma}^P_{hff} = \widehat{\Gamma}^{PT}_{hff} = 0, \quad \widehat{\Gamma}^{V_1}_{hff} = -\widehat{\Gamma}^{V_2}_{hff}, \quad \widehat{\Gamma}^{A_1}_{hff} = -\widehat{\Gamma}^{A_2}_{hff}. \tag{5.2}$$

The renormalized form factors are composed of the tree-level and the one-loop part as

$$\widehat{\Gamma}^X_{hf\bar{f}} = \Gamma^{X,\mathrm{tree}}_{hf\bar{f}} + \Gamma^{X,\mathrm{loop}}_{hf\bar{f}}, \quad (X = S, P, V_1, V_2, A_1, A_2, T, PT), \tag{5.3}$$

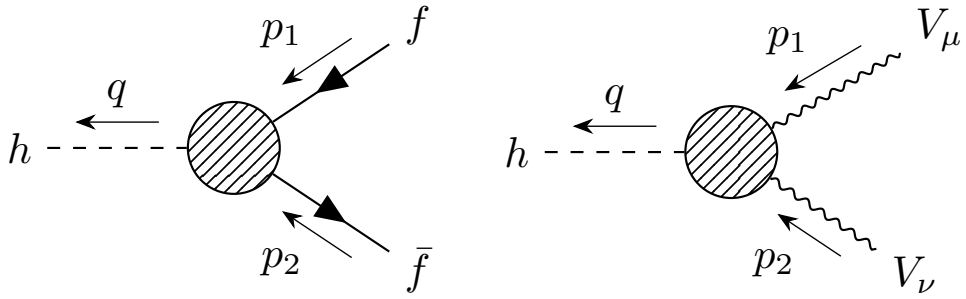

Figure 5.1: Momentum assignment for the renormalized $hf\bar{f}$ and hVV vertices.

where the one-loop part is further decomposed into the contributions from 1PI diagrams and the counterterms,

$$\Gamma^{X,\text{loop}}_{hf\bar{f}} = \Gamma^{X,\text{1PI}}_{hf\bar{f}} + \delta\Gamma^{X}_{hf\bar{f}}. \tag{5.4}$$

The tree-level coupling for $hf\bar{f}$ vertice is given by,

$$\Gamma^{S,\text{tree}}_{hf\bar{f}} = -\frac{m_f}{v}\kappa_f, \quad \Gamma^{X,\text{tree}}_{hf\bar{f}} = 0 \quad (X \neq S). \tag{5.5}$$

The analytic expressions for the 1PI contributions are presented in Ref. [74] for the HSM, Ref. [100] for the 2HDMs and Ref. [101] for the IDM.

hVV vertex

The renormalized hVV vertex is defined by

$$\widehat{\Gamma}^{\mu\nu}_{hVV}(p_1,p_2,q) = \left[g^{\mu\nu}\widehat{\Gamma}^{1}_{hVV} + \frac{p_1^\nu p_2^\mu}{m_V^2}\widehat{\Gamma}^{2}_{hVV} + i\epsilon^{\mu\nu\rho\sigma}\frac{p_{1\rho}p_{2\sigma}}{m_V^2}\widehat{\Gamma}^{3}_{hVV}\right](p_1^2,p_2^2,q^2), \tag{5.6}$$

where p_1^μ and p_2^μ are incoming four-momenta of the weak bosons, and q^μ is the outgoing four-momentum of the Higgs boson (see Fig. 5.1). We can further decompose these vertices into the tree-level and one-loop level contributions

$$\hat{\Gamma}^{X}_{hVV} = \Gamma^{i,\text{tree}}_{hVV} + \Gamma^{i,\text{loop}}_{hVV}, \quad \text{with} \quad \Gamma^{i,\text{loop}}_{hVV} = \Gamma^{i,\text{1PI}}_{hVV} + \delta\Gamma^{i}_{hVV}, \quad (i=1,2,3). \tag{5.7}$$

The tree-level couplings are given by,

$$\Gamma^{1,\text{tree}}_{hVV} = \frac{2m_V^2}{v}\kappa_V, \quad \Gamma^{2,\text{tree}}_{hVV} = \Gamma^{3,\text{tree}}_{hVV} = 0. \tag{5.8}$$

The form factor $\widehat{\Gamma}^{3}_{hZZ}$ is non-zero only when the SM-like Higgs boson is a CP-mixed state. Therefore this form factor vanishes in the model with CP conservation in the Higgs sector. The analytic expressions for the 1PI diagrams and counterterms are presented in Ref. [74] for the HSM, Ref. [100] for the 2HDMs and Ref. [101] for the IDM.

Similarly, the loop-induced $h\mathcal{V}\mathcal{V}'$ vertex is defined by

$$\hat{\Gamma}^{\mu\nu}_{h\mathcal{V}\mathcal{V}'}(p_1^2,p_2^2,q^2) = g^{\mu\nu}\hat{\Gamma}^{1}_{h\mathcal{V}\mathcal{V}'} + \frac{p_1^\nu p_2^\mu}{q^2}\hat{\Gamma}^{2}_{h\mathcal{V}\mathcal{V}'} + i\epsilon^{\mu\nu\rho\sigma}\frac{p_{1\rho}p_{2\sigma}}{q^2}\hat{\Gamma}^{3}_{h\mathcal{V}\mathcal{V}'}. \tag{5.9}$$

For the on-shell photon and gluon with a four-momentum p_i^μ, the Ward-Takahashi identity holds, $p_{i\mu}\hat{\Gamma}^{\mu\nu}_{h\mathcal{V}\mathcal{V}'} = 0$, and we have

$$\hat{\Gamma}^{2}_{h\mathcal{V}\mathcal{V}'} = -\frac{2q^2}{q^2 - p_1^2 - p_2^2}\hat{\Gamma}^{1}_{h\mathcal{V}\mathcal{V}'}. \tag{5.10}$$

The analytic expressions for the 1PI diagrams are presented in Refs. [98, 102].

$Zf\bar{f}$ vertex

The renormalized $Zf\bar{f}$ vertex can be decomposed in the massless limit of external fermions as

$$\widehat{\Gamma}^{\mu}_{Zf\bar{f}}(p_f, p_{\bar{f}}, p_Z) = g_Z \gamma^{\mu} \left[\widehat{\Gamma}^{V}_{Zf\bar{f}} - \gamma_5 \widehat{\Gamma}^{A}_{Zf\bar{f}} \right] (p_f^2, p_{\bar{f}}^2, p_Z^2), \tag{5.11}$$

where $p_f\,(p_{\bar{f}})$ is the incoming four-momentum of the fermion (anti-fermion), and p_Z is the outgoing four-momentum of the Z boson. We can further decompose these vertices into the tree-level and one-loop level contributions

$$\widehat{\Gamma}^{i}_{Zf\bar{f}} = \Gamma^{i,(0)}_{Zf\bar{f}} + \Gamma^{i,(1)}_{Zf\bar{f}}, \quad \text{with} \quad \Gamma^{i,(1)}_{Zf\bar{f}} = \Gamma^{i,1\text{PI}}_{Zf\bar{f}} + \delta\Gamma^{i}_{Zf\bar{f}}, \quad (i = V, A). \tag{5.12}$$

The tree-level contribution is given by

$$\Gamma^{V,(0)}_{Zf\bar{f}} = \frac{I_f}{2} - Q_f s_W^2, \quad \Gamma^{A,(0)}_{Zf\bar{f}} = \frac{I_f}{2}. \tag{5.13}$$

In the massless limit of external fermions, expressions of these vertices in the HSM, the 2HDMs and the IDM are the same as those in the SM. Analytic expressions for the 1PI diagrams and counterterms are presented in Appendix B in Ref. [98].

5.1.2 Decay rates of $h \to f\bar{f}$

The decay rate for the $h \to f\bar{f}$ $(f \neq t)$ process is given by

$$\Gamma(h \to f\bar{f}) = \Gamma_{\text{LO}}(h \to f\bar{f}) \left[1 + \Delta^{f}_{\text{EW}} + \Delta^{f}_{\text{QCD}} \right], \tag{5.14}$$

where Γ_{LO} is the decay rate at LO expressed as

$$\Gamma_{\text{LO}}(h \to f\bar{f}) = N_c^f \frac{m_h}{8\pi} \left| \Gamma^{S,\text{tree}}_{hff} \right|^2 \beta_f^3, \tag{5.15}$$

with $\beta_f = (1 - 4m_f^2/m_h^2)^{1/2}$. Δ^{f}_{EW} and Δ^{f}_{QCD} denote the EW and QCD corrections, respectively. For the leptonic decay, $f = \ell$, we use the lepton pole mass in $\Gamma^{S,\text{tree}}_{hff}$, while for the light quarks, $f = q\,(\neq t)$, we use the $\overline{\text{MS}}$ mass $\bar{m}_q\,(\mu = m_h)$.

The EW correction is decomposed into weak and QED corrections as

$$\Delta^{f}_{\text{EW}} = \Delta^{f}_{\text{weak}} + \Delta^{f}_{\text{QED}}. \tag{5.16}$$

Here, the weak correction denotes loop contributions except for photon and gluon loops. The QED correction is composed of the contributions of virtual-photon loops and those from the real-photon emissions. The expression for Δ^{f}_{weak} is given by

$$\Delta^{f}_{\text{weak}} = \frac{2}{\Gamma^{S,\text{tree}}_{hff}} \text{Re} \left\{ \left[\Gamma^{S,\text{loop}}_{hff} + 2m_f \Gamma^{V_1,\text{loop}}_{hff} + m_h^2 \left(1 - \frac{m_f^2}{m_h^2} \right) \Gamma^{T,\text{loop}}_{hff} \right] (m_f^2, m_f^2, m_h^2) \right\} - \Delta r. \tag{5.17}$$

For the leptonic decays, the QED correction in the on-shell scheme is given by [103–105]

$$\Delta^{\ell}_{\text{QED}} = \frac{\alpha_{\text{em}}}{\pi} Q_\ell^2 \left[\frac{1}{\beta} A_{\text{QED}}(\beta) + \frac{1}{16\beta^3} (3 + 34\beta^2 - 13\beta^4) \log \frac{1+\beta}{1-\beta} + \frac{3}{8\beta^2} (7\beta^2 - 1) \right], \tag{5.18}$$

with

$$A_{\rm QED}(\beta) = (1+\beta^2)\left[4{\rm Li}_2\left(\frac{1-\beta}{1+\beta}\right) + 2{\rm Li}_2\left(-\frac{1-\beta}{1+\beta}\right) - 3\log\frac{1+\beta}{1-\beta}\log\frac{2}{1+\beta} - 2\log\frac{1+\beta}{1-\beta}\log\beta\right] - 3\beta\log\frac{4}{1-\beta^2} - 4\beta\log\beta. \tag{5.19}$$

For the hadronic decays, the QED correction in the $\overline{\rm MS}$ scheme [106] with the renormalization scale μ is given by

$$\Delta^q_{\rm QED} = \frac{\alpha_{\rm em}}{\pi}Q_q^2\left(\frac{17}{4} + \frac{3}{2}\log\frac{\mu^2}{m_h^2}\right). \tag{5.20}$$

The QCD correction in the $\overline{\rm MS}$ scheme [106] is given by

$$\Delta^q_{\rm QCD} = \Delta_{qq} + \Delta_h. \tag{5.21}$$

The quark-mass independent part Δ_{qq} is given by

$$\Delta_{qq} = \frac{\alpha_s(\mu)}{\pi}C_F\left(\frac{17}{4} + \frac{3}{2}\log\frac{\mu^2}{m_h^2}\right) + \left(\frac{\alpha_s(\mu)}{\pi}\right)^2(35.94 - 1.36N_f), \tag{5.22}$$

with $C_F = 4/3$. The quark-mass dependent part Δ_h is given by

$$\Delta_h = \left(\frac{\alpha_s(\mu)}{\pi}\right)^2\left(1.57 - \frac{2}{3}\log\frac{m_h^2}{m_t^2} + \frac{1}{9}\log^2\frac{\bar{m}_q^2}{m_h^2}\right). \tag{5.23}$$

5.1.3 Decay rates of $h \to ZZ^* \to Zf\bar{f}$

The decay rate for the $h \to ZZ^* \to Zf\bar{f}$ process is given by

$$\Gamma(h \to Zf\bar{f}) = \Gamma_{\rm LO}(h \to Zf\bar{f})\left[1 + \Delta^Z_{\rm EW} + \Delta^Z_{\rm QCD}\right]. \tag{5.24}$$

In the following, we neglect the masses of final-state fermions. The decay rate at LO is given by

$$\Gamma_{\rm LO}(h \to Zf\bar{f}) = \int_0^{(m_h - m_Z)^2} |\overline{\mathcal{M}_0^Z}|^2\,{\rm d}s, \tag{5.25}$$

with the Mandelstam variable $s = (p_f + p_{\bar{f}})^2$. The squared tree-level amplitude $|\overline{\mathcal{M}_0^Z}|^2$ is given by

$$|\overline{\mathcal{M}_0^Z}|^2 = \frac{g_Z^2\left|\Gamma^{1,\rm tree}_{hZZ}\right|^2}{256\pi^3 m_h^3}\frac{v_f^2 + a_f^2}{(x_s - x_Z)^2}\frac{\lambda(x_Z, x_s) + 12x_Z x_s}{3x_Z}\lambda^{1/2}(x_Z, x_s), \tag{5.26}$$

with $x_Z = m_Z^2/m_h^2$, $x_s = s/m_h^2$ and $\lambda(x,y) = (1-x-y)^2 - 4xy$.

The EW correction is composed of the weak and QED corrections,

$$\Delta^Z_{\rm EW} = \Delta^Z_{\rm weak} + \Delta^Z_{\rm QED}. \tag{5.27}$$

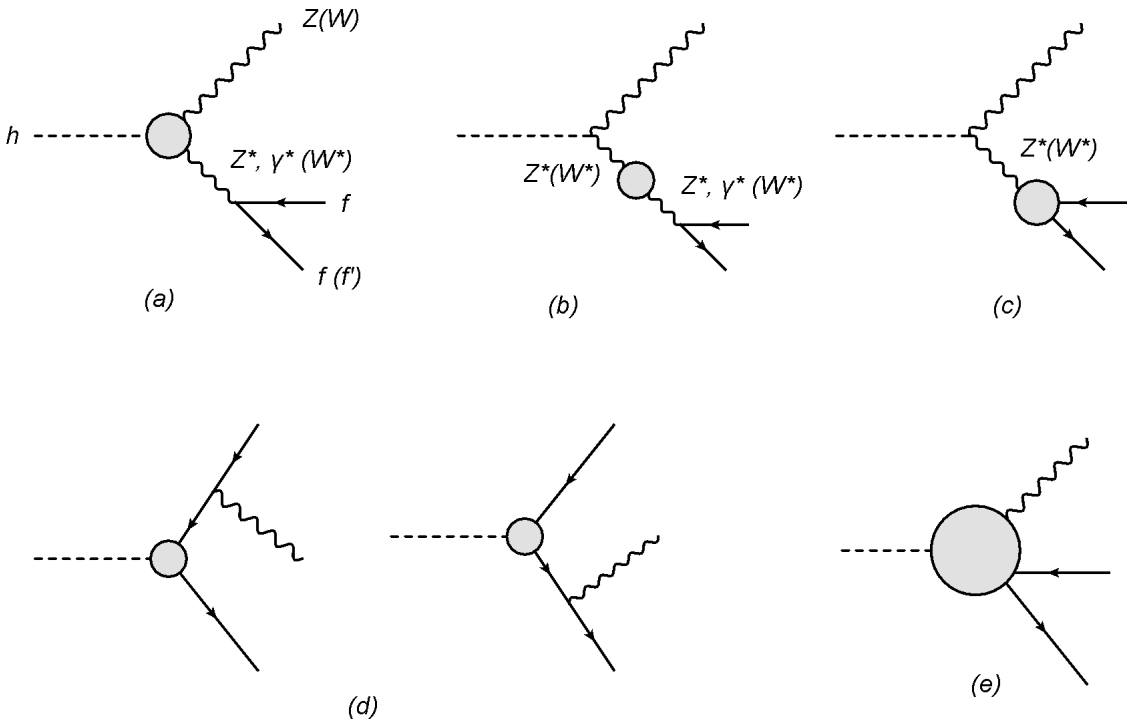

Figure 5.2: Diagrams contributing to the $h \to ZZ^* \to Zf\bar{f}$ ($h \to WW^* \to Wf\bar{f}'$) mode at NLO. Each diagram denotes the contributions from hVV vertex corrections (a), oblique corrections (b), $Vf\bar{f}$ vertex corrections (c), $hf\bar{f}$ vertex corrections (d) and box corrections (e).

The weak correction $\Delta^Z_{\rm weak}$ is given by

$$\begin{aligned}
\Delta^Z_{\rm weak} = \frac{2}{\Gamma_{\rm LO}} \int_0^{(m_h-m_Z)^2} {\rm d}s\, |\overline{\mathcal{M}^Z_0}|^2 \Bigg\{ & {\rm Re}\left[\frac{\Gamma^{1,\rm loop}_{hZZ}}{\Gamma^{1,\rm tree}_{hZZ}} + \frac{\bar{\lambda}(x_Z,x_s)}{x_Z}\frac{\Gamma^{2,\rm loop}_{hZZ}}{\Gamma^{1,\rm tree}_{hZZ}}\right](m_Z^2,s,m_h^2) \\
& + \frac{v_f Q_f c_W s_W}{v_f^2+a_f^2}\frac{s-m_Z^2}{s}{\rm Re}\left[\frac{\hat{\Gamma}^1_{hZ\gamma}}{\Gamma^{1,\rm tree}_{hZZ}} + \bar{\lambda}(x_Z,x_s)\frac{\hat{\Gamma}^2_{hZ\gamma}}{\Gamma^{1,\rm tree}_{hZZ}}\right](m_Z^2,s,m_h^2) \\
& + \frac{{\rm Re}[v_f\Gamma^{V,\rm loop}_{Zff} + a_f\Gamma^{A,\rm loop}_{Zff}](0,0,s)}{v_f^2+a_f^2} - \frac{{\rm Re}\,\hat{\Pi}_{ZZ}(s)}{s-m_Z^2} - \frac{v_f Q_f s_W c_W}{v_f^2+a_f^2}\frac{{\rm Re}\,\hat{\Pi}_{Z\gamma}(s)}{s}\Bigg\} \\
& + \frac{1}{\Gamma_{\rm LO}}\int_0^{(m_h-m_Z)^2}{\rm d}s\int_{u_{\rm min}}^{u_{\rm max}}{\rm d}u\,{\rm Re}\left(T^Z_{hff}+B_Z\right) \\
& - 2\Delta r - {\rm Re}\hat{\Pi}'_{ZZ}(m_Z^2),
\end{aligned} \tag{5.28}$$

with

$$\bar{\lambda}(x,y) = \frac{1-x-y}{2}\frac{\lambda(x,y)}{\lambda(x,y)+12xy}. \tag{5.29}$$

The first and second lines denote the contributions from the diagram (a) in Fig. 5.2. The third line denotes the contributions from diagrams (b) and (c). In the fourth line, the T^Z_{hff} and B_Z terms represent the contribution from the $hf\bar{f}$ vertex corrections and the box diagrams shown as the diagrams (d) and (e) in Fig. 5.2, respectively. Both T^Z_{hff} and B_Z depend on the Mandelstam variable $u = (p_Z + p_{\bar{f}})^2$ in loop functions. The integration range of u is given by

$$u_{\rm max,min} = \frac{m_h^2}{2}[1 + x_Z - x_s \pm \lambda^{1/2}(x_Z,x_s)]. \tag{5.30}$$

The fifth line denotes the finite contributions originated from the replacement of VEV and the wave function renormalization of the external Z boson.

The QED and QCD corrections only enter the $Zf\bar{f}$ vertex correction depicted in the diagram (c) in Fig. 5.2. They are given by [107]

$$\Delta^Z_{\rm QED} = Q_f^2 \frac{3\alpha_{\rm em}}{4\pi}, \quad \Delta^Z_{\rm QCD} = C_F \frac{3\alpha_s(\mu)}{4\pi}. \tag{5.31}$$

Although diagrams (d) and (e) also receive both QED and QCD corrections, they vanish in the massless limit for the external fermions.

5.1.4 Decay rates of $h \to WW^* \to Wf\bar{f}'$

The decay rate for the $h \to WW^* \to Wf\bar{f}'$ process is given by

$$\Gamma(h \to Wf\bar{f}') = \Gamma_{\rm LO}(h \to Wf\bar{f}')\big[1 + \Delta^W_{\rm EW} + \Delta^W_{\rm QCD}\big]. \tag{5.32}$$

In the following, we neglect the masses of final-state fermions. The decay rate at LO is given by

$$\Gamma_{\rm LO}(h \to Wf\bar{f}') = \int_0^{(m_h - m_W)^2} |\overline{\mathcal{M}_0^W}|^2 \, {\rm d}s, \tag{5.33}$$

with the Mandelstam variable $s = (p_f + p_{\bar{f}'})^2$. The squared tree-level amplitude $|\overline{\mathcal{M}_0^W}|^2$ is given by

$$|\overline{\mathcal{M}_0^W}|^2 = \frac{g^2 \big|\Gamma^{1,\rm tree}_{hWW}\big|^2}{512\pi^3 m_h^3} \frac{\lambda(x_W, x_s) + 12 x_W x_s}{3 x_W (x_s - x_W)^2} \lambda^{1/2}(x_W, x_s), \tag{5.34}$$

with $x_W = m_W^2/m_h^2, x_s = s/m_h^2$.

The EW correction $\Delta^W_{\rm EW}$ is given by

$$\begin{aligned}
\Delta^W_{\rm EW} = \frac{1}{\Gamma_{\rm LO}} \int_0^{(m_h - m_W)^2} {\rm d}s \, |\overline{\mathcal{M}_0^W}|^2 \Bigg\{ & {\rm Re}\left[\frac{2\Gamma^{1,\rm loop}_{hWW}}{\Gamma^{1,\rm tree}_{hWW}} + \frac{\bar{\lambda}(x_W, x_s)}{x_W} \frac{\Gamma^{2,\rm loop}_{hWW}}{\Gamma^{1,\rm tree}_{hWW}}\right](m_W^2, s, m_h^2) \\
& + 2{\rm Re}[\Gamma^{V,\rm loop}_{Wff} + \Gamma^{A,\rm loop}_{Wff}](0,0,s) - \frac{2{\rm Re}\,\hat{\Pi}_{WW}(s)}{s - m_W^2} \Bigg\} \\
& + \frac{1}{\Gamma_{\rm LO}} \left[\int_0^{(m_h - m_W)^2} {\rm d}s \int_{u_{\rm min}}^{u_{\rm max}} {\rm d}u \, \left(T^W_{hff} + B_W\right) + \Gamma(h \to Wf\bar{f}'\gamma)\right] \\
& - 2\Delta r - {\rm Re}\hat{\Pi}'_{WW}(m_W^2),
\end{aligned} \tag{5.35}$$

Differently from the $h \to Zf\bar{f}$ mode, we cannot separate the weak and QED corrections because virtual photons appear together with virtual W bosons in vertex corrections. The IR divergences are cancelled by adding the real photon emissions $\Gamma(h \to Wf\bar{f}'\gamma)$.

The QCD correction is the same as that given in Eq. (5.31) because the gluon loop corrections only appear in the $W\bar{f}f'$ vertex similar to the $h \to Zf\bar{f}$ decay [108].

5.1.5 Decay rates of $h \to \gamma\gamma$, $Z\gamma$, gg

The decay rate for the $h \to \mathcal{V}\mathcal{V}'$ process is given by

$$\Gamma_{\rm LO}(h \to \mathcal{V}\mathcal{V}') = \frac{\left|\hat{\Gamma}^1_{h\mathcal{V}\mathcal{V}'}(m^2_{\mathcal{V}}, m^2_{\mathcal{V}'}, m^2_h)\right|^2}{8\pi m_h} \lambda^{1/2}\left(\frac{m^2_{\mathcal{V}}}{m^2_h}, \frac{m^2_{\mathcal{V}'}}{m^2_h}\right). \tag{5.36}$$

For $h \to gg$ decay, the QCD corrected decay rate in the $\overline{\rm MS}$ scheme is given by [109]

$$\Gamma(h \to gg) = \Gamma_{\rm LO}(h \to gg)\left[1 + \frac{\alpha_s(\mu)}{\pi}\left(\frac{95}{4} - \frac{7}{6}N_f + \frac{33 - 2N_f}{6}\log\frac{\mu^2}{m^2_h}\right)\right], \tag{5.37}$$

in the heavy top limit $m_t \to \infty$.

For $h \to \gamma\gamma$ and $h \to Z\gamma$, we take into account the NLO QCD correction only for the top-loop contributions because those for the other quarks loops are negligible. In the heavy top limit, the QCD correction in the $\overline{\rm MS}$ scheme is given by [109]

$$\hat{\Gamma}^1_{h\mathcal{V}\gamma}(m^2_{\mathcal{V}}, 0, m^2_h)_t \to \hat{\Gamma}^1_{h\mathcal{V}\gamma}(m^2_{\mathcal{V}}, 0, m^2_h)_t\left[1 - \frac{\alpha_s(\mu)}{\pi}\right], \quad (\mathcal{V} = \gamma,\ Z), \tag{5.38}$$

where $\hat{\Gamma}^1_{h\mathcal{V}\gamma}(m^2_{\mathcal{V}}, 0, m^2_h)_t$ is the top-quark loop contribution to the renormalized $h\gamma\gamma$ and $hZ\gamma$ vertices.

5.2 Numerical results

In this section, we discuss the predictions for the branching ratios of the SM-like Higgs boson at NLO in the HSM, the IDM and the four types of 2HDM. The deviation in the branching ratios from those SM predictions is parametrized by

$$\Delta\mu_{XY} \equiv \frac{{\rm BR}_{\rm NP}(h \to XY)}{{\rm BR}_{\rm SM}(h \to XY)} - 1. \tag{5.39}$$

We can expand $\Delta\mu_{XY}$ up to NLO as

$$\Delta\mu_{XY} \approx \Delta\Gamma_{XY} - \Delta\Gamma_{\rm tot}, \tag{5.40}$$

where

$$\Delta\Gamma_{XY} \equiv \frac{\Gamma_{\rm NP}(h \to XY)}{\Gamma_{\rm SM}(h \to XY)} - 1, \tag{5.41}$$

$$\Delta\Gamma_{\rm tot} \equiv \frac{\Gamma_{\rm tot,NP}}{\Gamma_{\rm tot,SM}} - 1. \tag{5.42}$$

Thus, the qualitative behavior of $\Delta\mu_{XY}$ can be understood by analyzing $\Delta\Gamma_{XY}$ and $\Delta\Gamma_{\rm tot}$.

5.2.1 Deviation in partial decay widths

Fig. 5.3 shows the correlation between between $\Delta\Gamma_{\tau\tau}$ and $\Delta\Gamma_{bb}$ in the HSM and the 2HDMs. The colored regions correspond to the predictions in these models; i.e., yellow, red, blue, green and purple correspond to the HSM, Type-I, II, X and Y 2HDMs, respectively. The contrast of the colors represents the mass scales of the additional Higgs bosons. The left (right) panel

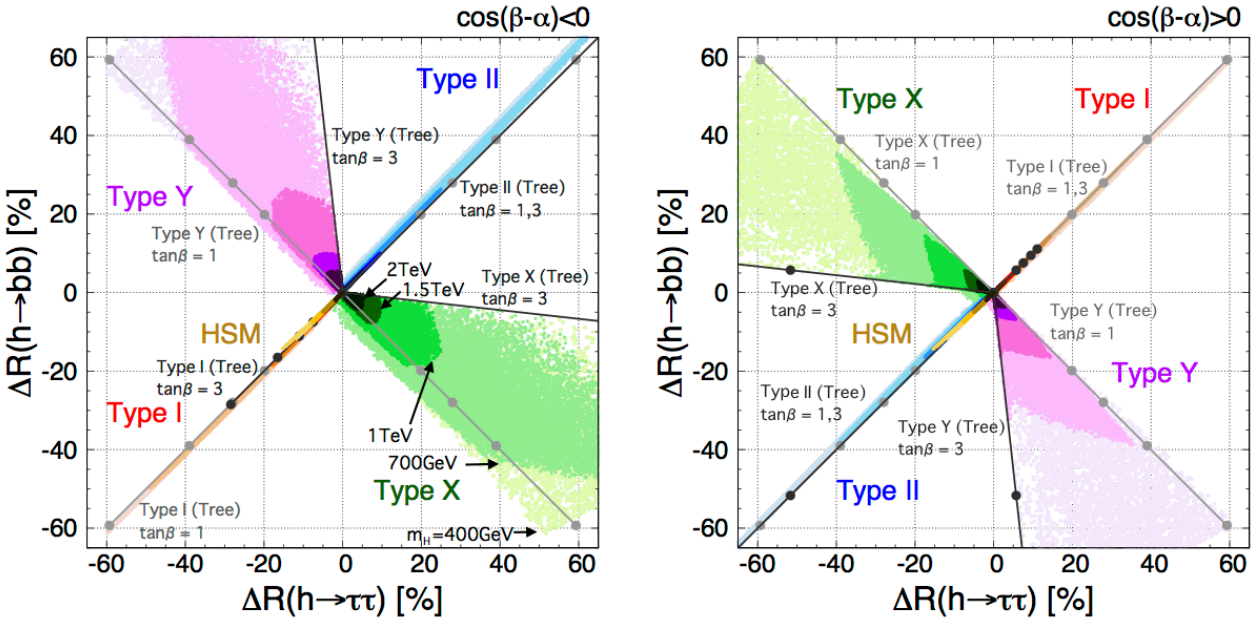

Figure 5.3: Correlation between $\Delta\Gamma_{\tau\tau}$ and $\Delta\Gamma_{bb}$ in the HSM (yellow) and the Type-I (red), Type-II (blue), Type-X (green), Type-Y (purple) 2HDMs. The left (right) panel shows the case for $c_{\beta-\alpha} < 0\,(> 0)$ in the 2HDMs. The ranges of the parameters are described in the text. The tree-level predictions with $\tan\beta = 1$ and 3 in the 2HDMs are also presented by gray and black lines, respectively.

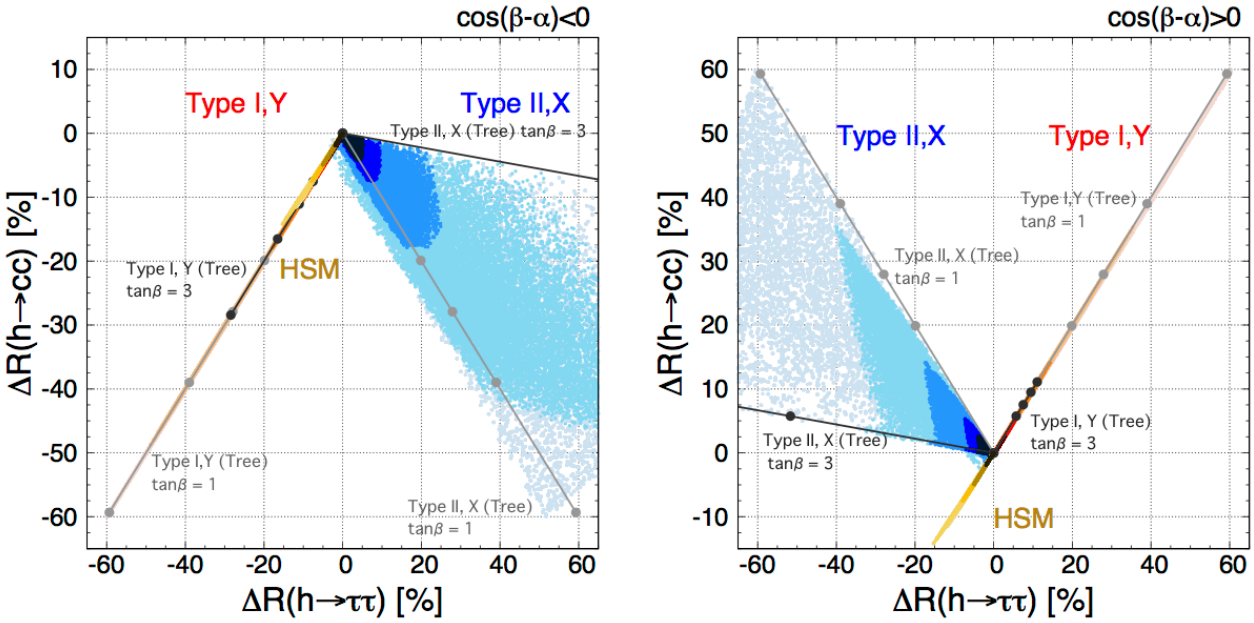

Figure 5.4: Correlation between $\Delta\Gamma_{\tau\tau}$ and $\Delta\Gamma_{cc}$ in the HSM (yellow), the Type-I and Y (red) and Type-II and X (blue) 2HDMs. The ranges of the scanned parameters are the same as in those of Fig. 5.3.

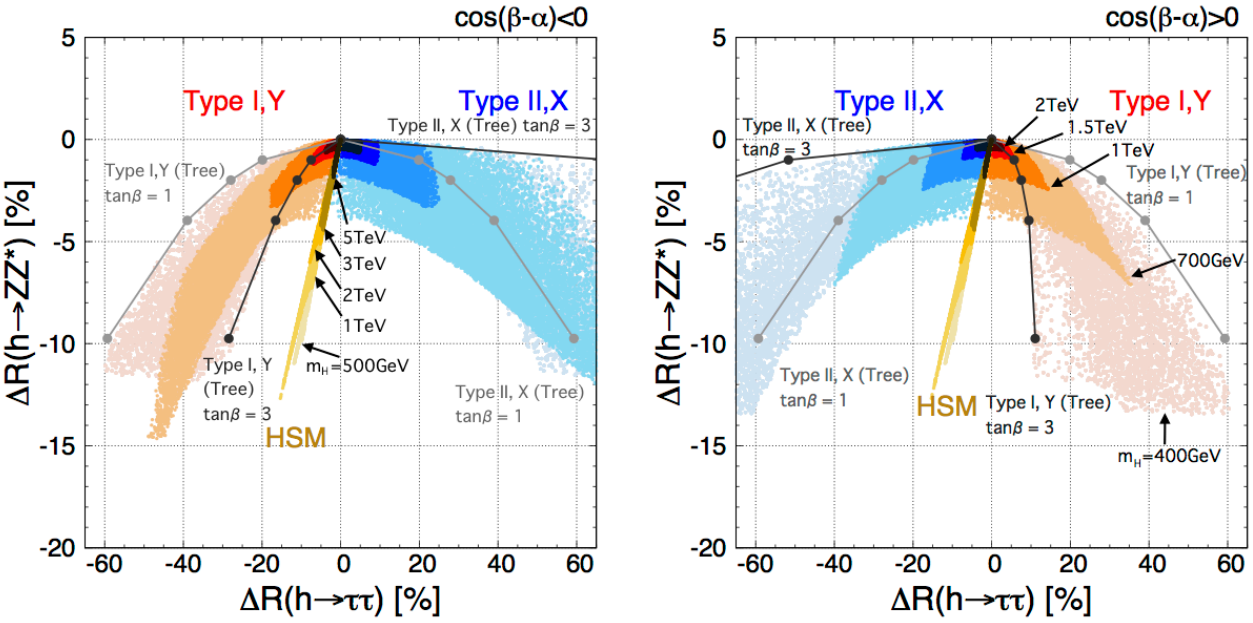

Figure 5.5: Correlation between $\Delta\Gamma_{\tau\tau}$ and $\Delta\Gamma_{ZZ^*}$ in the HSM (yellow), the Type-I and Y (red) and Type-II and X (blue) 2HDMs. The ranges of the scanned parameters are the same as in those of Fig. 5.3.

shows the results with $c_{\beta-\alpha} < 0$ ($c_{\beta-\alpha} > 0$) in the 2HDMs, while the results in the HSM are the same both in the left and right panels. The tree-level predictions with $\tan\beta = 1\,(3)$ in the 2HDMs are shown by gray (black) lines with dots denoting $s_{\beta-\alpha} = 1$, 0.995, 0.99, 0.98, 0.95 from the origin.

The patterns of the deviations are mainly determined by the mixing on the tree-level couplings [110]. In the HSM, the decay widths are monotonically decreasing from the SM predictions both for the $\tau\tau$ and bb modes as the mixing angle c_α is decreasing from the SM limit ($c_\alpha = 1$). On the other hand, those in each type of the 2HDM show characteristic patterns due to the Yukawa structures. The size of the mixing parameters is constrained by theoretical constraints such as perturbative unitarity and vacuum stability. The darker-colored regions include the lighter-colored regions. Therefore, we can set the upper bound of the additional Higgs boson masses when a deviation is observed.

Fig. 5.4 shows the correlation the correlation between between $\Delta\Gamma_{\tau\tau}$ and $\Delta\Gamma_{cc}$. At the tree level, the results in the Type-I (Type-II) 2HDM coincide with those in the Type-Y (Type-X) 2HDM, because the Yukawa structures for up-type quarks and leptons are the same. In contrast to the case in Fig. 5.3, the predictions in the Type-II and Y 2HDM spread out since the Yukawa structures between up-type quarks and leptons are different. From the correlations among the three different fermionic decay modes of the Higgs boson shown in Figs. 5.3 and 5.4, we can identify a type of the 2HDM independently of the model parameters when a deviation is observed in experiments.

Fig. 5.5 shows the correlation the correlation between between $\Delta\Gamma_{\tau\tau}$ and $\Delta\Gamma_{ZZ^*}$. Similar to the discussion in Fig. 5.3, patterns of the deviations can be mainly determined by the mixing in the tree-level Higgs couplings. The HSM can be distinguished from the 2HDMs if the deviation ΔR_{ZZ^*} is larger than a few percent. On the other hand, the results in the Type-I (Type-II) 2HDM coincide with those in the Type-Y (Type-X) 2HDM at the tree level, as the Yukawa structures for leptons are the same. An important remark on the 2HDMs is the difference of the magnitude of the deviations between $h \to ff$ and $h \to VV^*$ [100]. The 5% deviation for

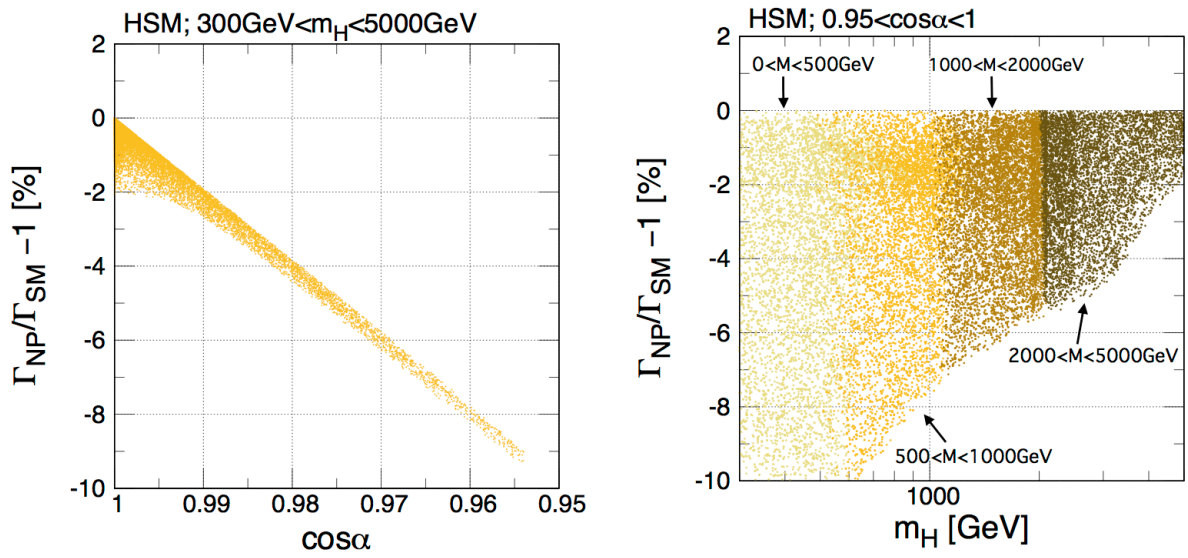

Figure 5.6: Deviation in the total width from the SM prediction as a function of c_α (left) and m_H (right) in the HSM with $\mu_S = 0$ and $\lambda_S = 0.1$. The values of c_α, m_H and M^2 are scanned within $0.95 < c_\alpha < 1$, $300 \leq m_H \leq 5000$ GeV and $0 \leq M^2 \leq m_H^2$, respectively.

the coupling in the gauge sector (i.e. $s_{\beta-\alpha} = 0.95$) gives rise to $\Delta R_{ZZ^*} \sim -10\% - -15\%$, while $\Delta R_{ff} \sim \pm 60\%$ or more. We also remark that the dependence on the extra Higgs boson masses are different between the HSM and the 2HDMs. The deviations in the HSM can be larger than those in the 2HDMs for $m_H > 1$ TeV [111, 112].

5.2.2 Deviation in the total decay width

Higgs singlet model

We first discuss the total width of the SM-like Higgs boson. Fig. 5.6 shows the deviation in the total width from the SM prediction in the HSM. The dependences on c_α and m_H are then displayed in the left and right panels, respectively. At LO, the deviation in the width is determined by s_α^2, and it corresponds to the upper edge of the distribution in the left panel. The loop effects reduce the width by at most about 2% level. In the right panel, it is seen that the magnitude of deviations becomes smaller for larger mass regions because the large mixing is excluded by the theoretical bounds. The precision measurement of the total width is important to identify the HSM since the branching ratios of the SM-like Higgs boson are almost the same as those in the SM due to nearly universal suppression of the partial decay rates.

Two Higgs doublet model

Fig. 5.7 shows the deviation in the total width as a function of $\tan\beta$ in four types of the 2HDMs with $s_{\beta-\alpha} = 0.99$ and $c_{\beta-\alpha} < 0$ (> 0) in the left (right) panel. The values of m_Φ and M^2 are scanned within $300 \leq m_\Phi \leq 1000$ GeV and $0 \leq M^2 \leq m_\Phi^2$, respectively.

In the case with $c_{\beta-\alpha} < 0$ (the left panel), the width becomes larger as $\tan\beta$ increases except for the Type-I 2HDM. This is because some of the partial widths have a $\tan\beta$ enhancement, e.g., the $h \to b\bar{b}$ ($h \to \tau\bar{\tau}$) mode in the Type-II and Type-Y (Type-II and Type-X) 2HDMs.

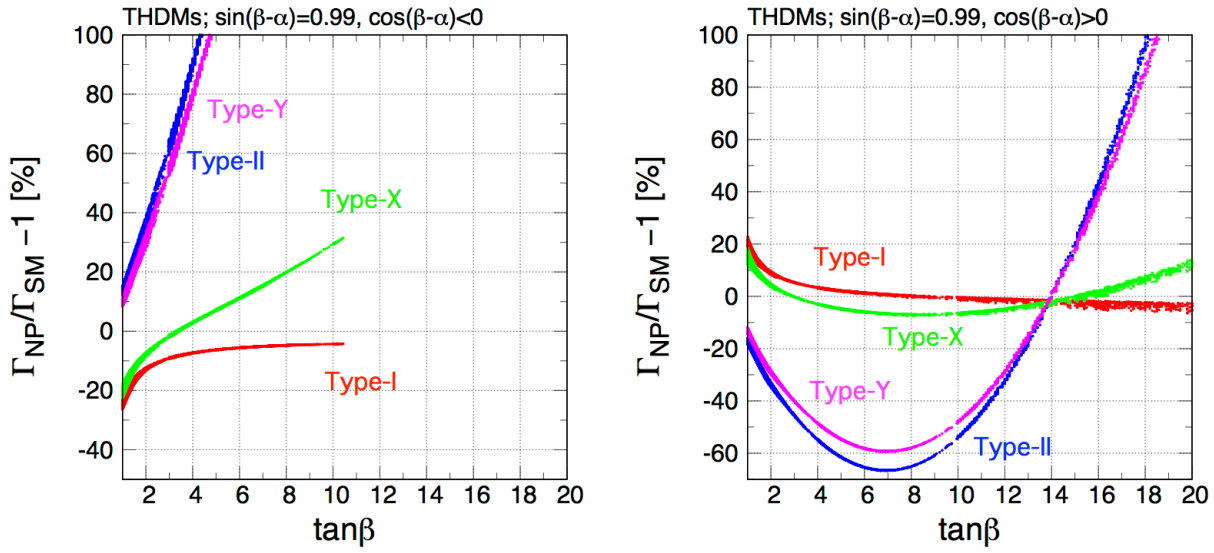

Figure 5.7: Deviation in the total width from the SM prediction in four types of the 2HDMs with $s_{\beta-\alpha} = 0.99$ as a function of $\tan\beta$. The left (right) panel shows the case of $c_{\beta-\alpha} < 0\,(> 0)$.

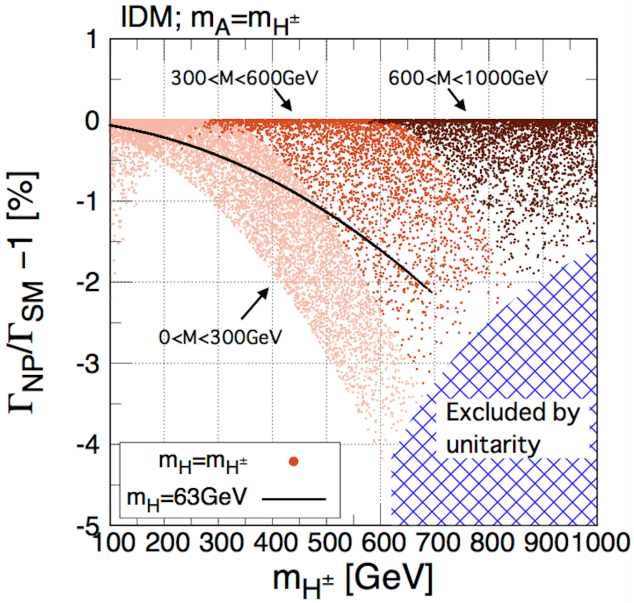

Figure 5.8: Deviation in the total width from the SM prediction in the IDM with $\lambda_2 = 0.1$. The value M^2 is scanned for the case with $m_H = m_{H^\pm}$ shown by dots. The black curve shows the case for $m_H = 63$ GeV.

In the Type-I 2HDM on the contrary, the total width approaches $s^2_{\beta-\alpha}\Gamma_{\rm SM}$, at the large $\tan\beta$ region. The region with $\tan\beta \gtrsim 11$ is eliminated by the theoretical constraints.

In the case with $c_{\beta-\alpha} > 0$ (the right panel), the total width has the minimal value at $\tan\beta \sim 7$ in the Type-II, Type-X and Type-Y 2HDMs, due to the cancellation between the $s_{\beta-\alpha}$ term and the $c_{\beta-\alpha}$ term in κ_f, see Table 7.3. This behavior is remarkably observed in the Type-II and Type-Y 2HDMs, because the $h \to b\bar{b}$ mode, which is the biggest partial width of h in the SM. We can also see that the deviation in the total width becomes zero at $\tan\beta \simeq 14$, as we have $\kappa_f^2 \simeq 1$ for all the types of Yukawa interaction. In the Type-I 2HDM, the width

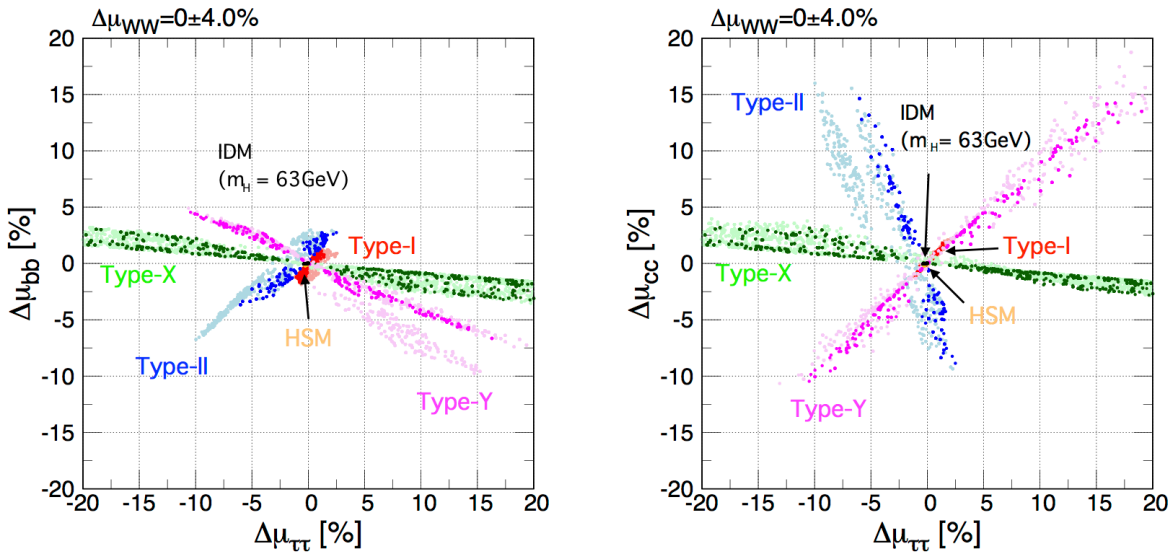

Figure 5.9: Correlation between $\Delta\mu_{\tau\tau}$ and $\Delta\mu_{bb}$ in the Type-I (red), Type-II (blue), Type-X (green), Type-Y (magenta) 2HDMs, the HSM (orange) and the IDM (black). The left (right) panel shows the case with $\Delta\mu_{WW} = 0 \pm 2\%$ ($0 \pm 4\%$). In the 2HDMs, we scan $1.5 \leq \tan\beta \leq 10$, $0 \leq M^2 \leq m_\Phi^2$ and 300 (600) $\leq m_\Phi \leq 1000$ GeV for (darker) colored points. In the HSM, we scan $300 \leq m_H \leq 5000$ GeV and $0 \leq M^2 \leq m_H^2$, while in the IDM we fix m_H to be 63 GeV and scan $100 \leq m_A (= m_{H^\pm}) \leq 1000$ GeV.

approaches to the SM value at a large value of $\tan\beta$ as in the case with $c_{\beta-\alpha} < 0$.

Inert doublet model

Fig. 5.8 shows the total width in the IDM as a function of $m_{H^\pm}$ with $m_A = m_{H^\pm}$. The following two cases, (i) m_H is fixed to 63 GeV and (ii) $m_H = m_{H^\pm}$, are studied. Case (i) is motivated by the scenario where the dark matter abundance is explained by the thermal freeze-out mechanism [113, 114], where H can be a dark matter candidate. In the IDM, the total width does not change from the SM value at the tree level, so any deviation is purely due to loop effects. In case (i), the total width monotonically decreases and the deviation is larger as $m_{H^\pm}$ is getting larger. The black curve is truncated at around $m_{H^\pm} = 700$ GeV, because of the unitarity constraint. In the case (ii), the maximal deviation is given at $M^2 = 0$ for $m_{H^\pm} < 600$ GeV. On the other hand, the unitarity constrains the minimal value of M^2 above $m_{H^\pm} \simeq 600$ GeV, and possible deviations become smaller.

5.2.3 Deviation in branching ratios

The branching ratios of the SM-like Higgs boson will be measured with a few percent accuracies at future collider experiments such as ILC.

First, we discuss the case where the central value of $\Delta\mu_{WW}$ is consistent with zero at the 2σ level. The left (right) panel of Fig. 5.9 shows the correlation between $\Delta\mu_{\tau\tau}$ and $\Delta\mu_{bb}$ ($\Delta\mu_{cc}$) in the HSM, four types of the 2HDMs and the IDM. The error for $\Delta\mu_{WW}$ is taken to consider about 2σ level region at ILC250 [36]. Parameters of each model are scanned as it is described in the caption. We see that the predictions in the HSM and the IDM are given almost at the origin of this plane. This is because the partial decay rates are almost universally suppressed

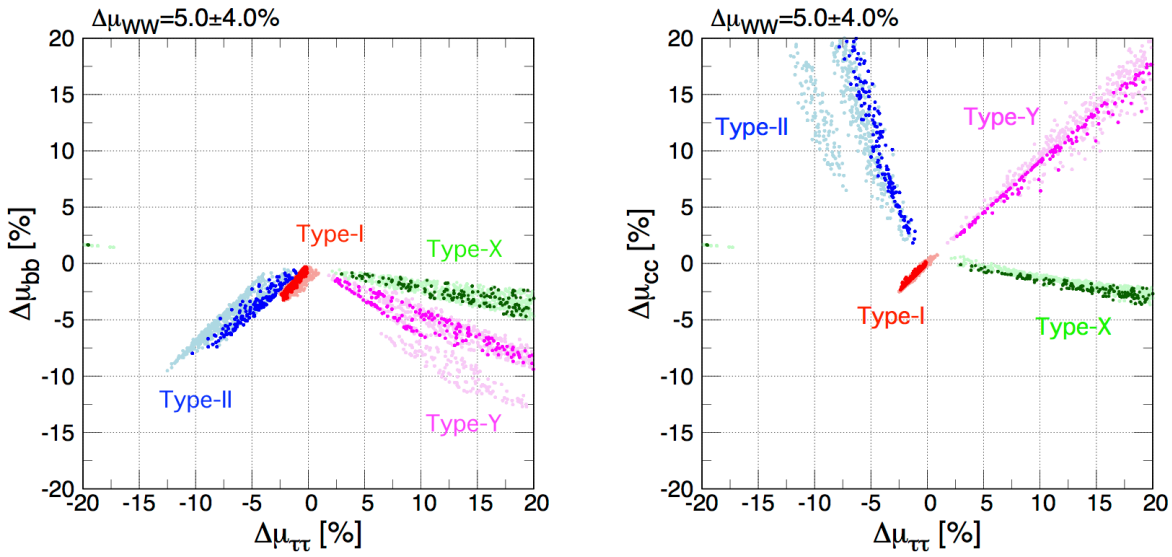

Figure 5.10: Same as Fig. 5.9, but for the case with $\Delta\mu_{WW}$ to be $+5 \pm 4\%$.

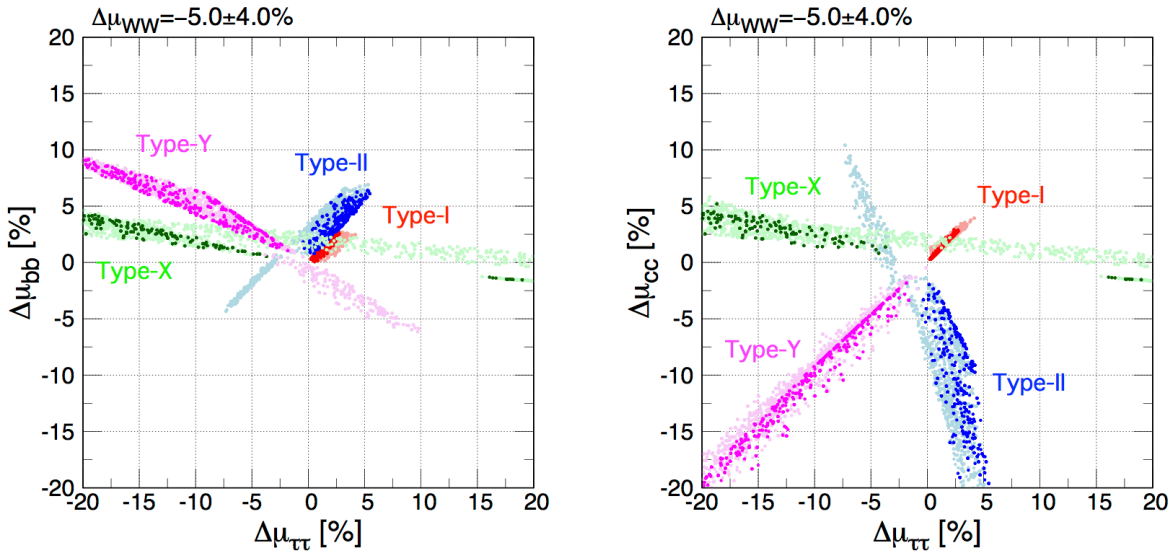

Figure 5.11: Same as Fig. 5.9, but for the case with $\Delta\mu_{WW}$ to be $-5 \pm 4\%$.

in these models. On the other hand, the predictions in the 2HDMs are spread out in different directions depending on the type of Yukawa interactions.

Next, we discuss the case where the central value of $\Delta\mu_{WW}$ is found to be nonzero, and $\Delta\mu_{WW} = 0$ is excluded at the 2σ level. In this case, the HSM and the IDM are excluded since predictions for $\Delta\mu_{WW}$ in these models are almost zero. On the other hand, the 2HDMs can explain such a deviation.

The left panel of Fig. 5.10 shows the correlation between $\Delta\mu_{\tau\tau}$ and $\Delta\mu_{bb}$ in the 2HDMs with $\Delta\mu_{WW} = +5.0 \pm 4.0\%$. The predictions appear in the regions with $\Delta\mu_{bb} < 0$ independently of the types of 2HDMs. This is because the positive value of $\Delta\mu_{WW}$ requires the reduction of the other decay rates, especially the $h \to b\bar{b}$ mode since the partial width of $h \to WW^*$ decreases by the tree-level mixing and the one-loop effects. From the sign of $\Delta\mu_{\tau\tau}$, we can distinguish Type-I and II 2HDMs from Type-X and Y 2HDMs. In order to distinguish Type-I and II, or Type-X and Y, $\Delta\mu_{cc}$ is useful. The right panel of Fig. 5.10 shows the correlation between $\Delta\mu_{\tau\tau}$

and $\Delta\mu_{cc}$. The predictions in the four types of 2HDMs are clearly separated from one another, and we can distinguish the four types of 2HDMs when the deviations are measured.

The left panel of Fig. 5.11 shows the correlation between $\Delta\mu_{\tau\tau}$ and $\Delta\mu_{bb}$ in the 2HDMs with $\Delta\mu_{WW} = -5.0 \pm 4.0\%$. The predictions in different types of 2HDMs are overlapped. This is because the negative value of $\Delta\mu_{WW}$ can be realized by either decreasing the partial width of the $h \to WW^*$ mode or increasing the other partial widths. Therefore, the sign of $\Delta\mu_{bb}$ can take both positive and negative. The right panel of Fig. 5.11 shows the correlation between $\Delta\mu_{\tau\tau}$ and $\Delta\mu_{cc}$. The predictions in the four types of 2HDMs are separated from one another except for the case in the Type-X 2HDM with lighter additional Higgs bosons. Thus, the correlation between $\Delta\mu_{\tau\tau}$ and $\Delta\mu_{bb}$ helps for further discrimination of the models.

Part II

Study on extended Higgs sectors

Chapter 6

Higgs strahlung process in electron–positron colliders

The $e^+e^- \to hZ$ process is the dominant production process at the early stage of the future lepton colliders such as the ILC, and the production cross section will be measured with a few percent accuracies. Thus, it is important to perform the theoretical calculation compatible with future precision measurements by including the higher-order corrections. In this chapter, we discuss the cross section for the Higgs strahlung process $e^+e^- \to hZ$ with arbitrary sets of electron and Z boson polarization at the full next-to-leading order. We systematically perform the complete one-loop calculations to the helicity amplitudes in the HSM, IDM, and 2HDMs based on the on-shell renormalization scheme. We present the full analytic results, as well as numerical evaluations. We find that the extended Higgs models can be classified by measuring the pattern of deviations from the SM prediction in the cross section times decay branching ratio.

6.1 Electroweak corrections to the process $e^+e^- \to hZ$

In this section, we define the notation for the process $e^+e^- \to hZ$ and discuss the helicity amplitudes based on the form-factor decomposition. We list relevant renormalized quantities for this process and give the formulae of form factors including the one-loop corrections. The differential cross section with arbitrary sets of electron and Z boson polarization is also presented.

6.1.1 Helicity amplitudes and cross section

The process

$$e^-(p_e, \sigma_e) + e^+(p_{\bar{e}}, \sigma_{\bar{e}}) \to h(k_h) + Z(k_Z, \lambda) \tag{6.1}$$

is depicted in Fig. 6.1. The momenta and helicities of the incoming electron and positron are denoted by (p_e, σ_e) and $(p_{\bar{e}}, \sigma_{\bar{e}})$, respectively. Correspondingly, (k_Z, λ) is used for the outgoing Z boson, and k_h is the momentum of the outgoing Higgs boson. The signs '+' and '−' of the variables σ_e and $\sigma_{\bar{e}}$ refer to helicities $+1/2$ and $-1/2$, respectively. The helicity λ takes '±' or '0'. In the following discussion, we neglect the mass of the electron whenever it is possible.

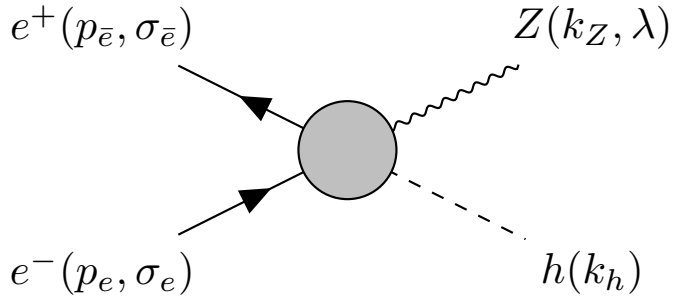

Figure 6.1: The process $e^+e^- \to hZ$ with momentum and helicity assignments. The momenta p_e and $p_{\bar{e}}$ are incoming, while k_h and k_Z are outgoing.

The Mandelstam variables are given by

$$s = (p_e + p_{\bar{e}})^2 = (k_Z + k_h)^2, \tag{6.2}$$
$$t = (p_e - k_Z)^2 = (p_{\bar{e}} - k_h)^2, \tag{6.3}$$
$$u = (p_e - k_h)^2 = (p_{\bar{e}} - k_Z)^2, \tag{6.4}$$

and they satisfy $s + t + u = m_Z^2 + m_h^2$. In the center-of-mass (CM) frame of the e^+e^- collision, the momenta of each external particle are

$$p_e^\mu = \frac{\sqrt{s}}{2}(1, 0, 0, 1), \tag{6.5}$$
$$p_{\bar{e}}^\mu = \frac{\sqrt{s}}{2}(1, 0, 0, -1), \tag{6.6}$$
$$k_Z^\mu = \frac{\sqrt{s}}{2}\left(1 + \frac{m_Z^2 - m_h^2}{s}, \beta \sin\theta, 0, \beta\cos\theta\right), \tag{6.7}$$
$$k_h^\mu = \frac{\sqrt{s}}{2}\left(1 - \frac{m_Z^2 - m_h^2}{s}, -\beta \sin\theta, 0, -\beta\cos\theta\right), \tag{6.8}$$

where β is defined by

$$\beta = \frac{|\mathbf{k}_Z|}{E} = \frac{1}{s}\sqrt{[s - (m_Z + m_h)^2][s - (m_Z - m_h)^2]}, \tag{6.9}$$

with the beam energy $E = \sqrt{s}/2$. We use the scattering angle θ between e^- and Z boson; $\hat{\mathbf{p}}_e \cdot \hat{\mathbf{k}}_Z = \cos\theta$ where the hat indicates the unit vector. The scattering angle θ is related to t and u via

$$t = \frac{1}{2}(m_Z^2 + m_h^2 - s) + \frac{s}{2}\beta\cos\theta, \tag{6.10}$$
$$u = \frac{1}{2}(m_Z^2 + m_h^2 - s) - \frac{s}{2}\beta\cos\theta. \tag{6.11}$$

The helicity amplitudes for $e^+e^- \to hZ$ vanish for $\sigma_e = \sigma_{\bar{e}}$ in the limit $m_e \to 0$ due to the chirality conservation. Therefore, we use $\sigma = \sigma_e = -\sigma_{\bar{e}}$ for the non-vanishing amplitudes. The helicity amplitude $\mathcal{M}_{\sigma\lambda}(s,t)$ can be decomposed into a set of basic matrix elements $\mathcal{M}_{i,\sigma\lambda}(s,t)$ and corresponding form factors $F_{i,\sigma}(s,t)$ as [115]

$$\mathcal{M}_{\sigma\lambda}(s,t) = \sum_{i=1}^{3} F_{i,\sigma}(s,t)\mathcal{M}_{i,\sigma\lambda}(s,t). \tag{6.12}$$

The basic matrix elements are given by

$$\mathcal{M}_{i,\sigma\lambda} = j_{\sigma,\mu}(p_e, p_{\bar{e}}) T_i^{\mu\nu}(s,t) \varepsilon_\nu^*(k_Z, \lambda), \tag{6.13}$$

where $\varepsilon^{*\mu}(k_Z, \lambda)$ is the polarization vector for Z boson, and $j_\sigma^\mu(p_e, p_{\bar{e}})$ is the fermion current of the initial electron and positron,

$$\varepsilon^{*\mu}(k_Z, \pm) = \frac{1}{\sqrt{2}}[0, \mp\cos\theta, i, \pm\sin\theta], \tag{6.14}$$

$$\varepsilon^{*\mu}(k_Z, 0) = \frac{\sqrt{s}}{2m_Z}[\beta, \alpha\sin\theta, 0, \alpha\cos\theta], \tag{6.15}$$

$$j_\sigma^\mu(p_e, p_{\bar{e}}) = \bar{v}(p_{\bar{e}})\gamma^\mu P_\sigma u(p_e) = \sqrt{s}[0, 1, \sigma i, 0], \tag{6.16}$$

with the chirality projection operator $P_\sigma = (1 + \sigma\gamma_5)/2$ and $\alpha = 1 + (m_Z^2 - m_h^2)/s$. The three basis tensor $T_i^{\mu\nu}$ are defined by

$$T_1^{\mu\nu} = g^{\mu\nu}, \quad T_2^{\mu\nu} = k_Z^\mu (p_e + p_{\bar{e}})^\nu, \quad T_3^{\mu\nu} = k_Z^\mu (p_e - p_{\bar{e}})^\nu. \tag{6.17}$$

In the CM frame, the first elements of basic matrix $\mathcal{M}_{1,\sigma\lambda}$ become

$$\mathcal{M}_{1,\,\sigma\pm} = \sigma\sqrt{\frac{s}{2}}(1 \pm \sigma\cos\theta) = \sigma\sqrt{2s}\, d^1_{\sigma,\pm}(\theta), \tag{6.18}$$

$$\mathcal{M}_{1,\,\sigma 0} = -\frac{s\alpha}{2m_Z}\sin\theta = \sigma\frac{s\alpha}{\sqrt{2}m_Z}\, d^1_{\sigma,0}(\theta), \tag{6.19}$$

where $d^j_{m',m}(\theta)$ is the Wigner's d function. The second elements $\mathcal{M}_{2,\sigma\lambda}$ are

$$\mathcal{M}_{2,\sigma\pm} = 0, \tag{6.20}$$

$$\mathcal{M}_{2,\sigma 0} = -\frac{s^2\beta^2}{4m_Z}\sin\theta = \sigma\frac{s^2\beta^2}{2\sqrt{2}m_Z}\, d^1_{\sigma,0}(\theta). \tag{6.21}$$

The third elements $\mathcal{M}_{3,\sigma\lambda}$ are

$$\mathcal{M}_{3,\,\sigma\pm} = \pm\frac{s\beta}{2}\sqrt{\frac{s}{2}}\sin^2\theta = \pm s\beta\sqrt{\frac{s}{3}}\, d^2_{2,0}(\theta), \tag{6.22}$$

$$\mathcal{M}_{3,\,\sigma 0} = \frac{s^2\alpha\beta}{4m_Z}\cos\theta\sin\theta = -\frac{s^2\alpha\beta}{4m_Z^2}\big[d^2_{2,1}(\theta) - d^2_{2,-1}(\theta)\big]. \tag{6.23}$$

The six physical helicity amplitudes are given in terms of the form factors $F_{i,\sigma}$ by

$$\mathcal{M}_{\sigma\pm}(s,t) = \sqrt{\frac{s}{2}}\left[F_{1,\sigma}(s,t) \pm \frac{s\beta}{2}(\sigma \mp \cos\theta)F_{3,\sigma}(s,t)\right](\sigma \pm \cos\theta), \tag{6.24}$$

$$\mathcal{M}_{\sigma 0}(s,t) = -\frac{s}{2m_Z}\left[\alpha F_{1,\sigma}(s,t) + \frac{s\beta^2}{2}F_{2,\sigma}(s,t) - \frac{s\alpha\beta}{2}\cos\theta F_{3,\sigma}(s,t)\right]\sin\theta. \tag{6.25}$$

We denote the tree- and one-loop contributions to the helicity amplitude as

$$\mathcal{M}^{(0)}_{\sigma\lambda}(s,t) = \sum_{i=1}^{3} F^{(0)}_{i,\sigma}(s,t)\mathcal{M}_{i,\sigma\lambda}, \tag{6.26}$$

$$\mathcal{M}^{(1)}_{\sigma\lambda}(s,t) = \sum_{i=1}^{3} F^{(1)}_{i,\sigma}(s,t)\mathcal{M}_{i,\sigma\lambda}. \tag{6.27}$$

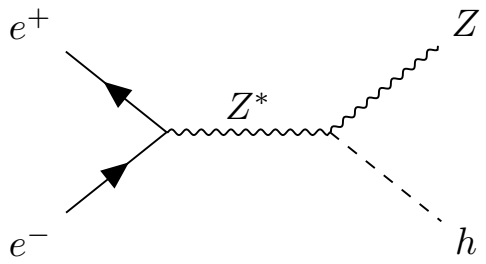

Figure 6.2: Tree-level diagram for the process $e^+e^- \to hZ$.

The helicity-dependent differential cross section at NLO in EW is given by

$$\frac{\mathrm{d}\sigma}{\mathrm{d}\Omega}(\sigma,\lambda;s,t) = \frac{\beta}{64\pi^2 s}\Big\{|\mathcal{M}^{(0)}_{\sigma\lambda}(s,t)|^2 + 2\,\mathrm{Re}[\mathcal{M}^{(0)}_{\sigma\lambda}(s,t)\mathcal{M}^{(1)*}_{\sigma\lambda}(s,t)]\Big\}. \tag{6.28}$$

The helicity-dependent cross section $\sigma(\sigma,\lambda;s)$ can be obtained by integrating Eq. (6.28) over the solid angle.

In a realistic setup, one needs to introduce the degree of polarization of initial electron P_e and positron $P_{\bar{e}}$. We use the convention where a purely left-handed (right-handed) electron corresponds to $P_e = -1$ $(+1)$. The polarized differential cross section is given by

$$\frac{\mathrm{d}\sigma}{\mathrm{d}\Omega}(P_e,P_{\bar{e}},\lambda;s,t) = \sum_{\sigma=\pm}\frac{1}{4}(1+\sigma P_e)(1-\sigma P_{\bar{e}})\frac{\mathrm{d}\sigma}{\mathrm{d}\Omega}(\sigma,\lambda;s,t). \tag{6.29}$$

The unpolarized cross section $\sigma(\lambda;s)$ corresponds to $P_e = P_{\bar{e}} = 0$. $(P_e,P_{\bar{e}}) = (\mp 0.8,\pm 0.3)$ is planned polarization at the ILC [36].

The polarized cross section can be rewritten in terms of the helicity-dependent cross section as [116]

$$\begin{aligned}\sigma(P_e,P_{\bar{e}},\lambda;s) &= \frac{1}{4}(1-P_e)(1+P_{\bar{e}})\sigma(-,\lambda;s) + \frac{1}{4}(1+P_e)(1-P_{\bar{e}})\sigma(+,\lambda;s)\\ &= \sigma(\lambda;s)(1-P_eP_{\bar{e}})(1-P_{\mathrm{eff}}A_{\mathrm{LR}}),\end{aligned} \tag{6.30}$$

where the effective polarization P_{eff} and the left-right asymmetry A_{LR} are defined as

$$P_{\mathrm{eff}} = \frac{P_e - P_{\bar{e}}}{1-P_eP_{\bar{e}}}, \tag{6.31}$$

$$A_{\mathrm{LR}} = \frac{\sigma(-,\lambda;s)-\sigma(+,\lambda;s)}{\sigma(-,\lambda;s)+\sigma(+,\lambda;s)}. \tag{6.32}$$

By using Eq. (6.30), one can easily evaluate the effect of the beam polarization from the helicity-dependent cross sections. Therefore, in the following discussion, we focus on the unpolarized and helicity-dependent cross section to exhibit analytical behaviors.

6.1.2 Tree-level contribution to the helicity amplitudes

At LO, only one diagram of Fig. 6.2 is relevant since the electron-Higgs coupling is proportional to m_e, and it is negligible. The contribution of the tree-level diagram to the form factors is expressed as

$$F^{(0)}_{i,\sigma} = \frac{g_Z\Gamma^{1,(0)}_{hZZ}}{s-m_Z^2}g_\sigma f^{(0)}_i, \tag{6.33}$$

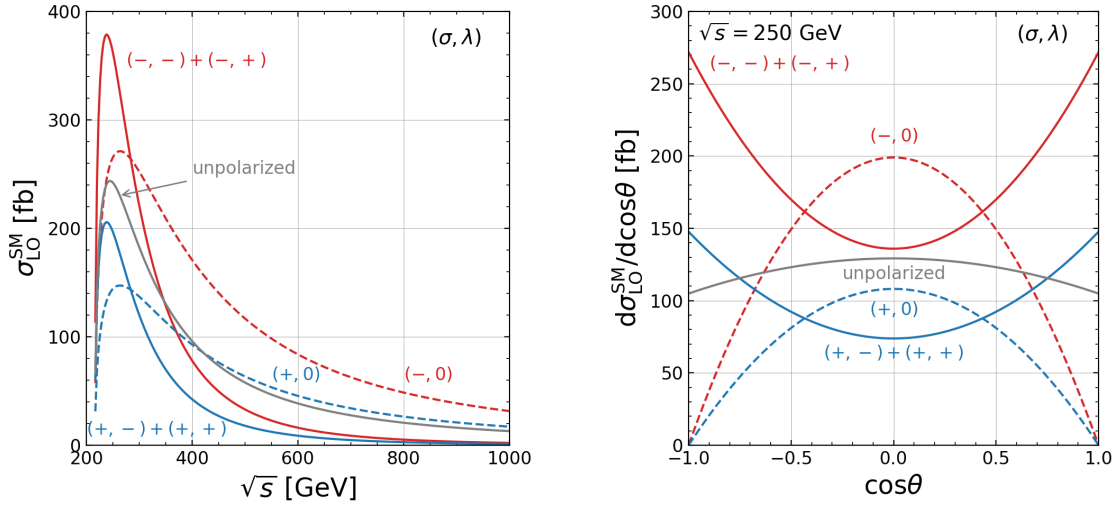

Figure 6.3: (Left) Helicity-dependent cross sections of $e^+e^- \to hZ$ at LO in the SM as a function of the CM energy. The red lines show the results for the left-handed electron and the right-handed positron, while the blue lines show those for the right-handed electron and the left-handed positron. The solid (dashed) lines show the results for the transversely (longitudinally) polarized Z bosons. The black solid line corresponds to that for the unpolarized cross section where the polarization of Z boson is also summed. (Right) Helicity-dependent differential cross sections of $e^+e^- \to hZ$ at LO in the SM as a function of $\cos\theta$ at $\sqrt{s} = 250$ GeV. The line colors and styles are the same as those of the left figure.

with the tree-level hZZ coupling $\Gamma^{1,(0)}_{hZZ} = 2\kappa_Z m_Z^2/v$. The scaling factor κ_Z is given in Table 3.2. If there is no mixing between CP-even scalars, the cross section in the extended Higgs models is the same as that in the SM at LO. The couplings $g_\pm$ are defined by

$$g_+ = s_W^2, \quad g_- = -\frac{1}{2} + s_W^2. \tag{6.34}$$

The coefficients $f_i^{(0)}$ are

$$f_1^{(0)} = 1, \quad f_2^{(0)} = f_3^{(0)} = 0. \tag{6.35}$$

The lowest order differential cross section is given by

$$\frac{\mathrm{d}\sigma_{\mathrm{LO}}}{\mathrm{d}\Omega}(\sigma,\lambda;s,t) = \frac{\beta}{64\pi^2 s}\left|F^{(0)}_{1,\sigma}\right|^2 \begin{cases} 2s\left|d^1_{\sigma,\pm}(\theta)\right|^2 & (\lambda = \pm), \\ \dfrac{s^2\alpha^2}{2m_Z^2}\left|d^1_{\sigma,0}(\theta)\right|^2 & (\lambda = 0). \end{cases} \tag{6.36}$$

In the left panel of Fig. 6.3, we show the helicity-dependent cross sections at LO as a function of the CM energy. In the numerical evaluation, we take G_F as an input given in Appendix A and use the tree-level relation $v = (\sqrt{2}G_F)^{-1/2}$. The solid and dashed lines correspond to the transversely ($\lambda = \pm$) and the longitudinally ($\lambda = 0$) polarized Z bosons, respectively. The cross sections peak just above the threshold $\sqrt{s} = m_Z + m_h$ and monotonically decrease at higher energies. For energies well above the threshold, the longitudinally polarized Z boson dominates the cross section. This is due to the factor s/m_Z^2 originated from the longitudinal polarization vector defined in Eq. (6.15). The cross section for the left-handed electron is larger than that for the right-handed electron because the left-handed electron more strongly couples to the Z

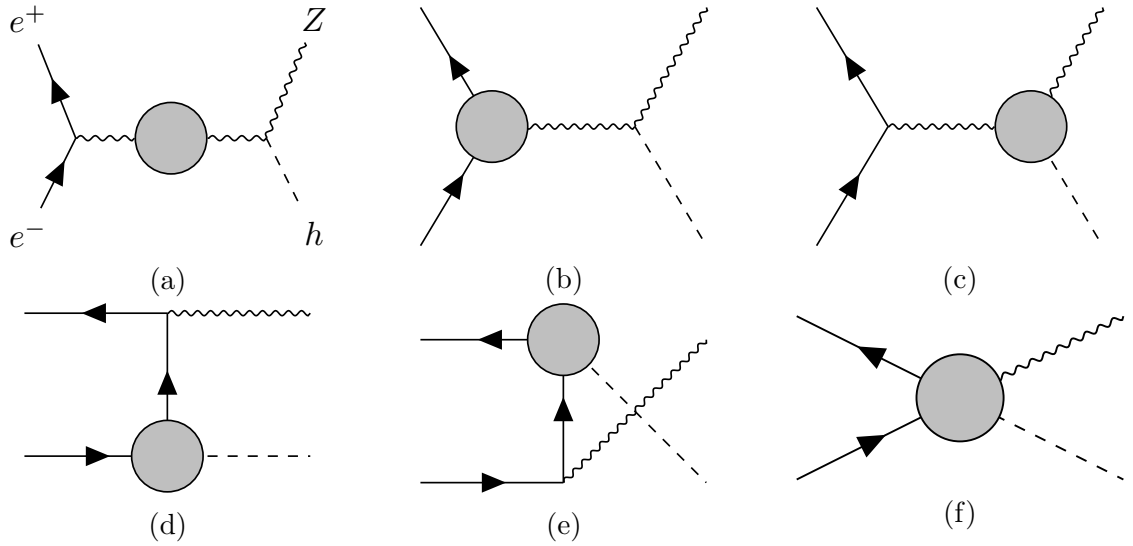

Figure 6.4: NLO corrections for $e^+e^- \to hZ$; (a) Gauge boson self-energy, (b) $Ze\bar{e}$ vertex, (c) hZZ and $hZ\gamma$ vertices, (d-e) $he\bar{e}$ vertex, (f) Box diagrams.

boson than the right-handed electron $(g_-/g_+)^2 \simeq 1.8$. At $\sqrt{s} = 250$ GeV, the unpolarized cross section is 242 fb, and the polarized cross section is 379 fb with $(P_e, P_{\bar{e}}) = (-0.8, 0.3)$. Therefore, the beam polarization significantly changes the size of the cross section. We note that the predicted value of the LO cross section highly depends on the input schemes.

The angular distributions of the LO cross section at $\sqrt{s} = 250$ GeV are given in the right panel of Fig. 6.3. They are determined by $d^1_{\sigma,\lambda}(\theta)$. The cross section for the transversely polarized Z boson is proportional to $1 + \cos^2\theta$, and it takes maximal value in the forward-backward direction. On the other hand, that for the longitudinally polarized Z boson is proportional to $1 - \cos^2\theta$, and it vanishes in the forward-backward direction and takes maximal value at $\cos\theta = 0$.

6.1.3 One-loop contributions to the form factors

As shown in Fig. 6.4, the one-loop contributions to the form factors $F^{(1)}_{i,\sigma}$ consist of (a) the Z boson self-energy and the $Z\gamma$ mixing, (b) the $Ze\bar{e}$ vertex correction, (c) the hZZ and $hZ\gamma$ vertex corrections, (d-e) the $he\bar{e}$ vertex correction and (f) the box diagrams. In addition, the renormalization factors of the weak gauge bosons are not to be unity in our renormalization scheme [95, 96]. Therefore, we have the term $-\mathrm{Re}\{\Pi'_{ZZ}(m_Z^2)\}/2$ from the wave function renormalization of the on-shell Z boson. Furthermore, the EW correction to the Fermi decay constant Δr appears when one replaces the VEV in the tree-level amplitude with G_F, since the tree-level relation between these two parameters is no longer valid at the one-loop level. This replacement corresponds to the resummation of universal higher-order leading corrections such as large logarithms from light fermion masses [117]. The one-loop contributions to the form factors $F^{(1)}_{i,\sigma}$ are given by

$$\begin{aligned} F^{(1)}_{i,\sigma} = {} & F^{ZZ}_{i,\sigma} + F^{Z\gamma}_{i,\sigma} + F^{Ze\bar{e}}_{i,\sigma} + F^{hZZ}_{i,\sigma} + F^{hZ\gamma}_{i,\sigma} + F^{he\bar{e}}_{i,\sigma} + F^{\mathrm{Box}}_{i,\sigma} \\ & + F^{\Pi'_{ZZ}}_{i,\sigma} + F^{\Delta r}_{i,\sigma}, \end{aligned} \tag{6.37}$$

where the terms in the first line correspond to the contributions from the diagrams in Fig. 6.4, while the terms in the second line come from the renormalization procedure. For the computation of these EW corrections, we adopt the modified on-shell renormalization scheme defined

in Ref. [112]. In the on-shell renormalization scheme, all the counterterms in the amplitude of $e^+e^- \to hZ$ are determined in terms of the one-particle irreducible (1PI) diagrams for one- and two-point functions of Higgs bosons, gauge bosons and fermions by imposing a set of the renormalization conditions. Adding these counterterms, one can obtain the ultra-violet (UV) finite one-loop corrected vertices.

In the wide range of extended Higgs models, there are mixings among Higgs bosons, and the gauge dependence appears in the renormalization of these mixing angles. We apply the pinch technique to remove the gauge dependence in the renormalized vertex functions [112, 118, 119].

Apart from the UV divergences, there are infrared (IR) divergences when we calculate virtual photon loop contributions. In the calculation of individual photon loop contributions, we regularize them with a finite photon mass μ. The photon mass dependences in the one-loop calculation are exactly canceled by adding contributions of real photon emissions. The analytic expression of the real photon contribution with the soft-photon approximation is given by [115, 117, 120],

$$\mathrm{d}\sigma_{\rm soft} = \mathrm{d}\sigma_{\rm LO}\left\{-\frac{\alpha}{\pi}\left[\ln\frac{4\Delta E^2}{\mu^2}\left(1+\ln\frac{m_e^2}{s}\right)+\frac{1}{2}\ln^2\frac{m_e^2}{s}+\ln\frac{m_e^2}{s}+\frac{\pi^2}{3}\right]\right\}, \tag{6.38}$$

with the photon energy cutoff ΔE. The dependence of ΔE vanishes in the inclusive cross section where one also includes the contribution of hard photon emissions [117]. The inclusive cross section still depends on $\ln(m_e^2/s)$, and this logarithmic term potentially takes a large value. This dependence can also be eliminated by introducing the electron structure functions as discussed in Ref. [121]. However, the treatment of hard photon emission highly depends on the experimental setup. The hard photon changes the kinematics of the process, and these effects would be eliminated by applying appropriate experimental cuts. In addition, if one considers the scenario with $\kappa_Z \simeq 1$, these effects in extended Higgs models are almost the same as in the SM. Therefore, we do not consider the electromagnetic effects when we focus on the difference between the predictions in the extended models and those in the SM.

In the one-loop calculation, we choose the fine structure constant $\alpha_{\rm em}$, the Fermi constant G_F and the Z boson mass m_Z as the input EW parameters. In addition to these EW parameters, we also use the shift of the fine structure constant $\Delta\alpha_{\rm em}$, the strong coupling constant α_s and the masses of the fermions and the discovered Higgs boson as the input parameters. The values of these SM input parameters are given in Appendix A. We use the input parameters given in Eqs. (3.21), (3.49) and (3.66) in the HSM, the 2HDMs and the IDM, respectively.

Expression of form factors including one-loop corrections

We list the one-loop contributions to the form factors in terms of the renormalized quantities. The one-loop propagator corrections appear in the sum in Eq. (6.37) as the term

$$F_{i,\sigma}^{\rm SE} = \frac{g_Z\Gamma_{hZZ}^{1,(0)}}{s-m_Z^2}\left[-g_\sigma\frac{\widehat{\Pi}_{ZZ}^T(s)}{s-m_Z^2}-Q_e s_W c_W\frac{\widehat{\Pi}_{Z\gamma}^T(s)}{s}\right]f_i^{(0)}, \tag{6.39}$$

with the renormalized self-energies $\widehat{\Pi}_{VV'}^T(s)$ of the neutral vector bosons. The renormalized $Ze\bar{e}$ corrections appear as

$$F_{i,\sigma}^{Ze\bar{e}} = \frac{g_Z\Gamma_{hZZ}^{1,(0)}}{s-m_Z^2}\left\{\left[\widehat{\Gamma}_{Ze\bar{e}}^V-\sigma\widehat{\Gamma}_{Ze\bar{e}}^A\right](m_e^2,m_e^2,s)\right\}f_i^{(0)}. \tag{6.40}$$

The renormalized hZV ($V = Z,\ \gamma$) corrections appear as

$$F^{hZV}_{i,\sigma} = \frac{g_Z}{s - m_Z^2} g_\sigma f_i^{Z(1)}(s) + \frac{g_Z}{s} Q_e s_W c_W f_i^{\gamma(1)}(s), \tag{6.41}$$

with

$$f_1^{Z(1)}(s) = \widehat{\Gamma}^1_{hZZ}(m_Z^2, s, m_h^2), \tag{6.42}$$

$$f_2^{Z(1)}(s) = -\frac{1}{m_Z^2}\widehat{\Gamma}^2_{hZZ}(m_Z^2, s, m_h^2), \tag{6.43}$$

$$f_1^{\gamma(1)}(s) = \widehat{\Gamma}^1_{hZ\gamma}(m_Z^2, s, m_h^2), \tag{6.44}$$

$$f_2^{\gamma(1)}(s) = -\frac{1}{m_h^2}\widehat{\Gamma}^2_{hZ\gamma}(m_Z^2, s, m_h^2). \tag{6.45}$$

The renormalized $he\bar{e}$ corrections appear as

$$F^{he\bar{e}}_{i,\sigma} = -g_Z g_\sigma \Big\{ \Big[\widehat{\Gamma}^{V_1}_{he\bar{e}} + \sigma\widehat{\Gamma}^{A_1}_{he\bar{e}}\Big](t, 0, m_h^2) - \Big[\widehat{\Gamma}^{V_2}_{he\bar{e}} + \sigma\widehat{\Gamma}^{A_2}_{he\bar{e}}\Big](0, u, m_h^2)\Big\} f_i^{(0)}. \tag{6.46}$$

The $1/t$ and $1/u$ terms originated from the fermion propagator are canceled by the vertex corrections [115]. However, the renormalized vertices depend on t and u, and they cause non-trivial $\cos\theta$ dependence.

There are the five W boson mediated and one Z boson mediated box diagrams in the massless limit of the electron. The amplitudes of the W boson mediated diagrams can be written as

$$\mathcal{M}^k_{\sigma\lambda} = \frac{\kappa_V}{16\pi^2}\delta_{\sigma-}\sum_{i=1}^{3} C^k F_i^k(s,t)\mathcal{M}_{i,\sigma\lambda}, \quad (k = 1, 2, \cdots, 5), \tag{6.47}$$

with

$$F_1^k(s,t) = F^k(s,t), \tag{6.48}$$

$$F_2^k(s,t) = \frac{1}{2}\big[F_e^k(s,t) + F_{\bar{e}}^k(s,t)\big], \tag{6.49}$$

$$F_3^k(s,t) = \frac{1}{2}\big[F_e^k(s,t) - F_{\bar{e}}^k(s,t)\big]. \tag{6.50}$$

The amplitude of the Z boson mediated diagram has a different structure from others, and it can be written as

$$\mathcal{M}^6_{\sigma\lambda} = \frac{\kappa_V}{16\pi^2}\sum_{i=1}^{3} g_\sigma^3 C^6 F_i^6(s,t)\mathcal{M}_{i,\sigma\lambda}, \tag{6.51}$$

with

$$F_1^6(s,t) = F^6(s,t), \tag{6.52}$$

$$F_2^6(s,t) = \frac{1}{2}\big[F_e^6(s,t) + F_{\bar{e}}^6(s,t)\big], \tag{6.53}$$

$$F_3^6(s,t) = \frac{1}{2}\big[F_e^6(s,t) - F_{\bar{e}}^6(s,t)\big]. \tag{6.54}$$

The expressions of C^k and $F_i^k(s,t)$ are given in Appendix B in Ref. [41]. We define $B_{i,\sigma}(s,t)$ by

$$B_{i,\sigma}(s,t) = \frac{\kappa_V}{16\pi^2}\left[\delta_{\sigma-}\sum_{k=1}^{5} C^k F_i^k(s,t) + g_\sigma^3 C^6 F_i^6(s,t)\right]. \tag{6.55}$$

Finally, the form factors at one-loop level are given by

$$\begin{aligned}
F_{i,\sigma}^{(1)} = {} & \frac{g_Z}{s-m_Z^2}\left\{\Gamma_{hZZ}^{1,(0)}\left[-g_\sigma\frac{\widehat{\Pi}_{ZZ}^T(s)}{s-m_Z^2} + \left[\widehat{\Gamma}_{Ze\bar{e}}^V - \sigma\widehat{\Gamma}_{Ze\bar{e}}^A\right](m_e^2,m_e^2,s)\right]f_i^{(0)} + g_\sigma f_i^{Z(1)}(s)\right\} \\
& + \frac{eQ_e}{s}\left[-\Gamma_{hZZ}^{1,(0)}\frac{\widehat{\Pi}_{Z\gamma}^T(s)}{s-m_Z^2}f_i^{(0)} + f_i^{\gamma(1)}(s)\right] \\
& - g_Z g_\sigma\left\{\left[\widehat{\Gamma}_{he\bar{e}}^{V_1} + \sigma\widehat{\Gamma}_{he\bar{e}}^{A_1}\right](t,0,m_h^2) - \left[\widehat{\Gamma}_{he\bar{e}}^{V_2} + \sigma\widehat{\Gamma}_{he\bar{e}}^{A_2}\right](0,u,m_h^2)\right\}f_i^{(0)} \\
& + B_{i,\sigma}(s,t) + \frac{g_Z\Gamma_{hZZ}^{1,(0)}}{s-m_Z^2}g_\sigma\left[-\frac{1}{2}\,\mathrm{Re}\{\Pi'_{ZZ}(m_Z^2)\} - \Delta r\right]f_i^{(0)}.
\end{aligned} \tag{6.56}$$

6.2 Numerical results

In this section, we begin with an analysis of the behavior of the NLO weak corrections to the cross section of the $e^+e^- \to hZ$ process in the SM. We then analyze the deviations from the SM values at NLO in the HSM, the IDM and the 2HDMs.

We have newly implemented the formulae of $F_{i,\sigma}^{(1)}$ into the `H-COUP` program [45, 46], and enabled to evaluate the cross section of $e^+e^- \to hZ$ including the higher-order corrections. In order to compare our results in the SM with the previous works [115, 122–124], we extend the `H-COUP` program and take m_W as an input instead of G_F. With this extension, we have confirmed that our results are in agreement with the previous results. In the following, we show the results obtained in the scheme where $\alpha_{\rm em}(0), G_F$ and m_Z are input parameters.

In order to study the theoretical behavior of the one-loop corrections, we parametrize the differential cross section as

$$\mathrm{d}\sigma = \mathrm{d}\sigma_{\rm LO}(1 + \delta_{\rm weak} + \delta_{\rm em}), \tag{6.57}$$

where $\delta_{\rm weak}$ and $\delta_{\rm em}$ denote the relative weak and electromagnetic corrections, respectively.

As we will see below, the NP effects mainly come from $\widehat{\Gamma}_{hZZ}^1$ vertex, and that appear independently of σ and λ. Therefore, we show the results of the unpolarized cross section where the polarization of the Z boson is also summed. In order to analyze the NP effects in each renormalized quantity, we introduce $\overline{\Delta}_X^{\rm EW}$,

$$\overline{\Delta}_X^{\rm EW} = \Delta_{X,\rm NP}^{\rm EW} - \Delta_{X,\rm SM}^{\rm EW}, \quad (X = ZZ,\ Z\gamma,\ Ze\bar{e},\ hZZ,\ hZ\gamma,\ he\bar{e},\ \mathrm{Box},\ \Pi'_{ZZ},\ \Delta r), \tag{6.58}$$

with $\Delta_X^{\rm EW} = \sigma_X/\sigma_{\rm LO}$. We evaluate σ_X by substituting

$$\mathcal{M}_{\sigma\lambda}^{(1)X}(s,t) = \sum_{i=1}^{3} F_{i,\sigma}^X \mathcal{M}_{i,\sigma\lambda} \tag{6.59}$$

into $\mathcal{M}_{\sigma\lambda}^{(1)}(s,t)$ in Eq. (6.28), where $F_{i,\sigma}^X$ is defined in Eq. (6.37). We also evaluate the ratios of the total cross sections to exhibit the deviations from the predictions in the SM,

$$\Delta R^{hZ} = \frac{\sigma_{\rm NP}}{\sigma_{\rm SM}} - 1. \tag{6.60}$$

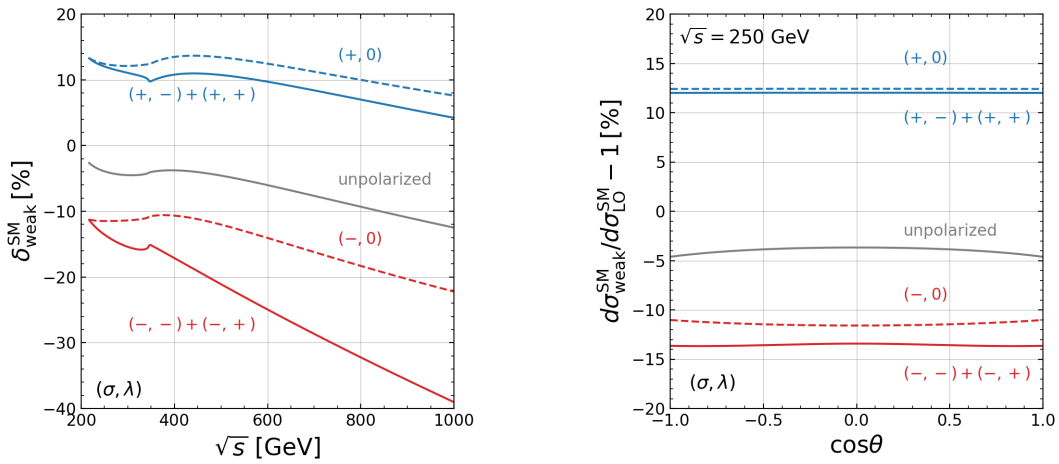

Figure 6.5: (Left) Weak corrections to the helicity-dependent cross sections in the SM. The red lines show the results for the left-handed electron and the right-handed positron, while the blue lines show those for the right-handed electron and the left-handed positron. The solid (dashed) lines show the results for the transversely (longitudinally) polarized Z bosons. The black solid line corresponds to that for the unpolarized cross section where the polarization of Z boson is also summed. (Right) Weak corrections to the helicity-dependent differential cross sections in the SM at $\sqrt{s} = 250$ GeV. The line colors and styles are the same as those of the left figure.

6.2.1 Standard Model

In the left panel of Fig. 6.5, we show the weak one-loop corrections to the helicity-dependent cross sections as a function of the CM energy. The weak corrections to the cross section for the right-handed electron are positive, and they increase the cross section by about 10%. On the other hand, those for the left-handed electron are negative, and the size of these corrections strongly depends on the CM energy. The reason for this difference comes from negative contributions from the box diagrams. Among the six box diagrams, the five W boson mediated diagrams only contribute to the helicity amplitudes for the left-handed electron. They give negative contributions to the helicity-dependent cross sections for the left-handed electron. In addition, their effects become relevant at higher energies and give large negative corrections. The peak around $\sqrt{s} \simeq 350$ GeV corresponds to the threshold at $2m_t$ in the top-loop contributions. We note that the NNLO electroweak-QCD corrections have been estimated in Refs. [123, 124], and the magnitude is about a percent.

In the right panel of Fig. 6.5, we show the weak one-loop corrections to the differential cross sections as a function of the CM energy. From Eq. (6.55), we can see that only the $he\bar{e}$ vertex and box corrections cause different $\cos\theta$ dependence from those at LO. At $\sqrt{s} = 250$ GeV, this effect is not so large, and the angular distribution of the Z boson is almost determined by the $d^1_{\sigma,\lambda}(\theta)$ functions. At higher energies, the angular distribution of the Z boson is significantly modified through the box contributions [115]. However, the size of the cross sections decreases in such a higher energy region.

6.2.2 Higgs singlet model

First, we consider the Z_2 symmetric scenario in the HSM where $c_\alpha = 1$ and $\mu_S = 0$. There remain three input parameters, m_H, $\lambda_{\Phi S}$ and λ_S. In the following analysis, we impose perturbative unitarity, vacuum stability, avoiding wrong vacua, and the constraints on the S and T

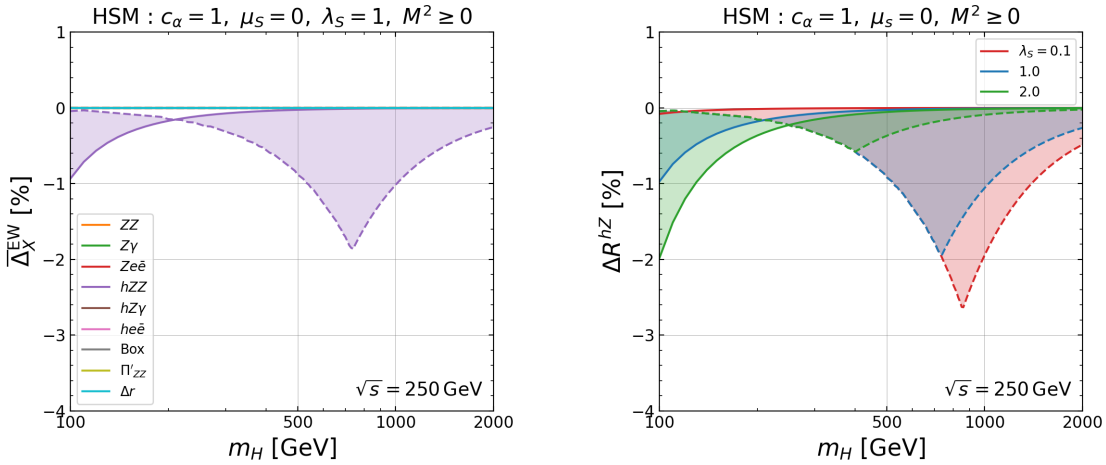

Figure 6.6: NP effects in the EW corrections as a function of the mass of the additional Higgs boson in the Z_2 symmetric HSM at $\sqrt{s} = 250$ GeV. The left panel shows $\overline{\Delta}_X^{\rm EW}$ with $\lambda_S = 1$. The right panel shows ΔR^{hZ} with $\lambda_S = 0.1$ (red), 1 (blue) and 2 (green). The solid and dashed curves denote the case with the maximal and minimal values of M^2, respectively. Perturbative unitarity, vacuum stability, avoiding wrong vacua, and the constraints on the S and T parameters are imposed.

parameters. In order to analyze the theoretical behavior, we here do not impose the constraints from the direct searches of the additional Higgs boson and the Higgs coupling measurements. In addition, we impose $M^2 > 0$ as in the case of the IDM and the 2HDMs.

In the left panel of Fig. 6.6, we show $\overline{\Delta}_X^{\rm EW}$ defined in Eq. (6.58) as a function of the mass of the additional Higgs boson in the Z_2 symmetric HSM at $\sqrt{s} = 250$ GeV. We here take $\lambda_S = 1$ and scan $\lambda_{\Phi S}$ for $|\lambda_{\Phi S}| < 4\pi$. In the Z_2 symmetric HSM, only $\overline{\Delta}_{hZZ}^{\rm EW}$ takes non-zero value. Furthermore, among the components of the renormalized hZZ vertex in Eq. (**??**), the wave function renormalization factor of the SM-like Higgs boson δZ_h only gives the NP effects. δZ_h is defined by the two-point function of the SM-like Higgs boson $\Pi_{hh}^{\rm 1PI}(p^2)$ as

$$\delta Z_h = -\frac{\rm d}{{\rm d}p^2}\Pi_{hh}^{\rm 1PI}(p^2)\Big|_{p^2=m_h^2}. \tag{6.61}$$

As the NP contributions, there are two H propagated diagrams in $\Pi_{hh}^{\rm 1PI}(p^2)$. One of them is proportional to λ_{hhHH}, while the other is proportional to λ_{hHH}^2. However, the former does not contribute to δZ_h because the loop function $A(m_H)$ does not depend on the external momentum p^2. Therefore, only the latter contributes to the helicity amplitude as the NP effect,

$$\delta Z_h^{\rm HSM} - \delta Z_h^{\rm SM} = -\frac{\lambda_{hHH}^2}{16\pi^2}\frac{\rm d}{{\rm d}p^2}B_0(p^2; m_H^2, m_H^2)\Big|_{p^2=m_h^2}, \tag{6.62}$$

with $\lambda_{hHH} = -\lambda_{\Phi S} v$. We note that this difference does not directly depend on λ_S, but it indirectly determines the possible size of the NP effects through the perturbative unitarity and vacuum stability bounds.

The magnitude of $\overline{\Delta}_{hZZ}^{\rm EW}$ becomes larger when the mass of the extra Higgs boson is taken to be larger up to around 700 GeV. This peak corresponds to the point where the minimum value of $M^2 = m_H^2 - \lambda_{\Phi S} v^2$ changes from zero to non-zero due to the perturbative unitarity bound.

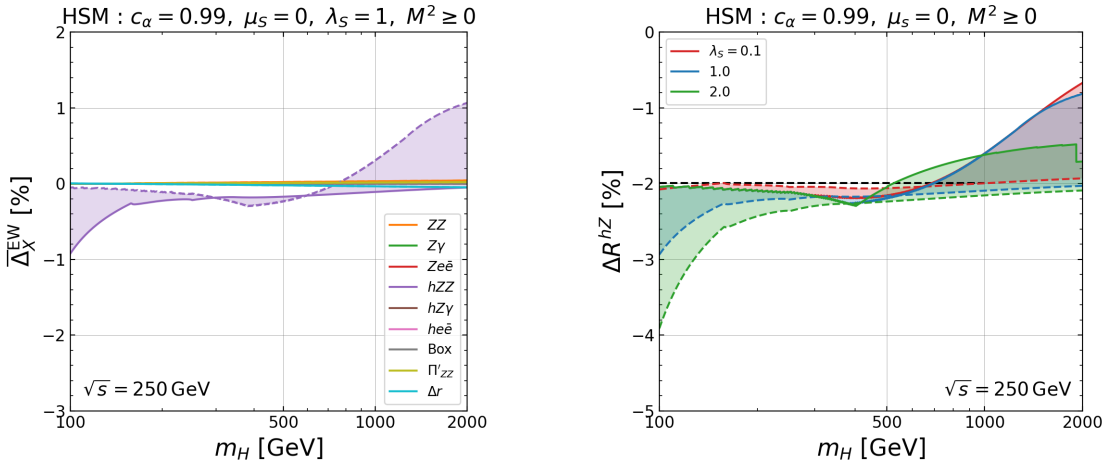

Figure 6.7: NP effects in the EW corrections as a function of the mass of the additional Higgs boson in the HSM with $c_\alpha = 0.99$ and $\mu_S = 0$ at $\sqrt{s} = 250$ GeV. The left panel shows $\overline{\Delta}_X^{\rm EW}$ with $\lambda_S = 1$. The right panel shows ΔR^{hZ} with $\lambda_S = 0.1$ (red), 1 (blue) and 2 (green). The solid and dashed curves denote the case with the maximal and minimal values of M^2, respectively. The black dashed line shows the size of the LO deviation due to the mixing of the CP-even states. Perturbative unitarity, vacuum stability, avoiding wrong vacua, and the constraints on the S and T parameters are imposed.

At this point, $\lambda_{\Phi S}$ takes the maximal value, and it triggers a sizable effect. In the case of larger values of m_H, the magnitude of $\overline{\Delta}_{hZZ}^{\rm EW}$ monotonically decreases because perturbative unitarity constrains the size of $\lambda_{\Phi S}$. In such a large mass region, m_H is approximately equal to M, and the additional Higgs boson almost decouples following the decoupling theorem [34].

We can also see the relatively large NP effects when the mass of the additional Higgs boson is below 200 GeV. In this region, $\lambda_{\Phi S}$ takes a negative value satisfying the vacuum stability bound thanks to the sizable λ_S. While the sign of $\lambda_{\Phi S}$ is flipped, only $|\lambda_{\Phi S}|^2$ appears in Eq. (6.62). Therefore, $\overline{\Delta}_{hZZ}^{\rm EW}$ is negative independently of the sign of $\lambda_{\Phi S}$.

In the right panel of Fig. 6.6, we show the predictions of ΔR^{hZ} in Eq. (6.60) as a function of the mass of the additional Higgs boson in the Z_2 symmetric HSM at $\sqrt{s} = 250$ GeV. We here take λ_S to $0.1, 1$ and 2 and scan $\lambda_{\Phi S}$ for $|\lambda_{\Phi S}| < 4\pi$. In the Z_2 symmetric HSM, the Z_2 symmetry prohibits the mixing of the CP-even states, and $\Delta R^{hZ} = 0$ at LO. The behavior of ΔR^{hZ} is only determined by δZ_h, and almost the same as that of $\overline{\Delta}_{hZZ}^{\rm EW}$. The possible magnitude of ΔR^{hZ} indirectly depends on the value of λ_S through the conditions of perturbative unitarity and vacuum stability. For $m_H \geq 200$ GeV, the possible magnitude of ΔR^{hZ} decreases as λ_S becomes large. On the other hand, for $m_H < 200$ GeV, the possible magnitude of ΔR^{hZ} increases as λ_S becomes large because a large negative value of $\lambda_{\Phi S}$ is allowed under the vacuum stability bound.

We here mention the scenario where μ_S softly breaks the Z_2 symmetry. We note that ΔR^{hZ} does not directly depend on μ_S, and the behavior of ΔR^{hZ} is the same as that in the Z_2 symmetric HSM. However, μ_S indirectly affects the possible size of the NP effects through the conditions for avoiding wrong vacua. For example, the region where $m_H \lesssim 300$ GeV is excluded if $\mu_S = 100$ GeV.

Next, we consider the scenario with the mixing of the CP-even states. In the left panel of Fig. 6.7, we show $\overline{\Delta}_X^{\rm EW}$ as a function of the mass of the additional Higgs boson with $c_\alpha = 0.99$

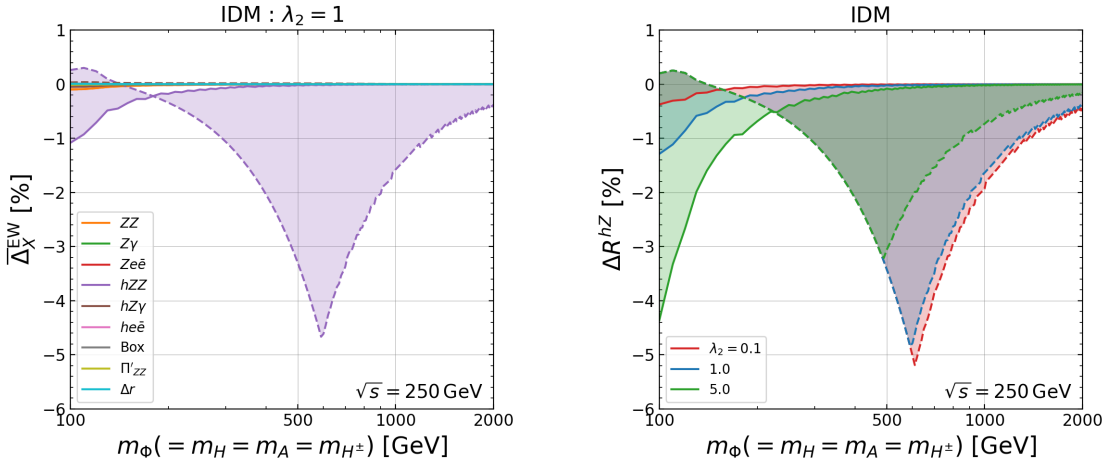

Figure 6.8: NP effects in the EW corrections as a function of the masses of the additional Higgs bosons in the IDM at $\sqrt{s} = 250$ GeV. We take $m_H = m_A = m_{H^\pm}$. The left panel shows $\overline{\Delta}_X^{\rm EW}$ with $\lambda_2 = 1$. The right panel shows ΔR^{hZ} with $\lambda_2 = 0.1$ (red), 1 (blue) and 5 (green). The solid and dashed curves denote the case with the maximal and minimal value of M^2, respectively. Perturbative unitarity and vacuum stability bounds and the constraints on the S and T parameters are imposed.

and $\mu_S = 0$ at $\sqrt{s} = 250$ GeV. We here take $\lambda_S = 1$ and scan $\lambda_{\Phi S}$ for $|\lambda_{\Phi S}| < 4\pi$. We note that not only the renormalized hZZ vertex but also the other renormalized quantities differ from the SM values unlike the case in the Z_2 symmetric HSM. However, the magnitude of $\overline{\Delta}_{hZZ}^{\rm EW}$ is larger than that of the others. For $m_H \lesssim 700\,\text{GeV}$, $\overline{\Delta}_{hZZ}^{\rm EW}$ takes a negative value, while it takes a positive value for $m_H > 700$ GeV. In order to realize the finite mixing of the CP-even states with a large mass of the additional Higgs boson, the Higgs quartic couplings should take large values, and it triggers a so-called non-decoupling effect.

In the right panel of Fig. 6.7, we show the predictions of ΔR^{hZ} as a function of the mass of the additional Higgs boson with $c_\alpha = 0.99$ and $\mu_S = 0$ at $\sqrt{s} = 250$ GeV. We here take λ_S to 0.1, 1 and 2 and scan $\lambda_{\Phi S}$ for $|\lambda_{\Phi S}| < 4\pi$. If there is the mixing of the CP-even states, the LO cross section decreases from its SM value. When $c_\alpha = 0.99$, the size of deviation is $\Delta R^{hZ} = -s_\alpha^2 \simeq -0.02$ at LO. We can see that the magnitude of one-loop effects is comparable with that of the LO contribution, and the NP effects sizably change the predictions for ΔR^{hZ}. The behavior of ΔR^{hZ} is almost the same as that of $\overline{\Delta}_{hZZ}^{\rm EW}$. For $m_H \lesssim 500\,\text{GeV}$, $\overline{\Delta}_{hZZ}^{\rm EW}$ increases the magnitude of ΔR^{hZ}, while it decreases the magnitude of ΔR^{hZ} for $m_H > 500$ GeV. For $m_H \geq 1000$ GeV, the possible magnitude of ΔR^{hZ} decreases as λ_S becomes large. On the other hand, for $m_H < 500$ GeV, it increases as λ_S becomes large.

6.2.3 Inert doublet model

In the IDM, the Z_2 symmetry prohibits the mixing of the CP-even states, and $\Delta R^{hZ} = 0$ at LO, similarly to the case in the Z_2 symmetric HSM. In the following analysis, we assume that the additional Higgs bosons are degenerate in their mass, $m_\Phi \equiv m_H = m_{H^\pm} = m_A$. There remain two input parameters, λ_2 and M^2. We impose perturbative unitarity, vacuum stability, avoiding wrong vacua, and the constraints on the S and T parameters. In order to analyze the theoretical behavior, we here do not impose the constraints from the direct searches of the additional Higgs boson, the Higgs coupling measurements and the dark matter experiments.

In the left panel of Fig. 6.8, we show $\overline{\Delta}_X^{\rm EW}$ as a function of the mass of the additional Higgs bosons in the IDM at $\sqrt{s} = 250\,\text{GeV}$. We here take $\lambda_2 = 1$ and scan M^2 for $0 \leq M^2 \leq (3\,\text{TeV})^2$. We note that not only the renormalized hZZ vertex but also the other renormalized quantities differ from the SM values unlike in the Z_2 symmetric HSM. This is because the additional Higgs bosons are charged under the SM gauge group. However, the magnitude of $\overline{\Delta}_{hZZ}^{\rm EW}$ is larger than that of the others in most cases. In the IDM, there are two main contributions to $\overline{\Delta}_{hZZ}^{\rm EW}$. The first one is $\lambda_{h\Phi\Phi}^2$ terms originated from δZ_h, similarly to the case in the Z_2 symmetric HSM. In addition, there are 1PI diagram contributions proportional to $\lambda_{h\Phi\Phi}$, where the additional Higgs bosons propagate internal lines. The couplings $\lambda_{h\Phi\Phi}$ are proportional to $(m_\Phi^2 - M^2)/v$, and large corrections appear when one consider the sizable differences between m_Φ and M. In general, δZ_h governs the magnitude of $\overline{\Delta}_{hZZ}^{\rm EW}$, and its behavior is almost the same as that in the Z_2 symmetric HSM. The maximal deviation in the IDM is larger than that in the Z_2 symmetric HSM because we have more than one additional Higgs boson running in the loop in the IDM. It monotonically decreases when $m_\Phi > 600$ GeV following the decoupling theorem.

We can also see the sizable NP effects when m_Φ is below 200 GeV, similarly to the case in the HSM. In addition, $\overline{\Delta}_{hZZ}^{\rm EW}$ can be positive if m_Φ is lighter than about 150 GeV. This is because of the contributions from 1PI diagrams. While δZ_h gives negative contributions to $\overline{\Delta}_{hZZ}^{\rm EW}$, 1PI diagrams for the hZZ vertex give positive contributions. As we have already mentioned, δZ_h generally gives larger contributions than 1PI diagram contributions. However, if $\lambda_{h\Phi\Phi}$ is not so large, 1PI diagram contributions can overcome the contribution of δZ_h, and there are parameter points, where $\overline{\Delta}_{hZZ}^{\rm EW}$ is positive.

In the right panel of Fig. 6.8, we show the predictions of ΔR^{hZ} as a function of the mass of the additional Higgs bosons in the IDM at $\sqrt{s} = 250$ GeV. We here take λ_2 to $0.1, 1$ and 5 and scan M^2 for $0 \leq M^2 \leq (3\,\text{TeV})^2$. The behavior of ΔR^{hZ} is almost the same as that of $\overline{\Delta}_{hZZ}^{\rm EW}$. The possible magnitude of ΔR^{hZ} indirectly depends on the value of λ_2 through the conditions of perturbative unitarity and vacuum stability. For $m_\Phi \geq 200$ GeV, the possible magnitude of ΔR^{hZ} decreases as λ_2 becomes large. On the other hand, for $m_\Phi < 200$ GeV, the possible magnitude of ΔR^{hZ} increases as λ_2 becomes large, similarly to the case in the Z_2 symmetric HSM.

6.2.4 Two Higgs doublet model

First, we consider the alignment limit with $s_{\beta-\alpha} = 1$, where $\Delta R^{hZ} = 0$ at LO. We also assume that the additional Higgs bosons are degenerate in their mass, $m_\Phi \equiv m_H = m_{H^\pm} = m_A$. There remain two input parameters, $\tan\beta$ and M^2. We impose perturbative unitarity, vacuum stability, avoiding wrong vacua, and the constraints on the S and T parameters. In order to analyze the theoretical behavior, we here do not impose the constraints from the direct searches of the additional Higgs boson, the Higgs coupling measurements and the flavor measurements.

We analyze all the four types of 2HDMs, and it turns out that predictions for $\overline{\Delta}_X^{\rm EW}$ and ΔR^{hZ} are almost the same. This is because differences among the four types of 2HDMs appear through the down-type quark and lepton Yukawa interactions with the SM-like Higgs boson. As we will see later, the magnitude of $\overline{\Delta}_{hZZ}^{\rm EW}$ is larger than that of the others in the 2HDMs, similarly to the case in the HSM and the IDM. In $\overline{\Delta}_{hZZ}^{\rm EW}$, the top-quark contributions dominate fermionic contributions, and there is no sizable difference among the four types of 2HDMs. Therefore, we show the predictions for ΔR^{hZ} in the Type-I 2HDM as a representative in the following.

In the left panel of Fig. 6.9, we show $\overline{\Delta}_X^{\rm EW}$ as a function of the mass of the additional Higgs

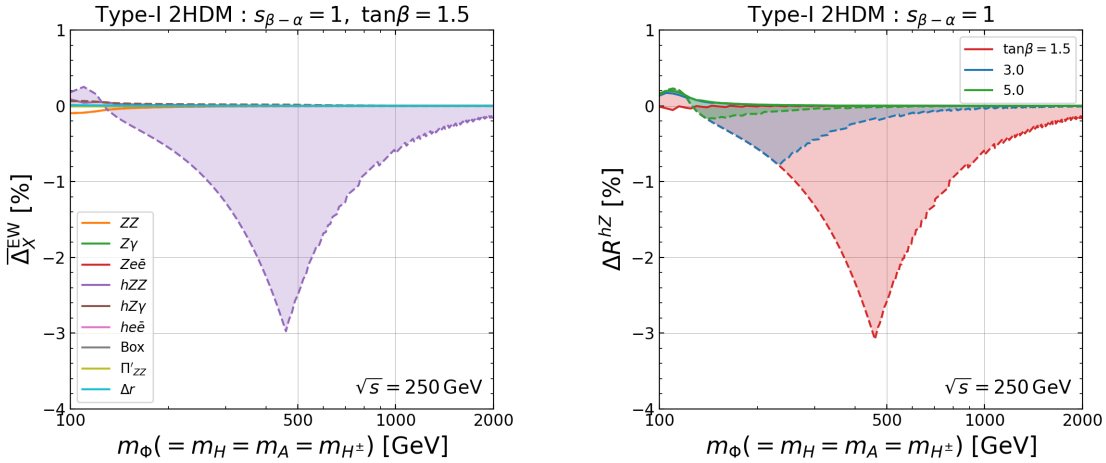

Figure 6.9: NP effects in the EW corrections as a function of masses of the additional Higgs bosons in the Type-I 2HDM with $s_{\beta-\alpha} = 1$ at $\sqrt{s} = 250$ GeV. We take $m_H = m_A = m_{H^\pm}$. The left panel shows $\overline{\Delta}_X^{\rm EW}$ with $\tan\beta = 1.5$. The right panel shows ΔR^{hZ} with $\tan\beta = 1.5$ (red), 3 (blue) and 5 (green). The solid and dashed curves denote the case with the maximal and minimal value of M^2, respectively. Perturbative unitarity and vacuum stability bounds and the constraints on the S and T parameters are imposed.

bosons in the Type-I 2HDM with $s_{\beta-\alpha} = 1$ at $\sqrt{s} = 250\,\text{GeV}$. We here take $\tan\beta = 1.5$ and scan M^2 for $0 \leq M^2 \leq (3\,\text{TeV})^2$. We note that not only the renormalized hZZ vertex but also the other renormalized quantities differ from the SM values because the additional Higgs bosons interact with the gauge bosons, the quarks and the leptons. Qualitative behaviors of $\overline{\Delta}_X^{\rm EW}$ are almost the same as those in the Z_2 symmetric HSM and the IDM except for $m_\Phi \leq 200\,\text{GeV}$. The magnitude of $\overline{\Delta}_{hZZ}^{\rm EW}$ is larger than that of the others in most of the parameter space. It monotonically decreases when $m_\Phi > 450$ GeV following the decoupling theorem.

There is no sizable negative correction below 200 GeV unlike in the Z_2 symmetric HSM and the IDM. This is because the Higgs quartic couplings in the 2HDMs are more constrained by vacuum stability than λ_S in the HSM and λ_2 in the IDM. If m_Φ is lighter than about 150 GeV, $\overline{\Delta}_X^{\rm EW}$ can be positive due to the 1PI diagram contributions, similarly to the case in the IDM.

In the right panel of Fig. 6.9, we show the predictions of ΔR^{hZ} as a function of the mass of the additional Higgs bosons in the Type-I 2HDM at $\sqrt{s} = 250$ GeV. We here take $\tan\beta$ to 1.5, 3 and 5 and scan M^2 for $0 \leq M^2 \leq (3\,\text{TeV})^2$. The behavior of ΔR^{hZ} is almost the same as that of $\overline{\Delta}_{hZZ}^{\rm EW}$. The possible magnitude of ΔR^{hZ} decreases as $\tan\beta$ becomes large due to the perturbative unitarity and vacuum stability bounds.

Next, we consider the scenario with the mixing of the CP-even states. In the top (bottom) left panel of Fig. 6.10, we show $\overline{\Delta}_X^{\rm EW}$ as a function of the mass of the additional Higgs bosons in the Type-I 2HDM with $s_{\beta-\alpha} = 0.99$ and $c_{\beta-\alpha} < 0$ ($c_{\beta-\alpha} > 0$) at $\sqrt{s} = 250\,\text{GeV}$. We here take $\tan\beta = 1.5$ and scan M^2 for $0 \leq M^2 \leq (3\,\text{TeV})^2$. The magnitude of $\overline{\Delta}_{hZZ}^{\rm EW}$ is larger than that of the others independently of the sign of $c_{\beta-\alpha}$. In addition, $\overline{\Delta}_{hZZ}^{\rm EW}$ takes a negative value except for the $m_H \lesssim 300\,\text{GeV}$ with $c_{\beta-\alpha} < 0$ unlike in the HSM. We can see the non-decoupling effect in a large mass region of the additional Higgs bosons because they cannot decouple while keeping the finite mixing of the CP-even states, similarly to the case in the HSM. The maximal value of m_Φ is about 900 GeV for $s_{\beta-\alpha} = 0.99$ with $c_{\beta-\alpha} < 0$, while it is about 600 GeV with $c_{\beta-\alpha} > 0$ for $\tan\beta = 1.5$.

In the top (bottom) right panel of Fig. 6.10, we show ΔR^{hZ} as a function of the mass of the additional Higgs bosons in the Type-I 2HDM with $s_{\beta-\alpha} = 0.99$ and $c_{\beta-\alpha} < 0$ ($c_{\beta-\alpha} > 0$) at $\sqrt{s} = 250\,\text{GeV}$. We here take $\tan\beta$ to 1.5, 3 and 5 and scan M^2 for $0 \leq M^2 \leq (3\,\text{TeV})^2$. The LO cross section decreases from its SM value due to the mixing of the CP-even states. When $s_{\beta-\alpha} = 0.99$, the size of deviation is $\Delta R^{hZ} = -c^2_{\beta-\alpha} \simeq -0.02$ at LO. We can see that the magnitude of one-loop effects is comparable with that of the LO contribution, and the NP effects sizably change the predictions for ΔR^{hZ}. The behavior of ΔR^{hZ} is almost the same as that of $\overline{\Delta}^{\text{EW}}_{hZZ}$. In the both signs of $c_{\beta-\alpha}$, $\overline{\Delta}^{\text{EW}}_{hZZ}$ generally increases the magnitude of $\left|\Delta R^{hZ}\right|$ except for the region with relatively lighter mass of the additional Higgs bosons. The possible magnitude of ΔR^{hZ} decreases as $\tan\beta$ becomes large due to the perturbative unitarity and vacuum stability bounds.

Finally, we mention the corrections to the angular distribution of the Z boson. As we have mentioned, the $he\bar{e}$ vertex and box contributions cause non-trivial $\cos\theta$ dependence. In the limit of the massless electron, only mixing of CP-even states modifies the $he\bar{e}$ vertex and box contributions. However, as we can see from Figs. 6.7 and 6.10, these effects are rather small at $\sqrt{s} = 250$ GeV. Therefore, the angular distribution of Z bosons is almost the same as the predictions in the SM.

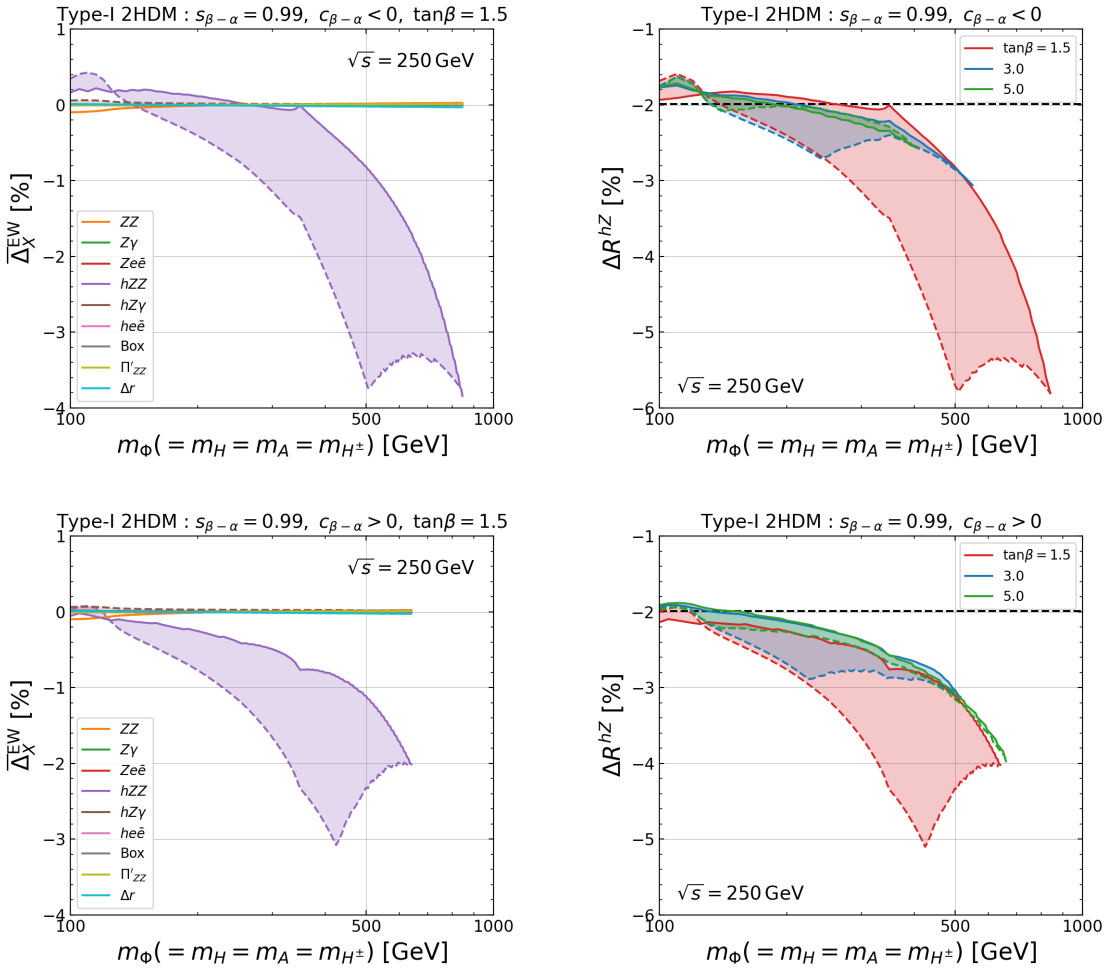

Figure 6.10: NP effects in the EW corrections as a function of masses of the additional Higgs bosons in the Type-I 2HDM with $s_{\beta-\alpha} = 0.99$ at $\sqrt{s} = 250$ GeV. We take $m_H = m_A = m_{H^\pm}$. The top left panel shows $\overline{\Delta}_X^{\rm EW}$ with $\tan\beta = 1.5$ and $c_{\beta-\alpha} < 0$. The top right panel shows ΔR^{hZ} with $\tan\beta = 1.5$ (red), 3 (blue) and 5 (green) and $c_{\beta-\alpha} < 0$. The bottom panels correspond to the case with $c_{\beta-\alpha} > 0$. The solid and dashed curves denote the case with the maximal and minimal value of M^2, respectively. The black dashed line shows the size of the LO deviation due to the mixing. Perturbative unitarity and vacuum stability bounds and the constraints on the S and T parameters are imposed.

$\sigma(e^+e^- \to Zh)$	$h \to b\bar{b}$	$h \to c\bar{c}$	$h \to \tau\bar{\tau}$	$h \to WW^*$	$h \to ZZ^*$	$h \to \gamma\gamma$
2%	1.3%	8.3%	3.2%	4.6%	18%	34%

Table 6.1: Expected 1σ accuracy for the SM-like Higgs boson measurements at the ILC. We quote the values at $\sqrt{s} = 250$ GeV with $250\,\text{fb}^{-1}$ for $(P_e, P_{\bar{e}}) = (-0.8, +0.3)$ in Table VI in Ref. [35]. Except for $\sigma(e^+e^- \to Zh)$, the numbers correspond to the accuracy of $\sigma(e^+e^- \to hZ) \times \text{BR}(h \to XY)$.

6.2.5 Correlation in the cross section times decay branching ratios

In this subsection, we analyze the correlation in the cross section times decay branching ratios of the SM-like Higgs boson in the HSM, the IDM and the four types of 2HDMs.

At future collider experiments such as the ILC, the cross section of $e^+e^- \to hZ$ can be measured without depending on the decay of the SM-like Higgs boson by utilizing the recoil mass technique [35, 125]. This makes it possible to measure the decay branching ratios of the SM-like Higgs boson independently of the cross section. However, the cross section times decay branching ratios of the SM-like Higgs boson can be measured more precisely. In Table 6.1, we summarize the expected accuracy of the cross section times decay branching ratios of the SM-like Higgs boson at the ILC at $\sqrt{s} = 250$ GeV with $250\,\text{fb}^{-1}$ for $(P_e, P_{\bar{e}}) = (-0.8, +0.3)$. The values in Table 6.1 are taken from Table VI in [35].

In the following, we analyze the predictions for $\sigma(e^+e^- \to hZ) \times \text{BR}(h \to XY)$ at one-loop level, where X and Y denote decay products of the SM-like Higgs boson. In order to discuss deviations from predictions in the SM, we evaluate the ratio of the total cross section times the decay branching ratios

$$\Delta R_{XY}^{hZ} = \frac{\sigma_{\text{NP}}(e^+e^- \to hZ)\text{BR}_{\text{NP}}(h \to XY)}{\sigma_{\text{SM}}(e^+e^- \to hZ)\text{BR}_{\text{SM}}(h \to XY)} - 1, \tag{6.63}$$

where we assume the beam polarization $(P_e, P_{\bar{e}}) = (-0.8, +0.3)$. In the evaluation of the decay branching ratios of the SM-like Higgs boson with the one-loop EW and QCD corrections, we use the `H-COUP` program [45, 46]. Although the magnitude of ΔR_{XY}^{hZ} depends on the treatment of the QED corrections, we do not consider these corrections and discuss the pattern of the deviations in the correlation of $\sigma(e^+e^- \to hZ) \times \text{BR}(h \to XY)$. The QED corrections in the cross section universally change the magnitude of $\sigma(e^+e^- \to hZ) \times \text{BR}(h \to XY)$. Therefore, the pattern of the deviations is not changed even if we include the QED corrections following a realistic experimental setup.

We scan the input parameters in each model in the following way. In the HSM, there are five input parameters as given in Eq. (3.21). We here use M^2 as an input parameter instead of $\lambda_{\Phi S}$. The mass of the additional Higgs boson H is scanned as

$$400\,\text{GeV} \leq m_H < 2000\,\text{GeV}, \tag{6.64}$$

while c_α and M^2 are scanned as

$$0.95 \leq c_\alpha < 1, \quad 0 \leq M^2 < (m_H + 250\ \text{GeV})^2. \tag{6.65}$$

We here take $\mu_s = 0$ and $\lambda_S = 0.1$ for simplicity.

In the 2HDMs, we have six input parameters given in Eq. (3.49). We assume that the additional Higgs bosons are degenerate in their mass as in the previous subsection. In this

κ_b	κ_τ	κ_γ	κ_g	κ_Z	κ_W
$1.03^{+0.19}_{-0.17}$	$1.05^{+0.16}_{-0.15}$	1.05 ± 0.09	$0.99^{+0.11}_{-0.10}$	1.11 ± 0.08	1.05 ± 0.09

Table 6.2: Current measurements κ_{XY} factors at 1σ accuracy. We quote the values in Table XI in [127]. We assume that there is no decay mode where the SM-like Higgs boson decays into additional Higgs bosons.

scenario, the constraint of the T parameter is satisfied independently of the type of the 2HDMs. The degenerate mass $m_\Phi (= m_{H^\pm} = m_H = m_A)$ is scanned as

$$400\,\text{GeV} \leq m_\Phi < 2000\,\text{GeV} \quad \text{for the Type-I and X 2HDMs,} \tag{6.66}$$

$$800\,\text{GeV} \leq m_\Phi < 2000\,\text{GeV} \quad \text{for the Type-II and Y 2HDMs.} \tag{6.67}$$

The lower bound of m_Φ in the Type-I and Type-X 2HDMs comes from the direct search for $A \to \tau\bar{\tau}$ at the LHC [42]. In the Type-I 2HDM, the parameter regions with $\tan\beta \gtrsim 2$ are not excluded. However, we take the above parameter regions for simplicity. In the Type-II and Type-Y 2HDMs, the lower bound comes from the flavor experiments, especially from $B_s \to X_s\gamma$ [126]. In addition, we scan the other parameters as

$$0.98 \leq s_{\beta-\alpha} < 1, \quad 2 \leq \tan\beta < 10, \quad 0 \leq M^2 < (m_\Phi + 250\ \text{GeV})^2. \tag{6.68}$$

The lower bound of $\tan\beta$ comes from the flavor experiments. We analyze both the positive and negative signs of $c_{\beta-\alpha}$.

In the IDM, we have five input parameters given in Eq. (3.66). We take $m_H = 63$ GeV which is favored by dark matter constraints. In order to satisfy the constraint on the T parameter, we assume that $H^\pm$ and A are degenerate in mass. The degenerate mass $m_{H^\pm} (= m_A)$, M^2 and λ_2 are scanned as

$$100\,\text{GeV} \leq m_{H^\pm} < 1000\,\text{GeV}, \tag{6.69}$$

$$0 \leq M^2 < (m_\Phi + 250\,\text{GeV})^2, \tag{6.70}$$

$$0 < \lambda_2 < 4\pi. \tag{6.71}$$

Over the above parameter spaces, we impose the constraints discussed in Chapter. 3 such as perturbative unitarity, vacuum stability, avoiding wrong vacua, and the constraints on the S and T parameters. In addition, we take into account the current data of the signal strengths of the discovered Higgs boson at the LHC. We evaluate the decay rates of the SM-like Higgs boson with higher-order corrections by using the `H-COUP` program [45,46]. We define the scaling factor $\kappa_{XY} = \sqrt{\Gamma^{\rm NP}_{h\to XY}/\Gamma^{\rm SM}_{h\to XY}}$ at the one-loop level, and remove the parameter points, where κ_{XY} deviates from the observed data at 95% C.L.. In Table 6.2, we summarize the current measurements of κ_{XY} factors at 1σ accuracy. The values in Table 6.2 are taken from Table XI in Ref. [127]. We assume that there is no decay mode where the SM-like Higgs boson decays into additional Higgs bosons.

In the Type-II, X and Y 2HDMs, we have parameter points where Yukawa coupling constants take the negative sign with a large value of $\tan\beta$ and $c_{\beta-\alpha} > 0$. These parameter points show the sizable deviation both in the Higgs branching ratio and cross section. However, we simply omit such particular parameter points in the following analysis in order to extract general features in the 2HDMs.

Before moving on to the numerical results, we discuss the general property of ΔR^{hZ}_{XY}. The ratio of the total cross section times the decay branching ratio ΔR^{hZ}_{XY} can be rewritten as

$$\Delta R^{hZ}_{XY} = \Delta R^{Zh} + \Delta R_{XY} + \Delta R^{Zh}\Delta R_{XY}, \tag{6.72}$$

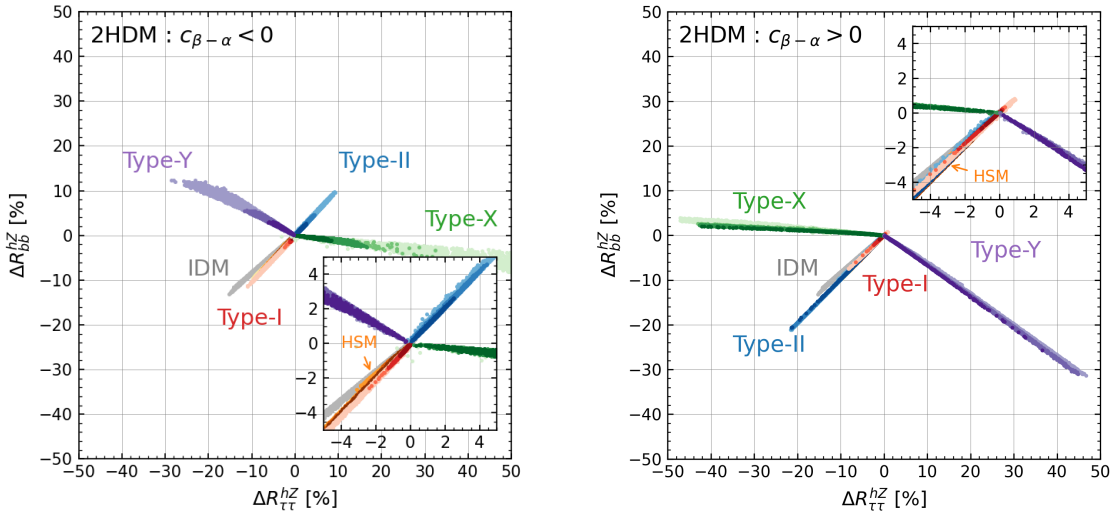

Figure 6.11: Correlation between $\Delta R^{hZ}_{\tau\tau}$ and ΔR^{hZ}_{bb} in the HSM (orange), the IDM (grey) and the Type-I (red), Type-II (blue), Type-X (green), Type-Y (purple) 2HDMs. The left panel shows the results with $c_{\beta-\alpha} < 0$ in the 2HDMs, and the right panel shows those with $c_{\beta-\alpha} > 0$. The ranges of the parameters are explained in the text. The lighter color corresponds to the lighter mass scale of the additional Higgs bosons, $m_\Phi \geq 400$, 800, 1200 and 1600 GeV in order.

with ΔR^{Zh} defined in Eq. (6.60) and ΔR_{XY} defined as

$$\Delta R_{XY} = \frac{\mathrm{BR}_{\mathrm{NP}}(h \to XY)}{\mathrm{BR}_{\mathrm{SM}}(h \to XY)} - 1. \tag{6.73}$$

The order of loop expansion of $\Delta R^{Zh}\Delta R_{XY}$ is $\mathcal{O}(\hbar^2)$, and it is sub-leading. Therefore, the qualitative behavior of ΔR^{hZ}_{XY} can be understood by independently analyzing ΔR^{Zh} and ΔR_{XY}.

The behavior of ΔR_{XY} has been studied in Ref. [98] by using the `H-COUP` program [45, 46]. For later convenience, we briefly summarize the behavior of ΔR_{XY} in the HSM, the IDM and the four types of 2HDMs. First, in the HSM, the decay branching ratios of h are almost the same as those in the SM predictions, because the partial decay widths are universally suppressed by the radiative corrections and the mixing of the CP-even states. In our study, both $\Delta R_{\tau\tau}$ and ΔR_{bb} are at most 0.5%.

The same argument has been claimed for the IDM in Ref. [98]. However, we find that the parameter regions where both ΔR_{bb} and $\Delta R_{\tau\tau}$ take a few percent deviations. This difference comes from the large value of λ_2. In Ref. [98], λ_2 has been fixed to 0.1. However, the magnitude of λ_2 indirectly controls the possible size of other Higgs quartic couplings especially through the vacuum stability bound given in Eq. (3.60). We have obtained the almost same results as those in Ref. [98] when we impose $\lambda_2 \leq 0.1$.

In the 2HDMs, the predictions to $\Delta R_{\tau\tau}$ and ΔR_{bb} spread out into different directions according to the type of the Yukawa interactions and the sign of $c_{\beta-\alpha}$. The possible magnitudes of the deviations in the Type-II, X and Y 2HDMs are rather large compared to the Type-I 2HDM, the HSM and the IDM. They can reach several tens of percent, and especially $\Delta R_{\tau\tau}$ reaches a hundred percent in the Type-X 2HDM.

In Fig. 6.11, we show the correlations between $\Delta R^{hZ}_{\tau\tau}$ and ΔR^{hZ}_{bb} in the HSM, the IDM and the four types of 2HDMs. We take the color codes where orange, grey, red, blue, green and purple correspond to the HSM, the IDM and the Type-I, II, X, Y 2HDMs, respectively.

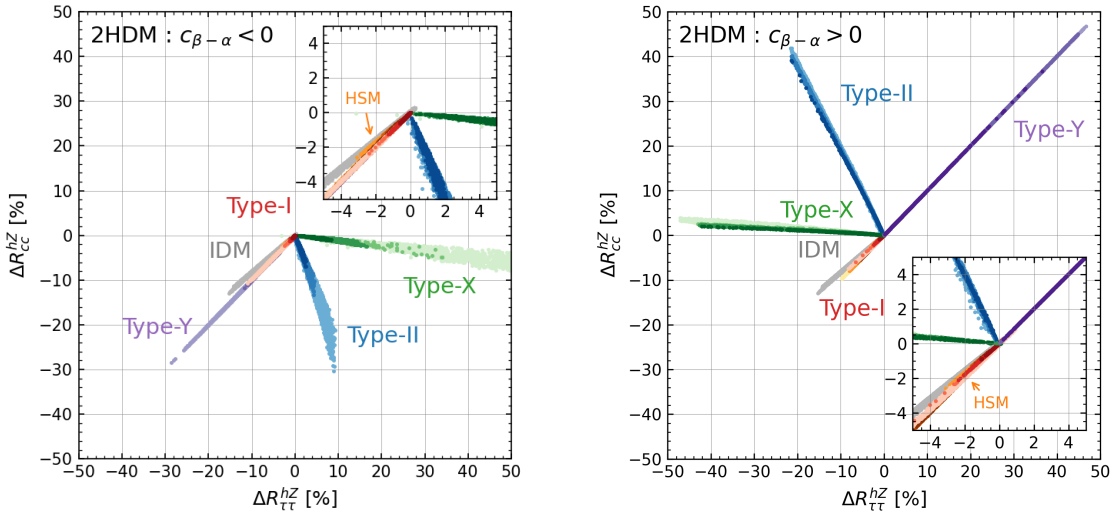

Figure 6.12: Correlation between $\Delta R^{hZ}_{\tau\tau}$ and ΔR^{hZ}_{cc}. Color codes and the ranges of the parameters are the same as in those of Fig. 6.11.

The lighter color corresponds to the lighter mass scale of the additional Higgs bosons, $m_\Phi \geq$ 400, 800, 1200 and 1600 GeV in order. In the left (right) panel, we show the results with $c_{\beta-\alpha} < 0$ ($c_{\beta-\alpha} > 0$). The results in the HSM and the IDM are the same both in the left and right panels.

As discussed in Eq. (6.72), ΔR^{hZ}_{XY} can be rewritten as the sum of ΔR^{Zh} and ΔR_{XY}, and ΔR^{Zh} takes a negative value in most cases. In the Type-II, X and Y 2HDMs, the typical size of ΔR_{XY} is larger than ΔR^{Zh}. Therefore, the pattern of the deviation is mainly determined by ΔR_{XY}, and it is consistent with previous analysis in Ref. [98]. In these models, the possible sizes of the deviations are large enough to be detected at the ILC if m_Φ is about one TeV or less.

In the HSM, the Type-I 2HDM and the IDM, we can see sizable deviations both in $\Delta R^{hZ}_{\tau\tau}$ and ΔR^{hZ}_{bb}, and they reach about 10%. Both $\Delta R^{hZ}_{\tau\tau}$ and ΔR^{hZ}_{bb} take larger values than those in $\Delta R_{\tau\tau}$ and ΔR_{bb}. This is because the typical size of ΔR^{Zh} is larger than ΔR_{XY} in these models, and ΔR_{XY} also takes a negative value in the HSM, the Type-I 2HDM with $c_{\beta-\alpha} < 0$ and the IDM. In the Type-I 2HDM with $c_{\beta-\alpha} > 0$, ΔR_{XY} takes a positive value. However, the typical size of ΔR_{XY} is smaller than ΔR^{hZ}, and ΔR^{Zh}_{XY} takes a negative value in most of the parameter regions. In the Type-I 2HDM, ΔR^{Zh}_{XY} quickly decouples. This is because a non-zero $c_{\beta-\alpha}$ realizes the maximal deviation in ΔR^{hZ}, especially at LO. If m_Φ is large, the possible value of $c_{\beta-\alpha}$ is constrained mainly by perturbative unitarity. On the contrary, in the other types of 2HDMs with $c_{\beta-\alpha} > 0$, the decoupling behavior is not clearly seen. This is because taking the inner parameter $\tan\beta$ large keeps the magnitude of the deviation to be large even in the case of large m_Φ. On the other hand, constraints from the Higgs signal strength in the HSM are weaker than those in the 2HDMs, and the deviation in c_α realizes the sizable ΔR^{Zh}_{XY} even if m_Φ is larger than 1 TeV. In the IDM, the decoupling limit cannot be applied because we fix $m_H = 63$ GeV. Therefore, we have a sizable deviation although there is no mixing between the CP-even states.

In Fig. 6.12, we show the correlations between $\Delta R^{hZ}_{\tau\tau}$ and ΔR^{hZ}_{cc} in the HSM, the IDM and the four types of 2HDMs. The color codes and gradations are the same as those in Fig. 6.11. In the left (right) panel, we show the results with $c_{\beta-\alpha} < 0$ ($c_{\beta-\alpha} > 0$). The results in the HSM

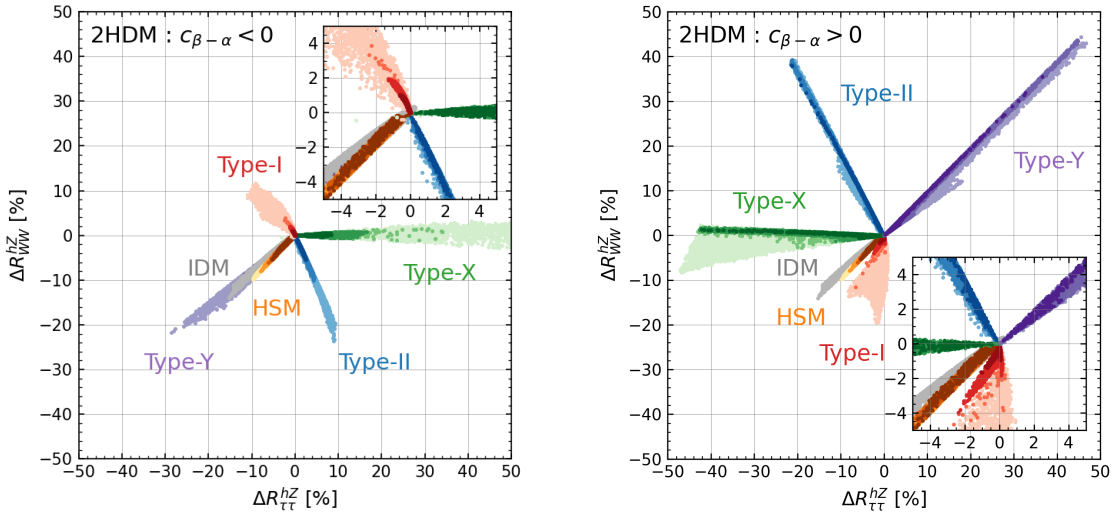

Figure 6.13: Correlation between $\Delta R^{hZ}_{\tau\tau}$ and ΔR^{hZ}_{WW}. Color codes and the ranges of the parameters are the same as in those of Fig. 6.11.

and the IDM are the same both in the left and right panels.

The qualitative behavior of the deviations in each model is the same as in Fig. 6.11. In the Type-II, X and Y 2HDMs, the typical size of ΔR_{XY} is larger than ΔR^{Zh}, and the pattern of the deviation is mainly determined by ΔR_{XY}. On the other hand, we also have sizable deviations in the HSM, the Type-I 2HDM and the IDM, and they reach about 10%. In the Type-I 2HDM with $c_{\beta-\alpha} > 0$, ΔR_{XY} takes a positive value. However, the typical size of ΔR_{XY} is smaller than ΔR^{hZ}, and ΔR^{Zh}_{XY} takes a negative value in most of the parameter regions.

If $c_{\beta-\alpha}$ is negative, the directions of the deviations in $\Delta R^{hZ}_{\tau\tau}$ and ΔR^{hZ}_{cc} are the same in the HSM, the IDM and the Type-I and Y 2HDMs. However, this overlap can be partially resolved by looking at the correlation between $\Delta R^{hZ}_{\tau\tau}$ and ΔR^{hZ}_{bb} where the Type-Y 2HDM shows a different correlation with others. On the other hand, if $c_{\beta-\alpha}$ is positive, the directions of the deviations in $\Delta R^{hZ}_{\tau\tau}$ and ΔR^{hZ}_{bb} are the same in the HSM, the IDM and the Type-I and II 2HDMs. This overlap can also be resolved by looking at the correlation between $\Delta R^{hZ}_{\tau\tau}$ and ΔR^{hZ}_{cc} where the Type-II 2HDM shows a different correlation with others.

In order to discriminate the Type-I 2HDM from the HSM and the IDM, we can use the correlation between $\Delta R^{hZ}_{\tau\tau}$ and ΔR^{hZ}_{WW}. In Fig. 6.13, we show the correlations between $\Delta R^{hZ}_{\tau\tau}$ and ΔR^{hZ}_{WW} in the HSM, the IDM and the four types of 2HDMs. The color codes and gradations are the same as those in Fig. 6.11. In the left (right) panel, we show the results with $c_{\beta-\alpha} < 0$ ($c_{\beta-\alpha} > 0$). The results in the HSM and the IDM are the same both in the left and right panels. Especially in the case of $c_{\beta-\alpha} < 0$, ΔR^{hZ}_{WW} takes a positive value in the Type-I 2HDM, while it takes a negative value in the HSM and the IDM. Even in the case of $c_{\beta-\alpha} > 0$, there is a stronger correlation between $\Delta R^{hZ}_{\tau\tau}$ and ΔR^{hZ}_{WW} in the HSM and the IDM than those in the Type-I 2HDM.

Finally, we discuss the discrimination between the HSM and the IDM. The deviation $\Delta R^{hZ}_{\gamma\gamma}$ might be useful to discriminate these models because it is mainly affected by the contribution of the charged Higgs bosons. The behaviors of $\Delta R^{hZ}_{\tau\tau}$ and $\Delta R^{hZ}_{\gamma\gamma}$ show a different correlation between the HSM and the IDM. However, the possible size of $\Delta R^{hZ}_{\gamma\gamma}$ is at most 20%, and it is rather challenging to discriminate them with 95% C.L. at the ILC. The large uncertainty in $\Delta R^{hZ}_{\gamma\gamma}$ at the ILC mainly comes from the low statistics [35], and this would be improved by

performing the combined study with the measurements at the ILC and the HL-LHC [128].

Chapter 7

Synergy between direct searches at the LHC and precision tests at future lepton colliders

In this chapter, we discuss the complementarity between direct searches for additional Higgs bosons at the (HL-)LHC and precision measurements of the Higgs boson properties at future electron-positron colliders such as the ILC. The direct search of additional Higgs bosons gives a lower bound for the mass scale of the additional Higgs bosons. On the other hand, if the couplings of the SM-like Higgs boson slightly deviate from those in the SM, the indirect search gives an upper bound for the mass scale of the additional Higgs bosons through the theoretical constraints. The decays of additional Higgs bosons into the SM-like Higgs boson can be a dominant decay process in the approximate alignment scenario, and such Higgs-to-Higgs decays are quite useful for the direct search of additional Higgs bosons. In the 2HDM, we concretely show that most of the parameter space can be explored by utilizing the synergy between the direct search of Higgs-to-Higgs decay at future hadron colliders and the indirect search at future lepton colliders.

7.1 Decays of the Higgs bosons

In this section, we give the analytic expressions for the decay rates of the Higgs bosons including higher-order corrections in QCD. In addition, some numerical results for the decays of the Higgs bosons are shown.

7.1.1 QCD corrections to the neutral Higgs decays

In the following, we describe how to include QCD corrections for processes of the neutral Higgs bosons ϕ $(= h, H, A)$ in our calculations. For the decay rates of h, we adopt the formulae of incorporating those QCD corrections in `H-COUP v2` [46].

The decay rate into a pair of light quarks $(q \neq t)$ including next-to-next-to-leading order (NNLO) QCD corrections in the $\overline{\text{MS}}$ scheme is given by [106, 129–132]

$$\Gamma(\phi \to q\bar{q}) = \Gamma_0(\phi \to q\bar{q})(1 + \Delta_q^\phi), \tag{7.1}$$

where

$$\Delta_q^\phi = \frac{\alpha_s(\mu)}{\pi} C_F \left(\frac{17}{4} + \frac{3}{2} \ln \frac{\mu^2}{m_\phi^2} \right) + \left(\frac{\alpha_s(\mu)}{\pi} \right)^2 (35.94 - 1.36 N_f) + \Delta_{\text{t-loop}}^\phi, \tag{7.2}$$

with the color factor $C_F = 4/3$. The last term $\Delta_{\text{t-loop}}^\phi$ indicates top-quark loop contributions, which calculated in the case with $m_t \gg m_\phi$ and $\mu = m_\phi$ as

$$\Delta_{\text{t-loop}}^H = \frac{\kappa_t^H}{\kappa_q^H} \left(\frac{\alpha_s(\mu)}{\pi} \right)^2 \left(1.57 - \frac{2}{3} \ln \frac{m_H^2}{m_t^2} + \frac{1}{9} \ln^2 \frac{\overline{m}_q^2(\mu)}{m_H^2} \right), \tag{7.3}$$

$$\Delta_{\text{t-loop}}^A = \frac{\kappa_t^A}{\kappa_q^A} \left(\frac{\alpha_s(\mu)}{\pi} \right)^2 \left(3.83 - \ln \frac{m_A^2}{m_t^2} + \frac{1}{6} \ln^2 \frac{\overline{m}_q^2(\mu)}{m_A^2} \right). \tag{7.4}$$

In the LO decay rate Γ_0, mass parameters arising from Yukawa couplings are replaced by the running masses $\overline{m}_q(\mu)$. Thereby, large logarithmic corrections induced by the light quark masses are resummed [133].

For the top pair, the QCD correction factor Δ_t^ϕ depends on the CP property of the Higgs boson. We obtain the decay rate at the NLO in the on-shell scheme as

$$\Gamma(\phi \to t\bar{t}) = \Gamma_0(\phi \to t\bar{t})(1 + \Delta_t^\phi), \tag{7.5}$$

where [134, 135]

$$\Delta_t^H = \frac{\alpha_s(\mu)}{\pi} C_F \left[\frac{L(\beta_t)}{\beta_t} - \frac{1}{16\beta_t^3}(3 + 34\beta_t^2 - 13\beta_t^4) \ln \rho_t + \frac{3}{8\beta_t^2}(7\beta_t^2 - 1) \right], \tag{7.6}$$

$$\Delta_t^A = \frac{\alpha_s(\mu)}{\pi} C_F \left[\frac{L(\beta_t)}{\beta_t} - \frac{1}{16\beta_t^3}(19 + 2\beta_t^2 + 3\beta_t^4) \ln \rho_t + \frac{3}{8}(7 - \beta_t^2) \right], \tag{7.7}$$

with $\beta_t = \lambda^{1/2}(m_t^2/m_\phi^2, m_t^2/m_\phi^2)$ and $\rho_t = (1 - \beta_t)/(1 + \beta_t)$, where the function λ is defined by

$$\lambda(x, y) = 1 + x^2 + y^2 - 2x - 2y - 2xy. \tag{7.8}$$

The function $L(\beta_t)$ is given by

$$\begin{aligned} L(\beta_t) = (1 + \beta_t^2) \left[4\text{Li}_2(\rho_t) + 2\text{Li}_2(-\rho_t) + 3 \ln \rho_t \ln \frac{2}{1 + \beta_t} + 2 \ln \rho_t \ln \beta_t \right] \\ - 3\beta_t \ln \frac{4}{1 - \beta_t^2} - 4\beta_t \ln \beta_t, \end{aligned} \tag{7.9}$$

where Li_2 is the dilog function. In the chiral limit $\beta_t \to 1$, we obtain

$$\Delta_t^\phi = \frac{\alpha_s(\mu)}{\pi} C_F \left(\frac{9}{4} + \frac{3}{2} \ln \frac{m_t^2}{m_\phi^2} \right). \tag{7.10}$$

Contributions of the top quark mass in the NLO QCD corrections are significant near the threshold region. On the other hand, dominant contributions in $m_\phi \gg m_t$ can be the logarithmic contribution, $\ln(m_t^2/m_\phi^2)$, which appears in the QCD corrections in the $\overline{\text{MS}}$ scheme. In order to take into account both of the effects, we use interpolation for the corrections to $\phi \to t\bar{t}$ as discussed in Ref. [68].

For the decays into an off-shell gauge boson $\phi \to VV^*$ and $\phi \to \phi V^*$ ($V = W, Z$), the QCD correction can enter in the $V^* \to q\bar{q}$ part. This effect can be included by [136]

$$\Gamma(\phi \to VV^* \to Vq\bar{q}) = \Gamma_0(\phi \to VV^* \to Vq\bar{q})(1 + \Delta_{\rm QCD}), \tag{7.11}$$

$$\Gamma(\phi \to \phi' V^* \to \phi' q\bar{q}) = \Gamma_0(\phi \to \phi' V^* \to \phi' q\bar{q})(1 + \Delta_{\rm QCD}), \tag{7.12}$$

where

$$\Delta_{\rm QCD} = C_F \frac{3\alpha_s(\mu)}{4\pi}. \tag{7.13}$$

The fermion loop contribution to the decay rate of $\phi \to \gamma\gamma$ receives QCD corrections. At the NLO, the QCD correction can be implemented by the following replacement of the quark loop function $I_F^\phi(\tau_q)$ in the $\overline{\rm MS}$ scheme [137, 138]

$$I_F^\phi(\tau_q) \to I_F^\phi(\tau_q) \left[1 + \frac{\alpha_s(\mu)}{\pi} C_\phi\right], \tag{7.14}$$

where $I_F^\phi(\tau_q)$ is defined in Appendix B, and the factor C_ϕ is determined by the scale μ and the mass ratio $\tau_q \equiv m_\phi^2/(4m_q^2)$. In our computation, we adopt the analytic expression of C_ϕ given in Ref. [139], in which C_ϕ is written in terms of the polylog functions, up to the Li_4 function. It has been known that the factor C_ϕ becomes the simple form in the large top mass limit, $\tau_t \to 0$, as [137, 138, 140]

$$C_H = -1, \quad C_A = 0. \tag{7.15}$$

On the other hand, in the large Higgs mass limit or equivalently the massless fermion limit, the factor C_ϕ is common to the case for the CP-even and CP-odd Higgs boson [138]:

$$\mathrm{Re} I_F^\phi C_\phi = -\frac{1}{18}\left[\ln^2(4\tau_q) - \pi^2 - \frac{2}{3}\ln(4\tau_q) + 2\ln\frac{\mu^2}{m_q^2}\right], \ \mathrm{Im} I_F^\phi C_\phi = \frac{\pi}{3}\left[\frac{1}{3}\ln(4\tau_q) + 2\right]. \tag{7.16}$$

For $H/A \to Z\gamma$ decays, we calculate them at the LO.

For the $\phi \to gg$ decays, we take into account the decay rate corrected up to NNLO expressed as,

$$\Gamma(\phi \to gg) = \Gamma_0(\phi \to gg)\left[1 + \frac{\alpha_s(\mu)}{\pi} E_\phi^{(1)} + \left(\frac{\alpha_s(\mu)}{\pi}\right)^2 E_\phi^{(2)}\right]. \tag{7.17}$$

For the NLO QCD corrections to the $\phi \to gg$ decays, there are contributions from virtual gluon loops and those from real emissions of a gluon ($\phi \to ggg$) and a gluon splitting into quark pair ($\phi \to gq\bar{q}$). $E_\phi^{(1)}$ in Eq. (7.17) can be decomposed as [138],

$$E_\phi^{(1)} = E_\phi^{\rm virt}(m_t \to \infty) + E_\phi^{\rm real}(m_t \to \infty) + \Delta E_\phi. \tag{7.18}$$

The first and second terms respectively denote the contribution from virtual gluon loops and that from real gluon emissions in the large top-quark mass limit. These are expressed by

$$E_H^{\rm virt}(m_t \to \infty) = \frac{11}{2} + \frac{33 - 2N_f}{6}\ln\frac{\mu^2}{m_H^2}, \tag{7.19}$$

$$E_A^{\rm virt}(m_t \to \infty) = 6 + \frac{33 - 2N_f}{6}\ln\frac{\mu^2}{m_A^2}, \tag{7.20}$$

$$E_H^{\rm real}(m_t \to \infty) = E_A^{\rm real}(m_t \to \infty) = \frac{73}{4} - \frac{7}{6}N_f. \tag{7.21}$$

The last term ΔE_ϕ vanishes in the large top-quark mass limit, which can be decomposed into the following three parts:

$$\Delta E_\phi = \Delta E_\phi^{\rm virt} + \Delta E_\phi^{ggg} + N_f \Delta E_\phi^{gq\bar{q}}. \tag{7.22}$$

Similar to the $\phi \to \gamma\gamma$ decays, we adopt the analytic expression for the virtual correction $\Delta E_\phi^{\rm virt}$ given in Ref. [139]. Those for the real emissions ΔE_ϕ^{ggg} and $\Delta E_\phi^{gq\bar{q}}$ are given in Ref. [138], which are expressed in the form with a double integral with respect to phase space variables. According to Ref. [138], the factor ΔE_ϕ is dominantly determined by the contribution from the virtual gluon loop $\Delta E_\phi^{\rm virt}$, so that in our computation we neglect the contributions from ΔE_ϕ^{ggg} and $\Delta E_\phi^{gq\bar{q}}$. From Eq. (7.21), E_ϕ is given to be about 18 at $\mu = m_\phi$ and $N_f = 5$, and it gives sizable correction to the decay rate; e.g., $\sim 70\%$ for $m_\phi = 100$ GeV. For NNLO contributions; i.e., $E_\phi^{(2)}$, we incorporate those in the limit with $m_t \gg m_\phi$ and setting as $\mu = m_\phi$, which are expressed as [141, 142]

$$\begin{aligned} E_H^{(2)} &= \frac{149533}{288} - \frac{363}{8}\zeta(2) - \frac{495}{8}\zeta(3) - \frac{19}{8}\ln\frac{m_t^2}{m_H^2} \\ &\quad + N_f\left(-\frac{4157}{72} + \frac{11}{2}\zeta(2) + \frac{5}{4}\zeta(3) - \frac{2}{3}\ln\frac{m_t^2}{m_H^2}\right) + N_f^2\left(\frac{127}{108} - \frac{1}{6}\zeta(2)\right), \end{aligned} \tag{7.23}$$

$$\begin{aligned} E_A^{(2)} &= \frac{51959}{96} - \frac{363}{8}\zeta(2) - \frac{495}{8}\zeta(3) + N_f\left(-\frac{473}{8} + \frac{11}{2}\zeta(2) + \frac{5}{4}\zeta(3) - \ln\frac{m_t^2}{m_A^2}\right) \\ &\quad + N_f^2\left(\frac{251}{216} - \frac{\zeta(2)}{6}\right). \end{aligned} \tag{7.24}$$

7.1.2 QCD corrections to the charged Higgs decays

The QCD corrections to charged Higgs decays into light quarks are presented in the $\overline{\rm MS}$ scheme. The expression can be written in the same way with the neutral Higgs boson decays as

$$\Gamma(H^\pm \to qq') = \Gamma_0(H^\pm \to qq')(1 + \Delta_q^{H^\pm}), \tag{7.25}$$

where the $\Delta_q^{H^\pm}$ is given by Eq. (7.2) but without the last term $\Delta^\phi_{\text{t-loop}}$. For the the decays into quarks including the top quark, we apply the QCD correction in the on-shell scheme. It is given in [135, 143]

$$\begin{aligned} \Gamma(H^\pm \to qq') = \frac{3G_F m_{H^\pm}}{4\sqrt{2}\pi}|V_{qq'}|^2\lambda_{qq'}^{1/2}\Bigg[(1-\mu_q-\mu_{q'})\left\{ m_q^2\zeta_q^2\left(1 + C_F\frac{\alpha_s(\mu)}{\pi}\Delta_{qq'}^+\right)\right. \\ \left. + m_{q'}^2\zeta_{q'}^2\left(1 + C_F\frac{\alpha_s(\mu)}{\pi}\Delta_{qq'}^-\right)\right\} - 4\sqrt{\mu_q\mu_{q'}}m_q m_{q'}\zeta_q\zeta_{q'}\Bigg], \end{aligned} \tag{7.26}$$

where $\mu_q = m_q^2/m_{H^\pm}^2$, $\lambda_{qq'} = (1-\mu_q-\mu_{q'})^2 - 2\mu_q\mu_{q'}$. The QCD corrections $\Delta_{qq'}^+$ and $\Delta_{qq'}^-$ are expressed by

$$\Delta_{qq'}^+ = \frac{9}{4} + \frac{3 - 2\mu_q + 2\mu_{q'}}{4}\ln\frac{\mu_q}{\mu_{q'}} + \frac{(\frac{3}{2} - \mu_q - \mu_{q'})\lambda_{qq'} + 5\mu_q\mu_{q'}}{2\lambda_{qq'}^{1/2}(1-\mu_q-\mu_{q'})}\ln x_q x_{q'} + B_{qq'}, \tag{7.27}$$

$$\Delta_{qq'}^- = 3 + \frac{\mu_{q'} - \mu_q}{2}\ln\frac{\mu_q}{\mu_{q'}} + \frac{\lambda_{qq'} + 2(1-\mu_q-\mu_{q'})}{2\lambda_{qq'}^{1/2}}\ln x_q x_{q'} + B_{qq'}, \tag{7.28}$$

where $x_q = 2\mu_q/(1-\mu_q-\mu_{q'}+\lambda_{qq'}^{1/2})$. A function $B_{qq'}$ is given in Ref. [135]. In these expressions, quark pole masses are used. Similar to $\phi \to t\bar{t}$, we incorporate the corrections with interpolation to consider the effect of the top quark mass and the logarithmic corrections due to light down-type quark masses.

For the off-shell decays into a neutral Higgs boson and a W boson, $H^\pm \to \phi W^*$, the QCD correction can be applied as similar to $\phi \to \phi' V^*$. It can be written as

$$\Gamma(H^\pm \to \phi W^{\pm *} \to \phi q q') = \Gamma_0(H^\pm \to \phi W^{\pm *} \to \phi q q')(1 + \Delta_{\rm QCD}), \tag{7.29}$$

where the QCD correction factor is given in Eq. (7.13). For loop induced decay processes of the charged Higgs bosons, $H^\pm \to W^\pm V$ ($V = Z, \gamma$), which have been studied in Refs. [144–147], we calculate them at the LO.

7.1.3 Total decay widths and decay branching ratios

We here discuss total widths and branching ratios for the neutral Higgs bosons and the charged Higgs bosons in four types of the 2HDMs in order for later discussion about direct searches of heavy Higgs bosons. We describe the behavior of the total widths and the branching ratios in cases with the alignment limit, $s_{\beta-\alpha} = 1$ and without taking the alignment limit, $s_{\beta-\alpha} = 0.995$. In the QCD correction functions C_ϕ and $E_\phi^{\rm virt}$, polylog functions appear. We use `CHAPLIN` [148] for the numerical evaluation of such polylog functions. We have confirmed that our numerical results for the total widths and the branching ratios are consistent with `2HDMC` [149].

We here show the case that masses of the additional Higgs bosons as well as M are degenerate; i.e., $m_\Phi \equiv m_H = m_A = m_{H^\pm}$ and $M = m_\Phi$. While the m_Φ is set to be $m_\Phi = 200$ GeV or 800 GeV, $\tan\beta$ is scanned in the following range, $0.5 < \tan\beta < 50$. We note that, without depending on $\tan\beta$, results with $m_\Phi = 200$ GeV for Type-II and Type-X are already excluded by the constraint from the flavor physics (also, for Type-I and Type-Y in lower $\tan\beta$ regions, $\tan\beta \lesssim 2$) [126,150]. Nevertheless, we show them in order to compare results among four types of the 2HDM. For the SM parameters, we use the following values of the $\overline{\rm MS}$ quark masses at a scale of each pole mass;

$$\overline{m}_b(m_b) = 4.18 \text{ GeV} \ \ [151], \quad \overline{m}_c(m_c) = 1.28 \text{ GeV} \ \ [151], \quad \overline{m}_t(m_t) = 162.3 \text{ GeV} \ \ [152]. \tag{7.30}$$

For the mass of the strange quark we use the running mass at $\mu = 2$ GeV [153], $\overline{m}_s(2 \text{ GeV}) = 0.097$ GeV. In the derivation, the running strong coupling is evaluated with the following values of $\Lambda_{\rm QCD}^{N_f}$ [151],

$$\Lambda_{\rm QCD}^6 = 89 \text{ MeV}, \quad \Lambda_{\rm QCD}^5 = 210 \text{ MeV}, \quad \Lambda_{\rm QCD}^4 = 292 \text{ MeV}, \quad \Lambda_{\rm QCD}^3 = 332 \text{ MeV}, \tag{7.31}$$

for N_f= 6, 5, 4, and 3, respectively. The input value of the CKM matrix elements and the total width for the weak gauge bosons as well as the top quark are taken as [151],

$$V_{tb} = 0.999172, \qquad V_{ts} = 0.3978, \qquad V_{cb} = 0.04053, \tag{7.32}$$

$$\Gamma_W = 2.085 \text{ GeV}, \qquad \Gamma_Z = 2.4952 \text{ GeV}, \qquad \Gamma_t = 1.42 \text{ GeV}. \tag{7.33}$$

The former is relevant for the charged Higgs decays into quarks, $H^\pm \to tb$, $H^\pm \to ts$ and $H^\pm \to cb$. The latter is used in the computation of the Higgs boson decays into off-shell particles.

Before we show numerical behaviors of the total widths and the branching ratios, we mention the loop-induced decays of the charged Higgs bosons. The branching ratio of $H^\pm \to W^\pm Z$

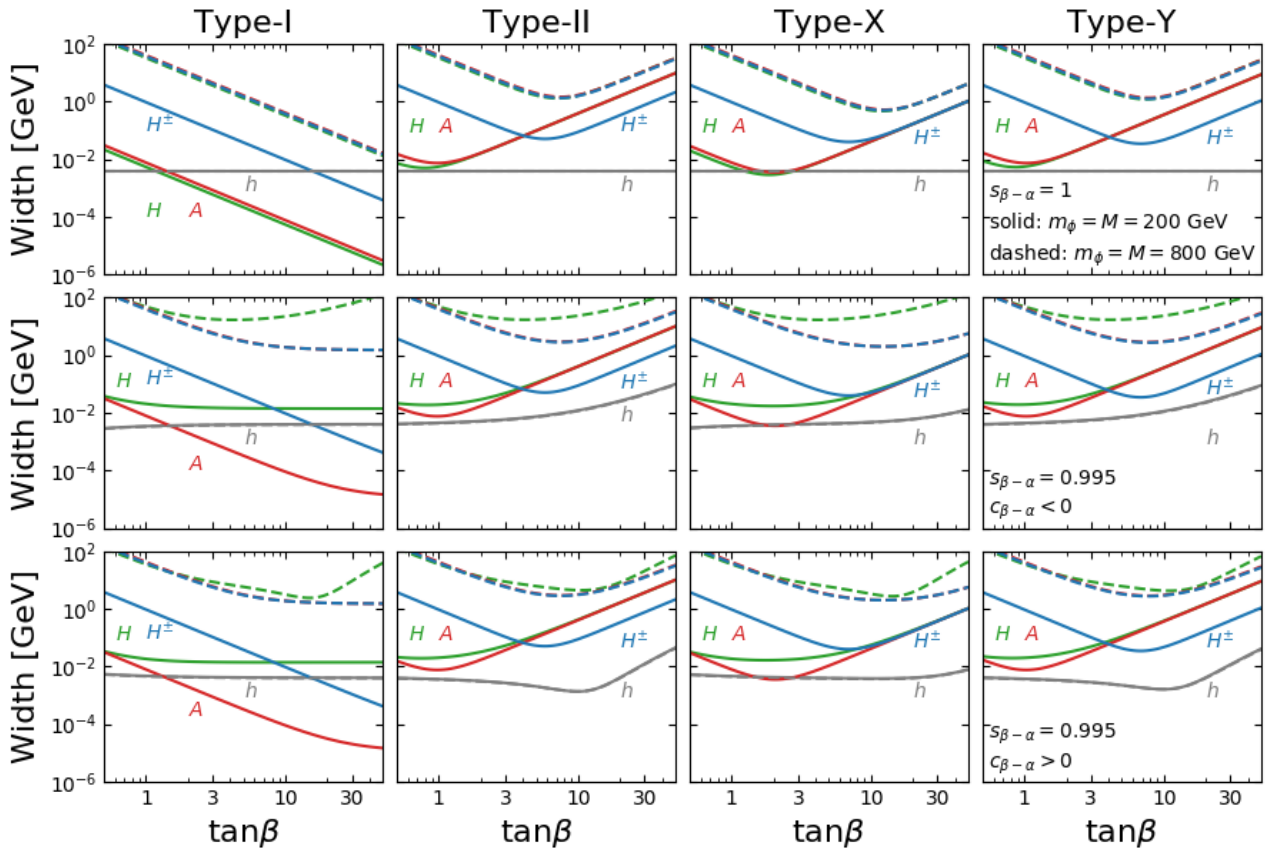

Figure 7.1: Total widths of h, H, A and $H^\pm$ as a function of $\tan\beta$ in Type-I, Type-II, Type-X and Type-Y of the 2HDM from the left panels to the right panels. Solid lines and dashed lines show results of $m_\Phi = M = 200$ GeV and $m_\Phi = M = 800$ GeV, respectively. In the top panels, $s_{\beta-\alpha}$ is set to be 1. In the middle and bottom panels, $s_{\beta-\alpha}$ is set to be 0.995 with $c_{\beta-\alpha} < 0$ and $c_{\beta-\alpha} > 0$, respectively.

can be enhanced when the mass difference between $H^\pm$ and A is taken to some extent [145]. Whereas, in the following numerical results, where the additional Higgs bosons are degenerate, the branching ratio of $H^\pm \to W^\pm Z$ is at most $\mathcal{O}(10^{-4})$ in the present parameter choices. Furthermore, the branching ratio of $H^\pm \to W^\pm\gamma$ is smaller than that of $H^\pm \to W^\pm Z$.

The following numerical results for the total widths and the branching ratios are similar to those given in Ref. [110], where the systematic studies have been done. Nevertheless, we here show them because there are some developments from the previous study. Main difference from Ref. [110] is that we compute the decay processes including higher-order QCD corrections. Also, we incorporate the above mentioned decay processes for the charged Higgs bosons, $H^\pm \to W^\pm Z$ and $H^\pm \to W^\pm\gamma$, in the evaluation of the total width.

In Fig. 7.1, we show the total decay widths for the neutral Higgs bosons and the charged Higgs bosons as a function of $\tan\beta$ in the cases of $m_\Phi = M = 200$ GeV and $m_\Phi = M = 800$ GeV. Different values of $s_{\beta-\alpha}$ are taken in each panel, namely $s_{\beta-\alpha} = 1$ in the top panels, $s_{\beta-\alpha} = 0.995$ with $c_{\beta-\alpha} < 0$ in the middle panels, and $s_{\beta-\alpha} = 0.995$ with $c_{\beta-\alpha} > 0$ in the bottom panels. For the h decays, in the alignment limit $s_{\beta-\alpha} = 1$, the couplings with fermions and weak gauge bosons coincide with those in the SM at tree level, so that the total decay width does not depend on $\tan\beta$. On the contrary, when $\tan\beta$ increases at $s_{\beta-\alpha} = 0.995$ with $c_{\beta-\alpha} < 0$, the total width also increases due to the effect of $\tan\beta$ enhancement on $h \to b\bar{b}$ ($h \to \tau\bar{\tau}$) in Type-II and Type-Y (Type-X). For the heavy Higgs bosons H, A and $H^\pm$, the total widths vary in the

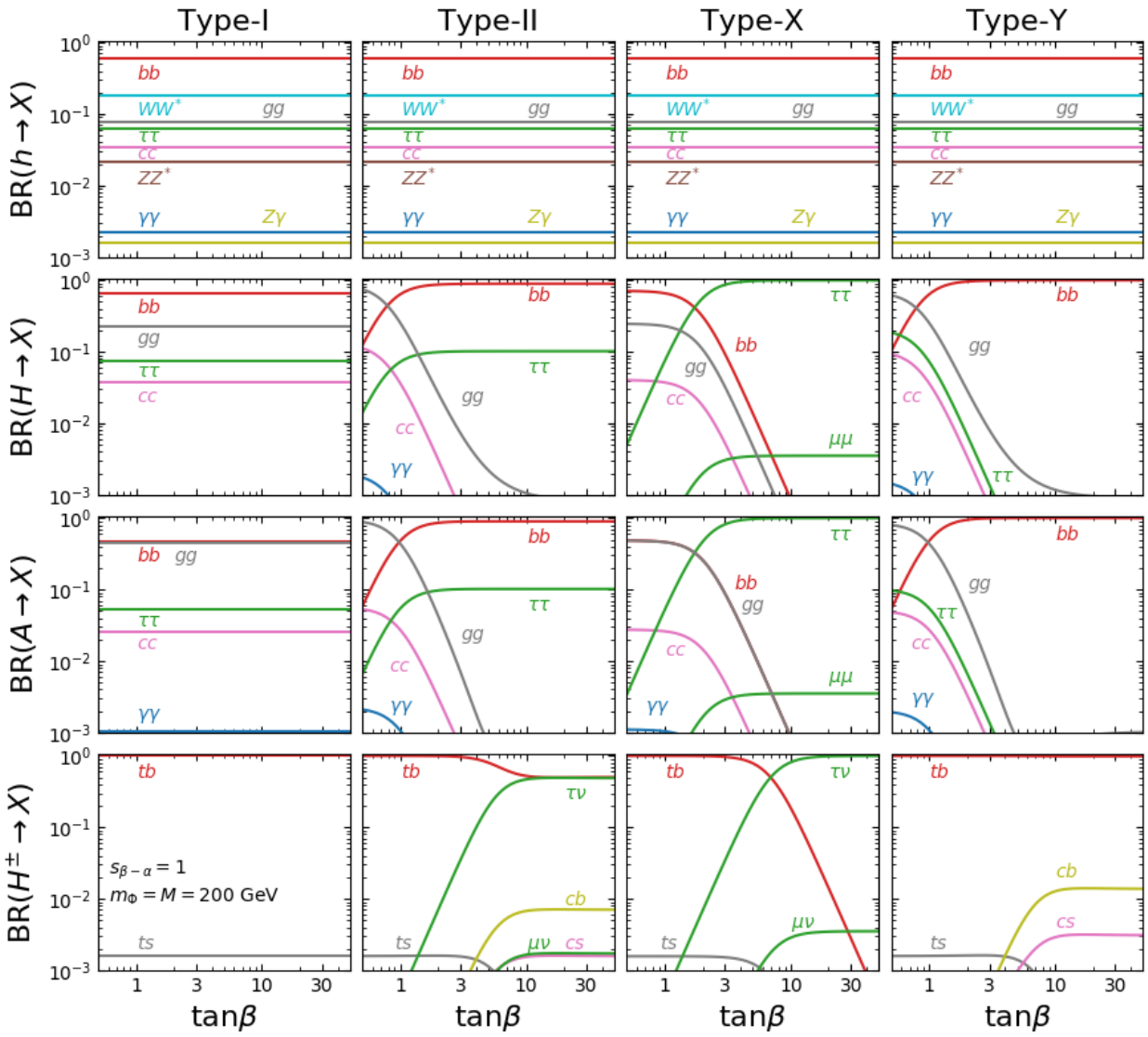

Figure 7.2: Decay branching ratios for h, H, A and $H^\pm$ as a function of $\tan\beta$ in the case of $m_\Phi = M = 200$ GeV and $s_{\beta-\alpha} = 1$. Results for Type-I, Type-II, Type-X and Type-Y of the 2HDM are shown from the left panels to the right panels.

both cases of $s_{\beta-\alpha} = 1$ and $s_{\beta-\alpha} \neq 1$. While those in Type-I monotonically decrease except for H with a mass of 800 GeV, there appears the dip at a certain value of $\tan\beta$ for each additional Higgs boson in Type-II, X and Y.

In Fig. 7.2, we show $\tan\beta$ dependence of the decay branching ratios for the neutral Higgs bosons and the charged Higgs bosons in the alignment limit, $s_{\beta-\alpha} = 1$, with $m_\Phi = M = 200$ GeV. For the SM-like Higgs boson decays, there is no $\tan\beta$ dependence of all the decay modes, since all the scaling factors κ_X^h are unity when $s_{\beta-\alpha} = 1$. We note that, in addition, the squared scaling factors of the fermion couplings for H and A are common and simply expressed by ζ_f parameters; i.e., $|\kappa_f^H|^2 = |\kappa_f^A|^2 = \zeta_f^2$ at $s_{\beta-\alpha} = 1$. In the case with $m_\Phi = M = 200$ GeV, the decay mode into a pair of the top quarks does not open for the $H(A)$ decays. Hence, for $\tan\beta > 1$, the main decay mode of H is $H \to b\bar{b}$ except for Type-X, as similar to the SM-like Higgs boson decays. For Type-X, the main decay mode is $H \to \tau\bar{\tau}$ due to the $\tan\beta$ enhancement for the leptonic decays, which also causes $H \to \mu\bar{\mu}$ with about 0.3% for $\tan\beta \gtrsim 4$.

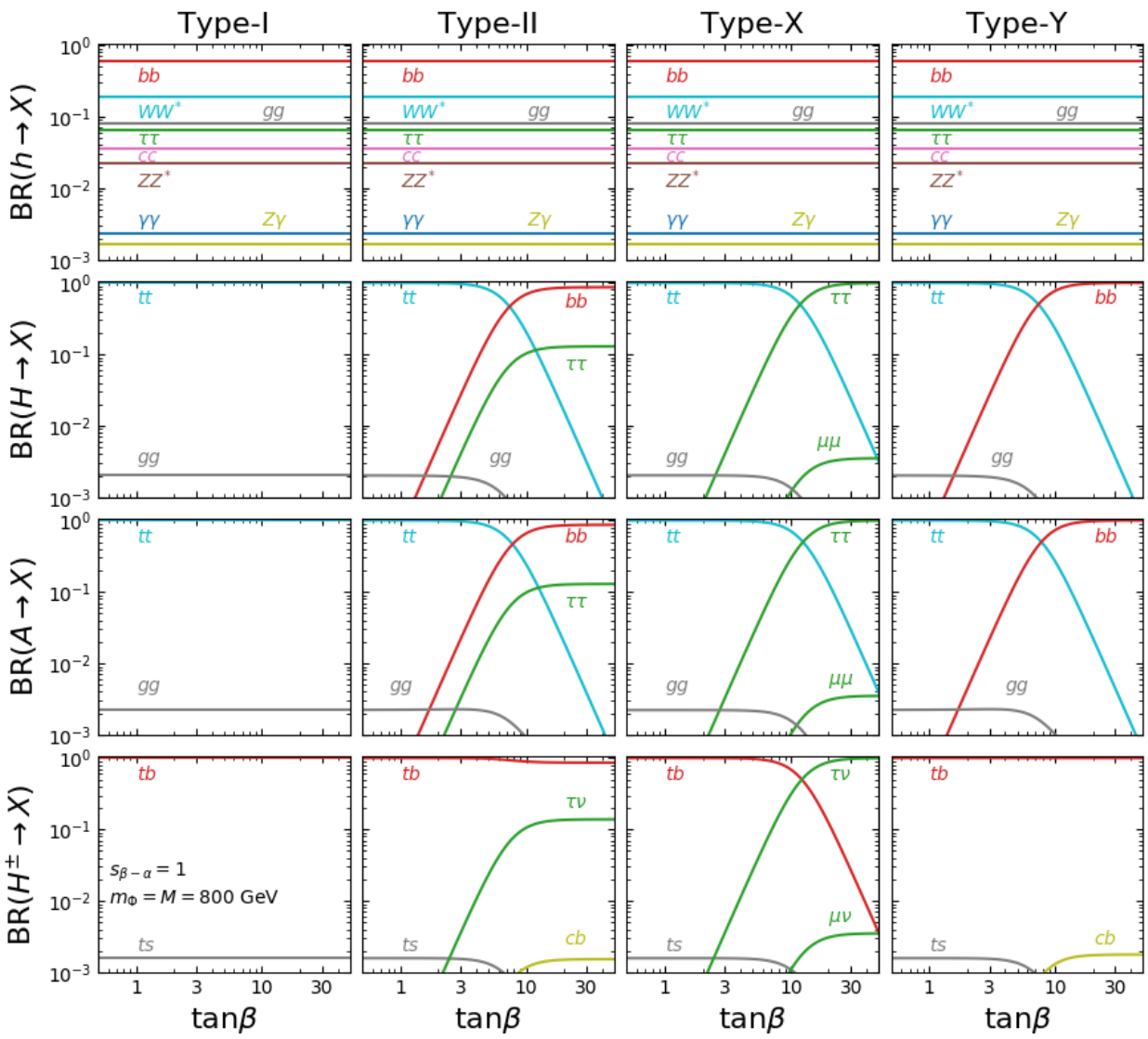

Figure 7.3: Decay branching ratios for h, H, A and $H^\pm$ as a function of $\tan\beta$ in the case of $m_\Phi = M = 800$ GeV and $s_{\beta-\alpha} = 1$. Results for Type-I, Type-II, Type-X and Type-Y of the 2HDM are shown from the left panels to the right panels.

For decays of A, one can see that the behavior of the branching ratios for decays into fermions is similar to those of H for all types of the 2HDM because of $|\kappa_f^H|^2 = |\kappa_f^A|^2$. The difference from H decays appears in the decay into gg. Namely, $\mathrm{BR}(A \to gg)$ is relatively larger than $\mathrm{BR}(H \to gg)$. This mainly comes from the fact that the NLO QCD correction is more significant than $H \to gg$, although the expressions at the LO are also different between H and A.

Apart from the neutral Higgs bosons, decays including a top quark exist for the charged Higgs bosons. While the decay into tb is the main decay mode for Type-I and Type-Y, the decay into $\tau\nu$ can be dominant in high $\tan\beta$ regions for Type-X. For Type-II both of the bottom Yukawa and the tau Yukawa coupling are enhanced by $\tan\beta$. As a consequence, the branching ratio $\mathrm{BR}(H^\pm \to \tau\nu)$ approaches to $\mathrm{BR}(H^\pm \to tb)$ in high $\tan\beta$ regions, in which effect of the top Yukawa coupling is negligible.

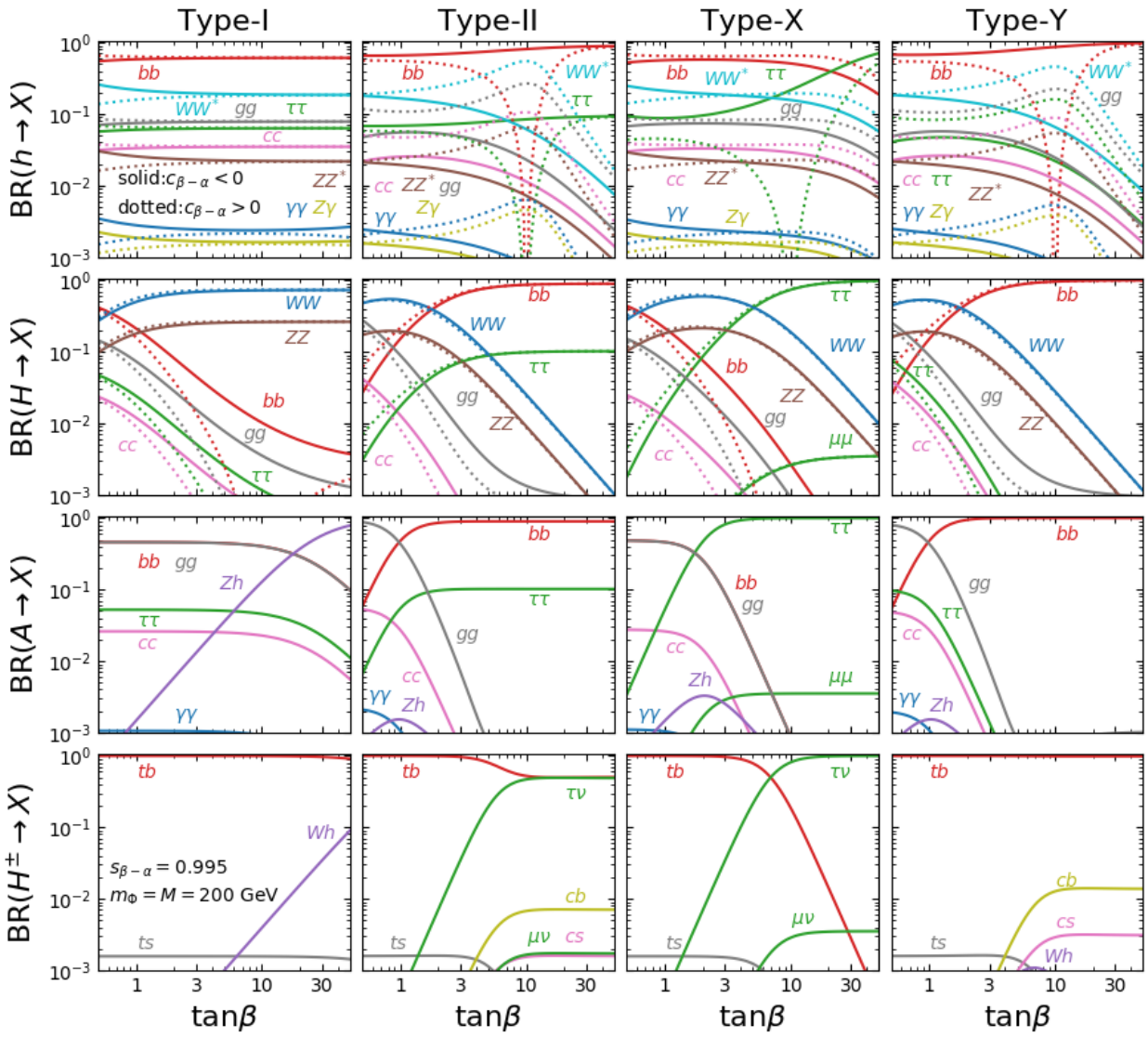

Figure 7.4: Decay branching ratios for h, H, A and $H^{\pm}$ as a function of $\tan\beta$ in the case of $m_\Phi = M = 200$ GeV and $s_{\beta-\alpha} = 0.995$. Solid lines show results of $c_{\beta-\alpha} < 0$ and dotted lines are those of $c_{\beta-\alpha} > 0$. Results for Type-I, Type-II, Type-X and Type-Y of the 2HDM are shown from the left panels to the right panels.

In Fig. 7.3, the branching ratios in the case of $s_{\beta-\alpha} = 1$ and $m_\Phi = M = 800$ GeV are shown as a function of $\tan\beta$. For h decays, the behavior does not change much from the case with $m_\Phi = M = 200$ GeV since the decay rates do not depend on the mass of the additional Higgs bosons at tree level. Main difference from Fig. 8.4 is appearance of the decays into $t\bar{t}$ in H and A. It dominates the branching ratios of H and A for Type-I with any value of $\tan\beta$. On the other hands, for Type-II, Type-X and Type-Y, $H \to t\bar{t}$ and $A \to t\bar{t}$ can be dominant only for $\tan\beta \lesssim 10$ since the decay rate is proportional to $\cot^2\beta$.

Next, we move on cases without taking the alignment limit, $s_{\beta-\alpha} \neq 1$. In these cases, the branching ratios of fermionic decay modes of H and h vary with a sign of $c_{\beta-\alpha}$. Furthermore, for decays of heavy Higgs bosons, additional decay modes, such as $H \to VV$ $(V = W, Z)$ $H \to hh$, $A \to Zh$ and $H^{\pm} \to W^{\pm}h$, shall appear. Therefore, their decay patterns can drastically change from the case of the alignment limit.

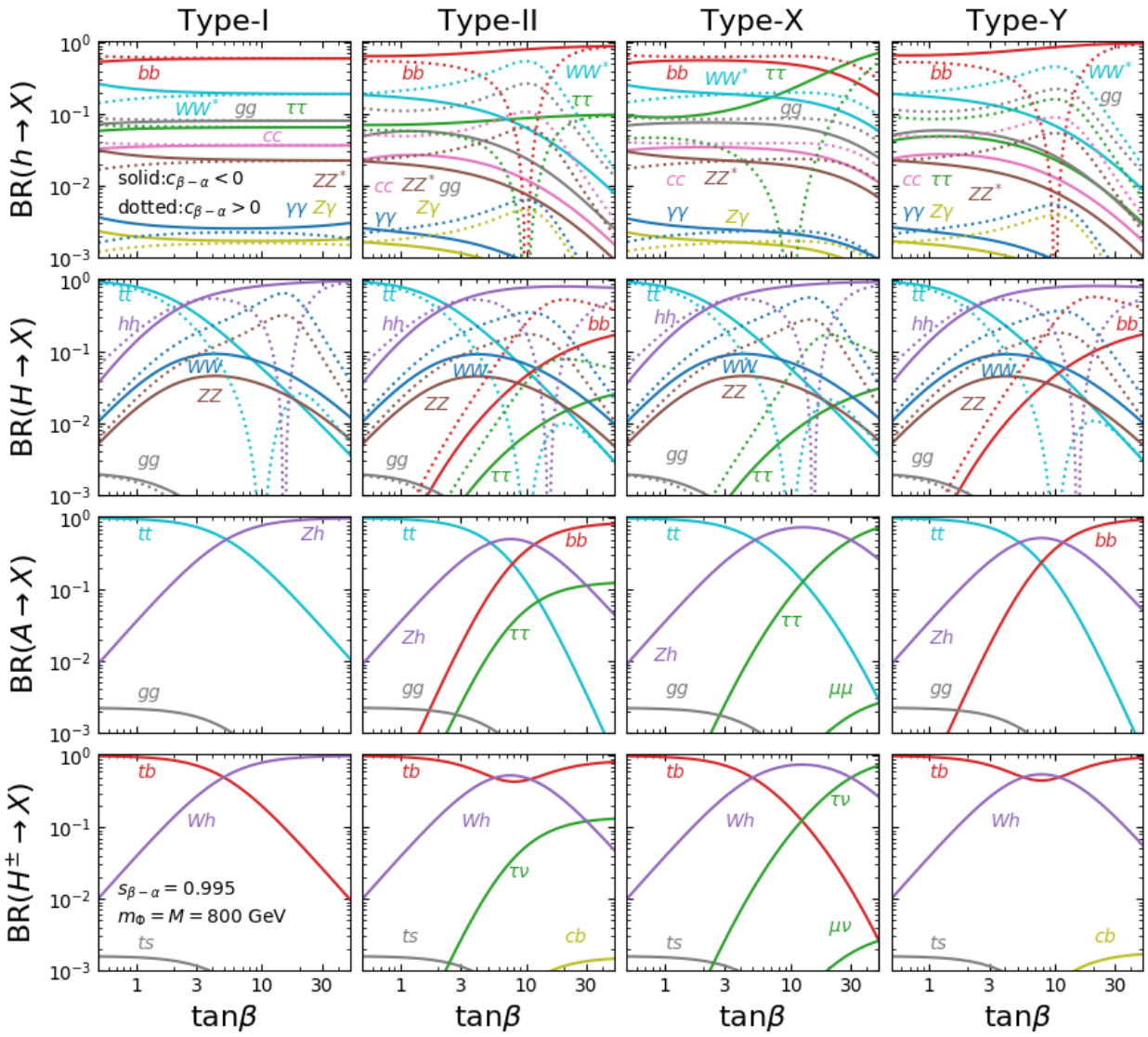

Figure 7.5: Decay branching ratios for h, H, A and $H^{\pm}$ as a function of $\tan\beta$ in the case of $m_\Phi = M = 800$ GeV and $s_{\beta-\alpha} = 0.995$. Solid lines show results of $c_{\beta-\alpha} < 0$ and dotted lines are those of $c_{\beta-\alpha} > 0$. Results for Type-I, Type-II, Type-X and Type-Y of the 2HDM are shown from the left panels to the right panels.

In Fig. 7.4, we show $\tan\beta$ dependence of the branching ratios for h, H, A and $H^{\pm}$ in the case with $s_{\beta-\alpha} = 0.995$ and $m_\Phi = M = 200$ GeV. For decays of h and H, predictions in the cases with $c_{\beta-\alpha} < 0$ and $c_{\beta-\alpha} > 0$ are separately plotted by solid lines and dotted lines, respectively. Regarding the decay of h one can see clear $\tan\beta$ dependence for all the decay modes. In particular, the branching ratio for $h \to b\bar{b}$ remarkably increases by $\tan\beta$. For the CP-even Higgs boson H, decays into the on-shell weak gauge bosons $H \to ZZ$ and $H \to W^+W^-$, which are proportional to m_H^3 as seen in Eq. (B.4) of Appendix B, can dominate. Whereas, the decay into $b\bar{b}$ ($\tau\bar{\tau}$) overcomes them for large $\tan\beta$ in Type-II and Type-Y (Type-X). Similarly, decays into a scalar boson and an off-shell vector boson $A \to hZ^*$ and $H^{\pm} \to hW^{\pm *}$ can be sizable in Type-I for large $\tan\beta$.

In Fig. 7.5, the branching ratios in the case with $s_{\beta-\alpha} = 0.995$ and $m_\Phi = M = 800$ GeV are also shown. While $H \to t\bar{t}$ and $A \to t\bar{t}$ can be the main decay mode as similar to Fig. 7.3, for decays of H, $H \to hh$ can be dominant due to the large scalar coupling λ_{Hhh}. Apart from

Constrained quantity	Applicable mass region	Reference
$\sigma(\phi) \times \mathrm{BR}(\phi \to \tau\tau)$	$200 < m_\Phi < 2000$ GeV	Fig. 7(a) in [172]
$\sigma(\phi(bb)) \times \mathrm{BR}(\phi \to \tau\tau)$	$200 < m_\Phi < 2000$ GeV	Fig. 7(b) in [172]
$\sigma(\phi(bb)) \times \mathrm{BR}(\phi \to bb)$	$450 < m_\Phi < 1400$ GeV	Fig. 8 in [173]
$\sigma(\phi) \times \mathrm{BR}(\phi \to tt)$	$400 < m_\Phi < 5000$ GeV	Fig. 14 in [174]
$\sigma(H) \times \mathrm{BR}(H \to hh) \times \mathrm{BR}(h \to bb)^2$	$260 < m_\Phi < 2000$ GeV	Fig. 9(a) in [175]
$\sigma(H) \times \mathrm{BR}(H \to WW)$	$200 < m_\Phi < 2000$ GeV	Fig. 5 in [176]
$\sigma(H) \times \mathrm{BR}(H \to ZZ)$	$200 < m_\Phi < 2000$ GeV	Fig. 6 in [177]
$\sigma(A) \times \mathrm{BR}(A \to Zh) \times \mathrm{BR}(h \to bb)$	$200 < m_\Phi < 2000$ GeV	Fig. 6(a) in [178]
$\sigma(A(bb)) \times \mathrm{BR}(A \to Zh) \times \mathrm{BR}(h \to bb)$	$200 < m_\Phi < 2000$ GeV	Fig. 6(b) in [178]
$\sigma(tH^\pm) \times \mathrm{BR}(H^\pm \to tb)$	$200 < m_\Phi < 2000$ GeV	Fig. 8 in [179]
$\sigma(tH^\pm) \times \mathrm{BR}(H^\pm \to \tau\nu)$	$200 < m_\Phi < 2000$ GeV	Fig. 8(a) in [180]

Table 7.1: List of constraints used in this study from direct searches for heavy Higgs bosons at the 13 TeV LHC.

this, one can see that the branching ratio for $H \to t\bar{t}$ and $H \to hh$ are close to 0 at $\tan\beta \sim 10$ and $\tan\beta \sim 16$, respectively, when $c_{\beta-\alpha} > 0$. This is because the scaling factor κ_t^H and the scalar coupling λ_{Hhh} vanish at those values of $\tan\beta$. We note that the value of λ_{Hhh} depends on the value of M. Therefore, the decay width for $H \to hh$ can change if we consider the non-degenerate case; i.e., $m_\Phi \neq M$.

The branching ratios including QCD corrections are discussed in the above paragraphs. On the other hands, there are a lots of studies on EW corrections to decays of the SM-like Higgs boson [97–100,112,121,154–160,160,161] and additional Higgs bosons [119,162–164]. NLO EW corrections to $h \to f\bar{f}$ can be evaluated by utilizing `H-COUP v2` [46]. Also, in the program, those to $h \to VV^* \to Vf\bar{f}$ are calculated. In `2HDECAY` [165], NLO corrections to on-shell two-body decays of h, H, A, and $H^\pm$ are evaluated. In addition, NLO EW corrections to $h/H \to V^{(*)}V^{(*)} \to 4f$ are calculated in `Prophecy4f` [70].

7.2 Direct searches at the LHC

In this section, we present current constraints on the parameter space in the 2HDMs from direct searches for heavy Higgs bosons with the LHC Run-II data.

Let us briefly summarize the procedure how we obtain the constraints on the parameters in the 2HDMs from model-independent analyses for heavy Higgs boson searches at the LHC. First, we compute production cross sections of heavy neutral Higgs bosons, $\phi = H$ and A, in the 2HDMs for the gluon-fusion process ($pp \to \phi$) and for the bottom-quark associated (or bottom-quark annihilate) process ($pp \to \phi(b\bar{b})$) at the NNLO in QCD by using `Sushi-1.7.0` [166,167]. For the charged Higgs boson production $pp \to tH^\pm$, we use the values given at the NLO QCD by the Higgs cross section working group (HXSWG) [66], based on Refs. [168–171]. Second, we calculate decay branching ratios of the Higgs bosons in the 2HDMs, including higher-order QCD corrections, as described in Sec. 7.1. Finally, we compute the production cross sections times the branching ratios for each parameter point for each search channel at the LHC listed in Table 7.1, and compared with the upper limits at 95% CL with 36 fb^{-1} data to obtain the constraints. Here, as in Sec. 7.1, we assume the common heavy Higgs boson masses $m_H = m_A = m_{H^\pm}$ ($\equiv m_\Phi$) and also $M = m_\Phi$. Because we are interested in the near

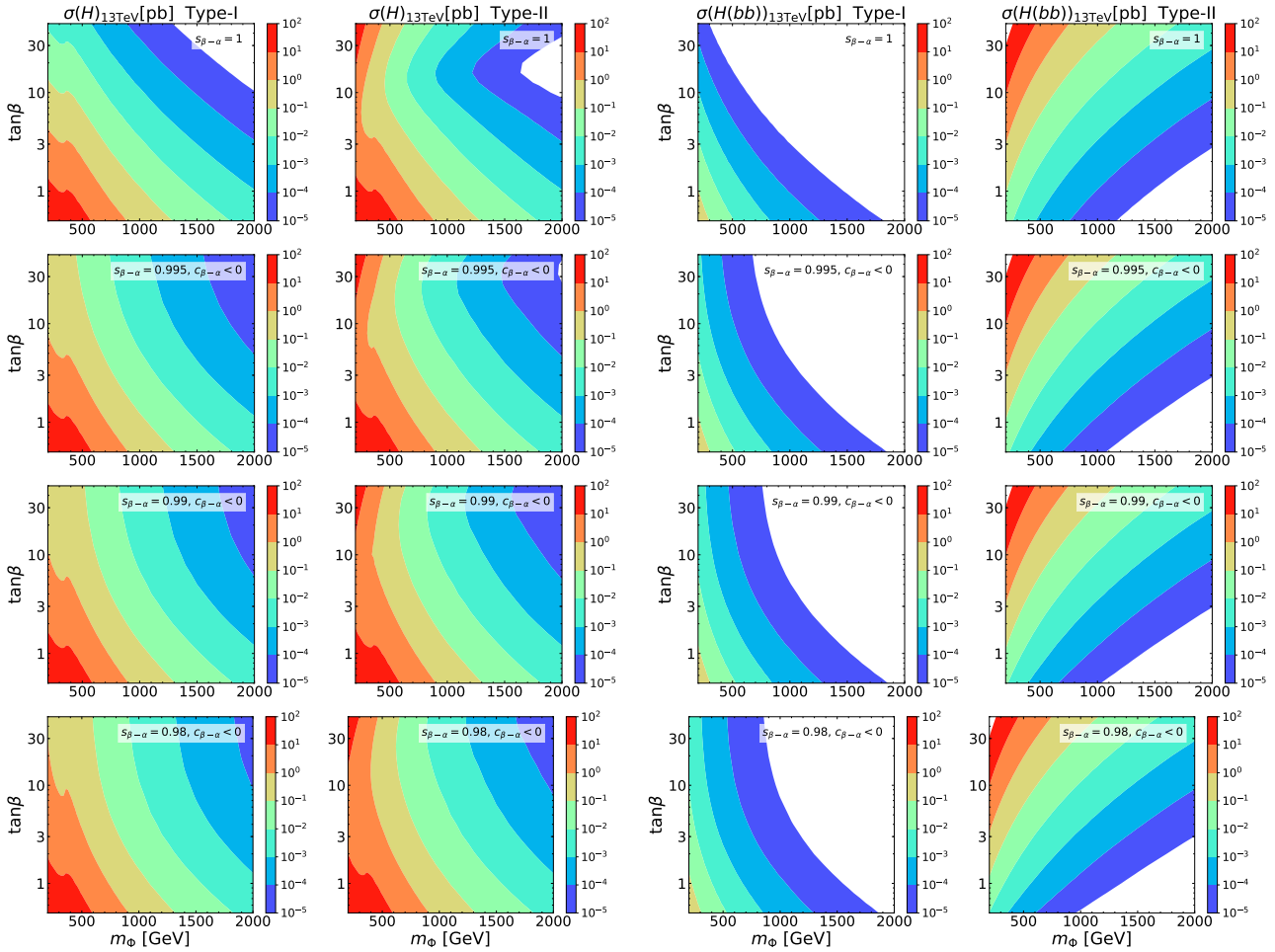

Figure 7.6: Production cross sections for the CP-even heavy Higgs boson H at the 13 TeV LHC on the m_Φ–$\tan\beta$ plane. Panels in two columns from the left (right) show the production via the gluon fusion (the bottom-quark associated) in the Type-I and Type-II 2HDMs, where the value of $s_{\beta-\alpha}$ is set to be 1, 0.995, 0.99 and 0.98 with $c_{\beta-\alpha} < 0$ from the top to the bottom panels. The cross sections are shown with different colors from blue to red, corresponding to from 10^{-5} pb to 10^{2} pb.

alignment scenario, we consider the value of $s_{\beta-\alpha}$ as 1, 0.995, 0.99 and 0.98 both for $c_{\beta-\alpha} < 0$ and $c_{\beta-\alpha} > 0$. We note that we use the expected upper limits, not the observed ones, from the LHC analyses in order for the HL-LHC projection. Although we use the ATLAS data, listed in Table 7.1, the similar limits have been reported by the CMS experiment [181–186]. We also note that, although new analyses with full Run-II data (139 fb^{-1}) are available for some channels; e.g., $\phi \to \tau\bar{\tau}$ [187], we use the upper limit with 36 fb^{-1} data for a fair comparison with the other channels. Similar phenomenological studies have been done earlier in; e.g., Refs. [188, 189].

7.2.1 Production cross sections for the additional Higgs bosons

Before we discuss current constraints on the parameter space from direct searches, we present production rates for the heavy Higgs bosons at the 13 TeV LHC. Figure 7.6 shows cross sections for the CP-even heavy Higgs boson H via the gluon fusion process (left two columns) and via the bottom-quark associated process (right two columns) on the m_Φ–$\tan\beta$ plane. We only show the cases in the Type-I and Type-II 2HDMs since the lepton sector is irrelevant for the

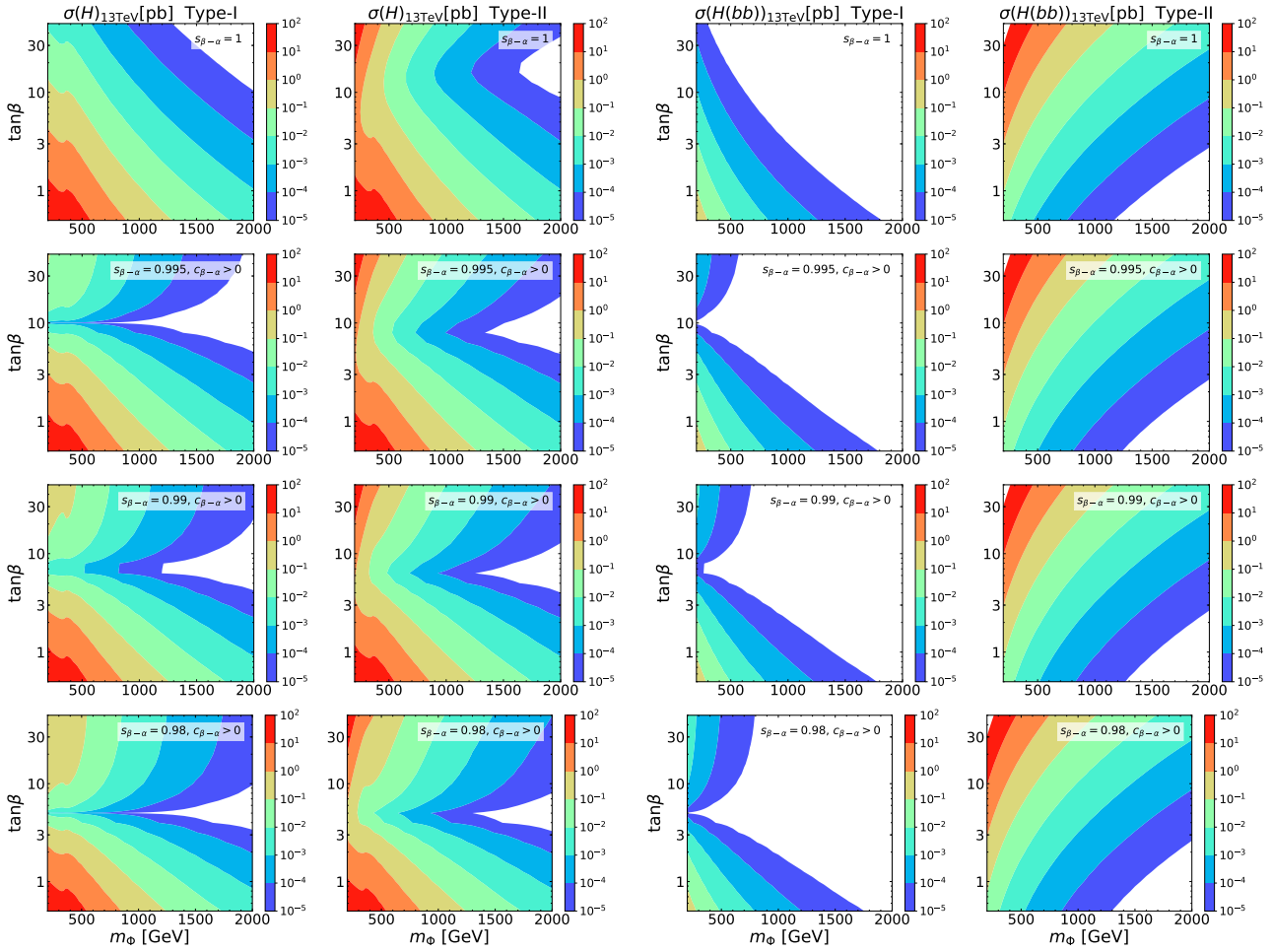

Figure 7.7: Production cross sections for the CP-even heavy Higgs boson H at the 13 TeV LHC on the m_Φ–$\tan\beta$ plane. Panels in two columns from the left (right) show the production via the gluon fusion (the bottom-quark associated) in the Type-I and Type-II 2HDMs, where the value of $s_{\beta-\alpha}$ is set to be 1, 0.995, 0.99 and 0.98 with $c_{\beta-\alpha} > 0$ from the top to the bottom panels. The cross sections are shown with different colors from blue to red, corresponding to from 10^{-5} pb to 10^{2} pb.

productions, namely, the productions in Type-X and Type-Y are the same as in Type-I and Type-II, respectively. The value of $s_{\beta-\alpha}$ is set to be 1, 0.995, 0.99, and 0.98 with $c_{\beta-\alpha} < 0$ from the top to the bottom panels.

For the gluon-fusion process, shown in the left two columns in Fig. 7.6, the Higgs bosons are produced via quark loops. Therefore, the difference of the Yukawa sector between Type-I and Type-II leads to significantly different dependence on the model parameters. In Type-I, where the top-quark loop is entirely dominant, the larger $\tan\beta$ is, the smaller the cross section is for a fixed mass. One can also see the threshold enhancement of the top-quark loop at $m_\Phi \sim 2m_t$. In Type-II, the top-quark loop is dominant for small $\tan\beta$, while the production via the bottom-quark loop becomes dominant for large $\tan\beta$ because of the bottom-Yukawa enhancement. The $s_{\beta-\alpha}$ dependence of the cross sections is very small for small $\tan\beta$. In the large $\tan\beta$ region, on the other hand, the cross sections for a fixed mass tend to be larger as $s_{\beta-\alpha}$ deviates from the alignment limit. The production via the bottom-quark associated process, shown in the right two columns in Fig. 7.6, is entirely subdominant in Type-I, while that becomes dominant for large $\tan\beta$ in Type-II.

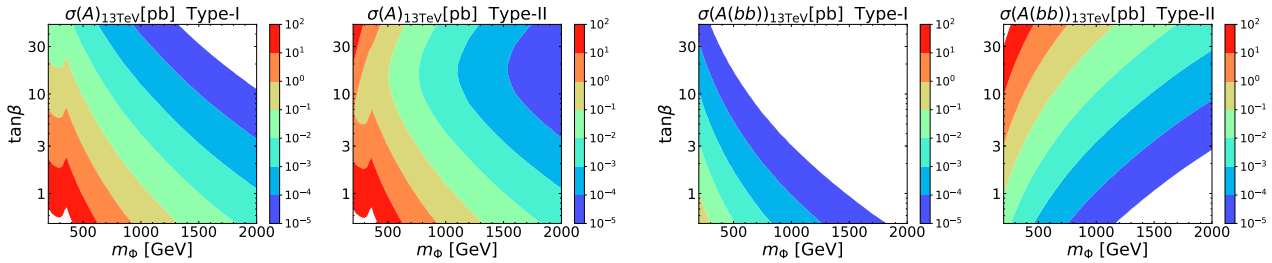

Figure 7.8: Production cross sections for the CP-odd Higgs boson A at the 13 TeV LHC on the m_Φ–$\tan\beta$ plane. Panels from the left to the right show the production via the gluon fusion in the Type-I and Type-II 2HDMs, and via the bottom-quark associated process in the Type-I and Type-II 2HDMs, respectively.

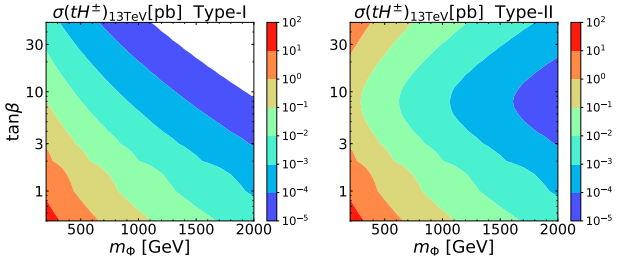

Figure 7.9: Production cross sections for the charged Higgs boson $H^\pm$ at the 13 TeV LHC on the m_Φ–$\tan\beta$ plane in the Type-I (left) and Type-II (right) 2HDMs.

In Fig. 7.7, similar to Fig. 7.6, but for $c_{\beta-\alpha} > 0$, we show the production rates. In this case, except for the b-associate process in Type-II, the cross sections show a peculiar $\tan\beta$ dependence since the top and the bottom Yukawa in Type-I and the top Yukawa in Type-II, vanishes for a certain $s_{\beta-\alpha}$ and $\tan\beta$; e.g., $\tan\beta \sim 10$ for the $s_{\beta-\alpha} = 0.995$ case.

Figure 7.8 presents production rates for the CP-odd Higgs boson A. The production processes are same as those for H, shown in Figs. 7.6 and 7.7, namely the gluon fusion process (left two columns) and the bottom-quark associated process (right two columns). Different from the CP-even Higgs bosons, the production rates only depend on $\tan\beta$ because of the Yukawa structure. The global parameter dependence of the cross sections via the gluon fusion is similar to that for H with $s_{\beta-\alpha} = 1$, but the production rate for A is slightly larger than that for H at each point on the m_Φ–$\tan\beta$ plane. The parameter dependence of the cross sections via the bottom-quark annihilation is as same as for H with $s_{\beta-\alpha} = 1$.

In Fig. 7.9, at the LHC charged Higgs bosons $H^\pm$ are mainly produced in association with a top quark via $gb \to tH^\pm$ for $m_{H^\pm} > m_t$, whose cross sections are shown. Similar to the productions for A, the cross section only depends on $\tan\beta$. For a fixed mass, in Type-I, the larger $\tan\beta$ is, the smaller the production rate is. In Type-II, on the other hand, up to $\tan\beta \sim 7$, the larger $\tan\beta$ is, the smaller the production rate is, similar to the Type-I case. However, for $\tan\beta \gtrsim 7$, the production rate becomes larger for larger $\tan\beta$ due to $\tan\beta$ enhancement of the bottom-Yukawa coupling.

We here mention other heavy Higgs boson productions. Although we assume $m_{H^\pm} = m_H$ in this study, if the $H/A \to H^\pm W^\mp$ decay is kinematically allowed, the production via $gg \to H \to H^\pm W^\mp$ can be comparable with that via $gb \to tH^\pm$ [190–193]. Heavy Higgs bosons are also produced in electroweak processes such as HA, $H^\pm h/H/A$, and H^+H^- [194, 195], as well as in loop induced processes such as $H^\pm W^\mp$ [196] and H^+H^- [197].

7.2.2 Constraints from the direct searches

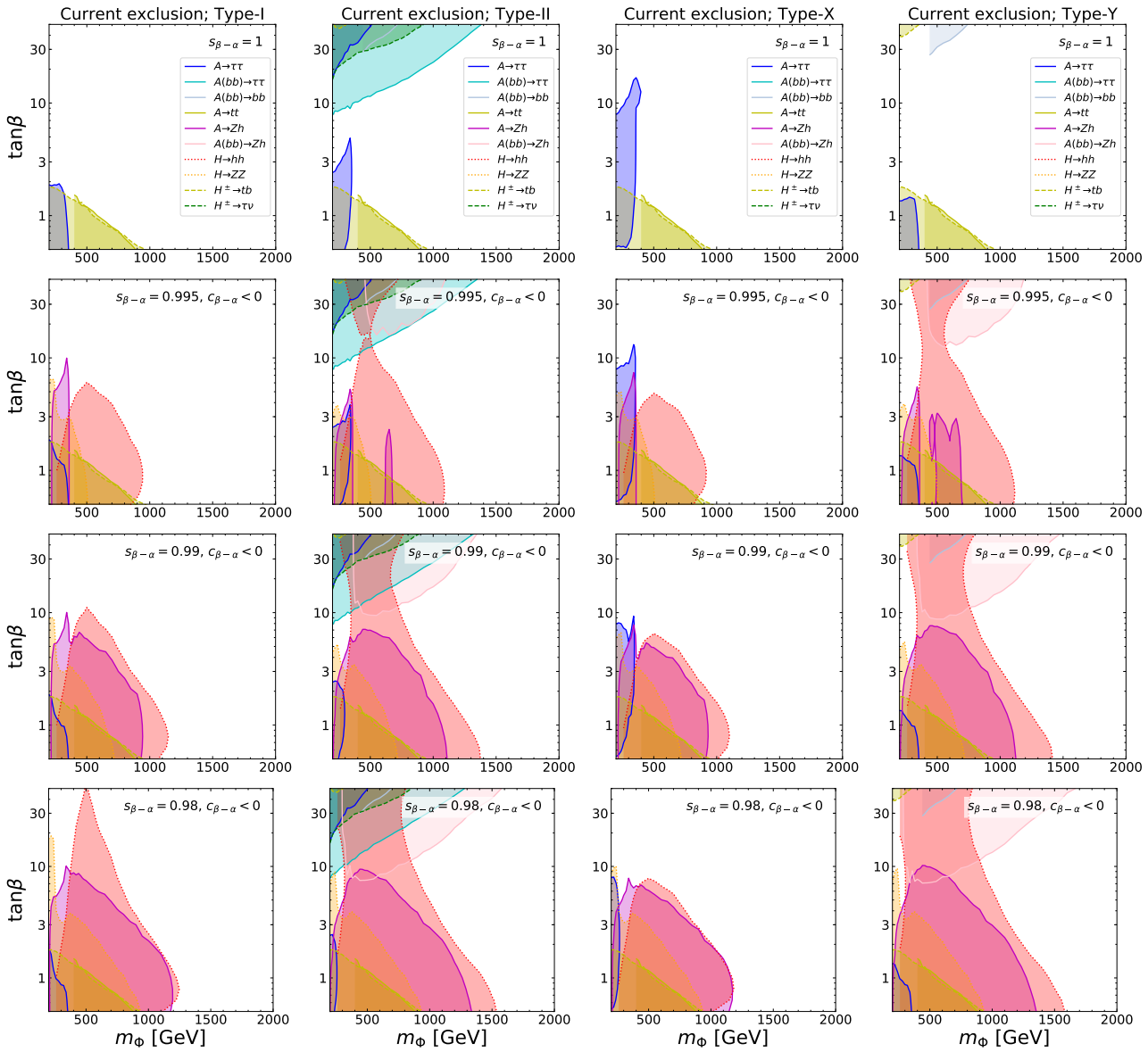

Figure 7.10: Regions on the m_Φ–tan β plane excluded at 95% CL in the Type-I, Type-II, Type-X and Type-Y 2HDMs (from the left to the right panels) via direct searches for heavy Higgs bosons with the 36 fb^{-1} LHC Run-II data. The value of $s_{\beta-\alpha}$ is set to be 1, 0.995, 0.99 and 0.98 with $c_{\beta-\alpha} < 0$ from the top to the bottom panels.

Now, let us turn to discuss constraints on the parameter space in each 2HDM from direct searches for heavy Higgs bosons with the LHC Run-II data.

In Fig. 7.10, we show exclusion regions at 95% CL on the m_Φ–tan β plane in the Type-I, Type-II, Type-X and Type-Y 2HDMs (from the left to the right panels) via various direct searches for heavy Higgs bosons with the 36 fb^{-1} LHC Run-II data listed in Table 7.1. The value of $s_{\beta-\alpha}$ is set to be 1, 0.995, 0.99 and 0.98 with $c_{\beta-\alpha} < 0$ from the top to the bottom panels. The shaded regions with dotted, solid, and dashed border lines denote the exclusion regions for H, A, and $H^\pm$, respectively.

Each exclusion region is understood by each production rate, shown in Figs. 7.6–7.9, times each branching ratio, depicted in Figs. 7.2–7.5. We highlight several points for A, H and $H^\pm$

in order.

Regarding to the CP-odd Higgs boson A;

- For large $\tan\beta$, exclusion regions only appear in the Type-II and the Type-Y 2HDMs, in which the production via the bottom-quark loop as well as the bottom-quark associated production becomes dominant.

- The $A \to \tau\bar{\tau}$ channel is significant only for $m_A < 2m_t$ or for large $\tan\beta$ in Type-II. We note that, although the branching ratio of the $A \to \tau\bar{\tau}$ decay is even dominant for large $\tan\beta$ in Type-X, the production rate is too small to be constrained.[1] For $m_A > 2m_t$, the $A \to t\bar{t}$ channel becomes relevant in the small $\tan\beta$ region in all the types.[2]

- Since the $A \to Zh$ decay only occurs for the non-alignment case, the exclusion regions are remarkably different between for the alignment case and for the non-alignment case. The region of the exclusion from the $A \to Zh$ channel becomes larger from $s_{\beta-\alpha} = 0.995$ to 0.98, since the decay rate for $A \to Zh$ is proportional to $c^2_{\beta-\alpha}$.

Regarding the CP-even heavier Higgs boson H;

- The production rate via the gluon fusion for the heavier CP-even Higgs boson H is smaller than that for the A production, as mentioned above. Moreover, in the non-alignment case, the fermionic branching ratios of H for low $\tan\beta$ is smaller than those for A due to the decays into a pair of the weak gauge bosons, which are forbidden for A. Therefore, the constraints are slightly weaker than the A case, and we do not present the exclusions explicitly for the $H \to \tau\bar{\tau}$, $H(b\bar{b}) \to \tau\bar{\tau}$, $H(b\bar{b}) \to b\bar{b}$ and $H \to t\bar{t}$ channels.

- For $m_H > 2m_{W,Z}$ and/or $m_H > 2m_h$, the peculiar decay modes for H are $H \to WW$, $H \to ZZ$ and $H \to hh$ for the non-alignment case and give rise to the relatively large exclusions. The region of the constraint from $H \to WW$ is similar to $H \to ZZ$, but smaller, so we do not show it explicitly.

- We note that, as mentioned in Sec. 7.1, the $H \to hh$ decay depends on M^2. For a non-degenerate case $M \neq m_\Phi$, the exclusion region from the $H \to hh$ channel can be different that for the degenerate case.

Regarding to the charged Higgs boson $H^\pm$;

- For the near alignment scenario, in the low $\tan\beta$ region ($\tan\beta \lesssim 5$), the $H^\pm \to tb$ decay is dominant for all the types, therefore the exclusions of the low-mass and low-$\tan\beta$ region from the $H^\pm \to tb$ channel are almost same for all the panels.

- In the large $\tan\beta$ region, the constraint from the $H^\pm \to \tau\nu$ channel can be significant only in Type-II. Although the branching ratio of the $H^\pm \to \tau\nu$ is even dominant for large $\tan\beta$ in Type-X, the constraint is insignificant due to the small production rate.

- We note that, as mentioned in Sec. 3.2, in Type-II and Type-Y there is an independent constrain from flavor observables on the mass of charged Higgs bosons, $m_{H^\pm} \gtrsim 800$ GeV.

[1] Four-τ final states from the $pp \to HA$ process in Type-X can be relevant [198].

[2] Because there is no specific analysis for the spin-0 resonance in the $t\bar{t}$ final state in the LHC Run-II, we use the limit for Z' [174], which is valid from the Run-I 8 TeV analysis [199].

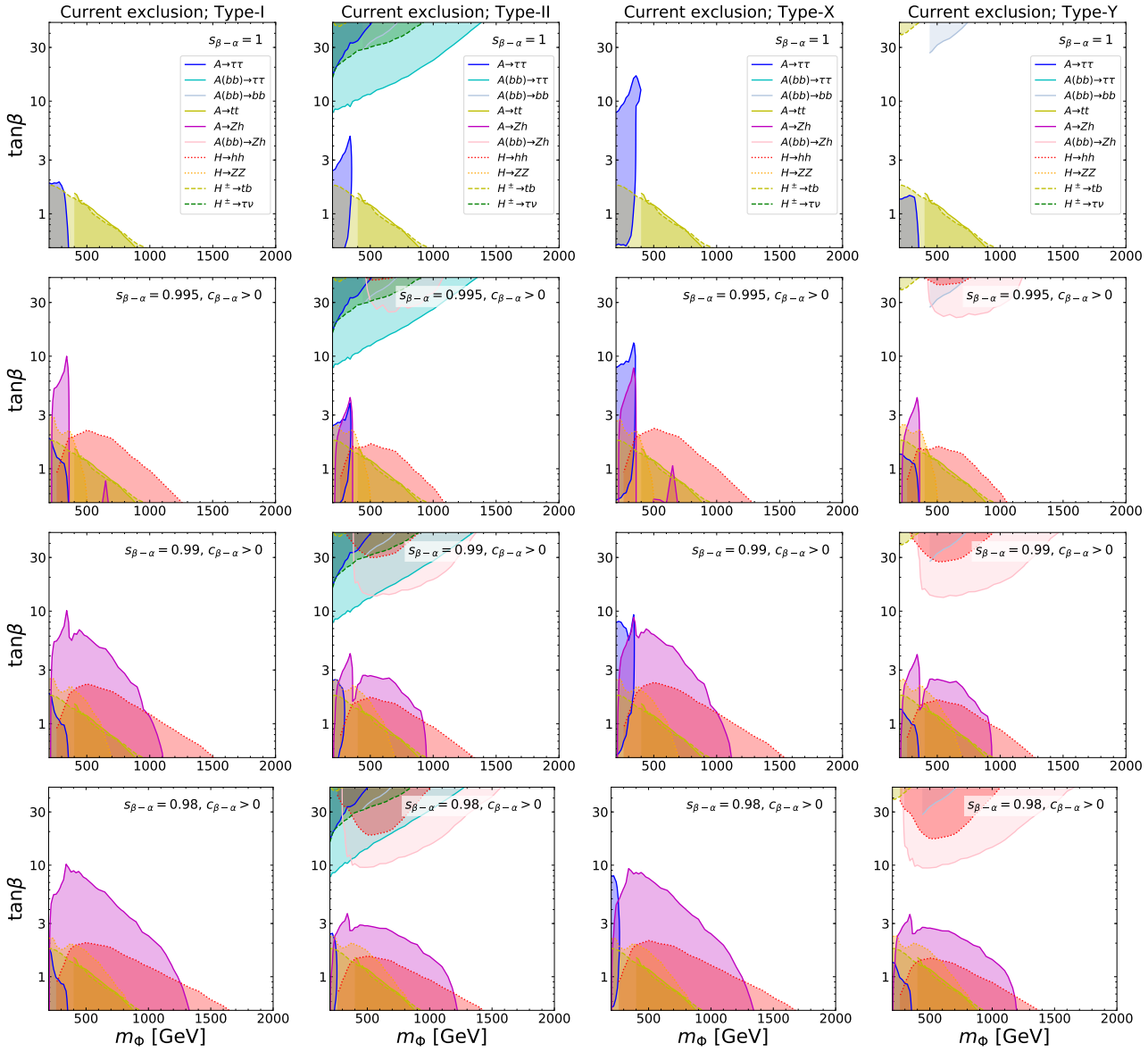

Figure 7.11: Regions on the m_Φ–$\tan\beta$ plane excluded at 95% CL in the Type-I, Type-II, Type-X and Type-Y 2HDMs (from the left to the right panels) via direct searches for heavy Higgs bosons with the 36 fb^{-1} LHC Run-II data. The value of $s_{\beta-\alpha}$ is set to be 1, 0.995, 0.99 and 0.98 with $c_{\beta-\alpha} > 0$ from the top to the bottom panels.

Figure 7.11 shows the same as in Fig. 7.10, but for the $c_{\beta-\alpha} > 0$ case. The global picture of the exclusion regions is same as for the $c_{\beta-\alpha} < 0$ case. A remarkable difference is that the constraints for H in the non-alignment case are much weaker for around $\tan\beta \sim 7-10$ due to the strong suppression of the production rates. Although $\sigma(A \to Zh)$ does not depend on the sign of $c_{\beta-\alpha}$, the exclusion regions for $c_{\beta-\alpha} > 0$ in Type-II and Y are smaller than those for $c_{\beta-\alpha} < 0$. This is because the analysis includes the $h \to b\bar{b}$ decay, whose branching ratio has a singular behavior for $c_{\beta-\alpha} > 0$; see Figs. 7.3 and 7.5.

Before closing this section, we briefly discuss the signal strength for the discovered Higgs boson measured at the LHC Run-II experiment, which provides independent constraints on the parameter space from those given by the direct searches discussed in this section. Measurements of the signal strength set constraints on the Higgs boson couplings; i.e., the κ values defined in Sec. 3.2, which can be translated into those on $s_{\beta-\alpha}$ and $\tan\beta$. In Table 7.2, we

$s_{\beta-\alpha}$	Type-I	Type-II	Type-X	Type-Y
0.995	$t_\beta \geq 0.54$ ($t_\beta \geq 0.54$)	– ($0.57 \leq t_\beta \leq 1.6$)	$0.43 \leq t_\beta \leq 4.1$ ($0.42 \leq t_\beta \leq 4.2$)	– (–)
0.990	$t_\beta \geq 0.86$ ($t_\beta \geq 0.86$)	– (–)	$0.71 \leq t_\beta \leq 2.0$ ($0.72 \leq t_\beta \leq 2.5$)	– (–)
0.980	$t_\beta \geq 1.3$ ($t_\beta \geq 1.3$)	– (–)	– (–)	– (–)

Table 7.2: 95% CL allowed range of $\tan\beta$ for the case with $c_{\beta-\alpha} < 0$ ($c_{\beta-\alpha} > 0$) from the signal strength of the discovered Higgs boson at the LHC [127]. The hyphen denotes no allowed region.

summarize the 95% CL allowed range of $\tan\beta$ in the 2HDMs with fixed values of $s_{\beta-\alpha}$. The κ values are extracted from Ref. [127], which are presented in Table 7.3 as a reference. We see that except for the Type-I 2HDM it gives severe constraints on $\tan\beta$, because κ_b and/or κ_τ can significantly differ from unity in the Type-II, Type-X and Type-Y 2HDMs even for the approximate alignment case.

7.3 Combined results of direct searches at the HL-LHC and precision tests at the ILC

Now, let us turn to investigate how the current parameter space in the 2HDMs discussed in the previous section can be explored further in future experiments, especially by direct searches for heavy Higgs bosons at the HL-LHC as well as by precision measurements of the Higgs boson couplings at the ILC. We note that complementarity for direct searches for heavy Higgs bosons between at the LHC and the ILC500 was discussed for the 2HDMs in Ref. [200].

In order to obtain the sensitivity projection to the HL-LHC with 3000 fb^{-1} of integrated luminosity, we rescale the current expected sensitivity by $\sqrt{3000/36} \sim 9.1$. We also perform a further rescaling of the sensitivity from $\sqrt{s} = 13$ TeV to $\sqrt{s} = 14$ TeV by taking into account the ratio of the signal cross sections, $\sigma(m_\Phi)_{14\text{TeV}}/\sigma(m_\Phi)_{13\text{TeV}}$. Here, we assume that signal and background increase by the same amount from 13 TeV to 14 TeV, which can be conservative particularly for the high-mass region. Detailed projection with systematic uncertainties for the $\phi \to \tau\bar{\tau}$ channel was performed in the report for the HL-LHC [201], where one can see the higher sensitivity for $m_\Phi \gtrsim 1200$ GeV.

In addition, from precision measurements of the 125 GeV Higgs boson couplings, we can further constrain the parameter space in the 2HDMs. In Table 7.3, we summarize the current measurements of the κ values at the LHC Run-II and the expected 1σ accuracies of their measurements at the HL-LHC and at the ILC. As we can see, the current uncertainties of the measured κ values are not small, 10% and 10–20% level for κ_V and κ_f, respectively. However, these uncertainties can be reduced significantly at those future collider experiments; e.g., κ_Z is expected to be measured with a few percent at the HL-LHC and less than 1% at the ILC. As we explained in Sec. 3.2, if a nonzero deviation in a Higgs boson coupling is confirmed, an upper limit on the mass of the additional Higgs bosons can be given because the decoupling limit is no longer realized. In the following discussion, we numerically derive the upper limit on the common mass of the additional Higgs bosons m_Φ by imposing the bounds from perturbative unitarity and vacuum stability, which are discussed in Sec. 3.2. We will see that the upper limit appears for the non-alignment case $s_{\beta-\alpha} \neq 1$, depending on the value of $\tan\beta$.

In Fig. 7.12, we show regions on the m_Φ–$\tan\beta$ plane expected to be excluded at 95% CL in the Type-I, Type-II, Type-X and Type-Y 2HDMs (from the left to the right panels) via

	Current (ATLAS, CMS)	HL-LHC (ATLAS, CMS)	ILC250	ILC500	(1σ [%])
κ_Z	$(1.11 \pm 0.08, 1.00 \pm 0.11)$	(2.6, 2.4)	0.38	0.30	
κ_W	$(1.05 \pm 0.09, -1.13^{+0.16}_{-0.13})$	(3.1, 2.6)	1.8	0.40	
κ_b	$(1.03^{+0.19}_{-0.17}, 1.17^{+0.27}_{-0.31})$	(6.2, 6.0)	1.8	0.60	
κ_t	$(1.09^{+0.15}_{-0.14}, 0.98 \pm 0.14)$	(6.3, 5.5)	–	6	
κ_c	(–, –)	(–, –)	2.4	1.2	
κ_τ	$(1.05^{+0.16}_{-0.15}, 1.02 \pm 0.17)$	(3.7, 2.8)	1.9	0.80	
κ_μ	$(-, 0.80^{+0.59}_{-0.80})$	(7.7, 6.7)	5.6	5.1	
κ_g	$(0.99^{+0.11}_{-0.10}, 1.18^{+0.16}_{-0.14})$	(4.2, 4.0)	2.2	0.97	
κ_γ	$(1.05 \pm 0.09, 1.07^{+0.14}_{-0.15})$	(3.7, 2.9)	1.1	1.0	
$\kappa_{Z\gamma}$	(–, –)	(12.7, –)	16	16	
κ_h	(–, –)	(–, –)	–	27	

Table 7.3: Summary for the current measurements and expected 1σ accuracies of the κ values. For the current measurements, we refer to the values, assuming that the branching ratio of the decay into BSM particles is zero, which are given by the ATLAS experiments with 80 fb^{-1} [127] and the CMS experiments with 35.9 fb^{-1} [20]. For the HL-LHC, we refer to the expected accuracies given in Ref. [201] using systematic uncertainties at the Run-II experiment. For the ILC250, we refer to the expected accuracies given by the ILC with 250 GeV and 2000 fb^{-1} [36]. For the ILC500, the expected accuracies are based on the results of the ILC250 combining the simulations at $\sqrt{s} = 350$ GeV with 200 fb^{-1} and those at $\sqrt{s} = 500$ GeV with 4000 fb^{-1} [36].

direct searches for heavy Higgs bosons at the HL-LHC and via precision measurements of the Higgs boson couplings at the ILC. The search channels we consider are same as for the current constraints in Figs. 7.10 and 7.11. The value of $s_{\beta-\alpha}$ is set to be 1, 0.995, 0.99 and 0.98 with $c_{\beta-\alpha} < 0$ from the top to the bottom panels. The shaded regions with solid, dotted, and dashed border lines denote the exclusion regions for A, H, and $H^\pm$, respectively.

The global picture of the exclusion regions from the direct searches is similar to the current exclusions, but much wider parameter regions are excluded. Especially, for the non-alignment case $s_{\beta-\alpha} \neq 1$, the large portion in this parameter space is excluded via the $A \to Zh$ and $H \to hh$ channels, which set the lower-mass limit with a given $\tan\beta$. We note again that the exclusion region from the $H \to hh$ channel can be different for the $M \neq m_\Phi$ case.

Black shaded regions are the regions excluded from the constraints of perturbative unitarity and/or vacuum stability. Here, we assume the precision at the ILC250, and the Higgs boson couplings with weak bosons deviate with 1σ (2σ) level, which corresponds to black solid (dashed) curves, as

$$\kappa_V^h = [0.995, 0.99, 0.98] \pm 0.0038\ (0.0076). \tag{7.34}$$

For these constraints, we scan the value of M^2 with $M^2 > 0$, so that the black shaded region indicates that there is no value of M^2 which simultaneously satisfies the unitarity and the vacuum stability bounds. In the above sense, the black region can be regarded as a conservative excluded region. Interestingly, it is seen that a non-zero deviation for the 125 GeV Higgs couplings from the SM prediction sets an upper limit of the heavy Higgs masses. For $s_{\beta-\alpha} = 0.995$, the alignment limit is included by the 2σ error, so that the dashed curve does not appear.

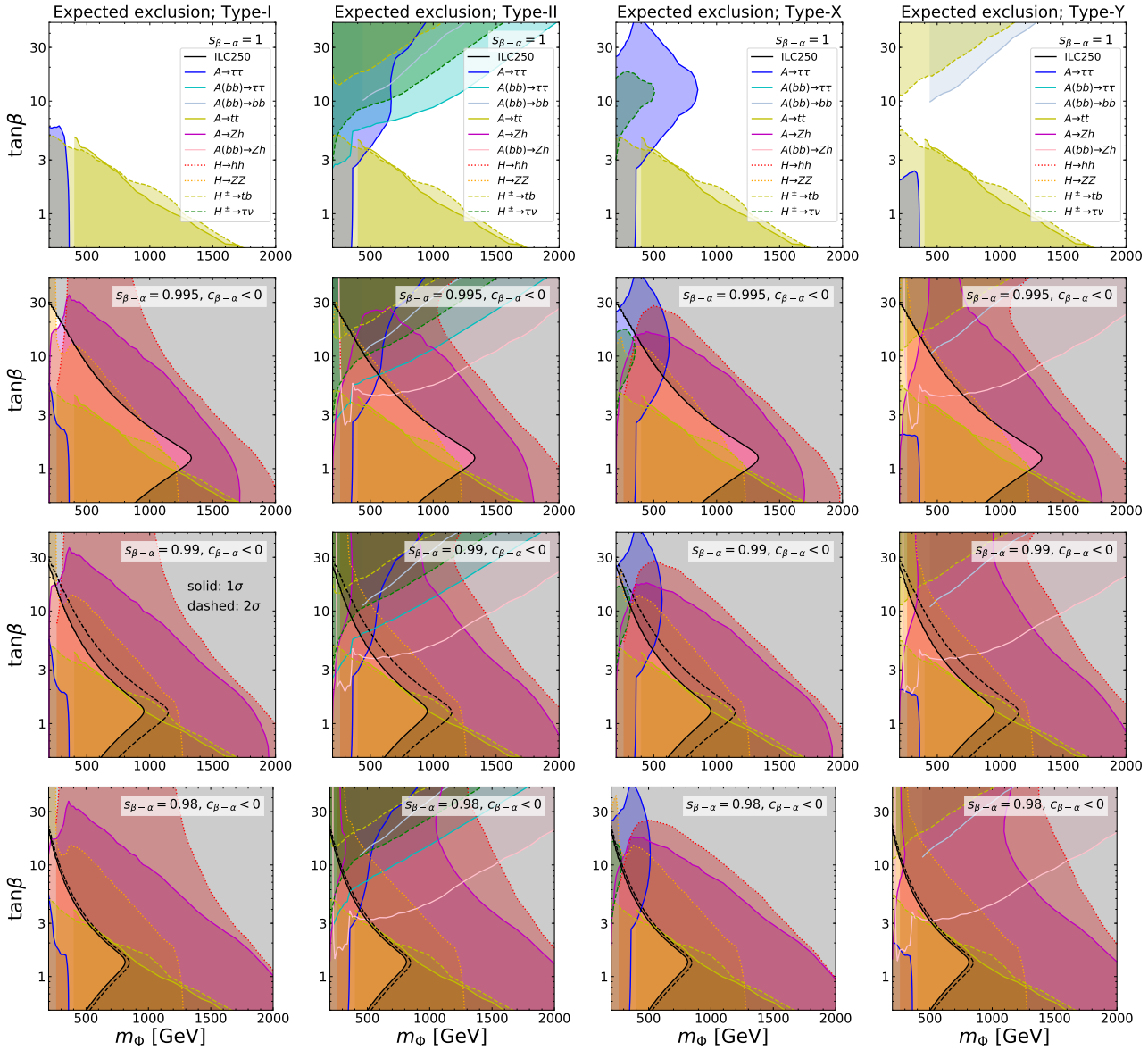

Figure 7.12: Regions on the m_Φ–$\tan\beta$ plane expected to be excluded at 95% CL in the Type-I, Type-II, Type-X and Type-Y 2HDMs (from the left to the right panels) via direct searches for heavy Higgs bosons at the HL-LHC and via precision measurements of the Higgs boson couplings at the ILC. The value of $s_{\beta-\alpha}$ is set to be 1, 0.995, 0.99 and 0.98 with $c_{\beta-\alpha} < 0$ from the top to the bottom panels.

Details of the behavior of the upper limit from precision measurements on m_Φ, shown in Fig. 7.12, are following, where explicit formulae of the constraints are given in Sec. 3.2. For $c_{\beta-\alpha} < 0$, the third condition of the vacuum stability bound given in Eq. (3.60) sets an upper limit on M which is slightly smaller than m_Φ almost without depending on the value of $\tan\beta$; e.g., $M \gtrsim 680$, 730 and 780 GeV being excluded for $x = -0.1$ and $m_\Phi = 800$, 900 and 1000 GeV, respectively, where $x \equiv \pi/2 - (\beta - \alpha)$. The important point here is that the required value of $m_\Phi^2 - M^2 (> 0)$ gets larger for a larger value of m_Φ. Whereas, the unitarity bound excludes a larger difference between M^2 and m_Φ^2, which makes magnitudes of the λ parameters larger. Therefore, for a fixed value of $s_{\beta-\alpha}$ and $\tan\beta$ we can find a critical value of m_Φ^2, above which the solution of the value of M^2 to satisfy both unitarity and vacuum stability bounds vanishes. Such an upper limit on m_Φ becomes stronger when the value of $\tan\beta$ differs from

unity because the λ_1 or λ_2 parameter becomes significant so that the unitarity bound sets more severe constraint on $|M^2 - m_\Phi^2|$. We here emphasize that the entire parameter space we consider is explored by combining the constraints from the direct searches at the HL-LHC and from the precision measurements of the 125 GeV Higgs boson couplings at the ILC.

Figure 7.13 shows the same as in Fig. 7.12, but for the $c_{\beta-\alpha} > 0$ case. Because of the singular behaviors of the production cross section for H and of the branching ratios for h around $\tan\beta \sim 7 - 10$, shown in Figs. 7.7 and 7.3, a narrow parameter region in the Type-II and the Type-Y models remains without any constraints from the direct searches even for low m_Φ. Similar to Fig. 7.12, there appears an upper limit on m_Φ by the constraints of unitarity and vacuum stability in Fig. 7.13. A remarkable difference, however, arises from the vacuum stability bound as compared with the case for $c_{\beta-\alpha} < 0$. In this case with a low $\tan\beta$ region, the condition $\lambda_2 > 0$ sets an upper limit on M^2 for a fixed value of m_Φ^2 with $M^2 \lesssim m_\Phi^2$. This upper limit on M^2 gets milder when $\tan\beta$ becomes larger. When $\tan\beta$ exceeds a certain value, the upper limit on M^2 is almost fixed to be m_Φ^2 due to the condition $\lambda_1 > 0$ instead of $\lambda_2 > 0$. Such a non-trivial $\tan\beta$ dependence on the vacuum stability bound provides two peaks of the upper limit on m_Φ as seen in Fig. 7.13. As a result, some small parameter regions remain uncovered by both the HL-LHC and the ILC250.

We here give a comment on the case, where the degeneracy between the common mass of the additional Higgs bosons m_Φ and M is relaxed. In the above analysis, we have set $M = m_\Phi$ in the analysis of the exclusion region by the direct searches for simplicity. As we have mentioned in Sec. 7.1, the decay width for $H \to hh$ depends on the value of M, and the exclusion region for H might change if we consider the case of $M \neq m_\Phi$. We note, however, that most of the parameter regions excluded by $H \to hh$ are also excluded by the $A \to Zh$ decay mode, which does not depend on the value of M. Therefore, our main conclusion does not change even if we relax the degeneracy among m_Φ and M.

To summarize, the entire parameter space in the 2HDMs can be explored by the synergy between the direct searches at the HL-LHC and the precision measurements of the 125 GeV Higgs boson couplings at the ILC. In other words, if we observed any deviations for the Higgs boson couplings at the ILC, we would be able to find additional Higgs bosons at the HL-LHC, or reject a certain type of new physics models. In order to quantify the above statement, we have also checked the 5σ discovery sensitivity by naive rescaling. We find that the discovery regions are certainly smaller than the 95% CL excluded region shown in Figs. 7.12 and 7.13. Consequently, for $c_{\beta-\alpha} < 0$, we find that most of the parameter space is covered by the direct searches at the HL-LHC and the precision tests at the ILC250. For $c_{\beta-\alpha} > 0$, on the other hand, some parameter regions appear, which requires more data and/or more precision to be explored.

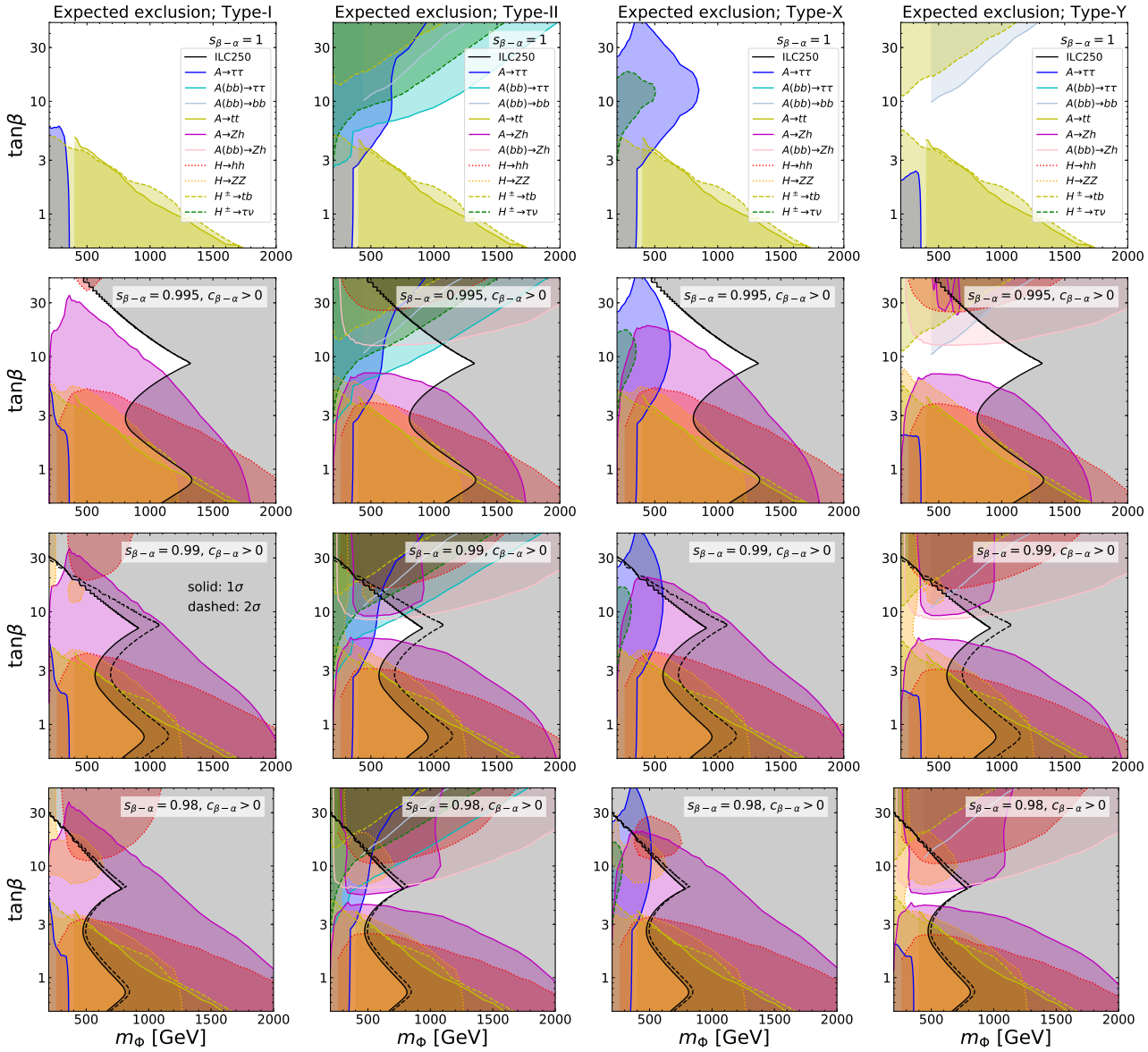

Figure 7.13: Regions on the m_Φ–$\tan\beta$ plane expected to be excluded at 95% CL in the Type-I, Type-II, Type-X and Type-Y 2HDMs (from the left to the right panels) via direct searches for heavy Higgs bosons at the HL-LHC and via precision measurements of the Higgs boson couplings at the ILC. The value of $s_{\beta-\alpha}$ is set to be 1, 0.995, 0.99 and 0.98 with $c_{\beta-\alpha}>0$ from the top to the bottom panels.

Chapter 8

One-loop calculations for decays of the charged Higgs bosons

In this chapter, we discuss the decay rates of charged Higgs bosons for various decay modes in the 2HDMs. Decay branching ratios of charged Higgs bosons are evaluated including NLO EW corrections, as well as QCD corrections up to NNLO. We have newly implemented them into the `H-COUP` program [45, 46]. We comprehensively study the impacts of the NLO EW corrections to the branching ratios in approximate alignment scenarios. We find that the $H^\pm \to W^\pm h$ decay modes can be dominant decay modes even in the case where deviation in hZZ couplings is quite small and cannot be detected at the ILC. Thus, we can extract the information on the mixing angle by studying the $H^\pm \to W^\pm h$ decay modes at future collider experiments.

8.1 Decay rates with higher order corrections

In this section, we explain calculations of the decay rates with NLO EW corrections for two-body decay of the charged Higgs bosons, i.e., $H^\pm \to f\bar{f}'$ and $H^\pm \to W^\pm\phi$ ($\phi = h, H, A$). For the decay into a pair of quarks $H^\pm \to q\bar{q}'$, QCD corrections up to NNLO are presented. Formulae for the loop-induced decay processes $H^\pm \to W^\pm V$ ($V = Z, \gamma$) are given at LO.

For the computations of the NLO EW corrections to the charged Higgs boson decays, we adopt the improved on-shell renormalization scheme [112]. While we do not give all descriptions for the renormalization scheme in this paper, we here highlight the main points, for details see Ref. [112]. In the Higgs sector, there are six free parameters given in Eq. (3.49). Together with the wave function renormalization constants, the masses of the additional Higgs bosons and the mixing angles are renormalized by the on-shell conditions for the Higgs bosons in the mass eigenstates. However, the gauge dependence appears in the renormalization of mixing angles [202], which are resolved by applying the pinch technique [112, 119]. The remaining parameter in the Higgs sector, M^2, is renormalized by the minimal subtraction [156]. On the other hand, the renormalization of the gauge sector and the fermion sector are performed by using on-shell conditions [96]. In our calculation for $H^\pm \to q\bar{q}'$, we do not take into account contributions arising by quark mixing at one-loop level, which is always suppressed by the CKM matrix element. Hence renormalization of the CKM matrix does not have to be carried out.

While the UV divergences are correctly removed by virtue of the mentioned above renormalization, IR divergences appear in one-loop diagrams containing a virtual photon, which cancel with those of real photon emission diagrams. We regularize them by introducing a small photon mass μ, and numerically confirm that IR divergences are canceled out when virtual corrections and real emissions are summed up.

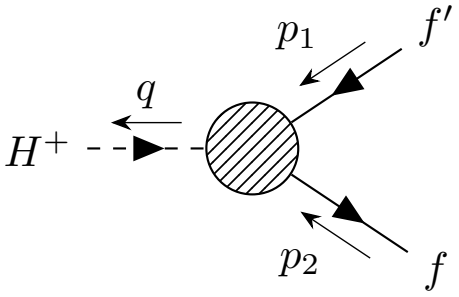

Figure 8.1: Momentum assignment for the renormalized $H^+ f \bar{f}'$ vertex.

8.1.1 Form factors for vertex functions of charged Higgs bosons

Before we give formulae for decay rates with higher corrections, we first define renormalized vertex functions of the charged Higgs bosons. All NLO EW corrections are expressed in terms of the form factors of the vertex functions.

$H^\pm f f'$ vertex

In the computations of the charged Higgs boson decays into two fermions $H^\pm \to f\bar{f}'$, the renormalized $H^\pm f f'$ vertex functions are needed. In general, the vertex functions can be expressed as [99]

$$\begin{aligned}\hat{\Gamma}_{H^\pm f f'} = {} & \hat{\Gamma}^{\rm S}_{H^\pm f f'} + \gamma_5 \hat{\Gamma}^{\rm P}_{H^\pm f f'} + \not{p}_1 \hat{\Gamma}^{\rm V1}_{H^\pm f f'} + \not{p}_2 \hat{\Gamma}^{\rm V2}_{H^\pm f f'} \\ & + \not{p}_1 \gamma_5 \hat{\Gamma}^{\rm A1}_{H^\pm f f'} + \not{p}_2 \gamma_5 \hat{\Gamma}^{\rm A2}_{H^\pm f f'} + \not{p}_1 \not{p}_2 \hat{\Gamma}^{\rm T}_{H^\pm f f'} + \not{p}_1 \not{p}_2 \gamma_5 \hat{\Gamma}^{\rm PT}_{H^\pm f f'},\end{aligned} \tag{8.1}$$

where p_1 and p_2 denote incoming momenta of a fermion f' and the SU(2) partner f, and q is the outgoing momentum of the charged Higgs bosons (see Fig. 8.1). The renormalized form factors can be commonly written by the tree-level part and the one-loop part as

$$\hat{\Gamma}^X_{H^\pm f f'} = \Gamma^{X,\rm tree}_{H^\pm f f'} + \Gamma^{X,\rm loop}_{H^\pm f f'}, \quad (\text{X=S, P, V1, V2, A1, A2, T, PT}), \tag{8.2}$$

where the one-loop parts are further divided into contributions from 1PI diagrams and counterterms, i.e., $\Gamma^{X,\rm loop}_{H^\pm f f'} = \Gamma^{X,\rm 1PI}_{H^\pm f f'} + \delta\Gamma^X_{H^\pm f f'}$. The 1PI diagrams contributions $\Gamma^{X,\rm 1PI}_{H^\pm f f'}$ are given in Appendix B.2. in Ref. [43].

The tree-level couplings for $H^\pm f f'$ vertices are given by,

$$\Gamma^{S,\rm tree}_{H^\pm f f'} = \pm \frac{V_{f f'}}{\sqrt{2}v}(m_f \zeta_f - m_{f'} \zeta_{f'}), \quad \Gamma^{P,\rm tree}_{H^\pm f f'} = \mp \frac{V_{f f'}}{\sqrt{2}v}(m_f \zeta_f + m_{f'} \zeta_{f'}), \tag{8.3}$$

$$\Gamma^{X,\rm tree}_{H^\pm f f'} = 0 \quad (X \neq S, P). \tag{8.4}$$

The counterterms for $H^\pm f f'$ vertices are presented by

$$\delta\Gamma^{S/P}_{H^\pm f f'} = \frac{1}{2}(\delta\Gamma^R_{H^\pm f f'} \pm \delta\Gamma^L_{H^\pm f f'}), \tag{8.5}$$

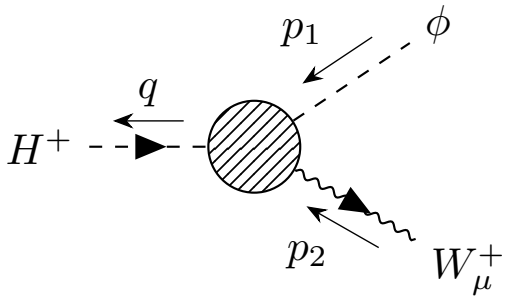

Figure 8.2: Momentum assignment for the renormalized $H^+W^{-\mu}\phi$ vertex.

with

$$\delta\Gamma^R_{H^\pm ff'} = \mp\frac{\sqrt{2}m_{f'}}{v}\zeta_{f'}\left[\frac{\delta m_{f'}}{m_{f'}} - \frac{\delta v}{v} - \zeta_{f'}\delta\beta + \frac{\delta Z_R^{f'} + \delta Z_L^f}{2} + \frac{\delta Z_{H^\pm}}{2}\right.$$
$$\left. + \frac{1}{\zeta_{f'}}\delta C_{H^\pm} - \left(\frac{1}{\zeta_{f'}} + \zeta_{f'}\right)\delta\beta^{\rm PT}\right], \tag{8.6}$$

$$\delta\Gamma^L_{H^\pm ff'} = \pm\frac{\sqrt{2}m_{f}}{v}\zeta_{f}\left[\frac{\delta m_{f}}{m_{f}} - \frac{\delta v}{v} - \zeta_{f}\delta\beta + \frac{\delta Z_R^{f} + \delta Z_L^{f'}}{2} + \frac{\delta Z_{H^\pm}}{2}\right.$$
$$\left. + \frac{1}{\zeta_{f}}\delta C_{H^\pm} - \left(\frac{1}{\zeta_{f}} + \zeta_{f}\right)\delta\beta^{\rm PT}\right], \tag{8.7}$$

where concrete expressions for the counterterms for fermion masses $\delta m^2_{f^{(\prime)}}$, the wave function renormalization $\delta Z^{f^{(\prime)}}_{R/L}$, the electroweak VEV δv, and the mixing angle $\delta\beta$ are presented in Appendix C of Ref. [112]. The wave function renormalization constants of the charged Higgs bosons are expressed by

$$\delta Z_{H^\pm} = -\left.\frac{d}{dq^2}\Pi^{\rm 1PI}_{H^+H^-}(q^2)\right|_{q^2=m^2_{H^\pm}}, \tag{8.8}$$

$$\delta C_{H^\pm} = \delta\beta + \frac{1}{m^2_{H^\pm}}\left(\Pi^{\rm 1PI}_{H^+G^-}(0) + s_{\beta-\alpha}\frac{T^{\rm 1PI}_H}{v} - c_{\beta-\alpha}\frac{T^{\rm 1PI}_h}{v}\right), \tag{8.9}$$

where 1PI diagram contributions to two point functions for the charged Higgs boson and H^+-G^- mixing, $\Pi^{\rm 1PI}_{H^+H^-}(q^2)$ and $\Pi^{\rm 1PI}_{H^+G^-}(q^2)$ are given in Appendix B.1. in Ref. [43]. Those to the one-point functions $T^{\rm 1PI}_H$ and $T^{\rm 1PI}_h$ are presented in Appendix C of Ref. [100]. The pinch term for the mixing angle in the Feynman gauge $\delta\beta^{\rm PT}$ is given by

$$\delta\beta^{\rm PT} = -\frac{1}{2m^2_A}\left(\Pi^{\rm PT}_{AG^0}(m^2_A) + \Pi^{\rm PT}_{AG^0}(0)\right). \tag{8.10}$$

The last term in Eqs. (8.6) and (8.7) corresponds to a subtraction term due to the following reason. The pinch terms for the mixing angle are only required for the counterterms arising from the shift of the couplings, and, for those arising from the shift of scalar fields, we use the counterterm $\delta\beta$ without the pinch terms.

$H^\pm W^\mp\phi$ vertex

For calculations of charged Higgs boson decays into a vector boson and a scalar boson $H^\pm \to W^\pm\phi$ ($\phi = h, H, A$), renormalization of $H^\pm W^\mp\phi$ vertex are needed. the vertex functions can

be commonly expressed as

$$\hat{\Gamma}^{\mu}_{H^{\pm}W^{\mp}\phi}(p_1^2, p_2^2, q^2) = (p_1+q)^{\mu}\hat{\Gamma}_{H^{\pm}W^{\mp}\phi}, \tag{8.11}$$

where p_1^μ and p_2^μ denote the incoming momenta of a scalar boson ϕ and a $W^\pm$ bosons, respectively. A momentum q^μ denotes the outgoing one of the charged Higgs boson (see Fig. 8.2). Since we here assume that the external gauge bosons are on-shell, the term proportional to $p_2 = q - p_1$ vanishes due to the orthogonality of the polarization vector. Similar to the $H^\pm f\bar{f}'$ vertex, the renormalized form factor can be decomposed as

$$\hat{\Gamma}_{H^{\pm}W^{\mp}\phi} = \Gamma^{\rm tree}_{H^{\pm}W^{\mp}\phi} + \Gamma^{\rm loop}_{H^{\pm}W^{\mp}\phi}. \tag{8.12}$$

with $\Gamma^{\rm tree}_{H^{\pm}W^{\mp}\phi} = -ig_{\phi H^{\pm}W^{\mp}}$. The one-loop part $\Gamma^{\rm loop}_{H^{\pm}W^{\mp}\phi}$ is schematically expressed in terms of 1PI diagram $\Gamma^{\rm 1PI}_{H^{\pm}W^{\mp}\phi}$ and the counterterm $\delta\Gamma_{H^{\pm}\phi W^{\mp}}$ as

$$\Gamma^{\rm loop}_{H^{\pm}W^{\mp}\phi} = \Gamma^{\rm 1PI}_{H^{\pm}W^{\mp}\phi} + \delta\Gamma_{H^{\pm}W^{\mp}\phi}. \tag{8.13}$$

The 1PI diagram contributions to these vertex functions are given in Appendix B.2. in Ref. [43].

The counterterms are expressed as

$$\begin{aligned}
\delta\Gamma_{H^{\pm}W^{\mp}h} = \mp\frac{m_W}{v}c_{\beta-\alpha}\Big[&\frac{\delta m_W^2}{2m_W^2} - \frac{\delta v}{v} + \frac{1}{2}(\delta Z_W + \delta Z_{H^\pm} + \delta Z_h) \\
&+ \tan(\beta-\alpha)(\delta\beta^{\rm PT} - \delta\alpha^{\rm PT} + \delta C_{H^\pm} - \delta C_h)\Big], \qquad (8.14)\\
\delta\Gamma_{H^{\pm}W^{\mp}H} = \pm\frac{m_W}{v}s_{\beta-\alpha}\Big[&\frac{\delta m_W^2}{2m_W^2} - \frac{\delta v}{v} + \frac{1}{2}(\delta Z_W + \delta Z_{H^\pm} + \delta Z_H) \\
&+ \cot(\beta-\alpha)(\delta\beta^{\rm PT} + \delta\alpha^{\rm PT} - \delta C_{H^\pm} - \delta C_h)\Big], \qquad (8.15)\\
\delta\Gamma_{H^{\pm}W^{\mp}A} = +i\frac{m_W}{v}\Big[&\frac{\delta m_W^2}{2m_W^2} - \frac{\delta v}{v} + \frac{1}{2}(\delta Z_W + \delta Z_{H^\pm} + \delta Z_A)\Big], \qquad (8.16)
\end{aligned}$$

where the $\delta\alpha^{\rm PT}$ denotes the pinch term contribution to $\delta\alpha$. In the Feynman gauge, it is expressed by

$$\delta\alpha^{\rm PT} = \frac{1}{2(m_H^2 - m_h^2)}\left(\Pi^{\rm PT}_{Hh}(m_h^2) + \Pi^{\rm PT}_{Hh}(m_H^2)\right). \tag{8.17}$$

Inclusion of the terms with $\delta\alpha^{\rm PT}$ and $\delta\beta^{\rm PT}$ has the same reason with the one presented in Sec. 8.1.1. We again refer Appendix C of Ref. [112] for concrete expressions to the $W^\pm$ boson mass counterterm δm_W and the wave function renormalization constants for the $W^\pm$ boson δZ_W and the Higgs bosons $\delta C_h,\ \delta Z_\phi$ $(\phi = h, H, A)$.

$H^\pm VW^\mp$ vertex

For computations of loop induced charged Higgs decays, i.e., $H^\pm \to ZW^\pm$ and $H^\pm \to \gamma W^\pm$, $H^\pm VW^\mp$ $(V = Z, \gamma)$ vertex appears. The renormalized tensor vertex functions can be expressed by [144, 145]

$$\Gamma^{\mu\nu}_{H^{\pm}VW^{\mp}} = g^{\mu\nu}\Gamma^1_{H^{\pm}VW^{\mp}} + p_1^\nu p_2^\mu \Gamma^2_{H^{\pm}VW^{\mp}} + i\epsilon^{\mu\nu\rho\sigma}p_{1\rho}p_{2\sigma}\Gamma^3_{H^{\pm}VW^{\mp}}, \tag{8.18}$$

where p_1^μ denotes an incoming momentum for a $W^\pm$ boson and p_2^ν is that of a Z boson or a photon, and q is the outgoing momentum of the charged Higgs bosons (see Fig. 8.3). In this

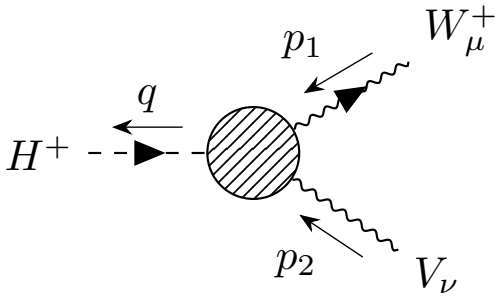

Figure 8.3: Momentum assignment for the renormalized $H^+V^\mu W^{-\nu}$ vertex.

expression, relations for on-shell vector bosons, $\epsilon_\mu(p_1)p_1^\mu = \epsilon_\nu(p_2)p_2^\nu = 0$, have been applied. Since $H^\pm ZW^\mp$ and $H^\pm\gamma W^\mp$ vertices do not exist at the tree level, form factors are written by the loop contributions,

$$\Gamma^i_{H^\pm VW^\mp} = \Gamma^{i,\mathrm{loop}}_{H^\pm VW^\mp} = \Gamma^{i,\mathrm{1PI}}_{H^\pm VW^\mp} + \delta\Gamma^i_{H^\pm VW^\mp}. \tag{8.19}$$

The 1PI diagram contributions are given in Appendix B.2. in Ref. [43]. While there is no tree-level contributions, counterterms are introduced from $G^\pm\gamma W^\mp$ vertices though the mixing with charged Higgs bosons. It is expressed by

$$\delta\Gamma^1_{H^\pm VW^\mp} = g_{G^\pm W^\mp V}(\delta C_{G^+H^-} + \delta\beta), \qquad \delta\Gamma^{2,3}_{H^\pm VW^\mp} = 0, \tag{8.20}$$

where the tree-level couplings for NG boson are $g_{G^\pm W^\mp\gamma} = egv/2$ and $g_{G^\pm W^\mp Z} = -gg_Z vs_W^2/2$.

8.1.2 Decay rates of $H^\pm \to ff'$

The decay rates for charged Higgs boson decays into a pair of fermions with NLO EW corrections and QCD corrections can be written as

$$\begin{aligned}\Gamma(H^\pm \to f\bar{f}') = \frac{N_c^f m_{H^\pm}|V_{ff'}|^2}{8\pi v^2}\lambda^{\frac{1}{2}}(\mu_f,\mu_{f'})\Bigg[&(1-\mu_f-\mu_{f'})\Big\{m_{f'}^2\zeta_{f'}^2\Big(1+\Delta^{\mathrm{QCD}}_{RR}+\Delta^{\mathrm{EW}}_{RR}\Big)\\ &+m_f^2\zeta_f^2\Big(1+\Delta^{\mathrm{QCD}}_{LL}+\Delta^{\mathrm{EW}}_{LL}\Big)\Big\}+4\sqrt{\mu_f\mu_{f'}}m_f m_{f'}\zeta_f\zeta_{f'}\Big(1+\Delta^{\mathrm{QCD}}_{RL}+\Delta^{\mathrm{EW}}_{RL}\Big)\Bigg]\\ &+\Gamma(H^\pm\to f\bar{f}'\gamma),\end{aligned} \tag{8.21}$$

with $\mu_{f^{(\prime)}} = m^2_{f^{(\prime)}}/m^2_{H^\pm}$ and the color factor $N_c^f = 3$ (1) for quarks (leptons). The kinematical factor $\lambda(x,y)$ is defined by

$$\lambda(x,y) = (1-x-y)^2 - 4xy. \tag{8.22}$$

Factors $\Delta^{\mathrm{QCD}}_{XX}$ and $\Delta^{\mathrm{EW}}_{XX}$ ($XX = LL,\ RR,\ RL$) denote QCD correction parts and EW correction parts, respectively. In this expression, the real photon emission contribution is included, by which the IR divergences are removed. The analytic formula is given in Appendix C. in Ref. [43]. The LO decay rate $\Gamma(H^\pm \to f\bar{f}')_{\mathrm{LO}}$ is easily obtained by omitting all NLO contributions, $\Delta^{\mathrm{QCD/EW}}_{XX} \to 0$ and $\Gamma(H^\pm\to f\bar{f}'\gamma)\to 0$.

The EW corrections parts are written by

$$\Delta_{RR}^{\rm EW} = -\frac{2v}{\sqrt{2}m_{f'}\zeta_{f'}V_{ff'}}{\rm Re}\big(G^{S,{\rm loop}}_{H^\pm ff'} + G^{P,{\rm loop}}_{H^\pm ff'}\big) - \frac{2}{\zeta_{f'}}\frac{{\rm Re}\hat{\Pi}_{H^+G^-}(m^2_{H^\pm})}{m^2_{H^\pm}} - \Delta r, \tag{8.23}$$

$$\Delta_{LL}^{\rm EW} = \frac{2v}{\sqrt{2}m_{f}\zeta_{f}V_{ff'}}{\rm Re}\big(G^{S,{\rm loop}}_{H^\pm ff'} - G^{P,{\rm loop}}_{H^\pm ff'}\big) - \frac{2}{\zeta_{f}}\frac{{\rm Re}\hat{\Pi}_{H^+G^-}(m^2_{H^\pm})}{m^2_{H^\pm}} - \Delta r, \tag{8.24}$$

$$\begin{aligned}\Delta_{RL}^{\rm EW} = &-\frac{v}{\sqrt{2}m_f m_{f'}\zeta_f\zeta_{f'}V_{ff'}}\Big[m_f\zeta_f{\rm Re}\big(G^{S,{\rm loop}}_{H^\pm ff'} + G^{P,{\rm loop}}_{H^\pm ff'}\big) - m_{f'}\zeta_{f'}{\rm Re}\big(G^{S,{\rm loop}}_{H^\pm ff'} - G^{P,{\rm loop}}_{H^\pm ff'}\big)\Big] \\ &- \left(\frac{1}{\zeta_f} + \frac{1}{\zeta_{f'}}\right)\frac{{\rm Re}\hat{\Pi}_{H^+G^-}(m^2_{H^\pm})}{m^2_{H^\pm}} - \Delta r,\end{aligned} \tag{8.25}$$

where functions $G^{S,{\rm loop}}_{H^\pm ff'}$ and $G^{P,{\rm loop}}_{H^\pm ff'}$ are expressed in terms of form factors for the $H^\pm ff'$ vertex as

$$G^{S,{\rm loop}}_{H^\pm ff'} = \Gamma^{S,{\rm loop}}_{H^\pm ff'} + m_{f'}\Gamma^{V1,{\rm loop}}_{H^\pm ff'} - m_f\Gamma^{V2,{\rm loop}}_{H^\pm ff'} + m^2_{H^\pm}\left(1 - \frac{m^2_-}{m^2_{H^\pm}} - \frac{m_f m_{f'}}{m^2_{H^\pm}}\right)\Gamma^{T,{\rm loop}}_{H^\pm ff'}, \tag{8.26}$$

$$G^{P,{\rm loop}}_{H^\pm ff'} = \Gamma^{P,{\rm loop}}_{H^\pm ff'} - m_{f'}\Gamma^{A1,{\rm loop}}_{H^\pm ff'} - m_f\Gamma^{A2,{\rm loop}}_{H^\pm ff'} + m^2_{H^\pm}\left(1 - \frac{m^2_+}{m^2_{H^\pm}} + \frac{m_f m_{f'}}{m^2_{H^\pm}}\right)\Gamma^{PT,{\rm loop}}_{H^\pm ff'}, \tag{8.27}$$

with $m_+ = m_f + m_{f'}$ and $m_- = m_f - m_{f'}$. The last term in Eqs. (8.23)-(8.25), Δr, denotes the one-loop weak corrections to the muon decay, which is introduced due to resummation of universal leading higher-order corrections, such as large logarithms from light fermion masses and contributions with the squared mass of the top quark [108, 203]. The contributions to the renormalized self-energy $\hat{\Pi}_{H^+G^-}$ come from H^+W^- and H^+G^- mixings, which are derived by using the Slavnov-Taylor identity [204].

Expressions for the QCD correction parts are different depending on the final state fermions. For the decays into a pair of light quarks, we apply the QCD corrections at NNLO in the $\overline{\rm MS}$ scheme [106, 129–132]. The correction factors are expressed by a common factor, i.e., $\Delta_{RR}^{\rm QCD} = \Delta_{LL}^{\rm QCD} = \Delta_{RL}^{\rm QCD} = \Delta_q^{H^\pm}$;

$$\Delta_q^{H^\pm} = \frac{\alpha_s(m_{H^\pm})}{\pi}C_F\frac{23}{4} + \left(\frac{\alpha_s(m_{H^\pm})}{\pi}\right)^2(35.94 - 1.36N_f), \tag{8.28}$$

where $\alpha_s(m_{H^\pm})$ denotes the strong coupling constant at the scale of $m_{H^\pm}$, C_F is the color factor $C_F = 4/3$, and N_f is the active flavor number. In the $\overline{\rm MS}$ scheme, the light quark masses in LO parts of Eq. (8.21), which comes from the Yukawa couplings of $H^\pm$, are replaced by the corresponding running masses, $m_{q^{(\prime)}} \to \bar{m}_{q^{(\prime)}}(m_{H^\pm})$. Thereby, large logarithm contributions at the higher-order are absorbed by the quark masses [133, 205–207]. On the other hand, for the decay into quarks including the top quark, we apply both QCD corrections in the on-shell scheme and those of $\overline{\rm MS}$ scheme and interpolate them following Ref. [68]. The reason is that the contributions of the top quark mass in the on-shell scheme are significant in the case of lighter charged Higgs bosons, $m_{H^\pm} \sim m_t + m_D$ ($D = b, s, d$), whereas the logarithm contributions $\log\big(m_t^2/m^2_{H^\pm}\big)$ can dominate in case of $m_{H^\pm} \gg m_t + m_D$. The QCD correction factors at NLO in the on-shell scheme are given by [135, 143]

$$\Delta_{RR}^{\rm QCD} = C_F\frac{\alpha_S(\mu)}{\pi}\Delta^+_{qq'}, \qquad \Delta_{LL}^{\rm QCD} = C_F\frac{\alpha_S(\mu)}{\pi}\Delta^+_{q'q}, \qquad \Delta_{RL}^{\rm QCD} = C_F\frac{\alpha_S(\mu)}{\pi}\Delta^-_{qq'}, \tag{8.29}$$

where

$$\Delta^{+}_{ff'} = \frac{9}{4} + \frac{3-2\mu_f+2\mu_{f'}}{4}\ln\frac{\mu_f}{\mu_{f'}} + \frac{(\frac{3}{2}-\mu_f-\mu_{f'})\lambda_{ff'}+5\mu_f\mu_{f'}}{2\lambda^{1/2}_{ff'}(1-\mu_f-\mu_{f'})}\ln x_f x_{f'} + B_{ff'}, \tag{8.30}$$

$$\Delta^{-}_{ff'} = 3 + \frac{\mu_{f'}-\mu_f}{2}\ln\frac{\mu_f}{\mu_{f'}} + \frac{\lambda_{ff'}+2(1-\mu_f-\mu_{f'})}{2\lambda^{1/2}_{ff'}}\ln x_q x_{f'} + B_{ff'}, \tag{8.31}$$

with $x_f = 2\mu_f/(1-\mu_f-\mu_{f'}+\lambda^{1/2}_{ff'})$. The function $B_{ff'}$ is given in Ref. [135]. When we apply the OS QCD corrections, quark pole masses are used in the LO parts.

8.1.3 Decay rates of $H^\pm \to W^\pm\phi$

We describe the one-loop corrected decay rates for the charged Higgs boson decay into the $W^\pm$ bosons and scalar bosons $H^\pm \to W^\pm\phi$ ($\phi = h, H, A$), with NLO EW corrections. They can be expressed by [119, 208–210]

$$\Gamma(H^\pm \to W^\pm\phi) = \Gamma(H^\pm \to W^\pm\phi)^{\rm LO}(1+\Delta^{\rm EW}_\phi) + \Gamma(H^\pm \to W^\pm\phi\gamma). \tag{8.32}$$

The LO decay rate $\Gamma(H^\pm \to W^\pm\phi)^{\rm LO}$ is written by

$$\Gamma(H^\pm \to W^\pm\phi)^{\rm LO} = \frac{m^3_{H^\pm}}{16\pi m^2_W}\lambda\left(\mu_\phi,\mu_W\right)^{\frac{3}{2}}|g_{\phi H^\pm W^\mp}|^2, \tag{8.33}$$

with $\mu_\phi = m^2_\phi/m^2_{H^\pm}$ and $\mu_W = m^2_W/m^2_{H^\pm}$. The NLO correction $\Delta^{\rm EW}_\phi$ is expressed by

$$\Delta^{\rm EW}_\phi = \frac{2{\rm Re}\left(\Gamma^{\rm tree}_{H^\pm W^\mp\phi}\Gamma^{\rm loop*}_{H^\pm W^\mp\phi}\right)}{\left|\Gamma^{\rm tree}_{H^\pm W^\mp\phi}\right|^2} - 2\frac{g_{\phi G^\pm W^\mp}}{g_{\phi H^\pm W^\mp}}\frac{{\rm Re}\hat{\Pi}_{H^+G^-}(m^2_{H^\pm})}{m^2_{H^\pm}} - \Delta r - {\rm Re}\hat{\Pi}'_{WW}(m_W), \tag{8.34}$$

where the tree-level couplings with the charged NG bosons are given by

$$g_{hG^\pm W^\mp} = \mp i\frac{m_W}{v}s_{\beta-\alpha}, \quad g_{HG^\pm W^\mp} = \mp i\frac{m_W}{v}c_{\beta-\alpha}, \quad g_{AG^\pm W^\mp} = 0. \tag{8.35}$$

The term $\hat{\Pi}'_{WW}(m^2_W)$ arises because we do not impose that the residue of renormalized $W^\pm$ bosons propagator is unity.

8.1.4 Decay rates of $H^\pm \to W^\pm V$

We present the loop induced decay rates for charged Higgs boson, $H^\pm \to W^\pm Z$ and $H^\pm \to W^\pm\gamma$. Using the form factors in Eq. (8.18), the decay rate for $H^\pm \to W^\pm Z$ are expressed as [144, 145]

$$\Gamma(H^\pm \to W^\pm Z) = \frac{1}{16\pi m_{H^\pm}}\lambda^{\frac{1}{2}}\left(\mu_W,\mu_Z\right)\left(|\mathcal{M}_{TT}|^2 + |\mathcal{M}_{LL}|^2\right), \tag{8.36}$$

$$|\mathcal{M}_{TT}|^2 = 2|\Gamma^1_{H^\pm ZW^\mp}|^2 + \frac{m^4_{H^\pm}}{2}\lambda\left(\mu_W,\mu_Z\right)|\Gamma^3_{H^\pm ZW^\mp}|^2, \tag{8.37}$$

$$|\mathcal{M}_{LL}|^2 = \frac{m^4_{H^\pm}}{4m^2_W m^2_Z}\left|\left(1-\mu_W-\mu_Z\right)\Gamma^1_{H^\pm ZW^\mp} + \frac{m^2_{H^\pm}}{2}\lambda\left(\mu_W,\mu_Z\right)\Gamma^2_{H^\pm ZW^\mp}\right|^2, \tag{8.38}$$

where $\mu_W = m_W^2/m_{H^\pm}^2$ and $\mu_Z = m_Z^2/m_{H^\pm}^2$. For $H^\pm \to W^\pm\gamma$, using the Ward identity, $\Gamma^1_{H^\pm\gamma W^\mp} = -p_1 \cdot p_2 \Gamma^2_{H^\pm\gamma W^\mp}$, one can obtain

$$\Gamma(H^\pm \to W^\pm\gamma) = \frac{m_{H^\pm}^3}{32\pi}\left(1 - \frac{m_W^2}{m_{H^\pm}^2}\right)^3 \left(|\Gamma^2_{H^\pm\gamma W^\mp}|^2 + |\Gamma^3_{H^\pm\gamma W^\mp}|^2\right). \tag{8.39}$$

Since there is no contribution from the longitudinal part in the process, this formula only involves the transverse part of gauge bosons in the final states.

8.2 Theoretical behaviors of charged Higgs boson decays with NLO corrections

8.2.1 Impact of NLO EW corrections to the decay rates

In this section, we examine the impact of NLO EW corrections on the decay rates of the charged Higgs boson in Type-I and Type-II. We here omit to show the results for Type-X and Type-Y, because they are very similar to those of Type-I or Type-II. In the next subsection and next section, we compare the results for all types of the Yukawa interactions. We use the following quantities to describe the magnitudes of NLO EW corrections,

$$\Delta_{\rm EW}(H^+ \to XY) = \frac{\Gamma^{\rm NLO\ EW}(H^+ \to XY)}{\Gamma^{\rm LO}(H^+ \to XY)} - 1, \tag{8.40}$$

where $\Gamma^{\rm NLO\ EW}(H^+ \to XY)$ corresponds to the decay rates without QCD corrections. For the calculation of decay rates at LO $\Gamma^{\rm LO}$, we employ the quark running masses not the pole masses. We evaluate this quantity in both the alignment scenario, $s_{\beta-\alpha} = 1$, and a nearly alignment scenario, $s_{\beta-\alpha} = 0.99$. For each scenario, $\tan\beta$ is taken to be the following three values, $\tan\beta = 1, 5$, and 10. The dimensionful parameter M is scanned in the region of $0 < M < 1500$ GeV. In this analysis, we impose the theoretical constraints discussed in Sec. **??**, i.e., the perturbative unitarity and the vacuum stability. On the other hand, we here do not take into account the constraint from the flavor physics in order to compare the difference of $\Delta_{\rm EW}$ among all the types, while the mass of charged Higgs boson is strictly constrained by $B_s \to X_s\gamma$, especially for Type-II and Type-X. All results with the constraints including the flavor experiments are presented in the next section.

In Fig. 8.4, we show the EW corrections to various charged Higgs boson decays as a function of degenerated mass of the additional Higgs bosons, $m_\Phi \equiv m_{H^\pm} = m_H = m_A$ in the alignment limit, $s_{\beta-\alpha} = 1$ with the different values of $\tan\beta$, $\tan\beta = 1$ (red), 3 (blue), and 10 (green). The solid (dashed) lines correspond to the results with a maximum (minimum) value of M satisfying the theoretical constraints, $M_{\rm max}$ ($M_{\rm min}$). In this case, charged Higgs decays into a pair of fermions are dominant. For the results of $H^+ \to t\bar{b}$ with $\tan\beta = 1$, one can see that there are kinks at $m_\Phi \simeq m_t + m_b$, $2m_t$ and 600 GeV. The first one comes from the threshold of the (t, b) loop diagram in the H^+-H^- self-energy. The second one comes from the threshold of the top loop diagram in the A-G^0 mixing self-energy, which appears in the counterterms for the H^+ff' vertex. The third kink corresponds to the points where the values of M change from zero to non-zero due to the perturbative unitarity. At this point, the scalar couplings $\lambda_{H^+H^-\phi}$ ($\phi = h, H, A$) are maximized under the constraint from the perturbative unitarity. Non-decoupling effects of h, H and A loops in the H^+-H^- self-energy are then dominant, and $\Delta_{\rm EW}(H^\pm \to t\bar{b})$ can be almost 10% for all the types of 2HDMs. On the other hand, even if m_Φ

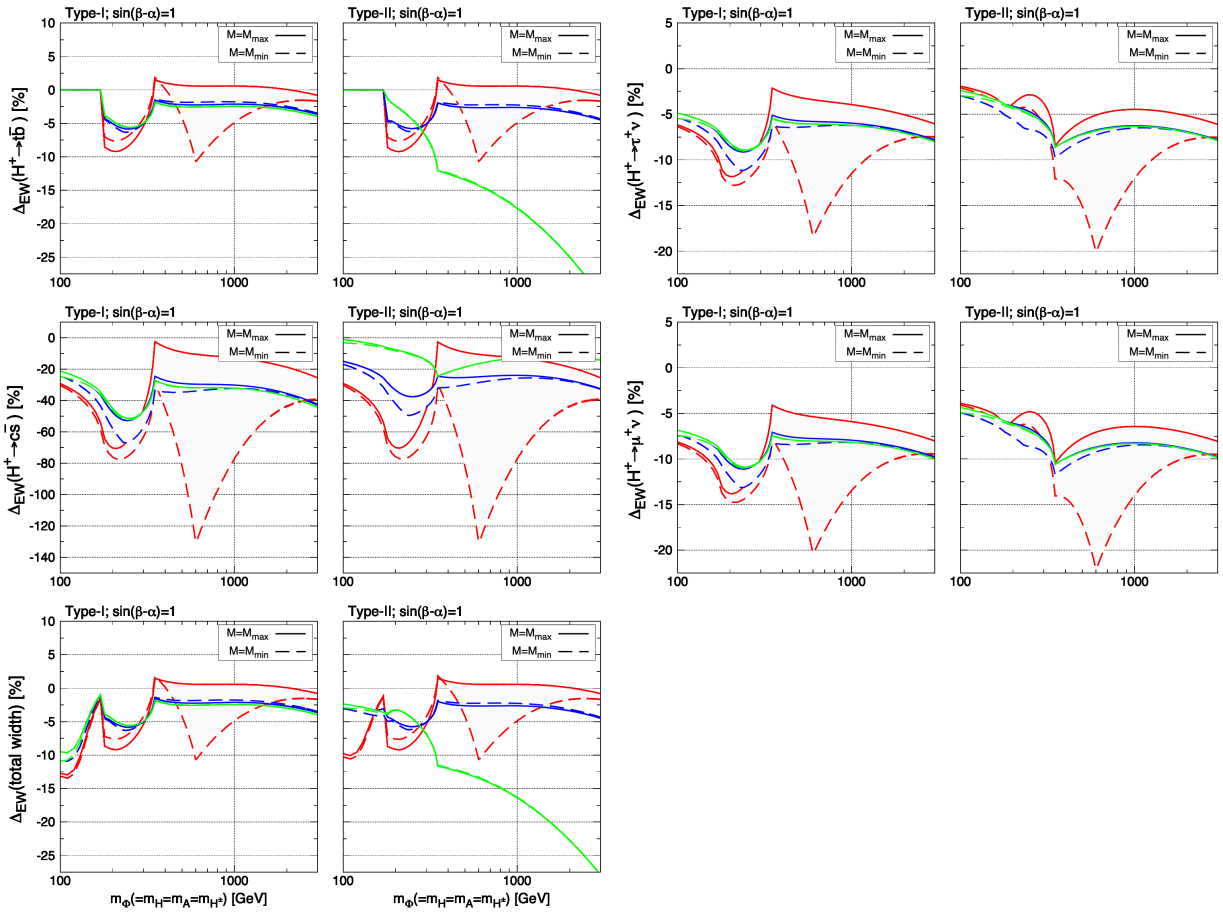

Figure 8.4: Magnitudes of NLO corrections to the decay widths for charged Higgs bosons in the alignment limit $s_{\beta-\alpha} = 1$ with $\tan\beta = 1$ (red), 3 (blue), 10 (green). We consider masses of additional Higgs bosons are degenerate, $m_\Phi \equiv m_{H^\pm} = m_A = m_H$. The dimensionful parameter $M_{\rm max}$ ($M_{\rm min}$) is the maximum (minimum) value of M under the theoretical constraints.

is sufficiently large, the EW corrections do not decouple. Namely, the decoupling theorem [34] is not applicable in this case, and non-decoupling effects are significant.

For the results with $\tan\beta = 3$, and 10, the possible values of M are almost constants due to the strict theoretical constraints, i.e. $M \sim m_\Phi$. While for Type-I, one do not see large difference between $\tan\beta = 3$, and $\tan\beta = 10$, for Type-II, the corrections can be sizable in the case of $\tan\beta = 10$, e.g., $\Delta_{\rm EW}(H^+ \to t\bar{b}) \simeq -25$ % at $m_\Phi = 2$ TeV. We find that these behaviors can be explained by large negative contributions from the tensor form factors $\Gamma^T_{H^+ff'}$ and $\Gamma^{TP}_{H^+ff'}$, which give the contributions proportional to the square of the charged Higgs boson mass in the decay rate (see Eqs. (8.26) and (8.27)).

For other decay modes, one can see the similar behaviors described above. On the other hand, the remarkable thing is that the correction $\Delta_{\rm EW}(H^+ \to c\bar{s})$ can be over -100% at $m_\Phi = 600$GeV. We note that $\Delta_{\rm EW}(H^+ \to c\bar{s})$ tends to be larger than the other decay modes for the following reason. The decay rate with NLO EW corrections $\Gamma(H^+ \to c\bar{s})$ is evaluated by using the pole masses for the charm quark and the strange quark while the LO decay rates are evaluated with the running masses at the scale of $\mu = m_{H^\pm}$. Consequently, the difference between the pole masses and the running masses enhances $\Delta_{\rm EW}(H^+ \to c\bar{s})$ [1].

[1]For instance, the ratios of the running masses and pole masses are estimated as $m_c/\bar{m}_c(m_{H^\pm}) =$

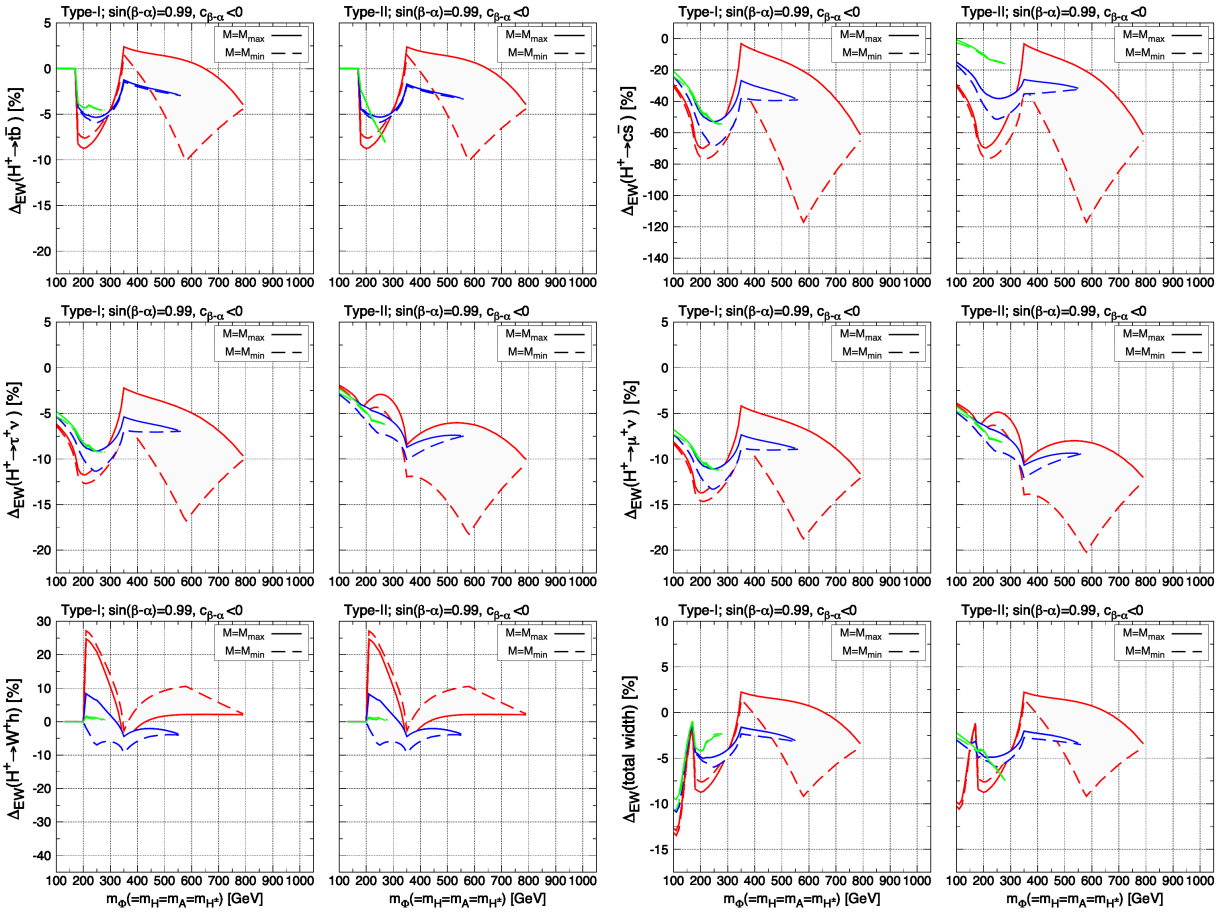

Figure 8.5: Magnitudes of NLO corrections to the decay widths for charged Higgs bosons in the case of $s_{\beta-\alpha} = 0.99$ with $c_{\beta-\alpha} < 0$. The masses of the additional Higgs bosons are degenerate, $m_\Phi \equiv m_{H^\pm} = m_A = m_H$. The dimensionful parameter $M_{\rm max}$ ($M_{\rm min}$) is the maximum (minimum) value of M under the theoretical constraints.

In Fig. 8.5, the results in the nearly alignment scenario, $s_{\beta-\alpha} = 0.99$ with $c_{\beta-\alpha} < 0$, are shown as a function of the degenerate mass m_Φ. In the non-alignment case, an upper bound of m_Φ is given for each value of $\tan\beta$ because of the theoretical constraints. However, the maximum magnitudes of NLO EW corrections for the case of $\tan\beta = 1$ are almost unchanged from the scenario of the alignment limit. Apart from that, the charged Higgs bosons can decay into W^+h in the nearly alignment scenario. For this decay mode, peaks appear at $m_{H^\pm} \simeq m_h + m_W$, which correspond to the thresholds of 1PI diagrams in the H^+W^-h vertex function such as $(W, H^\pm/G^\pm, h)$ and the $(h, h/H, W)$ loop diagrams. The maximum value of the corrections is 26% in the case of $\tan\beta = 1$ for all the types of 2HDMs.

In the Fig. 8.6, we also show the results with $s_{\beta-\alpha} = 0.99$ and $c_{\beta-\alpha} > 0$. The remarkable difference from the results with $c_{\beta-\alpha} < 0$ is that the allowed regions for $\tan\beta = 10$ are broader than those for $\tan\beta = 3$. Hence, compared with $c_{\beta-\alpha} < 0$, the corrections $\Delta_{\rm EW}$ for $\tan\beta = 10$ can be larger. In addition, for $H^+ \to W^+h$, direction of the threshold peak at $m_\phi \simeq m_h + m_W$ is opposite from $c_{\beta-\alpha} < 0$ because the contributions from the H^+W^-h vertex function depends

1.67 GeV/0.609 GeV = 2.74, $m_s/\bar{m}_s(m_{H^\pm})$ = 0.1 GeV/0.0491 GeV = 2.03. Magnitude of $\Delta_{\rm EW}(H^+ \to c\bar{s})$ is enlarged by these factors. The discussion does not depend on $s_{\beta-\alpha}$, so that the same holds in Fig. 8.5 and 8.6. Namely $\Delta_{\rm EW}(H^+ \to c\bar{s})$ can also be over -100% in case of $s_{\beta-\alpha} = 0.99$.

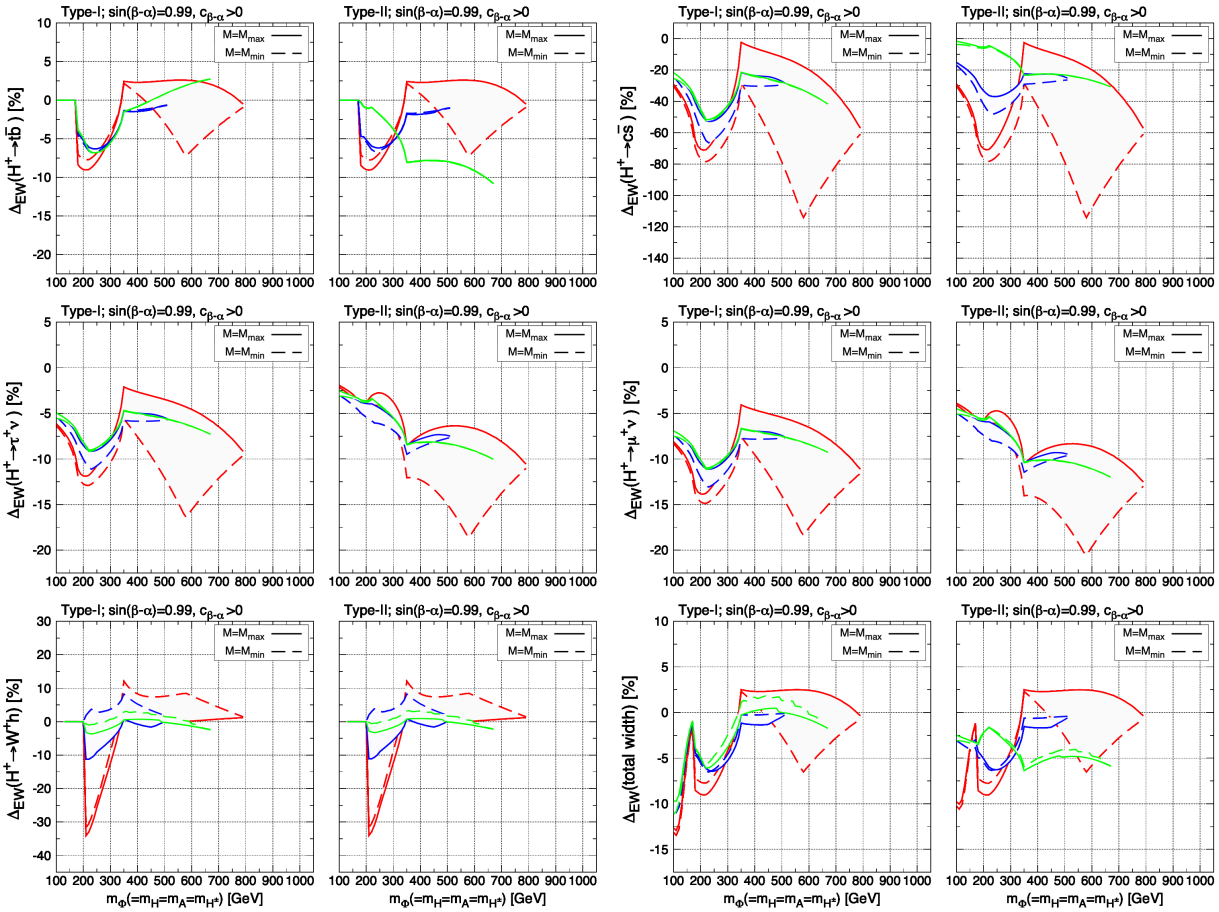

Figure 8.6: Magnitudes of NLO corrections to the decay widths for charged Higgs bosons in the case of $s_{\beta-\alpha} = 0.99$ with $c_{\beta-\alpha} > 0$. The masses of the additional Higgs bosons are degenerate, $m_\Phi \equiv m_{H^\pm} = m_A = m_H$. The dimensionful parameter $M_{\rm max}$ ($M_{\rm min}$) is the maximum (minimum) value of M under the theoretical constraints.

on the tree-level coupling $g_{hH^+W^-}$ (see Eq. (8.34)). On the other hand, one can see that the sign of $\Delta_{\rm EW}(H^+ \to W^+h)$ in the region $m_\Phi \gtrsim 500$ with $\tan\beta = 1$ are positive in the both cases of $c_{\beta-\alpha} < 0$ and $c_{\beta-\alpha} > 0$. The dominant contributions in this region mainly come from non-decoupling effects of additional Higgs bosons, i.e., pure scalar loop diagrams in δC_h and δC_{H^+}, which are proportional to the square of the scalar couplings $\lambda_{\phi_i\phi_j\phi_k}\lambda_{\phi_{i'}\phi_{j'}\phi_{k'}}$. Among them, there are contributions that are not proportional to $c_{\beta-\alpha}$, so that they do not depend on the sign of $c_{\beta-\alpha}$.

8.2.2 Branching ratios

In this subsection, we describe behaviors of the branching ratios with the NLO EW corrections as well as the QCD corrections. Similar to the previous section, we evaluate them in both the alignment scenario and the nearly alignment scenario under the theoretical constraints and the S, T parameters. We here consider the following three cases with a different mass spectrum of the additional Higgs bosons:

Case 1: A relatively small mass of $H^\pm$, $m_{H^\pm} = 160$ GeV, and degenerate masses of H and A with $H^\pm$, $m_H = m_A = m_{H^\pm}$. In this case, the on-shell decay $H^+ \to t\bar{b}$ does not open.

Case 2: A relatively large mass of $H^\pm$, $m_{H^\pm} = 600$ GeV, and degenerate masses of H and A with $H^\pm$, $m_H = m_A = m_{H^\pm}$.

Case 3: A relatively large mass of $H^\pm$, $m_{H^\pm} = 600$ GeV, degenerate masses of A with $H^\pm$, $m_A = m_{H^\pm}$, and lighter mass of H, $m_H = 300$ GeV. In this case, the on-shell decay $H^\pm \to W^+H$ is kinematically allowed.

Whereas masses of the additional Higgs bosons are fixed for each case, M and $\tan\beta$ are commonly scanned in the following regions of $0 < M < 1500$ GeV and $0.5 < \tan\beta < 50$. Taking into account the flavor constraints for Type-II and Type-Y, the mass of charged Higgs boson in each case would be too light. However, we dare to show the results for not only Type-I and Type-X but also Type-II and Type-Y for the comparison. For Case 2 and Case 3, we checked that behaviors of the charged Higgs bosons are similar if we change the mass of charged Higgs boson from $m_{H^\pm} = 600$ GeV to $m_{H^\pm} = 800$ GeV.

In Fig. 8.7, we show the results in Case 1 for the alignment scenario, $s_{\beta-\alpha} = 1$, and the nearly alignment scenarios, $s_{\beta-\alpha} = 0.99$ with $c_{\beta-\alpha} < 0$ and $c_{\beta-\alpha} > 0$ from top panels to bottom panels. For the results of Type-I in $s_{\beta-\alpha} = 1$, all decay modes into quarks and leptons are proportional to $1/\tan^2\beta$. Hence, except for $H^+ \to \gamma W^+$, the branching ratios are almost constants without depending on $\tan\beta$. As the results, the decay $H^+ \to t^*\bar{b}$ dominates in the whole region of $\tan\beta$. On the other hand, one can see that the branching ratio of $H^+ \to \gamma W^+$ can be much varied by the scale of M. This is due to contributions from the $(H, H^\pm, H^\pm)$ diagrams in the form factor $\Gamma^2_{H^+\gamma W}$. We note that another pure scalar loop diagram disappears in the alignment limit. In the case of M=$M_{\rm min}$ (black dashed line) and $\tan\beta \gg 1$, the relevant scalar coupling for this diagram, $\lambda_{H^+H^-H}$ can be sizable. Hence, the decay $H^+ \to \gamma W^+$ is enhanced. For the results of Type-II and Type-X, the main decay mode becomes $H^+ \to \tau^+\nu$ in the large $\tan\beta$ regions, since the tau Yukawa coupling is enhanced.

For the results of the nearly alignment scenario $s_{\beta-\alpha} = 0.99$, behaviors of the charged Higgs boson decays are similar to those of the alignment scenario, while the value of the $\tan\beta$ is bounded at $\tan\beta \simeq 10$ because of the theoretical constraints. In these scenarios, the decay into $H^+ \to W^+h$ opens. The branching ratio can exceed 3% when $\tan\beta = 10$ in Type-I.

In Fig. 8.8, we show the results in Case 2 for the alignment scenario and the nearly alignment scenario from the top panels to the bottom panels. Here we take the value of $s_{\beta-\alpha}$ in the nearly alignment scenario as $s_{\beta-\alpha} = 0.995$ in light of the severe theoretical constraints. In the bottom panels, the violet regions correspond to the ones excluded by the theoretical constraints. In Case 2, the on-shell decay into $t\bar{b}$ opens and it is the dominant decay mode in the alignment scenario expect for Type-X. However, the situation can be changed in the nearly alignment scenario with $c_{\beta-\alpha} > 0$. Namely, the additional decay mode $H^+ \to W^+h$ can overcome $H^+ \to t\bar{b}$ in Type- I and Type-X. Another remarkable behavior for Case 2 is that the EW corrections to the decay into $c\bar{s}$ can be considerably large at $\tan\beta \simeq 1$ because of the non-decoupling effects of the additional Higgs bosons as already seen in Fig. 8.4, while the magnitudes of the branching ratios are below 10^{-4}.

In Fig 8.9, the results of Case 3 are shown in the scenarios of $s_{\beta-\alpha} = 1$ and $s_{\beta-\alpha} = 0.995$. The feature of these scenarios is that the decay into W^+H opens. The decay rate can be significant since it is proportional to the cube of $m_{H^\pm}$. In addition, the corresponding tree-level coupling is proportional to $s_{\beta-\alpha}$, so that this decay mode appears even in the alignment scenario. Remarkably, if $\tan\beta \gtrsim 1$, the decay into $H^+ \to W^+H$ dominates the branching ratios in both the alignment and nearly alignment scenarios for all the types of 2HDMs.

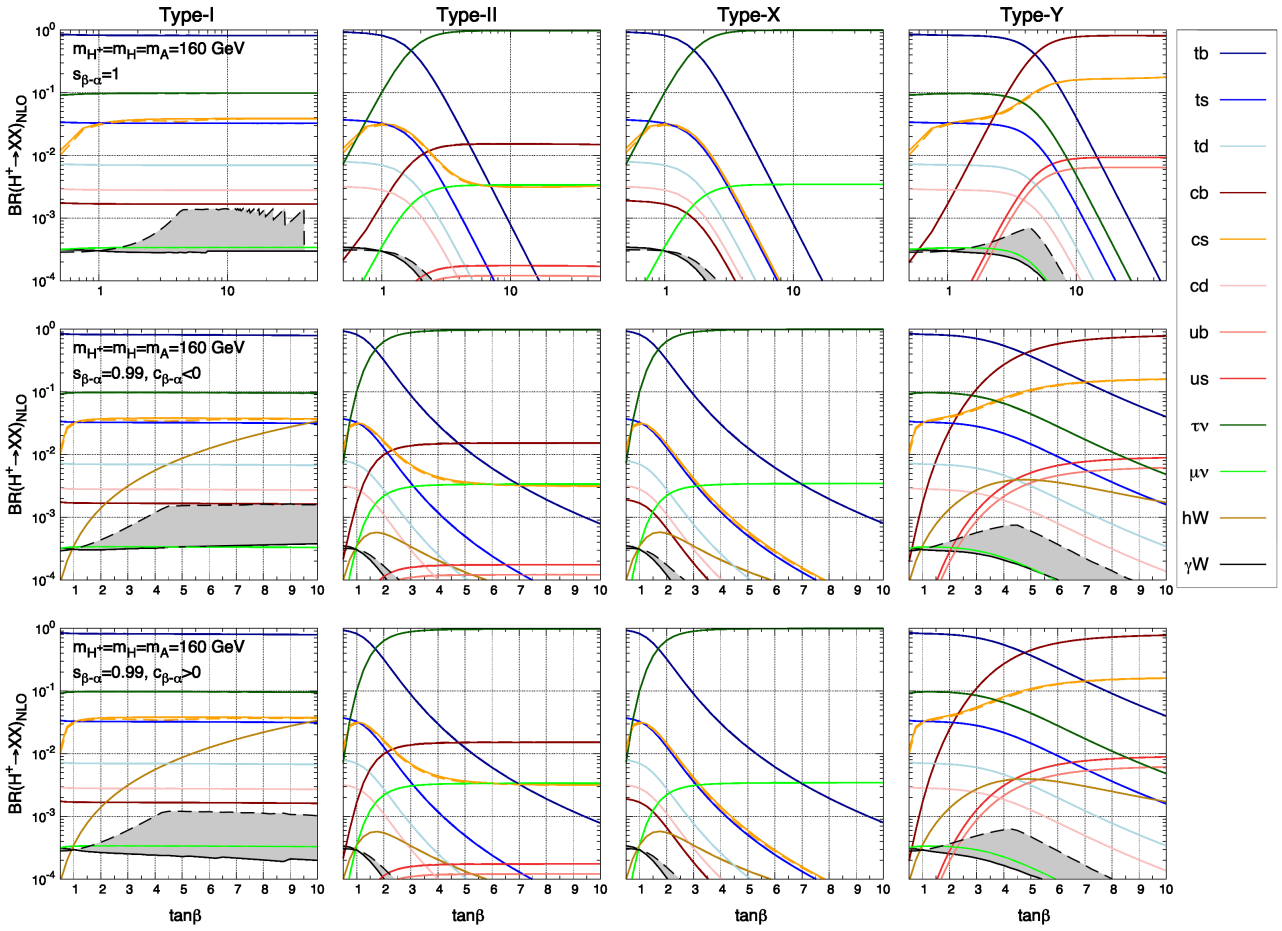

Figure 8.7: Decay branching ratios for charged Higgs bosons as a function of $\tan\beta$ in the alignment limit $s_{\beta-\alpha} = 1$ (top panels) and in the nearly alignment scenarios $s_{\beta-\alpha} = 0.99$ with $c_{\beta-\alpha} < 0$ (middle panels) and $c_{\beta-\alpha} > 0$ (bottom panels), where the NLO EW and NNLO QCD corrections are included if they are applicable. Masses of the charged Higgs boson as well as the neutral Higgs bosons are taken to be degenerate, i.e., $m_{H^\pm} = m_H = m_A = 160$GeV. Each decay mode is specified by color as given in the legend. Solid (dashed) lines correspond to the results with $M = M_{\rm max}$ ($M_{\rm min}$). The dimensionful parameter $M_{\rm max}$ ($M_{\rm min}$) is the maximum (minimum) value of M under the theoretical constraints. The gray region shows predictions on $\mathrm{BR}(H^+ \to W^+\gamma)$ in the region $M_{\rm min} < M < M_{\rm max}$.

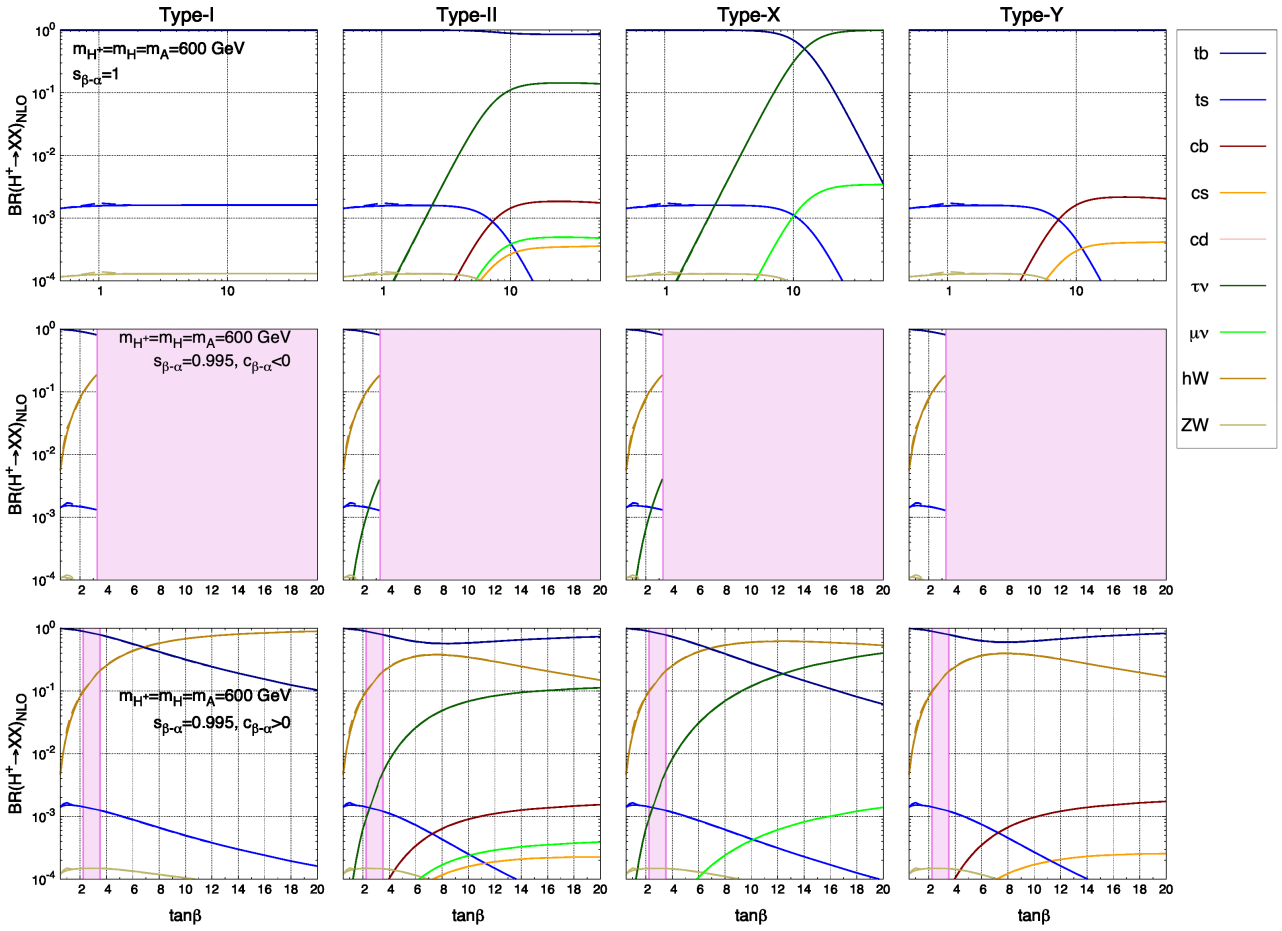

Figure 8.8: Decay branching ratios for charged Higgs bosons as a function of $\tan\beta$ in the alignment limit $s_{\beta-\alpha}=1$ (top panels) and in the nearly alignment scenarios $s_{\beta-\alpha}=0.995$ with $c_{\beta-\alpha}<0$ (middle panels) and $c_{\beta-\alpha}>0$ (bottom panels), where the NLO EW and the NNLO QCD corrections are included if they are applicable. The masses of the charged Higgs boson as well as the neutral Higgs bosons are taken to be degenerate, i.e., $m_{H^\pm}=m_H=m_A=600$GeV. Each decay mode is specified by color as given in the legend. Solid (dashed) lines correspond to the results with $M=M_{\rm Max}$ ($M_{\rm min}$). The dimensionful parameter $M_{\rm max}$ ($M_{\rm min}$) is the maximum (minimum) value of M under the theoretical constraints. The violet region corresponds to the one excluded by the theoretical constraints.

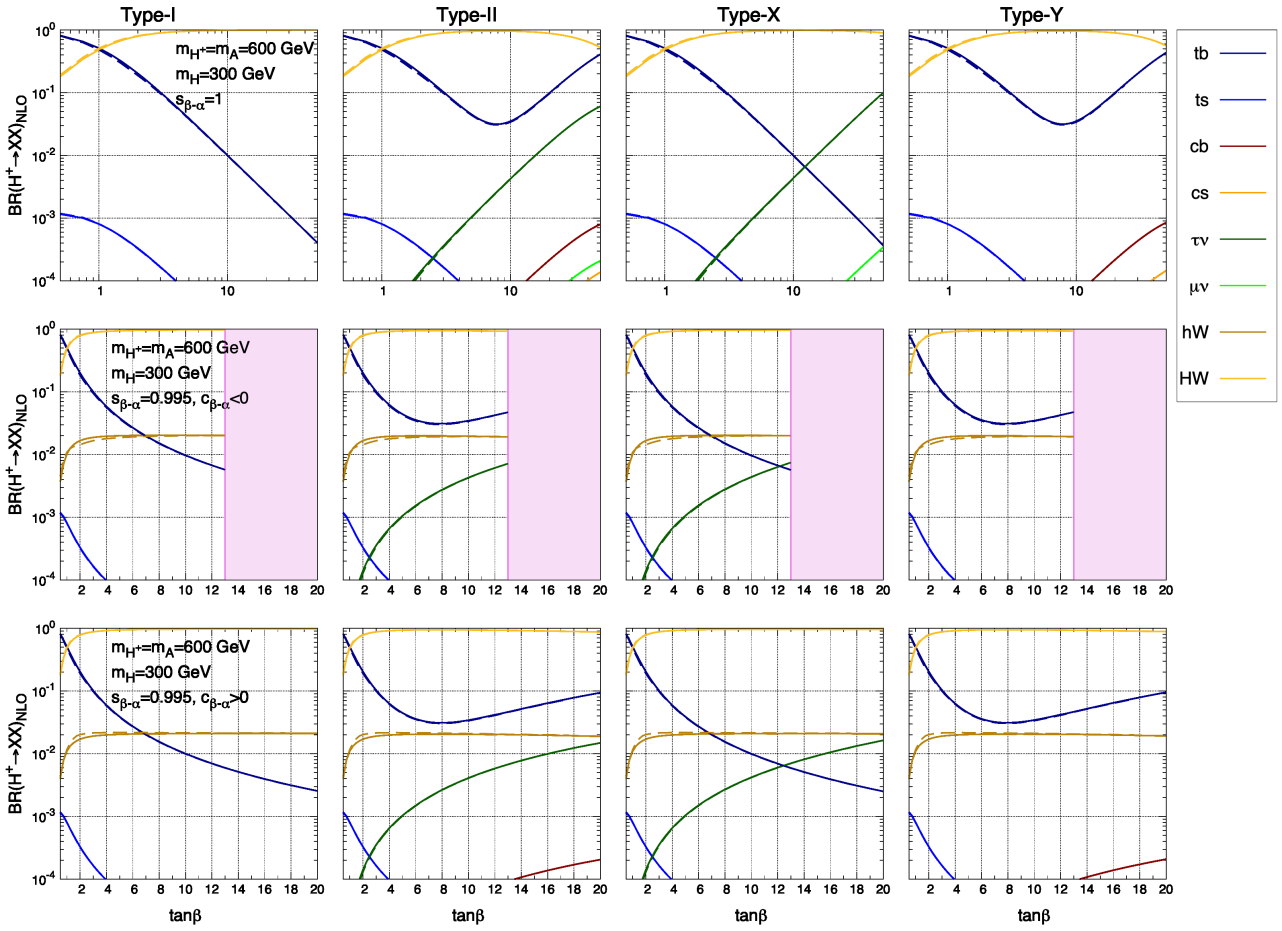

Figure 8.9: Decay branching ratios for charged Higgs bosons as a function of $\tan\beta$ in the alignment limit $s_{\beta-\alpha}=1$ (top panels) and in the nearly alignment scenarios $s_{\beta-\alpha}=0.995$ with $c_{\beta-\alpha}<0$ (middle panels) and $c_{\beta-\alpha}>0$ (bottom panels), where the NLO EW and the NNLO QCD corrections are included if they are applicable. The masses of the charged Higgs boson and the neutral Higgs bosons are taken to be degenerate, i.e., $m_{H^\pm}=m_H=m_A=600$ GeV and $m_H=300$ GeV. Each decay mode is specified by color as given in the legend. Solid (dashed) lines correspond to the results with $M=M_{\rm Max}$ ($M_{\rm min}$). The dimensionful parameter $M_{\rm max}$ ($M_{\rm min}$) is the maximum (minimum) value of M under the theoretical constraints. The violet region corresponds to the one excluded by the theoretical constraints.

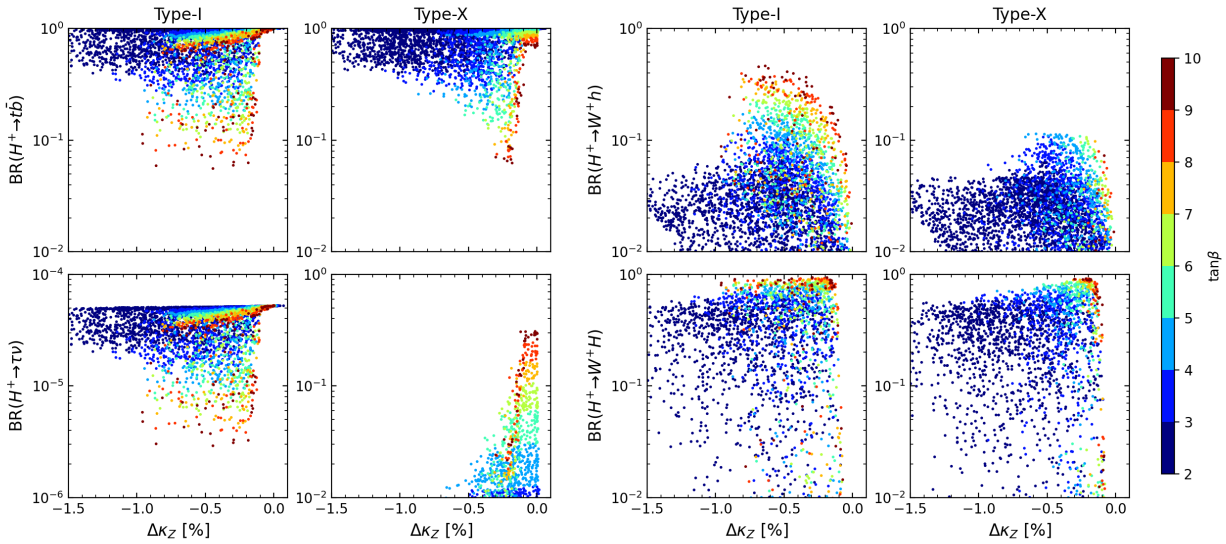

Figure 8.10: Decay branching ratios for the charged Higgs bosons as a function of $\Delta\kappa_Z (\equiv \kappa_Z - 1)$ in Scenario A, where colored points denote different values of $\tan\beta$. Predictions on Type-I (Type-X) are shown in the first and third columns (the second and fourth columns).

8.3 Phenomenological impact of the charged Higgs boson decays

8.3.1 Decay pattern of the charged Higgs bosons in the nearly alignment regions

In this subsection, we discuss whether or not four types of 2HDMs can be discriminated by looking at decay patterns of the charged Higgs bosons, and also whether or not information of the inner parameters can be extracted. As already studied, the discrimination of 2HDMs can be accomplished by patterns of the deviations from the SM predictions for the couplings [100, 110, 112] and/or the branching ratios [97, 98] of the discovered Higgs boson if the deviations are actually found in the future collider experiments. In particular, four types of 2HDMs can be clearly separated by a correlation of the hbb coupling and the $h\tau\tau$ coupling [100, 110, 112]. However, current experimental data from the LHC Run II favor the alignment regions, and such a desired situation would not be necessarily realized in the future. Hence, it would be worth investigating the impacts of discovery of the charged Higgs bosons for a test of 2HDMs especially in the case that the significant deviations in the h couplings are not detected in the future collider experiments.

To this end, we consider two distinct scenarios for the mass of the charged Higgs boson,

$$\text{(Scenario A)}: \quad m_{H^\pm} = 400 \text{ GeV} \tag{8.41}$$

$$\text{(Scenario B)}: \quad m_{H^\pm} = 1000 \text{ GeV}, \tag{8.42}$$

For Scenario A, Type II and Y are already excluded by the flavor constraint (see, e.g, Ref. [65]), so that we compare the difference of the branching ratios between Type-I and Type-X. For Scenario B, all the types of 2HDMs are not excluded by the flavor constraints. In order to avoid constraint from the T parameter, we set the mass of the CP-odd Higgs boson as $m_A = m_{H^\pm}$. Whereas, the mass of the heavier CP-even Higgs boson is taken in the following range for each

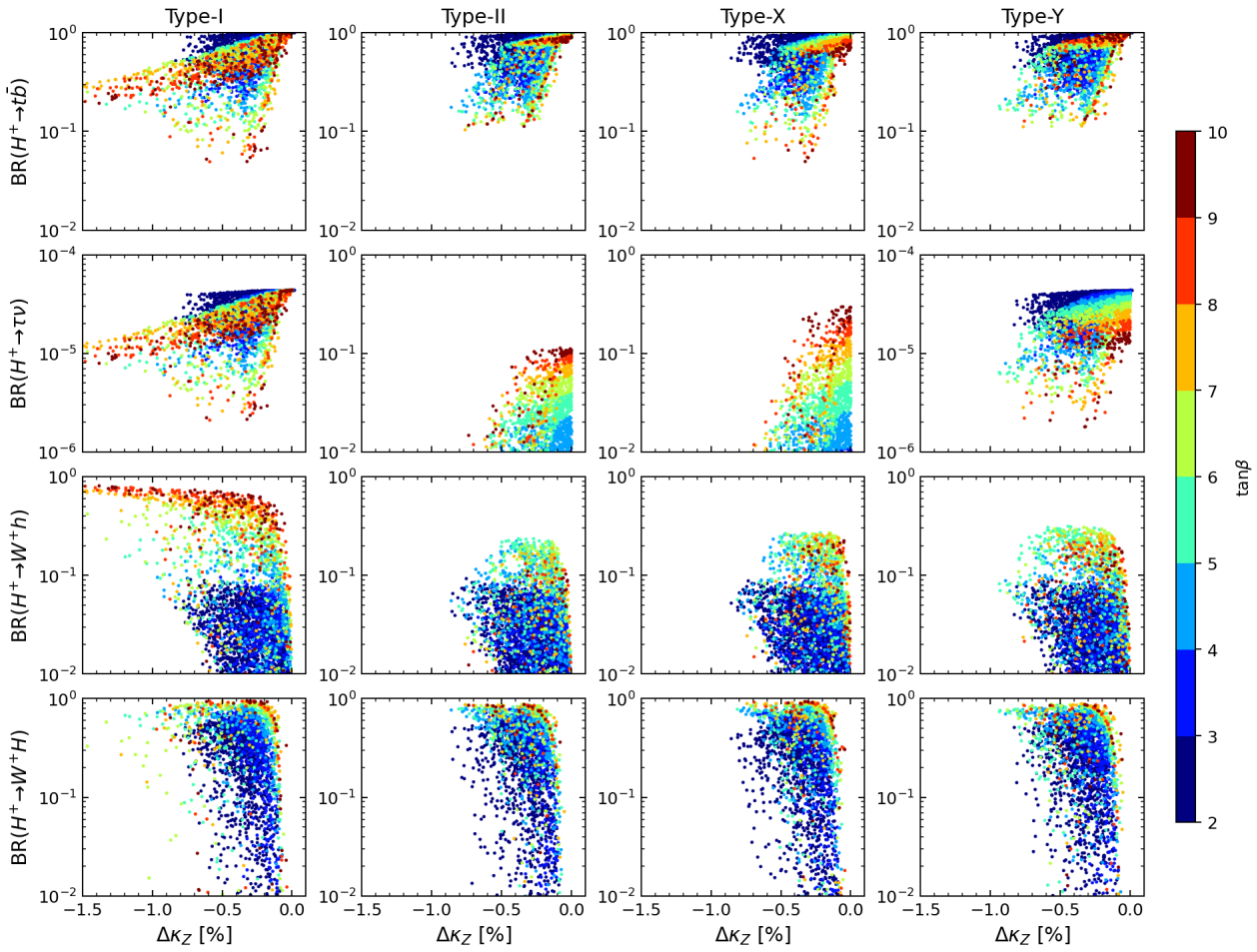

Figure 8.11: Decay branching ratios for the charged Higgs bosons as a function of $\Delta\kappa_Z(\equiv \kappa_Z - 1)$ in Scenario B, where colored points denote different values of $\tan\beta$. Predictions on Type-I, II, X and Y are shown from the left panels to the right panels.

scenario,

$$250\ \text{GeV} < m_H < 800\ \text{GeV} \qquad \text{for Scenario A,} \tag{8.43}$$

$$800\ \text{GeV} < m_H < 1200\ \text{GeV} \qquad \text{for Scenario B.} \tag{8.44}$$

For the lower bound of Scenario A, we take into account the constraint from the direct search for $H \to ZZ^*$, by which $m_H \lesssim 250$ GeV and $\tan\beta \lesssim 6$ (5) are excluded in the case of $s_{\beta-\alpha} = 0.995$ with $c_{\beta-\alpha} < 0$ for Type-I (X) [42]. The remaining parameters are scanned for both the scenarios as

$$0.995 < s_{\beta-\alpha} < 1, \quad 2 < \tan\beta < 10, \quad 0 < M < m_{H^\pm} + 500\text{GeV}, \tag{8.45}$$

considering both cases of $c_{\beta-\alpha} < 0$ and $c_{\beta-\alpha} > 0$. The lower bound of $\tan\beta$ comes from the consideration of the constraint from $B_d \to \mu\mu$ for Scenario A [65] and $H \to hh$ in the case of $s_{\beta-\alpha} = 0.995$ with $c_{\beta-\alpha} < 0$ for Scenario B [42]. With these scan regions, we impose the theoretical constraints and the S,T parameters in the same way as Sec. 8.2. Furthermore, we exclude parameter points that are not consistent with the current data of the Higgs signal strength at the LHC in Ref. [21]. We calculate the decay rates for h with NLO EW and NNLO QCD corrections by utilizing `H-COUP v2` [46] and evaluate the scaling factors $\kappa_X =$

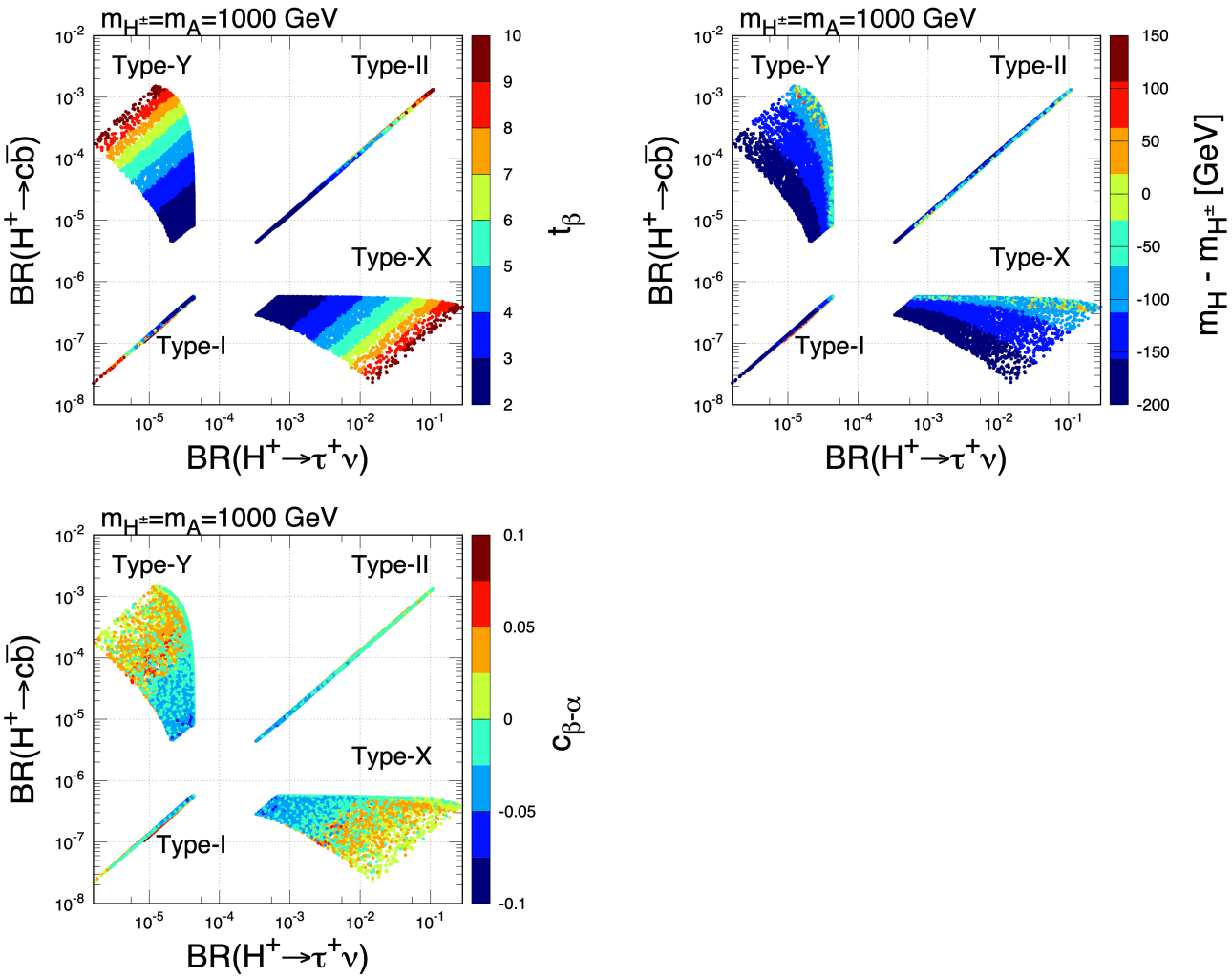

Figure 8.12: Correlation between BR($H^+ \to \tau^+\nu$) and BR($H^+ \to c\bar{b}$) for Scenario B in four types of 2HDMs. Colored dots correspond to different values of $\tan\beta$, $m_H - m_{H^\pm}$, and $c_{\beta-\alpha}$ in the left top panel, the right top panel and the bottom panel, respectively.

$\sqrt{\Gamma^{\rm 2HDM}_{h\to XX}/\Gamma^{\rm SM}_{h\to XX}}$ for each parameter point. We then remove parameter points if the calculated scaling factors deviate from the values presented in Table 11 (a) of Ref. [21] at 95 % CL.

While the alignment limit is defined by $s_{\beta-\alpha} = 1$ at tree level, this might not be valid beyond tree level. At loop levels, the quantum corrections by additional Higgs bosons can give non-zero contributions to Γ_{hVV^*} even in $s_{\beta-\alpha} = 1$. Hence, we use the scaling factor κ_Z and define the alignment limit as $\kappa_Z = 1$ at loop levels. At the ILC 250, expected 1σ ($2\ \sigma$) accuracies of κ_Z is 0.38% (0.76%) [36]. Thus, we mainly discuss the behavior of the branching ratios of H^+ for each type of 2HDMs within $\Delta\kappa_Z (\equiv \kappa_Z - 1) \lesssim 0.76\%$, assuming situations that the deviations in the h couplings are not found.

In Fig. 8.10, we present the branching ratios at NLO in Type-I (top panels) and Type-X (bottom panels) for Scenario A as a function of $\Delta\kappa_Z$, where the color points denote values of $\tan\beta$. For BR($H^+ \to t\bar{b}$), one can see that the size of the branching ratio can reach almost 100% without depending on $\Delta\kappa_Z$ as well as types of 2HDMs. The reason is that such sizable BR($H^+ \to t\bar{b}$) is realized in the low $\tan\beta$ region, where the top Yukawa coupling in the $H^+\bar{t}b$ vertex dominates for $H^+ \to t\bar{b}$. Thus, the difference between Type-I and Type-X does not appear. For BR($H^+ \to \tau^+\nu$), the prediction of Type-X is obviously larger than that of Type-I

because of the $\tan\beta$ enhancement for the τ Yukawa coupling in the $H^+\bar{\nu}_\tau\tau$ vertex for Type-X. Namely, in Scenario A, Type-X can be identified if $\mathrm{BR}(H^+ \to \tau^+\nu)$ is sizable for the discovered charged Higgs bosons. On the other hand, characteristic predictions of Type-I can be obtained in $H^+ \to W^+h$. The branching ratio $\mathrm{BR}(H^+ \to W^+h)$ in Type-I can exceed 20%, while the prediction of Type-X is maximally around 11%. Hence, a large $\mathrm{BR}(H^+ \to W^+h)$ is a clear signature in identifying Type-I. An intriguing point is that this signature can be mostly realized in the regions of $\Delta\kappa_Z \lesssim 0.76\%$. If the deviation in the hZZ coupling is $\Delta\kappa_Z \lesssim -1\%$, $\mathrm{BR}(H^+ \to W^+h)$ is less than 5% in both Type-I and Type-X. One can also see that these signatures of Type-I and Type-X contain information on the inner parameters of 2HDMs. Sizable values of $\mathrm{BR}(H^+ \to \tau\bar{\nu})$ in Type-X and $\mathrm{BR}(H^+ \to W^+h)$ in Type-I are caused in the large $\tan\beta$ region. Therefore, information on $\tan\beta$ can be extracted once these branching ratios are determined.

In addition, we comment on behavior of the branching ratio for $H^+ \to W^{+(*)}H$. This decay mode kinematically opens when the heavier CP-even Higgs boson is lighter than the charged Higgs bosons. The maximal size of $\mathrm{BR}(H^+ \to W^{+(*)}H)$ can reach almost 90% in both Type-I and Type-X. As can be seen by comparing values of $\tan\beta$ and $\Delta\kappa_Z$, parameter points with huge values of $\mathrm{BR}(H^+ \to W^{+(*)}H)$ correspond to those with suppressed $\mathrm{BR}(H^+ \to t\bar{b})$.

In Fig. 8.11, the branching ratios at NLO in Type-I, II, X and Y for Scenario B are shown as a function of $\Delta\kappa_Z$ from left to right panels. Behavior of the $\mathrm{BR}(H^+ \to t\bar{b})$ are similar to Scenario A, namely, the size of the branching ratio can be huge in the low $\tan\beta$ region for all types of 2HDMs. Behavior of the $\mathrm{BR}(H^+ \to W^+H)$ also does not almost change from Scenario A. In addition, for identification of Type-I and Type-X, one can rely on the processes $H^+ \to W^+h$ and $H^+ \to \tau^+\nu$ as same as Scenario A. In Scenario B, $\mathrm{BR}(H^+ \to W^+h)$ of Type-I can be considerably enhanced unlike other types of 2HDMs. The size of $\mathrm{BR}(H^+ \to \tau^+\nu)$ can reach 30% only in Type-X. An interesting feature of Scenario B is that a sizable $\mathrm{BR}(H^+ \to W^+h)$ is only realized in the case of $c_{\beta-\alpha} > 0$ differently from Scenario A[2]. Hence, not only the size of $\tan\beta$ but also the sign of $c_{\beta-\alpha}$ can be extracted from the size of $\mathrm{BR}(H^+ \to W^+h)$. We note that all points with $\mathrm{BR}(H^+ \to W^+h) > 10\%$ correspond to $c_{\beta-\alpha} > 0$ for all types of 2HDMs.

From the decay modes $H^+ \to t\bar{b}$, $H^+ \to \tau^+\nu$, $H^+ \to W^+h$ and $H^+ \to W^+H$, it would be difficult to separate Type-II and Type-Y. However, this can be performed by looking at the decay process $H^+ \to c\bar{b}$ as shown in Fig. 8.12[3]. For Type-II and Type-Y, $\mathrm{BR}(H^+ \to c\bar{b})$ can be larger than 0.1% and one can distinguish these types from Type-I and Type-X by this decay mode. Furthermore, Type-II and Type-Y can be discriminated from the size of $\mathrm{BR}(H^+ \to \tau^+\nu)$. As seen from the left top panel of the Fig. 8.12, enhancement of $\mathrm{BR}(H^+ \to c\bar{b})$ and/or $\mathrm{BR}(H^+ \to \tau^+\nu)$ is controlled by a value of $\tan\beta$ inType-II, Type-X and Type-Y. From the right top panel of the figure, one can also see that there is a correlation between the branching ratios and the mass difference $m_H - m_{H^\pm}$, in particular for Type-X and Type-Y. The reason for this can be understood as follows. When the mass difference is negatively large, $\mathrm{BR}(H^+ \to W^+H)$ becomes sizable without depending on the types of 2HDMs. This then reduces the size of $\mathrm{BR}(H^+ \to c\bar{b})$ and $\mathrm{BR}(H^+ \to \tau^+\nu)$. We have studied on theoretical possibilities that Type II and Type X are separated from the other types of the 2HDMs by correlation between $\mathrm{BR}(H^+ \to c\bar{b})$ and $\mathrm{BR}(H^+ \to \tau^+\nu)$. The predictions for $\mathrm{BR}(H^+ \to c\bar{b})$ in

[2]The branching ratio $\mathrm{BR}(H^+ \to W^+h)$ can be enhanced in large $\tan\beta$ regions, which does not occur in case of $c_{\beta-\alpha} < 0$ for Scenario B due to the theoretical constraints. The similar behavior can be seen in Figs. 8.8 and 8.9.

[3]For the evaluation of $\Gamma(H^+ \to c\bar{b})$, we only include QCD corrections. The EW corrections to this process are not implemented.

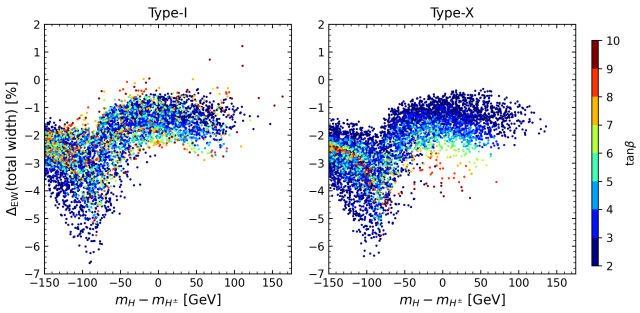

Figure 8.13: The total decay width of the charged Higgs bosons as a function of the mass difference $m_H - m_{H^\pm}$ in Scenario A for Type-I and Type-X. The colored dots correspond to different values of $\tan\beta$.

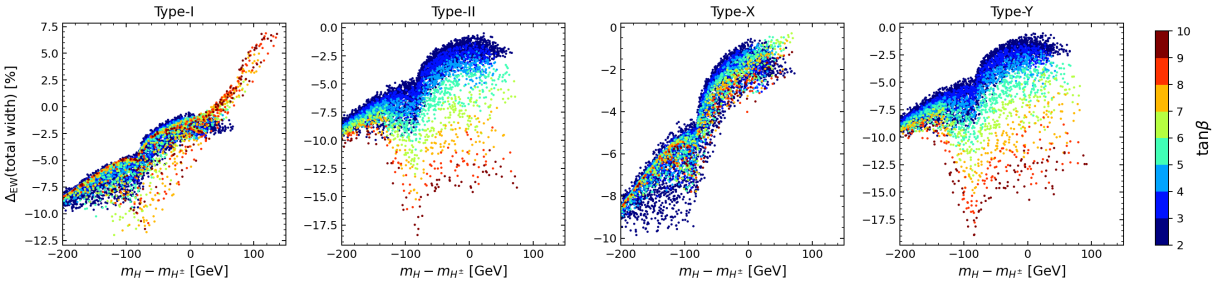

Figure 8.14: The total decay width of the charged Higgs bosons as a function of the mass difference $m_H - m_{H^\pm}$ in Scenario B for Type-I, II, X and Y. The colored dots correspond to different values of $\tan\beta$.

Type II and Type Y, which are maximally 0.1%, are not large. Phenomenological studies on expectation whether such a small branching ratio is measured at future colliders is beyond the scope of this paper.

We give a comment on the results in another case of the degenerated mass of the additional Higgs bosons, i.e., $m_{H^\pm} = m_H$, where the T parameter constraint is satisfied when $s_{\beta-\alpha} \simeq 1$. We have performed the same analysis in this case, and obtained qualitatively similar results for magnitudes of the branching ratios while the allowed parameter regions after imposing the constraints from theoretical bounds and the electroweak oblique parameters are more strict than the case of $m_{H^\pm} = m_A$.

Before we close this subsection, we mention the deviations in the h couplings for Scenario A and for Scenario B. For both the scenarios all types of 2HDMs can be identified by looking at the branching ratios of the charged Higgs bosons even in the case of $\Delta\kappa_Z \lesssim 0.76\%$, where the deviation in the hZZ coupling cannot be detected at the ILC [36]. At the same time, even in this case, the deviations in other h couplings like the Yukawa interactions can be sizable enough to be detected at the ILC 250 GeV [36]. Namely, the deviations $\Delta\kappa_b$ and $\Delta\kappa_\tau$ for Type-II, $\Delta\kappa_\tau$ for Type-X, and $\Delta\kappa_b$ for Type-Y can still deviate significantly enough to be detected at the ILC 250 GeV. Therefore, a combination of the charged Higgs boson decays and the h decays make it possible to identify details of 2HDMs.

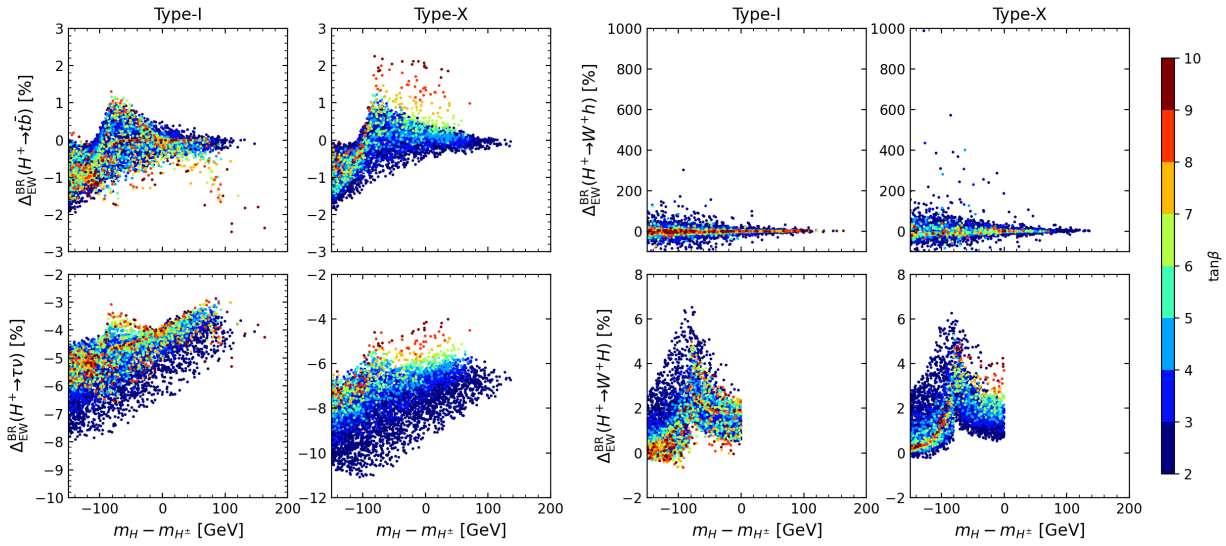

Figure 8.15: Decay branching ratios of the charged Higgs bosons as a function of the mass difference $m_H - m_{H^\pm}$ in Scenario A for Type-I and Type-X. The colored dots correspond to different values of $\tan\beta$.

8.3.2 Impact of one-loop corrections to the branching ratios

We next investigate the impact of NLO EW corrections on the branching ratios of H^+. In particular, we discuss how the size of the corrections changes depending on the mass difference between the charged Higgs bosons and the additional neutral Higgs bosons. Focusing on Scenario A and Scenario B, we consider the case where the masses of CP-odd Higgs boson and that of the charged Higgs bosons are degenerate, $m_A = m_{H^\pm}$. As pointed out in Ref. [211], in this case, the custodial symmetry is restored in the Higgs potential, so that the constraint from the T parameter is satisfied. We then scan m_H in the regions given in Eqs. (8.43) and (8.44). The other parameters are scanned as given in Eq. (9.57) for both scenarios. In the following discussions, we introduce a quantity to describe magnitudes of the NLO EW corrections to the branching ratios, i.e.,

$$\Delta_{\rm EW}^{\rm BR}(H^+ \to XY) = \frac{{\rm BR}^{\rm NLO\ EW}(H^+ \to XY)}{{\rm BR}^{\rm LO}(H^+ \to XY)} - 1, \tag{8.46}$$

where ${\rm BR}^{\rm NLO\ EW}(H^+ \to XY)$ denotes the branching ratios with NLO EW corrections. In the evaluation of the branching ratio at LO ${\rm BR}^{\rm LO}(H^+ \to XY)$, the quark running masses are applied for the decays into quarks. We also describes the NLO EW corrections for the total decay width, which is defined by

$$\Delta_{\rm EW}({\rm total\ width}) = \frac{\Gamma_{H^+}^{\rm NLO\ EW}}{\Gamma_{H^+}^{\rm LO}} - 1, \tag{8.47}$$

with the total decay width for H^+ at NLO EW (LO) being $\Gamma_{H^+}^{\rm NLO\ EW}$ ($\Gamma_{H^+}^{\rm LO}$). By definition, $\Delta_{\rm EW}^{\rm BR}$ can be reduced as $\Delta_{\rm EW}^{\rm BR} + 1 = (\Delta_{\rm EW} - 1)/(\Delta_{\rm EW}({\rm total\ width}) - 1)$. Namely, it is controlled by the correction factor for the total decay width $\Delta_{\rm EW}({\rm total\ width})$ and the one for partial decay width $\Delta_{\rm EW}(H^+ \to XY)$.

In Fig. 8.13, we present the correction factor for the total width in Scenario A as a function of the mass difference for the additional Higgs bosons. The color dots denote the values of

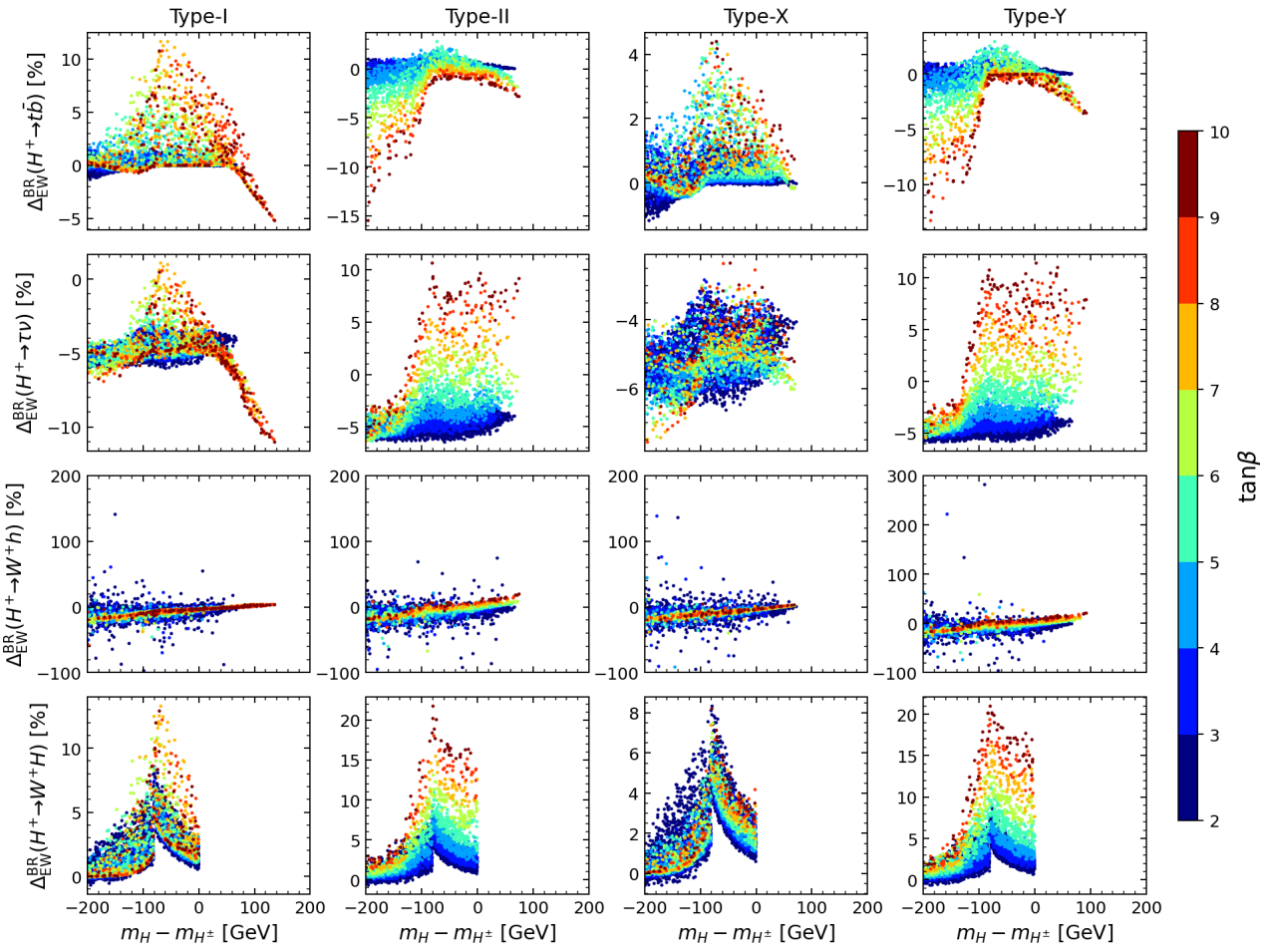

Figure 8.16: Decay branching ratios of the charged Higgs bosons as a function of the mass difference $m_H - m_{H^\pm}$ in Scenario B for Type-I, II, X and Y. The colored dots correspond to different values of $\tan\beta$.

$\tan\beta$. Behavior of the corrections for Type-I (left panel) and the one for Type-X (right panel) is similar with each other in the regions $\tan\beta \lesssim 4$, while these are different in $\tan\beta \gtrsim 6$. When $m_H - m_{H^\pm} \simeq -80$ GeV, there appear thresholds, in which $H^+ \to W^+H$ opens and the correction $\Delta_{\rm EW}$(total width) reaches -7%.

In Fig. 8.14, the results in Scenario B are shown for all types of 2HDMs. Similar to Scenario A, behavior for $\tan\beta \lesssim 4$ does not change match for all the types. Clear difference among the types of 2HDMs arises for $\tan\beta \gtrsim 4$. For Type-I, the allowed region of the mass difference $m_H - m_{H^\pm}$ is wider than the other types of 2HDMs. Consequently, the correction can be positive when $m_H - m_{H^\pm} \gtrsim 30$ GeV. On the other hand, for Type-II and Type-Y, the bulk of points with $\tan\beta \gtrsim 5$ shows large negative corrections, compared with those for $\tan\beta \lesssim 4$. This is because the bottom Yukawa coupling in $H^+\bar{t}b$ vertex is enhanced by large $\tan\beta$. The correction can reach -20 (-25) % when $m_H - m_{H^\pm} \simeq -80$GeV for Type-II (Type-Y) due to the effect of the threshold of the mode $H^+ \to W^+H$. For Type-X, the predictions in the high $\tan\beta$ region almost do not deviate from those in the low $\tan\beta$ region.

We now move on discussions of the correction factor for the branching ratios. In Fig. 8.15, $\Delta_{\rm EW}^{\rm BR}$'s for the decays $H^+ \to t\bar{b}$, $H^+ \to \tau^+\nu$, $H^+ \to W^+h$, $H^+ \to W^+H$ are shown. For $H^+ \to t\bar{b}$, The kink when $m_H - m_{H^\pm} \simeq 80$ GeV appears as with the correction for the total width (see

Fig. 8.13). The correction of the branching ratio distribute in narrow range, -2.75% $(-1.9) \lesssim \Delta^{\rm BR}_{\rm EW}(H^+ \to t\bar{b}) \lesssim +1.25$ $(+2.3)\%$, for Type-I (Type-X). This can be understood as follows. A value of the correction factor for the partial width $\Delta_{\rm EW}(H^+ \to t\bar{b})$ is close to $\Delta_{\rm EW}$(total width) in the bulk of parameter points. Thereby, they are canceled with each other in the definition of $\Delta^{\rm BR}_{\rm EW}$. On the other hand, behavior of $\Delta^{\rm BR}_{\rm EW}(H^+ \to W^+H)$ is different from that of $\Delta^{\rm BR}_{\rm EW}(H^+ \to t\bar{b})$. We note that $\Delta_{\rm EW}(H^+ \to W^+H)$ is relatively small, i.e., $-2.5\% \lesssim \Delta_{\rm EW} \lesssim 0\%$, for both Type-I and Type-X [4], so that $\Delta^{\rm BR}_{\rm EW}(H^+ \to W^+H)$ is dominated by the $\Delta_{\rm EW}$ (total width). In fact, behavior of $\Delta^{\rm BR}_{\rm EW}$ is reversal of $\Delta_{\rm EW}$ (total width).

One can also see that the size of the correction for $H^+ \to W^+h$ can be remarkably large. In the low $\tan\beta$ region, $\Delta^{\rm BR}_{\rm EW}(H^+ \to W^+h)$ can exceed $+100\%$. We note that $c_{\beta-\alpha}$ is close to 0, $|c_{\beta-\alpha}| \lesssim 2.5 \times 10^{-2}$, for all the parameter points with $\Delta^{\rm BR}_{\rm EW}(H^+ \to W^+h) \gtrsim +100\%$. In addition, the one-loop amplitude of $H^+ \to W^+h$ contains terms to be independent of $c_{\beta-\alpha}$. The counterterms δC_h and $\delta C_{H^\pm}$ induce such terms, which can be enhanced by the non-decoupling effect of the additional Higgs bosons in case of $M \sim v$. In this case, the one-loop amplitude can overcome the tree-level amplitude, and gives $\Delta^{\rm BR}_{\rm EW}(H^+ \to W^+h) \gtrsim 100\%$. Furthermore, we found that in some parameter points $\Delta^{\rm BR}_{\rm EW}(H^+ \to W^+h)$ can be smaller than -100%. The origin is considered due to the fact that terms of the squared one-loop amplitude are truncated in the calculation of the NLO corrections. The effect of the squared one-loop amplitude is discussed in the Sec.8.3.3.

In Fig. 8.16, we show the results for the correction factors of the charged Higgs bosons in Scenario B for all types of 2HDMs. For $H^+ \to t\bar{b}$, the same picture described in the results for Scenario A holds for the low $\tan\beta$ region. When $\tan\beta \simeq$ 2-3, the correction factor is close to zero, $-2.5\% \lesssim \Delta^{\rm BR}_{\rm EW}(H^+ \to t\bar{b}) \lesssim +1.5\%$ for all types of 2HDMs. For high $\tan\beta$ values the size of the correction can be much large. In Type-I, $\Delta^{\rm BR}_{\rm EW}(H^+ \to t\bar{b})$ can exceed 12% near the threshold region $m_H - m_{H^\pm} \simeq -80$ GeV, while $\Delta^{\rm BR}_{\rm EW}(H^+ \to t\bar{b})$ can be negative in the case of $m_H - m_{H^\pm} \gtrsim 50$ GeV due the effect of $\Delta_{\rm EW}$(total width). In Type-II and Y, $\Delta^{\rm BR}_{\rm EW}(H^+ \to t\bar{b})$ can be negatively large and can reach -15.5% due to the $\tan\beta$ enhancement of the bottom Yukawa coupling in the $H^+\bar{t}b$ vertex for $\Delta_{\rm EW}(H^+ \to t\bar{b})$, which can be seen in Fig. 8.6. For $H^+ \to \tau^+\nu$, one can see that behavior of $\Delta^{\rm BR}_{\rm EW}$ with the low $\tan\beta$ value is similar without depending on the type of 2HDMs, but the difference can appear in the high $\tan\beta$ region. For $H^+ \to W^+H$, we note that the correction factor for the partial width $\Delta_{\rm EW}(H^+ \to W^+H)$ monotonically decreases as the mass difference $m_H - m_{H^+}$ becomes negatively large, e.g., $\Delta_{\rm EW} \sim -8\%$ (-4%) when $m_H - m_{H^+}$ =200 GeV (100 GeV) for all types of 2HDMs. When the on-shell decay $H^+ \to W^+H$ is kinematically allowed, the correction $\Delta^{\rm BR}_{\rm EW}(H^+ \to W^+H)$ is determined by summation of $\Delta_{\rm EW}$(total width) and $\Delta_{\rm EW}(H^+ \to W^+H)$. The maximum value of the $\Delta^{\rm BR}_{\rm EW}(H^+ \to W^+H)$ is $+13\%$ and $+9\%$ for Type-I and Type-X, respectively, while that of Type-II and Type-Y is $+22\%$.

Finally, we comment on the results in the other case of the degenerate mass of the additional Higgs bosons, i.e., $m_H = m_{H^\pm}$. We find that for Scenario A the correction factor of the total decay width $\Delta_{\rm EW}$(total width) shows a cusp structure at $m_A = 2m_t$, which is realized by the threshold of the top loop diagrams in $\delta\beta$, so that behavior is changed from the case the $m_A = m_{H^\pm}$. However, the maximum and minimum values of $\Delta_{\rm EW}$(total width) are similar to the results of $m_A = m_{H^\pm}$. Behavior of the $\Delta^{\rm BR}_{\rm EW}$ for the processes discussed above is somewhat different from the case of $m_A = m_{H^\pm}$, while values of $\Delta^{\rm BR}_{\rm EW}$ distribute in the similar region to the case of $m_A = m_{H^\pm}$. For Scenario B, we also note that the size of $\Delta^{\rm BR}_{\rm EW}$ for all the processes

[4] We have calculated the NLO EW corrections to the on-shell two-body decay of $H^+ \to W^+H$. In the range of $m_W < m_H - m_{H^\pm} < 0$ GeV, where the off-shell decay $H^+ \to W^*H$ happens, the NLO EW corrections have not been implemented.

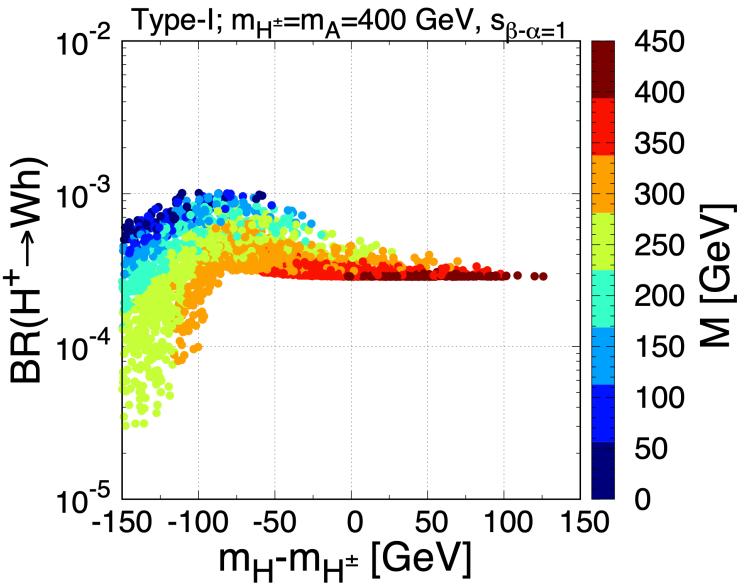

Figure 8.17: The decay branching ratio for $H^+ \to W^+h$ for Scenario A of Type-I in the alignment limit, $s_{\beta-\alpha} = 1$, as a function of the mass difference $m_H - m_{H^\pm}$, where the squared one-loop amplitude for $H^+ \to W^+h$ is included in the evaluation. The colored dots correspond to different values of M.

in the case of $m_H = m_{H^\pm}$ tend to be smaller than that of the case $m_A = m_{H^\pm}$ except for Type-I. For Type-I, the maximum value of $\Delta^{\rm BR}_{\rm EW}(H^+ \to t\bar{b})$ and $\Delta^{\rm BR}_{\rm EW}(H^+ \to \tau^+\nu)$ is +12.7% and +2.6%, respectively, while the one for $\Delta^{\rm BR}_{\rm EW}(H^+ \to W^+h)$ is similar to the case of $m_A = m_{H^\pm}$.

8.3.3 Effect of the squared one-loop amplitude to $H^+ \to W^+h$

Before we close this section, we discuss the effect of the squared one-loop amplitude for $H^+ \to W^+h$. The squared amplitude for this process can be expressed by

$$\begin{aligned} |\mathcal{M}(H^+ \to W^+h)|^2 &= C_{H^+W^-h}\left(|\Gamma^{\rm tree}_{H^+W^-h}|^2 + 2\Gamma^{\rm tree}_{H^+W^-h}{\rm Re}\Gamma^{\rm loop}_{H^+W^-h} + |\Gamma^{\rm loop}_{H^+W^-h}|^2\right) \\ &= C_{H^+W^-h}\left(\frac{g^2}{4}c^2_{\beta-\alpha} + gc_{\beta-\alpha}{\rm Re}\Gamma^{\rm loop}_{H^+W^-h} + |\Gamma^{\rm loop}_{H^+W^-h}|^2\right), \end{aligned} \tag{8.48}$$

where $C_{H^+W^-h} = m^4_{H^\pm}/m^2_W\lambda(\mu_h, \mu_W)$. The first (second) term corresponds to LO (NLO) contributions to $\Gamma(H^+ \to W^+h)$. We have involved up to the second term in above discussions. The third term $|\Gamma^{\rm loop}_{H^+W^-h}|^2$ is the same order as contributions from the tree-level amplitude times two-loop amplitude, namely NNLO contributions. It is notable that this term contains contributions that are not proportional to $c_{\beta-\alpha}$. Hence, the term $|\Gamma^{\rm loop}_{H^+W^-h}|^2$ does not disappear even in the alignment limit. The term $|\Gamma^{\rm loop}_{H^+W^-h}|^2$ can be identified as a leading contribution if one assumes $c_{\beta-\alpha}$ to be tiny and expands the squared amplitude $|\mathcal{M}(H^+ \to W^+h)|^2$ into a power series of $c_{\beta-\alpha}$. We notice from naive order estimation that the term $|\Gamma^{\rm loop}_{H^+W^-h}|^2$ can be comparable with the first and second terms in Eq. (8.48) under the situation where $|c_{\beta-\alpha}| \lesssim 0.1$ and $M \lesssim v$. Therefore, the third term of Eq. (8.48) could be significant in the alignment regions.

To discuss the effect of $|\Gamma^{\rm loop}_{H^+W^-h}|^2$ in the region of $0.995 \lesssim s_{\beta-\alpha} < 1$ is beyond the scope of this paper. If $s_{\beta-\alpha} \neq 1$, the third term $|\Gamma^{\rm loop}_{H^+W^-h}|^2$ contains the IR divergence and evaluation of real photon emissions at NNLO are required in order to obtain the IR finite result for $\Gamma(H^+ \to W^+h)$. As long as the case of the alignment limit $s_{\beta-\alpha} = 1$, the third term is IR finite. In addition, contributions to the squared amplitude from the tree-level amplitude times two-loop amplitude vanish in the alignment limit. Therefore, we only discuss two-loop corrections due to the third term in Eq. (8.48) to the branching ratio for $H^+ \to W^+h$ only in the case of $s_{\beta-\alpha} = 1$, and how this is important.

In Fig. 8.17, we show the branching ratio for $H^+ \to W^+h$ including the squared term $|\Gamma^{\rm loop}_{H^+hW^-}|^2$ for Scenario A of Type-I in the alignment limit $s_{\beta-\alpha} = 1$ as a function of the mass difference $m_H - m_{H^\pm}$. The other parameters $\tan\beta$ and M are scanned as in Eq. (9.57). One can see that the branching ratio can be 0.1% at most. The intriguing point is that the branching ratio is maximized when the soft-breaking parameter M is small. We have also calculated the branching ratio in Scenario A for Type-X and Scenario B for all types of 2HDMs. For Scenario A of Type-X, we have got the almost same results with Type-I. On the other hand, for Scenario B, the soft-breaking parameter M cannot be small under the theoretical consistencies such as the perturbative unitarity and the vacuum stability. Hence, the branching ratios are small, as compared to Scenario A. We find that the maximum value of the branching ratio is 0.004% in Scenario B for all types of 2HDMs. In short, the non-decoupling effect of the additional Higgs bosons enhances the decay $H^+ \to W^+h$ through the contribution from the term of $|\Gamma^{\rm loop}_{H^+hW^-}|^2$, and the branching ratio can be 0.1% when $m_{H^\pm} = 400$ GeV.

Chapter 9

One-loop calculations for decays of the CP-odd Higgs boson

In this chapter, we discuss the decay rates of the CP-odd Higgs boson for various decay modes in the 2HDMs. Decay branching ratios of the CP-odd Higgs boson are evaluated including NLO EW corrections, as well as QCD corrections up to NNLO. We have newly implemented them into the `H-COUP` program [45, 46]. We comprehensively study the impacts of the NLO EW corrections to the branching ratios in approximate alignment scenarios. We find that the $A \to Zh$ decay modes can be dominant decay modes even in the case where deviation in hZZ couplings is quite small and cannot be detected at the ILC. Thus, we can extract the information on the mixing angle by studying the $A \to Zh$ decay mode at future collider experiments. In addition, we find that the types of 2HDMs can be classified by studying the decay pattern of the CP-odd Higgs boson even in the alignment scenario. In the alignment scenario, it is difficult to distinguish the types of 2HDMs from the precision measurement of the SM-like Higgs boson. Thus, the study of the CP-odd Higgs boson is quite useful to investigate not only the approximate but also the exact alignment scenario.

9.1 Decay rates with higher-order corrections

9.1.1 Form factors for vertex functions of CP-odd Higgs boson

$Af\bar{f}$ vertex

The renormalized $Af\bar{f}$ vertex functions can be expressed as

$$\begin{aligned}\hat{\Gamma}_{Af\bar{f}}(p_1^2, p_2^2, q^2) = \hat{\Gamma}^S_{Af\bar{f}} + \gamma_5\hat{\Gamma}^P_{Af\bar{f}} + \not{p}_1\hat{\Gamma}^{V_1}_{Af\bar{f}} + \not{p}_2\hat{\Gamma}^{V_2}_{Af\bar{f}} + \not{p}_1\gamma_5\hat{\Gamma}^{A_1}_{Af\bar{f}} + \not{p}_2\gamma_5\hat{\Gamma}^{A_2}_{Af\bar{f}} \\ + \not{p}_1\not{p}_2\hat{\Gamma}^T_{Af\bar{f}} + \not{p}_1\not{p}_2\gamma_5\hat{\Gamma}^{PT}_{Af\bar{f}},\end{aligned} \tag{9.1}$$

where p_1 (p_2) is the incoming four-momentum of the fermion (anti-fermion), and $q^\mu\,(= p_1 + p_2)$ is the outgoing four-momentum of the CP-odd Higgs boson (see Fig. 9.1). The renormalized form factors are composed of the tree-level part and the one-loop part as

$$\hat{\Gamma}^X_{Af\bar{f}} = \Gamma^{X,\text{tree}}_{Af\bar{f}} + \Gamma^{X,\text{loop}}_{Af\bar{f}}, \quad (X = S,\, P,\, V_1,\, V_2,\, A_1,\, A_2,\, T,\, PT), \tag{9.2}$$

where the one-loop parts are further decomposed into contributions from 1PI diagrams and counterterms,

$$\Gamma^{X,\text{loop}}_{Af\bar{f}} = \Gamma^{X,\text{1PI}}_{Af\bar{f}} + \delta\Gamma^X_{Af\bar{f}}. \tag{9.3}$$

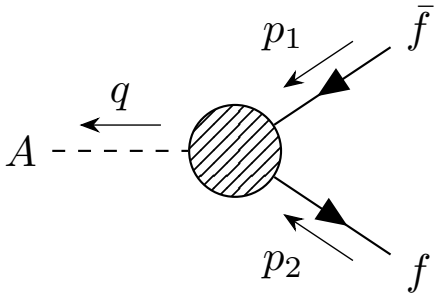

Figure 9.1: Momentum assignment for the renormalized $Af\bar{f}$ vertex.

The 1PI diagrams contributions $\Gamma^{X,\mathrm{1PI}}_{Af\bar{f}}$ are given in Appendix.

The tree-level couplings for $Af\bar{f}$ vertices are given by

$$\Gamma^{P,\mathrm{tree}}_{Af\bar{f}} = i2I_f\frac{m_f\zeta_f}{v}, \quad \Gamma^{X,\mathrm{tree}}_{Af\bar{f}} = 0, \quad (X \neq P). \tag{9.4}$$

The counterterms for $Af\bar{f}$ vertices are given by

$$\delta\Gamma^{P}_{Af\bar{f}} = \Gamma^{P,\mathrm{tree}}_{Af\bar{f}}\left[\frac{\delta m_f}{m_f} - \frac{\delta v}{v} - \zeta_f\delta\beta + \delta Z^f_V + \frac{\delta Z_A}{2} + \frac{\delta C_A}{\zeta_f} - \left(\frac{1}{\zeta_f} + \zeta_f\right)\delta\beta^{\mathrm{PT}}\right], \tag{9.5}$$

$$\delta\Gamma^{X}_{Af\bar{f}} = 0, \quad (X \neq P). \tag{9.6}$$

The contributions of AZ and AG^0 mixing vanish due to the on-shell condition. The ampitudes of AZ and AG^0 mixing are given by

$$\begin{aligned}\mathcal{M}_{\mathrm{mix}} &= -\left[\widehat{\Pi}_{AG}(m_A^2) - m_Z\widehat{\Pi}_{AZ}(m_A^2)\right]\frac{1}{\zeta_f(m_A^2 - m_Z^2)}\bar{u}(-p_2)\Gamma^{P,\mathrm{tree}}_{Af\bar{f}}\gamma_5 v(-p_1) \\ &= -\frac{\widehat{\Pi}_{AG}(m_A^2)}{\zeta_f m_A^2}\bar{u}(-p_2)\Gamma^{P,\mathrm{tree}}_{Af\bar{f}}\gamma_5 v(-p_1),\end{aligned} \tag{9.7}$$

where we have used the Slavnov-Taylor identity for AZ and AG^0 mixing in the last equality

$$\widehat{\Pi}_{AG^0}(m_A^2) + i\frac{m_A^2}{m_Z}\widehat{\Pi}_{AZ}(m_A^2) = 0. \tag{9.8}$$

Since $\widehat{\Pi}_{AG^0}(m_A^2) = 0$ by the on-shell renormalization condition, the contributions of AZ and AG^0 mixing vanish in the decay amplitude.

When we neglect the effects of the CP violation, on-shell amplitudes are CP invariant. The renormalized $Af\bar{f}$ vertex functions satisfy the following relations

$$\hat{\Gamma}^{S}_{Af\bar{f}} = \hat{\Gamma}^{T}_{Af\bar{f}} = 0, \quad \hat{\Gamma}^{V_1}_{Af\bar{f}} = \hat{\Gamma}^{V_2}_{Af\bar{f}}, \quad \hat{\Gamma}^{A_1}_{Af\bar{f}} = \hat{\Gamma}^{A_2}_{Af\bar{f}}, \quad (p_1^2 = p_2^2 = m_f^2). \tag{9.9}$$

$AV\phi$ vertex

The the renormalized $AV\phi$ vertex functions $(V, \phi) = (Z, h/H)$ can be expressed as

$$\hat{\Gamma}^{\mu}_{AV\phi}(p_1, p_2, q) = (p_1 + q)^{\mu}\hat{\Gamma}_{AV\phi}(p_1^2, p_2^2, q^2), \tag{9.10}$$

where p_1 and p_2 denote the incoming four-momentum of the scalar boson ϕ and the gauge boson V, respectively. The momentum $q\,(= p_1 + p_2)$ is the outgoing four-momentum of the CP-odd

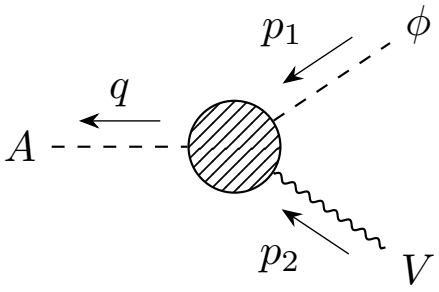

Figure 9.2: Momentum assignment for the renormalized $AV\phi$ vertex.

Higgs boson (see Fig. 9.2). Since we here assume that the external gauge boson is on-shell, the term proportional to p_2 vanishes due to the orthogonality of the polarization vector.

For the $A \to W^\pm H^\mp$ decays, we use the renormalized $H^\pm W^\mp A$ vertex function,

$$\begin{aligned}\hat{\Gamma}^\mu_{AW^\pm H^\mp}(p_1, p_2, q) &= \hat{\Gamma}^\mu_{H^\pm W^\pm A}(q, p_2, p_1) \\ &= -(q + p_1)^\mu \hat{\Gamma}_{H^\pm W^\pm A}(q^2, p_2^2, p_1^2),\end{aligned} \tag{9.11}$$

where p_1 and p_2 denote the incoming four-momentum of the charged Higgs bosons $H^\pm$ and the gauge boson $W^\pm$, respectively. The momentum $q\,(= p_1 + p_2)$ is the outgoing four-momentum of the CP-odd Higgs boson. The additional minus sign is needed due to the change of momentum assignment.

The renormalized form factors are composed of the tree-level part and the one-loop part as

$$\hat{\Gamma}_{AV\phi} = \Gamma^{\rm tree}_{AV\phi} + \Gamma^{\rm loop}_{AV\phi}, \tag{9.12}$$

where the one-loop parts are further decomposed into contributions from 1PI diagrams and counterterms,

$$\Gamma^{\rm loop}_{AV\phi} = \Gamma^{\rm 1PI}_{AV\phi} + \delta\Gamma_{AV\phi}. \tag{9.13}$$

The 1PI diagrams contributions $\Gamma^{\rm 1PI}_{AV\phi}$ are given in Appendix.

The tree-level couplings for $AV\phi$ vertices are given by

$$\Gamma^{\rm tree}_{AZh} = -ig_{hAZ} = i\frac{m_Z}{v}c_{\beta-\alpha}, \tag{9.14}$$

$$\Gamma^{\rm tree}_{AZH} = -ig_{HAZ} = -i\frac{m_Z}{v}s_{\beta-\alpha}, \tag{9.15}$$

$$\Gamma^{\rm tree}_{AW^\mp H^\pm} = -i \times (-g_{AH^\pm W^\mp}) = -i\frac{m_W}{v}. \tag{9.16}$$

The counterterms for $AV\phi$ vertices are given by

$$\begin{aligned}\delta\Gamma_{AZh} = \Gamma^{\rm tree}_{AZh}\Bigg[&\frac{\delta m_Z^2}{2m_Z^2} - \frac{\delta v}{v} + \frac{1}{2}(\delta Z_h + \delta Z_A + \delta Z_Z) \\ &+ \tan(\beta-\alpha)\big(\delta C_A - \delta C_h - \delta\beta^{\rm PT} + \delta\alpha^{\rm PT}\big)\Bigg],\end{aligned} \tag{9.17}$$

$$\begin{aligned}\delta\Gamma_{AZH} = \Gamma^{\rm tree}_{AZH}\Bigg[&\frac{\delta m_Z^2}{2m_Z^2} - \frac{\delta v}{v} + \frac{1}{2}(\delta Z_H + \delta Z_A + \delta Z_Z) \\ &- \cot(\beta-\alpha)\big(\delta C_A + \delta C_h - \delta\beta^{\rm PT} + \delta\alpha^{\rm PT}\big)\Bigg],\end{aligned} \tag{9.18}$$

$$\delta\Gamma_{AW^\mp H^\pm} = \Gamma^{\rm tree}_{AW^\mp H^\pm}\left[\frac{\delta m_W^2}{2m_W^2} - \frac{\delta v}{v} + \frac{1}{2}(\delta Z_{H^\pm} + \delta Z_A + \delta Z_W)\right]. \tag{9.19}$$

9.1.2 Decay rates of $A \to f\bar{f}$

The decay rates of the CP-odd Higgs boson into a pair of fermions with NLO EW and QCD corrections are given by

$$\Gamma(A \to f\bar{f}) = \Gamma_{\rm LO}(A \to f\bar{f})\Big(1 + \Delta^f_{\rm EW} + \Delta^f_{\rm QCD}\Big) + \Gamma(A \to f\bar{f}\gamma), \tag{9.20}$$

with the decay rate at LO

$$\Gamma_{\rm LO}(A \to f\bar{f}) = N_c^f \frac{\sqrt{2} G_F m_A}{8\pi} m_f^2 \zeta_f^2 \lambda^{1/2}\left(\frac{m_f^2}{m_A^2}, \frac{m_f^2}{m_A^2}\right), \tag{9.21}$$

where N_c^f is the color factor.

The EW correction $\Delta^f_{\rm EW}$ is given by

$$\Delta^f_{\rm EW} = \frac{\sqrt{2}}{G_F m_f^2 \zeta_f^2} \,{\rm Re}\left[\Gamma^{P,{\rm tree}}_{Af\bar{f}} G^{P,{\rm loop}*}_{Af\bar{f}}\right] - \Delta r, \tag{9.22}$$

with

$$\begin{aligned} G^{P,{\rm loop}}_{Af\bar{f}} &= \Gamma^{P,{\rm loop}}_{Af\bar{f}} - m_f\Big(\Gamma^{A_1,{\rm loop}}_{Af\bar{f}} + \Gamma^{A_2,{\rm loop}}_{Af\bar{f}}\Big) + (q^2 - p_1^2 - p_2^2 - m_f^2)\Gamma^{PT,{\rm loop}}_{Af\bar{f}} \\ &= \Gamma^{P,{\rm loop}}_{Af\bar{f}} - 2m_f\Gamma^{A_1,{\rm loop}}_{Af\bar{f}} + m_A^2\left(1 - \frac{3m_f^2}{m_A^2}\right)\Gamma^{PT,{\rm loop}}_{Af\bar{f}}, \end{aligned} \tag{9.23}$$

where we have used the relations in Eq. (9.9) in the last equality. The NLO EW corrections include the IR divergences, and we regulate them by introducing the finite photon mass. In order to remove the photon mass dependence, we add the decay rates of real photon emmision $A \to f\bar{f}\gamma$. The analytic expression of $\Gamma(A \to f\bar{f}\gamma)$ is given in Appendix **??**.

For the decays into a pair of light quarks, we apply the QCD corrections at NNLO in the $\overline{\rm MS}$ scheme. The QCD correction is given by

$$\Delta^q_{\rm QCD} = \Delta_{qq} + \Delta_A. \tag{9.24}$$

The correction Δ_{qq} in the limit of massless quarks is given by

$$\begin{aligned} \Delta_{qq} &= \frac{\alpha_s(\mu)}{\pi} C_F\left(\frac{17}{4} + \frac{3}{2}\ln\frac{\mu^2}{m_A^2}\right) \\ &\quad + \left(\frac{\alpha_s(\mu)}{\pi}\right)^2\left[\frac{10801}{144} - \frac{39}{2}\zeta_3 - \left(\frac{65}{24} - \frac{2}{3}\zeta_3\right)N_f - \pi^2\left(\frac{19}{12} - \frac{1}{18}N_f\right)\right] \\ &\simeq \frac{\alpha_s(\mu)}{\pi} C_F\left(\frac{17}{4} + \frac{3}{2}\ln\frac{\mu^2}{m_A^2}\right) + \left(\frac{\alpha_s(\mu)}{\pi}\right)^2 (35.94 - 1.36 N_f) \end{aligned} \tag{9.25}$$

The correction Δ_A includes logarithms of the light-quark and top-quark masses. It is given by

$$\Delta_A = \left(\frac{\alpha_s(\mu)}{\pi}\right)^2\left(3.83 + \ln\frac{m_t^2}{m_A^2} + \frac{1}{6}\ln^2\frac{\bar{m}_q^2}{m_A^2}\right) \tag{9.26}$$

For the decay into the top-quark pair, the effects of the top-quark mass in the QCD corrections are significant near the threshold region. On the other hand, dominant contributions in $m_A \gg m_t$ is the logarithmic contribution, which appears in the $\overline{\rm MS}$ scheme. In order to take

into account both of the effects, we use interpolation for the corrections to $A \to t\bar{t}$ as discussed in Ref. []. The QCD correction in the on-shell scheme is given by

$$\Delta^t_{\rm QCD} = \frac{\alpha_s(\mu)}{\pi} C_F \left[\frac{L(\beta_t)}{\beta_t} - \frac{1}{16\beta_t^3}(19 + 2\beta_t^2 + 3\beta_t^4) \ln \rho_t + \frac{3}{8}(7 - \beta_t^2) \right], \tag{9.27}$$

with $\beta_t = \lambda^{1/2}(m_t^2/m_A^2, m_t^2/m_A^2)$ and $\rho_t = (1 - \beta_t)/(1 + \beta_t)$. The function $L(\beta_t)$ is given by

$$\begin{aligned} L(\beta_t) = (1 + \beta_t^2) \Bigg[& 4{\rm Li}_2(\rho_t) + 2{\rm Li}_2(-\rho_t) + 3 \ln \rho_t \ln \frac{2}{1 + \beta_t} + 2 \ln \rho_t \ln \beta_t \Bigg] \\ & - 3\beta_t \ln \frac{4}{1 - \beta_t^2} - 4\beta_t \ln \beta_t, \end{aligned} \tag{9.28}$$

where ${\rm Li}_2(x)$ is the dilog function.

9.1.3 Decay rates of $A \to V\phi$

The decay rate for the CP-odd Higgs boson decays into a Z boson and a h boson with NLO EW corrections is given by

$$\Gamma(A \to Zh) = \Gamma_{\rm LO}(A \to Zh) \left[1 + \frac{\sqrt{2}}{G_F m_Z^2 c_{\beta-\alpha}^2} {\rm Re} \left(\Gamma^{\rm tree}_{AZh} \Gamma^{\rm loop*}_{AZh} \right) - \Delta r - {\rm Re}\, \hat{\Pi}'_{ZZ}(m_Z^2) \right], \tag{9.29}$$

where

$$\Gamma_{\rm LO}(A \to Zh) = \frac{\sqrt{2} G_F m_A^3 c_{\beta-\alpha}^2}{16\pi} \lambda^{3/2} \left(\frac{m_h^2}{m_A^2}, \frac{m_Z^2}{m_A^2} \right). \tag{9.30}$$

The decay rate for the CP-odd Higgs boson decays into a Z boson and a H boson with NLO EW corrections is given by

$$\Gamma(A \to ZH) = \Gamma_{\rm LO}(A \to ZH) \left[1 + \frac{\sqrt{2}}{G_F m_Z^2 s_{\beta-\alpha}^2} {\rm Re} \left(\Gamma^{\rm tree}_{AZH} \Gamma^{\rm loop*}_{AZH} \right) - \Delta r - {\rm Re}\, \hat{\Pi}'_{ZZ}(m_Z^2) \right], \tag{9.31}$$

where

$$\Gamma_{\rm LO}(A \to ZH) = \frac{\sqrt{2} G_F m_A^3 s_{\beta-\alpha}^2}{16\pi} \lambda^{3/2} \left(\frac{m_H^2}{m_A^2}, \frac{m_Z^2}{m_A^2} \right). \tag{9.32}$$

The decay rate for the CP-odd Higgs boson decays into a $W^\pm$ boson and a $H^\pm$ boson with NLO EW corrections is given by

$$\begin{aligned} \Gamma(A \to W^\pm H^\mp) = \Gamma_{\rm LO}(A \to W^\pm H^\mp) \Bigg[& 1 + \frac{\sqrt{2}}{G_F m_W^2} {\rm Re} \left(\Gamma^{\rm tree}_{AW^-H^+} \Gamma^{\rm loop*}_{AW^-H^+} \right) \\ & - \Delta r - {\rm Re}\, \hat{\Pi}'_{WW}(m_W^2) \Bigg] + \Gamma(A \to H^\pm W^\mp \gamma), \end{aligned} \tag{9.33}$$

where

$$\Gamma_{\rm LO}(A \to W^\pm H^\mp) = \frac{\sqrt{2} G_F m_A^3}{8\pi} \lambda^{3/2} \left(\frac{m_{H^\pm}^2}{m_A^2}, \frac{m_W^2}{m_A^2} \right). \tag{9.34}$$

The decay rates for $A \to H^\pm W^\mp \gamma$ is given in Appendix **??**.

9.1.4 Decay rates of loop-induced decays $A \to \gamma\gamma$, $Z\gamma$, gg

The decay rate of the CP-odd Higgs boson into a pair of photons is given by

$$\Gamma(A \to \gamma\gamma) = \frac{G_F \alpha_{\rm em}^2 m_A^3}{128\sqrt{2}\pi^3} \left| \sum_f N_c^f Q_f^2 \kappa_f^A I_F^A(\tau_f) \right|^2, \tag{9.35}$$

where $\kappa_f^A = -2iI_f\zeta_f$ and $\tau_f = m_A^2/(4m_f^2)$. The loop function $I_F^A(\tau_f)$ is given by

$$\begin{aligned} I_F^A(\tau_f) &= -4m_f^2 C_0(0,0,m_A^2; m_f, m_f, m_f) \\ &= \frac{2}{\tau_f} f(\tau_f), \end{aligned} \tag{9.36}$$

with

$$f(\tau) = \begin{cases} \arcsin^2(\sqrt{\tau}) & (\tau \le 1), \\ -\dfrac{1}{4}\left[\ln \dfrac{1+\sqrt{1-\tau^{-1}}}{1-\sqrt{1-\tau^{-1}}} - i\pi \right]^2 & (\tau > 1). \end{cases} \tag{9.37}$$

The quark-loop contributions receive QCD corrections. At the NLO, the QCD correction can be obtained in the $\overline{\rm MS}$ scheme by replacing the quark-loop function $I_F^A(\tau_q)$,

$$I_F^A(\tau_q) \to I_F^A(\tau_q)\left[1 + \frac{\alpha_s(\mu)}{\pi}\left(C_1^A(\tau_q) + C_2^A(\tau_q) \ln \frac{4\tau_q \mu^2}{m_A^2} \right) \right]. \tag{9.38}$$

The analytic expressions for QCD corrections are given by

$$\begin{aligned} I_F^A C_1^A = &-\frac{\theta(1+\theta^2)}{(1-\theta)^3(1+\theta)} \left[72{\rm Li}_4(\theta) + 96{\rm Li}_4(-\theta) - \frac{128}{3}[{\rm Li}_3(\theta) - {\rm Li}_3(-\theta)] \ln\theta \right. \\ &\left. + \frac{28}{3}{\rm Li}_2(\theta)\ln^2\theta + \frac{16}{3}{\rm Li}_2(-\theta)\ln^2\theta + \frac{1}{18}\ln^4\theta + \frac{8}{3}\zeta_2\ln^2\theta + \frac{32}{3}\zeta_3\ln\theta + 12\zeta_4 \right] \\ &+ \frac{\theta}{(1-\theta)^2}\left[-\frac{56}{3}{\rm Li}_3(\theta) - \frac{64}{3}{\rm Li}_3(-\theta) + 16{\rm Li}_2(\theta)\ln\theta + \frac{32}{3}{\rm Li}_2(-\theta)\ln\theta \right. \\ &\left. + \frac{20}{3}\ln(1-\theta)\ln^2\theta - \frac{8}{3}\zeta_2\ln\theta + \frac{8}{3}\zeta_3 \right] \\ &+ \frac{2\theta(1+\theta)}{3(1-\theta)^3}\ln^3\theta, \end{aligned} \tag{9.39}$$

$$I_F^A C_2^A = \frac{2}{\tau}[f(\tau) - \tau f'(\tau)], \tag{9.40}$$

with

$$\theta \equiv \theta(\tau_q) = \frac{\sqrt{1-\tau^{-1}} - 1}{\sqrt{1-\tau^{-1}} + 1}. \tag{9.41}$$

The decay rate of the CP-odd Higgs boson into a Z boson and a photon is given by

$$\Gamma(A \to Z\gamma) = \frac{\sqrt{2} G_F \alpha_{\rm em}^2 m_A^3}{128\pi^3}\left(1 - \frac{m_Z^2}{m_A^2}\right)^3 \left| \sum_f \kappa_f^A Q_f N_c^f v_f J_F^A \right|^2, \tag{9.42}$$

where

$$J_F^A = -\frac{4m_f^2}{s_W c_W} C_0(0, m_Z^2, m_A^2; m_f, m_f, m_f). \tag{9.43}$$

The decay rate of the CP-odd Higgs boson into a pair of gluon is given by

$$\Gamma(A \to gg) = \Gamma_{\rm LO}(A \to gg)\left[1 + \frac{\alpha_s(\mu)}{\pi} E_A^{(1)} + \left(\frac{\alpha_s(\mu)}{\pi}\right)^2 E_A^{(2)}\right], \tag{9.44}$$

where the decay rate at LO is given by

$$\Gamma_{\rm LO}(A \to gg) = \frac{\sqrt{2} G_F \alpha_s^2 m_A^3}{128\pi^3}\left|\sum_q \kappa_q^A I_F^A(\tau_q)\right|^2, \tag{9.45}$$

with the loop function $I_F^A(\tau)$ defined in Eq. (9.36).

The NLO QCD correction $E_A^{(1)}$ is given by

$$E_A^{(1)} = \frac{97}{4} - \frac{7}{6}N_f + \left(\frac{11}{2} - \frac{1}{3}N_f\right)\ln\frac{\mu^2}{m_A^2} + \Delta E_A^{(1)}, \tag{9.46}$$

where $\Delta E_A^{(1)}$ is the corrections which vanishes in the heavy top-mass limit ($2m_t \gg m_A$). $\Delta E_A^{(1)}$ is composed of the virtural corrections, real gluon emmision and light-quark splitting diagrams,

$$\Delta E_A^{(1)} = \Delta E_{\rm virt}^A + \Delta E_{ggg}^A + N_f \Delta E_{gq\bar{q}}^A. \tag{9.47}$$

We do not implement ΔE_{ggg}^A and $\Delta E_{gq\bar{q}}^A$. The analytic expression for virtual corrections is given by

$$\Delta E_{\rm virt}^A = c_A(\tau_q) - 6, \tag{9.48}$$

where

$$c_A = {\rm Re}\left\{\frac{\sum_q \kappa_q^A I_F^A(\tau_q)\left(B_1^A(\tau_q) + B_2^A(\tau_q)\ln\frac{\mu^2}{m_q^2}\right)}{\sum_q \kappa_q^A I_F^A(\tau_q)}\right\}. \tag{9.49}$$

with

$$\begin{aligned}
I_F^A B_1^A = {} & \frac{\theta}{(1-\theta)^2}\Big[48H(1,0,-1,-;\theta) + 4\ln(1-\theta)\ln^3\theta - 24\zeta_2 {\rm Li}_2(\theta) - 24\zeta_2\ln(1-\theta)\ln\theta \\
& - 72\zeta_3\ln(1-\theta) - \frac{220}{3}{\rm Li}_3(\theta) - \frac{128}{3}{\rm Li}_3(-\theta) + 68{\rm Li}_2(\theta)\ln\theta + \frac{64}{3}{\rm Li}_2(-\theta)\ln\theta \\
& + \frac{94}{3}\ln(1-\theta)\ln^2\theta^2 - \frac{16}{3}\zeta_2\ln\theta + \frac{124}{3}\zeta_3 + 3\ln^2\theta\Big] \\
& - \frac{24\theta(5+7\theta^2)}{(1-\theta)^3(1+\theta)}{\rm Li}_4(\theta) - \frac{24\theta(5+11\theta^2)}{(1-\theta)^3(1+\theta)}{\rm Li}_4(-\theta) \\
& + \frac{8\theta(23+41\theta^2)}{3(1-\theta)^3(1+\theta)}\Big[{\rm Li}_3(\theta) + {\rm Li}_3(-\theta)\Big]\ln\theta \\
& - \frac{4\theta(5+23\theta^2)}{3(1-\theta)^3(1+\theta)}{\rm Li}_2(\theta)\ln^2\theta - \frac{32\theta(1+\theta^2)}{3(1-\theta)^3(1+\theta)}{\rm Li}_2(-\theta)\ln^2\theta
\end{aligned}$$

$$+\frac{\theta(5-13\theta^2)}{36(1-\theta)^3(1+\theta)}\ln^4\theta+\frac{2\theta(1-17\theta^2)}{3(1-\theta)^3(1+\theta)}\zeta_2\ln^2\theta+\frac{4\theta(11-43\theta^2)}{3(1-\theta)^3(1+\theta)}\zeta_3\ln\theta$$
$$+\frac{24\theta(1-3\theta^2)}{(1-\theta)^3(1+\theta)}\zeta_4+\frac{2\theta(2+11\theta)}{3(1-\theta)^3}\ln^3\theta, \tag{9.50}$$

$$I_F^A B_2^A=\frac{4}{\tau}[f(\tau)-\tau f'(\tau)]. \tag{9.51}$$

The NNLO QCD correction $E_A^{(2)}$ in the heavy top-mass limit is given by

$$E_A^{(2)}=\frac{51959}{96}-\frac{363}{8}\zeta_2-\frac{495}{8}\zeta_3+N_f\left[-\frac{473}{8}+\frac{11}{2}\zeta_2+\frac{5}{4}\zeta_3-\ln\frac{m_t^2(\mu)}{m_A^2}\right]$$
$$+N_f^2\left(\frac{251}{216}-\frac{1}{6}\zeta_2\right)+\left(\frac{3405}{16}-\frac{73}{3}N_f+\frac{7}{12}N_f^2\right)\ln\frac{\mu^2}{m_A^2}$$
$$+\left(\frac{363}{16}-\frac{11}{4}N_f+\frac{1}{12}N_f^2\right)\ln^2\frac{\mu^2}{m_A^2}. \tag{9.52}$$

9.2 NLO EW corrections

9.2.1 Branching ratio

In this subsection, we examine the decay branching ratios of the CP-odd Higgs boson including the higher-order corrections in the four types of 2HDMs. The qualitative behavior does not change from those in LO while the size of higher-order corrections can reach several dozens of percent. Therefore, we discuss their behavior and summarize the dominant decay modes in each type of 2HDMs at first. Since BR($A \to Zh$) can become negative near $s_{\beta-\alpha}=1$, we include the contribution of the square of NLO amplitude. We discuss this point at the end of this subsection. The magnitude of the higher-order corrections will be examined in the next subsection.

Fig. 9.3 shows the BR($A \to XY$) including the higher-order corrections as a function of $\tan\beta$. We have assumed the masses of additional Higgs bosons are degenerate and $m_\Phi = 300$ GeV, where the CP-odd Higgs boson cannot decay into a pair of top-quarks. However, the magnitude of the three-body decay width of $A \to tt^*$ is not negotiable, and we include it at LO. We have scanned M under the theoretical constraints and S, T parameters, and M_{max} (M_{min}) denotes the maximum (minimum) value of M. In order to discuss the theoretical behavior of NLO EW corrections, we dare to omit the constraint from the direct and indirect search and flavor experiment. The results in the Type-I, II, X and Y 2HDMs are shown from the first to fourth columns in order. The results in the alignment limit are shown in the first row, while those in the approximate alignment scenario with $c_{\beta-\alpha} < 0$ and $c_{\beta-\alpha} > 0$are shown in the second and third row, respectively.

In the alignment limit, the CP-odd Higgs boson mainly decays into a pair of fermions and gluons. In the Type-I 2HDM, $\kappa_f = \cot\beta$ and the partial decay widths of $A \to f\bar{f}$ monotonically decrease as $\tan\beta$ increases. In addition, the loop-induced $A \to gg$ decay also monotonically decreases since the fermion loops, especially the top-quark loop, give the dominant contributions. Thus, the decay branching ratios are almost constant in the Type-I 2HDM. On the other hand, there is $\tan\beta$ enhancement in either or both decays into a pair of down-type quarks and leptons in the other types of 2HDMs. In the Type-II 2HDM, both $A \to bb$ and $A \to \tau\tau$ decays can be

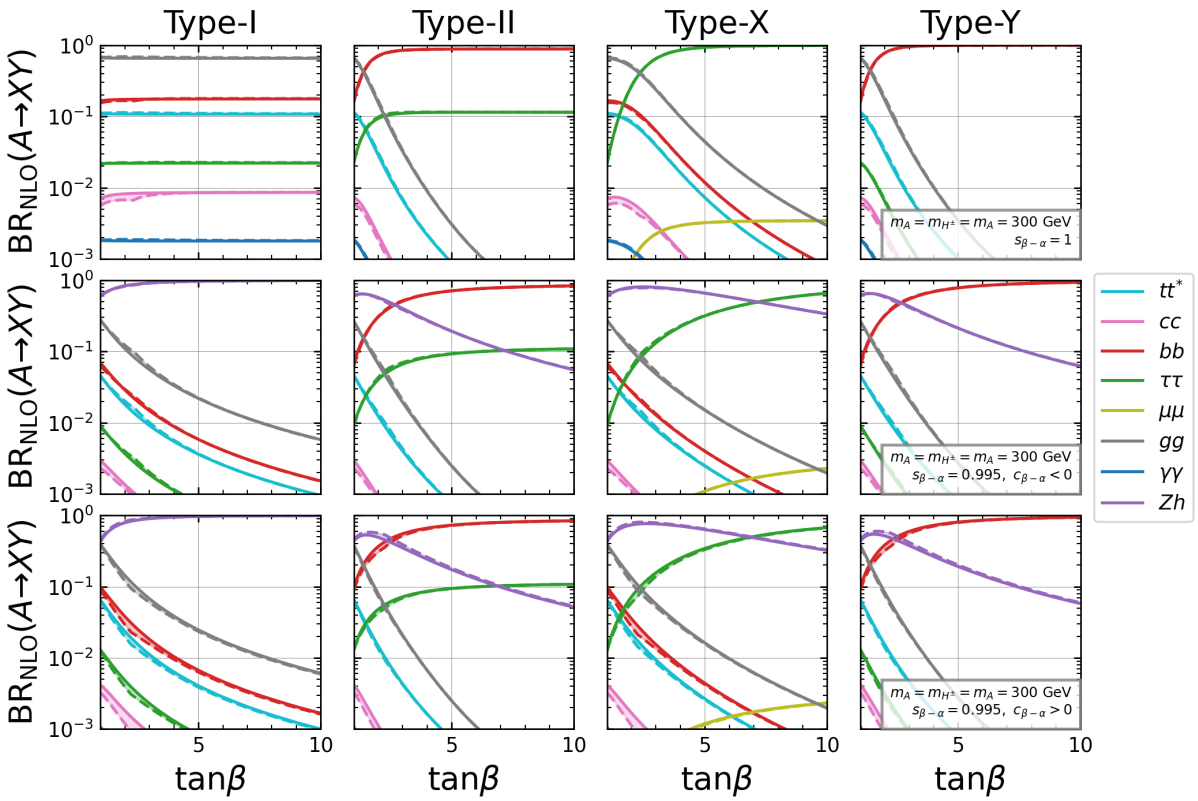

Figure 9.3: BR($A \to XY$) as a function of $\tan\beta$ in the alignment limit $s_{\beta-\alpha} = 1$ (first row) and in the approximate alignment case $s_{\beta-\alpha} = 0.995$ with $c_{\beta-\alpha} < 0$ (second row) and $c_{\beta-\alpha} > 0$ (third row) including the higher-order EW and QCD corrections. Masses of the additional Higgs bosons are degenerate and taken as $m_\Phi = 300$ GeV. Each decay mode is specified by color as given in the legend. Solid and dashed lines correspond to the results with $M = M_{\rm max}$ and $M_{\rm min}$, respectively, where $M_{\rm max}$ ($M_{\rm min}$) is the maximum (minimum) value of M under the theoretical constraints.

dominant with large $\tan\beta$, while the $A \to \tau\tau$ decay and the $A \to bb$ decay can be dominant in the Type-X and Y, respectively.

In the approximate alignment case, the CP-odd Higgs boson can decay into the Z boson and the SM-like Higgs boson. Since the tree-level hAZ vertex is independent of $\tan\beta$, the partial decay width of $A \to hZ$ is almost constant in all types of 2HDMs. In the Type-I 2HDM, the other decay modes are monotonically decreased as $\tan\beta$ becomes large, and $A \to Zh$ is the dominant decay mode despite the tree-level vertex being small in the approximate alignment case. In the other types of 2HDMs, the $A \to bb$ or $A \to \tau\tau$ decays are enhanced with large $\tan\beta$, but the size of the decay branching ratio of $A \to Zh$ is still several percent with $\tan\beta = 10$.

Fig. 9.4 shows the BR($A \to XY$) with $m_\Phi = 600$ GeV, where the CP-odd Higgs boson can decay into a pair of top-quarks. While the $A \to tt$ decay mode monotonically decreases as $\tan\beta$ becomes large, it is the dominant decay mode for all of the types of 2HDMs due to the large Yukawa coupling of the top quark. In the alignment limit, the CP-odd Higgs boson mainly decays into a pair of fermions. In the Type-I 2HDM, the $A \to tt$ decay is dominant, and the decay branching ratios are almost constant as similar to the case with $m_\Phi = 300$ GeV. In the Type-II 2HDM, both $A \to bb$ and $A \to \tau\tau$ decays are enhanced with large $\tan\beta$, and they are competitive with the $A \to tt$ decay. In the Type-X and Y 2HDM, the $A \to \tau\tau$ decay and the $A \to bb$ decay is enhanced, respectively and they are also competitive with the $A \to tt$

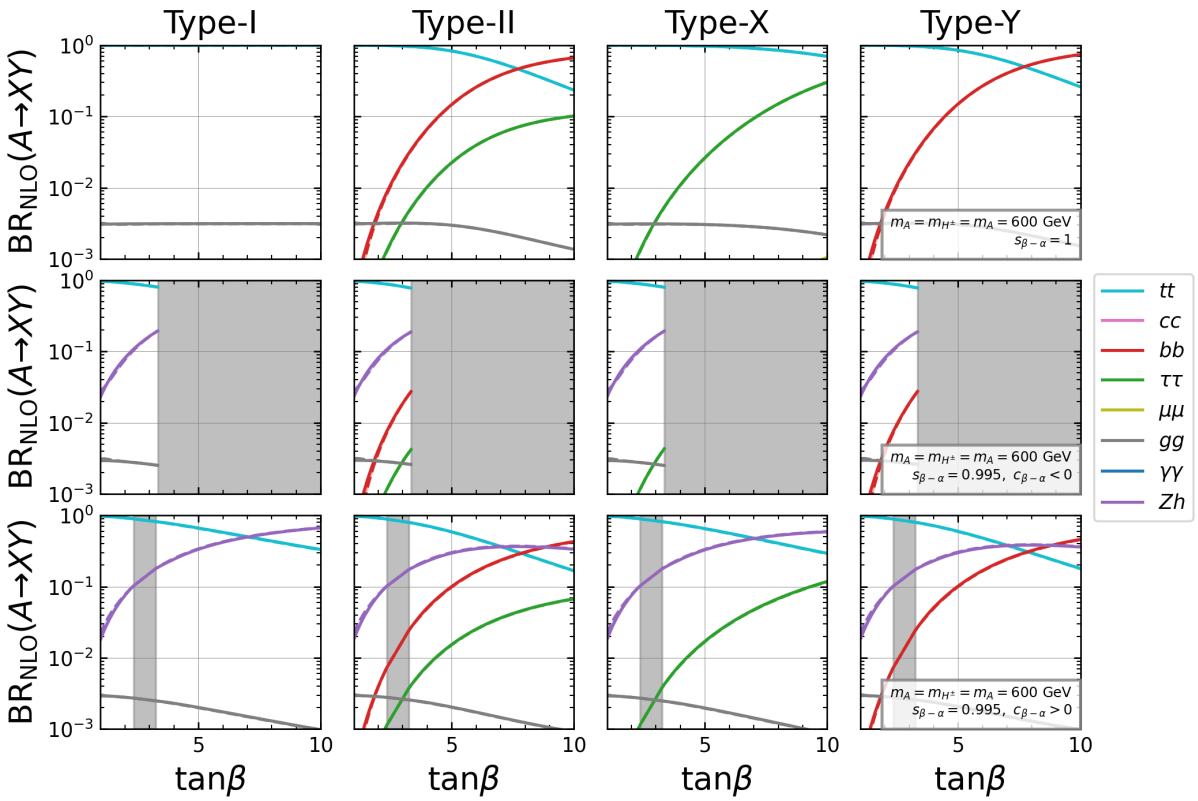

Figure 9.4: BR($A \to XY$) as a function of $\tan\beta$ in the alignment limit $s_{\beta-\alpha} = 1$ (first row) and in the approximate alignment case $s_{\beta-\alpha} = 0.995$ with $c_{\beta-\alpha} < 0$ (second row) and $c_{\beta-\alpha} > 0$ (third row) including the higher-order EW and QCD corrections. Masses of the additional Higgs bosons are degenerate and taken as $m_\Phi = 600$ GeV. Each decay mode is specified by color as given in the legend. Solid and dashed lines correspond to the results with $M = M_{\rm max}$ and $M_{\rm min}$, respectively, where $M_{\rm max}$ ($M_{\rm min}$) is the maximum (minimum) value of M under the theoretical constraints. The shaded regions are excluded by the theoretical constraints.

decay.

In the approximate alignment case with $s_{\beta-\alpha} = 0.995$ and $m_\Phi = 600$ GeV, the unitarity and vacuum stability bounds exclude the shaded regions. In the case with $c_{\beta-\alpha} < 0$, the $A \to tt$ decay is dominant in all of 2HDMs since the possible value of the $\tan\beta$ is not enough large. On the other hand, in the case with $c_{\beta-\alpha} < 0$, there are parameter regions with large $\tan\beta$, where $A \to Zh$ also becomes the dominant decay mode.

As we have mentioned, the partial decay width and the decay branching ratio for $A \to Zh$ can be negative if we truncate the perturbation up to NLO. Fig. 9.5 shows the BR($A \to Zh$) including the higher-order corrections with $\tan\beta$=2 (red), 3 (blue), 5 (green). We assume the masses of additional Higgs bosons are degenerate and $m_\Phi = 300$ GeV. The left and right panels correspond to the results in the Type-I and Type-II 2HDMs, respectively. We can see that NLO EW corrections modify the BR($A \to Zh$) sizably especially with small $\tan\beta$. Since we have truncated the square of NLO amplitude, which corresponds to the two-loop order, the decay branching ratio becomes negative near $s_{\beta-\alpha} \simeq 1$. The LO amplitude is proportional to $c_{\beta-\alpha}$, and it vanishes with the alignment limit. This is because the unphysical result near $s_{\beta-\alpha} \simeq 1$, where the LO contribution is smaller than the NLO corrections.

This problem can be solved by including the square of NLO amplitude. For the $A \to Zh$ decay, we have no infrared divergence in the NLO amplitude, and we can safely include the

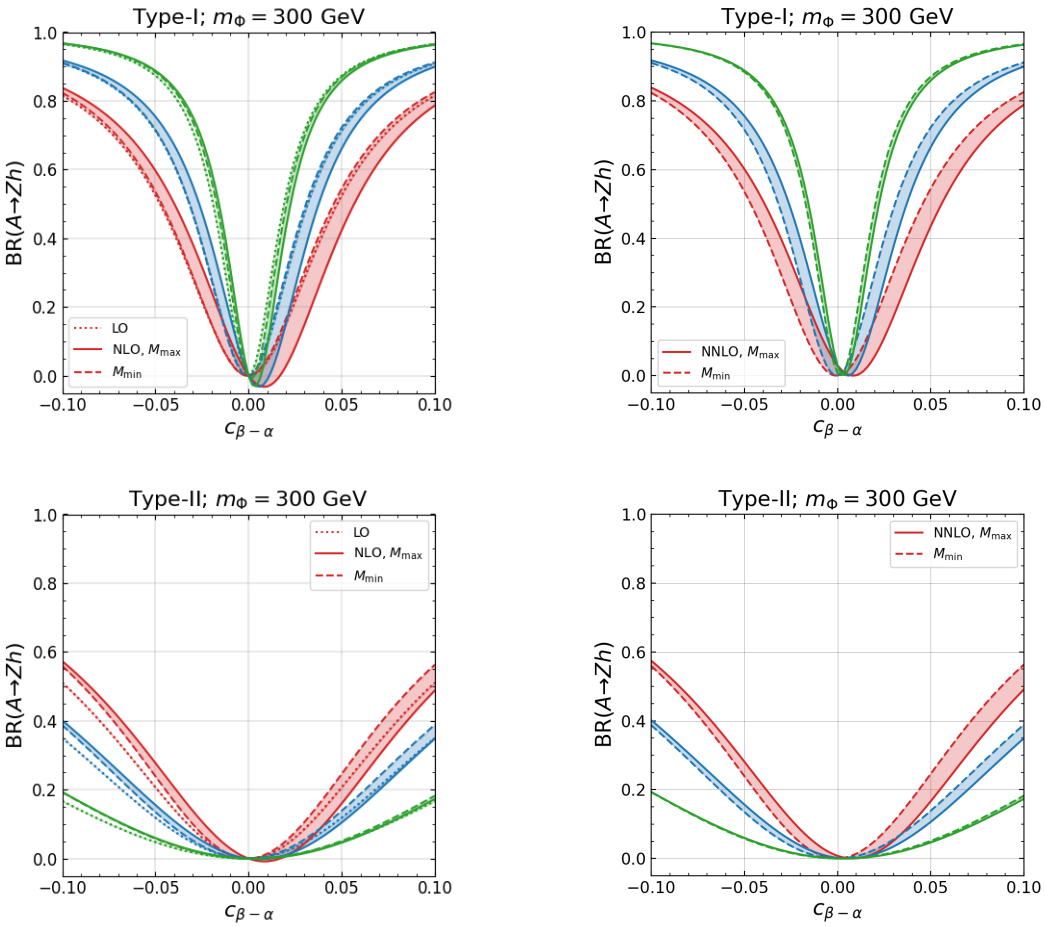

Figure 9.5: BR($A \to Zh$) including the higher-order corrections with $m_\Phi = 300$ GeV, and $\tan\beta$=2 (red), 3 (blue), 5 (green). The figures in the left column show the results with NLO EW corrections, while those in the right column show the results with partial NNLO EW corrections. The first (second) row shows the results in the Type-I (Type-II) 2HDM. We take masses of additional Higgs bosons are degenerate. M_{max} (M_{min}) denotes the maximum (minimum) value of M satisfying the theoretical constraints and S, T parameters.

square of NLO amplitude. The plots in the second row of Fig. 9.5 show the BR($A \to Zh$) including the partial NNLO corrections. We can see that the decay branching ratio takes positive values even at $s_{\beta-\alpha} \simeq 1$, and it gives a physically meaningful result.

Since the square of NLO amplitude corresponds to the NNLO, we should include the contribution from the LO amplitude times two-loop amplitude. In the alignment limit, this contribution vanishes due to the multiplication of the LO amplitude, and we expect that the two-loop diagram contribution is sub-leading even in the approximate alignment case up to NNLO.

9.2.2 Total decay width

In this subsection, we discuss the total decay width of the CP-odd Higgs boson including the higher-order corrections in the four types of 2HDMs. As similar to the decay branching ratio, the qualitative behavior does not change from those in LO.

Fig. 9.6 shows the total decay width of the CP-odd Higgs boson including the higher-order corrections as a function of $\tan\beta$. We have assumed the masses of additional Higgs bosons are

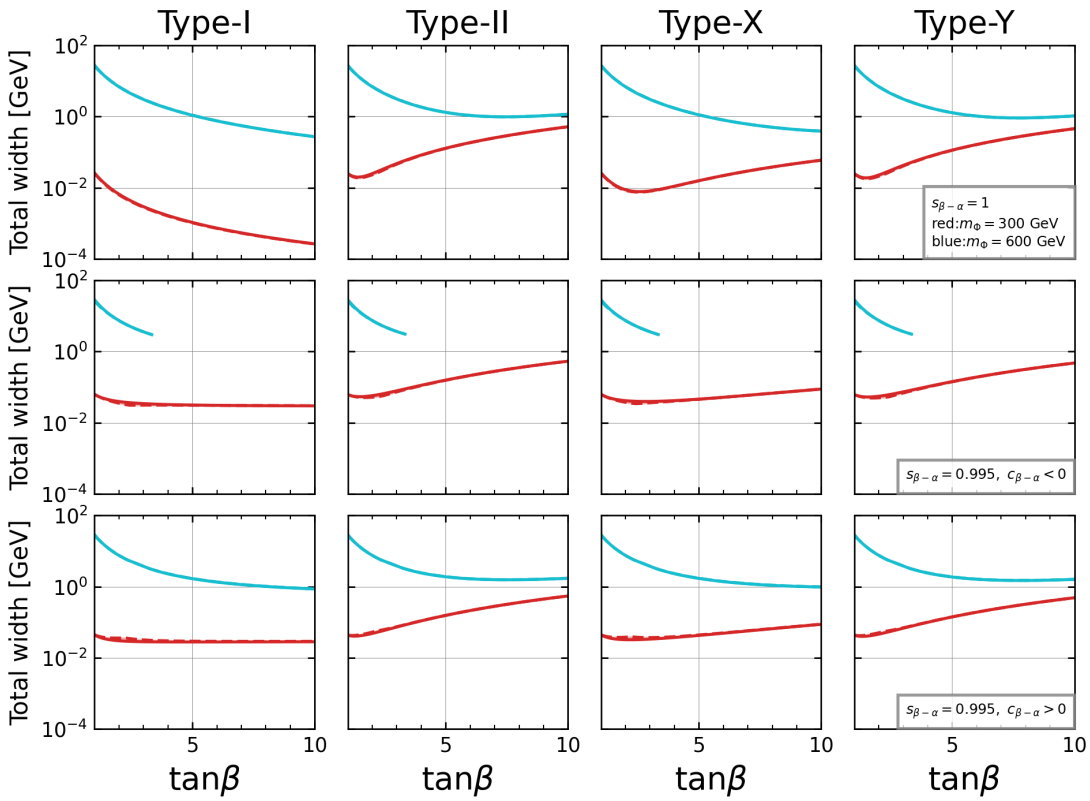

Figure 9.6: BR($A \to Zh$) including the higher-order corrections with $m_\Phi = 300$ GeV, and $\tan\beta$=2 (red), 3 (blue), 5 (green). The figures in the left column show the results with NLO EW corrections, while those in the right column show the results with partial NNLO EW corrections. The first (second) row shows the results in the Type-I (Type-II) 2HDM. We take masses of additional Higgs bosons are degenerate. M_{max} (M_{min}) denotes the maximum (minimum) value of M satisfying the theoretical constraints and S, T parameters.

degenerate, and the red and blue lines correspond to $m_\Phi = 300$ and 600 GeV, respectively. As similar to the Figs. 9.3 and 9.4, we have scanned M under the theoretical constraints and S, T parameters.

In the Type-I 2HDM with the alignment limit, the total decay width monotonically decreases as $\tan\beta$ becomes large because the partial decay widths of $A \to f\bar{f}$ and $A \to gg$ are proportional to $\cot^2\beta$. On the other hand, the total decay width increases as $\tan\beta$ becomes large since either or both $A \to bb$ and $A \to \tau\tau$ decays are enhanced in the other types of 2HDMs, especially with $m_\Phi = 300$ GeV. Above the top-quark thresholds, the $A \to tt$ decay becomes the dominant decay mode, and we cannot see the sizable enhancement in the total decay width below $\tan\beta = 10$.

In the Type-I 2HDM with the approximate alignment, the total decay width behaves as almost constant, since the dominant $A \to Zh$ decay process is independent of $\tan\beta$ at the LO. In the other types of 2HDMs, the $A \to bb$ or $A \to \tau\tau$ decays are enhanced as $\tan\beta$ becomes large, and they increase the total decay width. Above the top-quark thresholds, the $A \to tt$ decay becomes the dominant decay mode, and the behaviors are almost the same as those in the alignment limit. Since the unitarity and vacuum stability bounds exclude the parameter regions as shown in Fig. 9.4, the lines with $m_\Phi = 600$ GeV are terminated in a middle way.

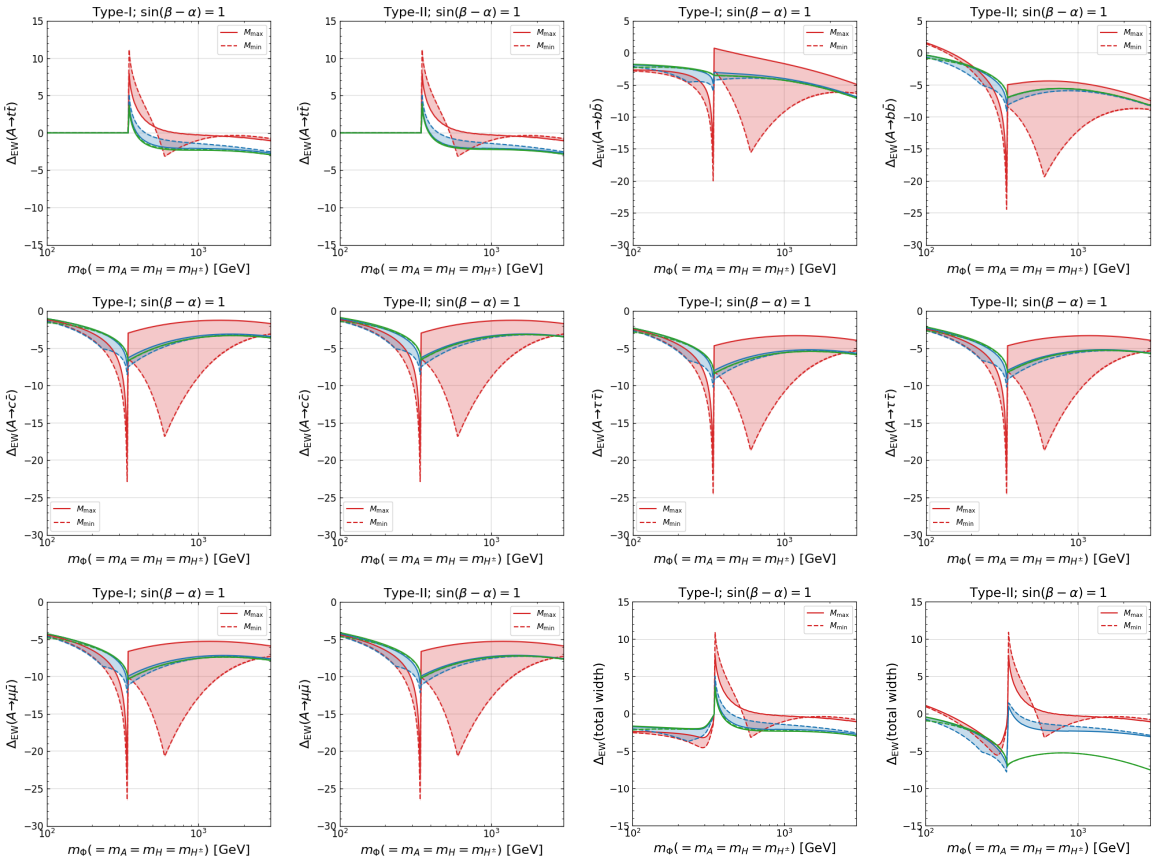

Figure 9.7: Size of NLO EW corrections to the partial decay widths of the CP-odd Higgs boson with $s_{\beta-\alpha} = 1$ and $\tan\beta$=1 (red), 3 (blue), 10 (green). Masses of additional Higgs bosons are degenerate, $m_\Phi = m_{H^\pm} = m_A = m_H$. $M_{max}(M_{min})$ denotes the maximum (minimum) value of M satisfying the theoretical constraints and S, T parameters.

9.2.3 Impact of NLO EW corrections to the decay rates

In this subsection, we examine the impact of NLO EW corrections on the decay rates of the CP-odd Higgs boson in the Type-I and Type-II 2HDMs. We do not show the results in the Type-X and Type-Y 2HDMs since they are almost similar to those in the Type-I or Type-II 2HDMs. We introduce the following quantity to describe the magnitudes of NLO EW corrections.

$$\Delta_{\rm EW}(A \to XY) = \frac{\Gamma_{\rm NLO\ EW}(A \to XY)}{\Gamma_{\rm LO}(A \to XY)} - 1, \tag{9.53}$$

where $\Gamma_{\rm NLO\ EW}(A \to XY)$ corresponds to the decay rates without QCD corrections. For the calculation of decay rates at LO $\Gamma^{\rm LO}$, we employ the quark pole masses, not the running masses. We evaluate $\Delta_{\rm EW}(A \to XY)$ in both the alignment limit, and the approximately alignment scenario, $s_{\beta-\alpha} = 0.995$. For each scenario, we take $\tan\beta$ as $\tan\beta = 1, 3$, and 10. We scan M in the region of $0 < M < 1500$ GeV.

Fig. 9.7 shows the NLO EW corrections to the partial decay widths of the CP-odd Higgs boson as a function of the masses of additional Higgs bosons with $s_{\beta-\alpha} = 1$. The red, blue, and green colored regions correspond to $\tan\beta$=1, 3, and 10, respectively. We assume the masses of additional Higgs bosons are degenerate. The solid and dashed lines correspond to the results with maximum and minimum values of M under the constraints, respectively.

The behavior of the NLO EW corrections on the $A \to ff$ decays is almost the same except

for the $A \to tt$ decay. For the decay into light fermions, there is the threshold effect of top-quark loop diagrams in the two-point function of the neutral Higgs bosons. On the other hand, the 1PI diagrams in $At\bar{t}$ vertex also show characteristic behavior at $m_\Phi \simeq 2m_t$ and this cause the different behavior on the $A \to tt$ decay. We note that the NLO EW corrections do not decouple even if m_Φ is sufficiently large since the decoupling theorem [34] is not applicable.

In the case with $\tan\beta = 1$, there is additional kinks at $m_\Phi \simeq 600$ GeV. This corresponds to the points where the values of M change from zero to non-zero due to the perturbative unitarity. At this point, the scalar couplings take maximal value under the constraints especially from perturbative unitarity, and the non-decoupling effects of Higgs boson's loops become dominant. The magnitude of the non-decoupling effects reaches 20% for $A \to bb$ and $A \to \tau\tau$, while it is below 5% for $A \to tt$.

For the case with $\tan\beta = 3$ and 10, M is almost degenerate with m_Φ due to the strict theoretical constraints. However, we have several percent deviations, and the corrections, especially on $A \to bb$ and $A \to \tau\tau$, become large when the additional Higgs bosons become heavy. We can also see the sizable negative corrections on the total decay width in the Type-II 2HDM, which mainly come from the $A \to bb$ and $\tau\tau$ decays.

Fig. 9.8 shows the results with $s_{\beta-\alpha} = 0.995$ and $c_{\beta-\alpha} < 0$ as a function of m_Φ. Since the deviation from the alignment limit is small, the qualitative behavior of the NLO EW corrections on the $A \to ff$ decays is almost unchanged. The main differences between the case with $s_{\beta-\alpha} = 1$ and $s_{\beta-\alpha} \neq 1$ are upper bound on the masses of the additional Higgs bosons and the $A \to Zh$ decay. Since we cannot take the decoupling limit keeping $s_{\beta-\alpha} \neq 1$, the masses of the additional Higgs bosons should be below 1 TeV with $s_{\beta-\alpha} = 0.995$ and $\tan\beta = 1$ under the theoretical constraints, especially perturbative unitarity.

In the $A \to Zh$ decay, there are two kinks at $m_\Phi \simeq 200$ GeV and 350 GeV. The first one corresponds to the threshold effect of Zh, and the second one corresponds to those of top-quark. Near the top-quark threshold, the magnitude of the NLO EW correction is above 50%, while it decreases as m_Φ becomes large. The behavior of the NLO EW correction to the total decay width is mainly determined by the $A \to tt$ and $A \to Zh$ decays. When $\tan\beta \simeq 1$, the $A \to tt$ decay is the main decay mode, and it determines the shape of the NLO EW correction above the top-quark threshold. Below the top-quark threshold with $\tan\beta \simeq 1$, the $A \to Zh$ decay is the main decay mode, and NLO EW correction increases the total decay width about 10%. When $\tan\beta > 1$, the $A \to tt$ decay is suppressed, and the $A \to Zh$ decay is dominant, while $A \to bb$ and $A \to \tau\tau$ also contribute in the Type-II, X and Y 2HDMs.

Fig. 9.9 shows the results with $s_{\beta-\alpha} = 0.995$ and $c_{\beta-\alpha} > 0$ as a function of m_Φ. The main differences between the case with $c_{\beta-\alpha} > 0$ are the possible value of $\tan\beta$ and the sign of the NLO EW corrections to the $A \to Zh$ decay. The allowed regions for $\tan\beta = 10$ are broader than those for $\tan\beta = 3$, and the corrections $\Delta_{\rm EW}$ for $\tan\beta = 10$ can be larger compared with $c_{\beta-\alpha} < 0$. In addition, the sign of the NLO EW corrections to the $A \to Zh$ decay is opposite to those with $c_{\beta-\alpha} < 0$, and higher-order corrections decrease the partial decay width. The behavior of the NLO EW correction to the total decay width is mainly determined by the $A \to tt$ and $A \to Zh$ decays as similar to the case with $c_{\beta-\alpha} < 0$.

9.3 Decay pattern of the CP-odd Higgs boson in the approximate alignment scenario

In this section, we discuss the decay pattern of the CP-odd Higgs boson in the approximate alignment scenario under the current experimental constraints. In addition to the theoretical

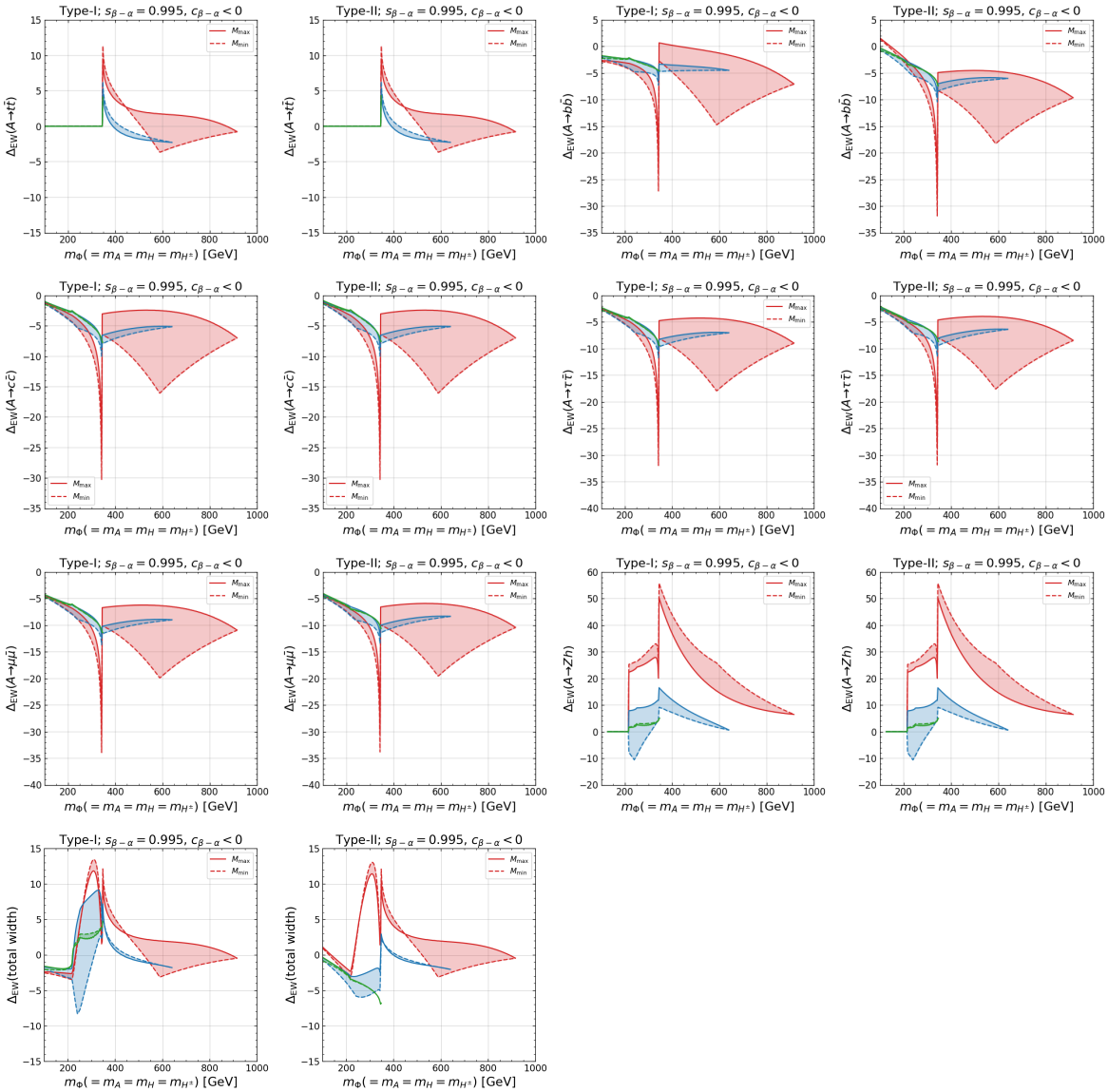

Figure 9.8: Size of NLO corrections for the decay widths of the CP-odd Higgs boson with $s_{\beta-\alpha}=0.995$, $c_{\beta-\alpha}<0$ and $\tan\beta$=1 (red), 3 (blue), 10 (green).

constraints and the S, T parameters, we take into account the constraint from the direct search for the additional Higgs bosons decay into a pair of fermions, Higgs signal strength, and flavor experiments. Although there are constraints from the direct search for $A\to Zh$ and $H\to hh$ decays at the LHC, they are quite sensitive to the value of $s_{\beta-\alpha}$ and the excluded region would be changed when we include the higher-order corrections. Therefore, we dare to omit the constraint from the Higgs-to-Higgs decay modes in this thesis. We will study how the higher-order corrections modify the constraint from the direct search for the additional Higgs bosons elsewhere.

We consider two distinct scenarios for the mass of the CP-odd Higgs boson,

$$\text{Scenario A}: \quad m_A = 300 \text{ GeV}, \tag{9.54}$$

$$\text{Scenario B}: \quad m_A = 800 \text{ GeV}, \tag{9.55}$$

For scenario A, the Type II and Y 2HDMs are already excluded by the flavor constraints (see, e.g, Ref. [65]). They impose $m_{H^\pm}\geq 800\,\text{GeV}$, and a large mass difference between A and $H^\pm$

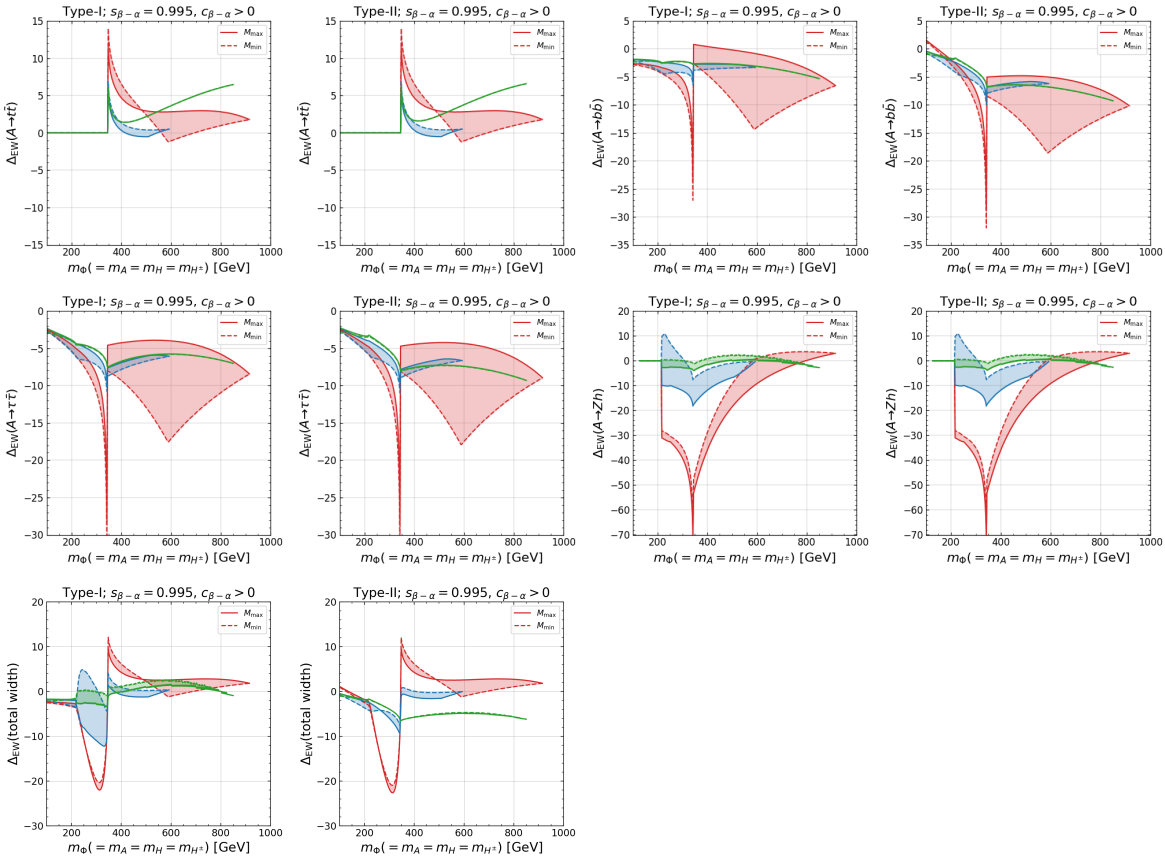

Figure 9.9: Size of NLO corrections for the decay widths of the CP-odd Higgs boson with $s_{\beta-\alpha}=0.995$, $c_{\beta-\alpha}>0$ and $\tan\beta$=1 (red), 3 (blue), 10 (green).

leads breakdown of perturbative unitarity. For scenario B, we examine all the types of 2HDMs.

In order to avoid constraint from the T parameter, we assume the mass of the CP-odd and charged Higgs bosons are degenerate as $m_A = m_{H^\pm}$. If the CP-even or charged Higgs bosons are lighter than the CP-odd Higgs boson, the $A \to ZH$ or $A \to W^\pm H^\mp$ decays are open. The tree-level AHZ and $AH^\pm W^\mp$ vertices do not vanish even in the alignment limit, and these decay modes can be dominant if there is a sizable mass difference. They drastically change the decay pattern of the CP-odd Higgs boson, and we also need to take into account the constraints from the additional Higgs-to-Higgs decay searches. Therefore, we focus on the scenario where the CP-odd Higgs boson is the lightest additional Higgs boson and clarify the phenomenological impact of a small deviation from the alignment limit.

The mass of the heavier CP-even Higgs bosons are scanned as following in both of the scenario,

$$m_A < m_H < m_A + 500 \text{ GeV}. \tag{9.56}$$

The remaining parameters are scanned for both the scenarios as

$$0.995 < s_{\beta-\alpha} < 1, \quad 2 < \tan\beta < 10, \quad 0 < M < m_A + 500\text{GeV}, \tag{9.57}$$

considering both cases of $c_{\beta-\alpha} < 0$ and $c_{\beta-\alpha} > 0$. For the lower bound of $\tan\beta$, we take into account the constraint from $B_d \to \mu\mu$ for scenario A [65]. In addition, $\tan\beta \lesssim 2$ is excluded by the direct search for the $A \to tt$ and $H^\pm \to tb$ decay mode.

We exclude the parameter points that are not consistent with the current measurement of the Higgs signal strength at the LHC in Ref. [21]. We evaluate the decay rates for h including

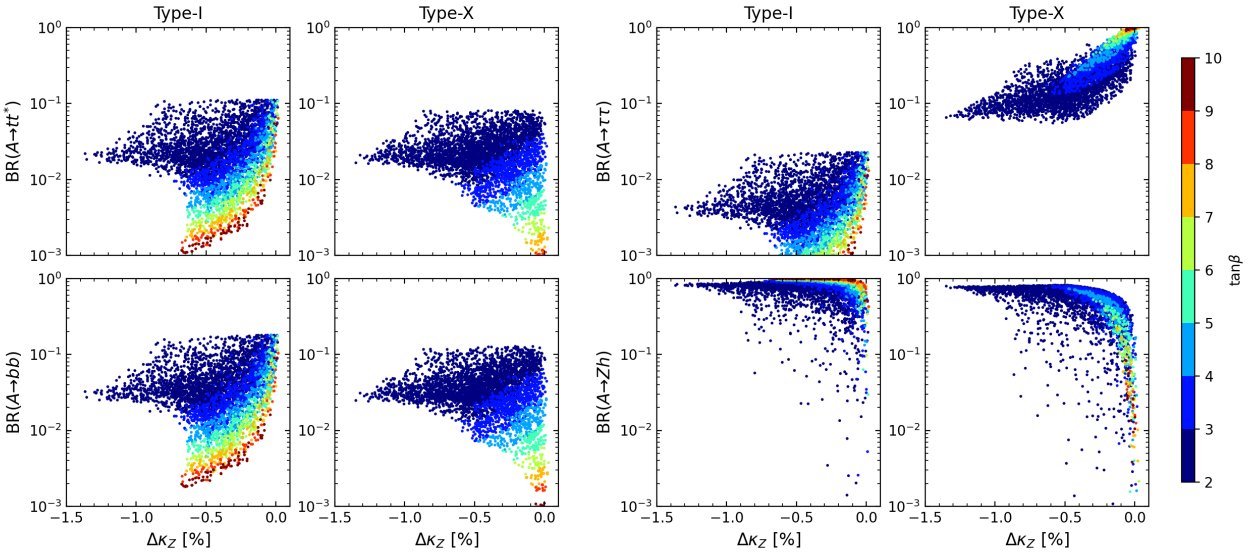

Figure 9.10: Decay branching ratios for the CP-odd Higgs boson as a function of $\Delta\kappa_Z (\equiv \kappa_Z - 1)$ in scenario A. The color differences correspond to the value of $\tan\beta$. Predictions on the Type-I (Type-X) are shown in the first and third columns (the second and fourth columns).

the NLO EW and NNLO QCD corrections by using `H-COUP v2` [46]. We define the scaling factors at the one-loop level,

$$\kappa_X = \sqrt{\frac{\Gamma^{\rm 2HDM}(h \to XY)}{\Gamma^{\rm SM}(h \to XY)}}, \tag{9.58}$$

We remove the parameter point, where the scaling factors for $XY = bb, \tau\tau, \gamma\gamma, gg, ZZ^*$ deviate from the values presented in Table 11 (a) of Ref. [21] at 95 % CL.

Fig. 9.10 shows the branching ratios of the CP-odd Higgs boson including the NLO EW corrections in Type-I and Type-X 2HDMs for scenario A as a function of $\Delta\kappa_Z$. The color differences correspond to the value of $\tan\beta$. For $\mathrm{BR}(A \to tt^*)$, the size of the branching ratio reaches about 10% with small $\tan\beta$ despite the phase space suppression of the three-body decay. Since the tree-level top Yukawa coupling is proportional to $\cot\beta$, $\mathrm{BR}(A \to tt^*)$ becomes small with large $\tan\beta$, especially in the Type-X 2HDM. In the Type-I 2HDM with the alignment limit, the LO amplitude of $A \to Zh$ vanishes, and other decay modes also monotonically decrease as $\tan\beta$ becomes large. Therefore, $\mathrm{BR}(A \to tt^*)$ can be about 10% even with large $\tan\beta$ near $\Delta\kappa_Z = 0$. Since the tree-level bottom Yukawa coupling is also proportional to $\cot\beta$ both in the Type-I and X 2HDMs, $\mathrm{BR}(A \to bb)$ shows almost the same behavior as in $\mathrm{BR}(A \to tt^*)$.

For $\mathrm{BR}(A \to \tau\tau)$, the size of the branching ratio reaches a few percent in the Type-I 2HDM, while that in the Type-X 2HDM reaches almost 100% with large $\tan\beta$ and $\Delta\kappa_Z \simeq 0$. Since the tree-level tau Yukawa coupling is proportional to $\tan\beta$ in the Type-X 2HDM, $\mathrm{BR}(A \to \tau\tau)$ enhances with large $\tan\beta$, while both $\mathrm{BR}(A \to tt^*)$ and $\mathrm{BR}(A \to bb)$ are suppressed. In addition, $\mathrm{BR}(A \to Zh)$ is also suppressed due to the small tree-level coupling. Therefore, $\mathrm{BR}(A \to \tau\tau)$ can be dominant in the near alignment limit with large $\tan\beta$.

For $\mathrm{BR}(A \to Zh)$, the size of the branching ratio reaches almost 100% percent both in the Type-I and X 2HDM, especially in the region with $\Delta\kappa_Z \neq 0$. We note that $\mathrm{BR}(A \to Zh)$ can reach about 100% even with $\Delta\kappa_Z \leq 0.6$, where we cannot observe the deviation in the hZZ coupling at the ILC. In this sense, the $A \to Zh$ decay is useful to investigate whether $s_{\beta-\alpha} = 1$

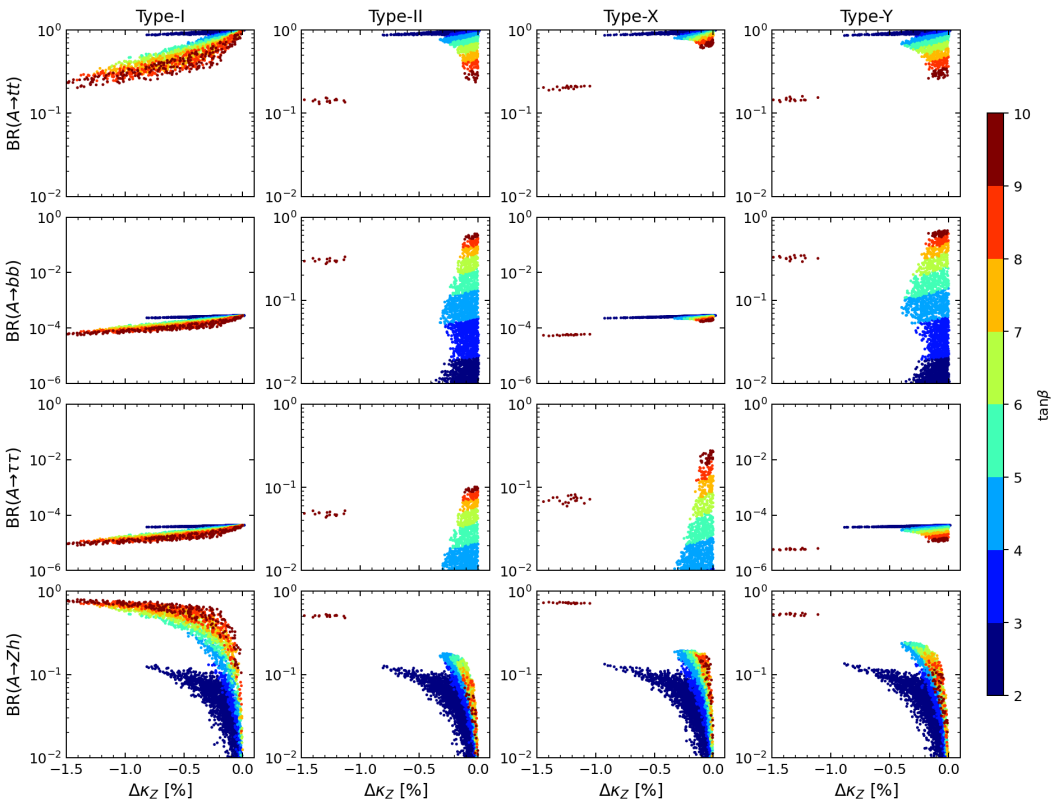

Figure 9.11: Decay branching ratios for the CP-odd Higgs boson as a function of $\Delta\kappa_Z (\equiv \kappa_Z - 1)$ in scenario B. The color differences correspond to the value of $\tan\beta$. Predictions on the Type-I, II, X and Y are shown from the left to right pannels in order.

or not.

Fig. 9.11 shows the branching ratios of the CP-odd Higgs boson including the NLO EW corrections in the Type-I, II, X, and Type-X 2HDMs for scenario B as a function of $\Delta\kappa_Z$. The color codes are the same as those in Fig. 9.10. In the Type-II, X, and Y 2HDMs, $|\Delta\kappa_Z| \gtrsim 10\%$ is excluded by the constraint from the Higgs signal measurements. In the Type-I 2HDM, we can take large $\tan\beta$ with sizable $\Delta\kappa_Z$, while such parameter regions are already excluded in the Type-II, X, and Y 2HDMs.

For $\mathrm{BR}(A \to tt)$, the size of the branching ratio reaches about 100% with small $\tan\beta$ independently of the types of 2HDMs. When $\tan\beta$ becomes large, the $A \to tt$ decay is suppressed by $\cot\beta$. However, the size of the branching ratio is several dozens percent even with $\tan\beta = 10$ for all types of the 2HDMs.

For $\mathrm{BR}(A \to bb)$, the size of the branching ratio is below a per-mill order in the Type-I and X 2HDMs, while that in the Type-X 2HDM reaches almost 60% with large $\tan\beta$ and $\Delta\kappa_Z \simeq 0$. Since the tree-level bottom Yukawa coupling is proportional to $\tan\beta$ in the Type-II and Y 2HDMs, $\mathrm{BR}(A \to bb)$ enhances with large $\tan\beta$.

For $\mathrm{BR}(A \to \tau\tau)$, the size of the branching ratio is below a per-mill order in the Type-I and Y 2HDMs, while that in the Type-II and X 2HDMs reaches almost 10% and 30%, respectively, with large $\tan\beta$ and $\Delta\kappa_Z \simeq 0$. This is because the tree-level tau Yukawa coupling is proportional to $\tan\beta$ in the Type-II and X 2HDMs. In the Type-II 2HDM, both $\mathrm{BR}(A \to bb)$ and $\mathrm{BR}(A \to \tau\tau)$ are enhanced, while only $\mathrm{BR}(A \to \tau\tau)$ is enhanced in the Type-X 2HDM.

For $\mathrm{BR}(A \to Zh)$, the size of the branching ratio reaches almost 100% percent in the Type-I 2HDM, especially in the region with $\Delta\kappa_Z \neq 0$. In the Type-II, X, and Y 2HDMs, $\mathrm{BR}(A \to Zh)$

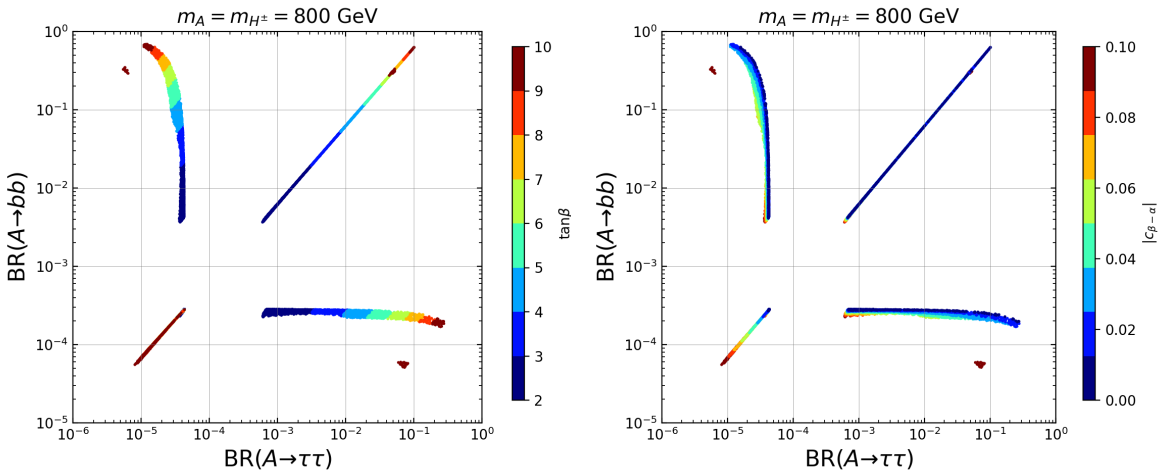

Figure 9.12: Correlation between BR($A \to \tau\tau$) and BR($A \to bb$) in Type-I, II, X and Y 2HDMs for scenario B. The color differences correspond to the value of $\tan\beta$ and $|c_{\beta-\alpha}|$ in the left and right panels, respectively.

reaches several dozen percent even with $\Delta\kappa_Z \leq 0.6$. Therefore, the $A \to Zh$ decay is still useful to investigate the approximate alignment case with relatively heavy additional Higgs bosons.

Fig. 9.11 shows the correlation between BR($A \to \tau\tau$) and BR($A \to bb$) in the Type-I, II, X and Y 2HDMs for scenario B. As we have seen, the decay pattern of the CP-odd Higgs boson mainly depends on the value of $\tan\beta$. In the Type-I 2HDM, both BR($A \to \tau\tau$) and BR($A \to bb$) become small, while both of them can take several dozen percent in the Type-II 2HDM. In the Type-X and Y 2HDM, only BR($A \to \tau\tau$) and BR($A \to bb$) becomes large, respectively. Therefore, we can distinguish the types of the Yukawa interactions by examing the decay pattern of the CP-odd Higgs boson. We would like to emphasize that discrimination via CP-odd Higgs measurements can work even in the approximate alignment case, as Fig. 9.11. Thus, in the case with no deviation in the SM-like Higgs boson couplings, the study of the CP-odd Higgs boson becomes important to reveal the nature of the 2HDMs.

Chapter 10

Higgs alignment from the twisted custodial symmetry at higher energy

In this chapter, we propose a new scenario of the 2HDM, where the current experimental data for the electroweak rho parameter and those for the Higgs boson couplings can be simultaneously explained as a consequence of the global symmetry in the Higgs potential at a high energy scale. In this scenario, the 2HDM is supposed to be a low energy effective theory up to a high energy scale Λ, above which a fundamental theory should appear. We assume that the Higgs potential respects a global symmetry at Λ, which is to be given as a consequence of the global symmetry structure of the fundamental theory. By the analysis using one-loop renormalization group equations, we find that the above experimental data can be explained in a natural way even when the masses of the extra Higgs bosons are near the electroweak scale. In this scenario, we have the characteristic predictions on the mass spectrum of the additional Higgs bosons and the SM-like Higgs boson couplings, and this scenario can be tested at future collider experiments.

10.1 Two Higgs doublet models and the twisted custodial symmetry

In this section, we discuss the twisted custodial symmetry in the 2HDM.

10.1.1 2HDMs with the softly-broken $\mathbb{Z}_2$ symmetry

In the softly-broken $\mathbb{Z}_2$ symmetric scenario, the Higgs potential is given by

$$\begin{aligned} V(\Phi_1,\Phi_2) = {} & m_{11}^2\Phi_1^\dagger\Phi_1 + m_{22}^2\Phi_2^\dagger\Phi_2 - (m_{12}^2\Phi_1^\dagger\Phi_2 + h.c.) \\ & + \frac{1}{2}\lambda_1(\Phi_1^\dagger\Phi_1)^2 + \frac{1}{2}\lambda_2(\Phi_2^\dagger\Phi_2)^2 + \lambda_3(\Phi_1^\dagger\Phi_1)(\Phi_2^\dagger\Phi_2) + \lambda_4(\Phi_1^\dagger\Phi_2)(\Phi_2^\dagger\Phi_1) \\ & + \frac{1}{2}\left[\lambda_5(\Phi_1^\dagger\Phi_2)^2 + h.c.\right], \end{aligned} \tag{10.1}$$

where m_{11}^2, m_{22}^2 and λ_{1-4} are real parameters while m_{12}^2 and λ_5 are complex in general. In the following, we analyze CP conserving Higgs sector. This additional assumption is required when we consider the custodial symmetric Higgs sector as we discuss later.

It is useful to work in the Higgs basis [80] to study the SM like limit in the 2HDM;

$$\begin{pmatrix} H_1 \\ H_2 \end{pmatrix} = \begin{pmatrix} \cos\beta & \sin\beta \\ -\sin\beta & \cos\beta \end{pmatrix} \begin{pmatrix} \Phi_1 \\ \Phi_2 \end{pmatrix}, \tag{10.2}$$

where the mixing angle is defined by $\tan\beta = v_2/v_1$ ($0 \le \beta \le \pi/2$), and v_i ($i = 1, 2$) are the vacuum expectation values (VEVs) of the neutral component of doublets in the $\mathbb{Z}_2$ basis given in Eq. (10.1); $\langle\Phi_i^0|\Phi_i^0\rangle = v_i/\sqrt{2}$. In the Higgs basis, only one of the Higgs doublets, H_1, has the VEV, $v = \sqrt{v_1^2 + v_2^2} = (\sqrt{2}G_F)^{-1/2} \simeq 246$ GeV where G_F is Fermi constant. We parameterize the doublets by

$$H_1 = \begin{pmatrix} G^+ \\ \frac{1}{\sqrt{2}}(v + h_1 + iG) \end{pmatrix}, \quad H_2 = \begin{pmatrix} H^+ \\ \frac{1}{\sqrt{2}}(h_2 + iA) \end{pmatrix}. \tag{10.3}$$

In this basis, the Higgs potential can be expressed as

$$\begin{aligned} V(H_1, H_2) = {} & Y_1^2 H_1^\dagger H_1 + Y_2^2 H_2^\dagger H_2 - Y_3^2 (H_1^\dagger H_2 + H_2^\dagger H_1) \\ & + \frac{1}{2} Z_1 (H_1^\dagger H_1)^2 + \frac{1}{2} Z_2 (H_2^\dagger H_2)^2 + Z_3 (H_1^\dagger H_1)(H_2^\dagger H_2) + Z_4 (H_1^\dagger H_2)(H_2^\dagger H_1) \\ & + \left\{ \frac{1}{2} Z_5 (H_1^\dagger H_2)^2 + \left[Z_6 H_1^\dagger H_1 + Z_7 H_2^\dagger H_2 \right] H_1^\dagger H_2 + h.c. \right\}, \end{aligned} \tag{10.4}$$

where Y_i^2 and Z_i are functions of m_{ij}^2 and λ_i. The stationary conditions are given by

$$Y_1^2 = -\frac{1}{2} Z_1 v^2, \quad Y_3^2 = \frac{1}{2} Z_6 v^2. \tag{10.5}$$

We note that not all of the parameters in the Higgs basis are independent in the softly-broken $\mathbb{Z}_2$ conserving scenario.

The mass matrices of charged state and CP-odd state are diagonalized in the Higgs basis,

$$m_{H^\pm} = Y_2^2 + \frac{1}{2} Z_3 v^2 = M^2 - \frac{1}{2}(\lambda_4 + \lambda_5) v^2, \tag{10.6}$$

$$m_A = Y_2^2 + \frac{1}{2}(Z_3 + Z_4 - Z_5) v^2 = M^2 - \lambda_5 v^2, \tag{10.7}$$

where we have introduced softly $\mathbb{Z}_2$ breaking scale $M = m_{12}/\sqrt{\sin\beta\cos\beta}$. The mass matrix for the CP-even states is not diagonarazed in the Higgs basis,

$$\frac{1}{2} \begin{pmatrix} h_1, & h_2 \end{pmatrix} \mathcal{M} \begin{pmatrix} h_1 \\ h_2 \end{pmatrix} = \frac{1}{2} \begin{pmatrix} h_1, & h_2 \end{pmatrix} \begin{pmatrix} Z_1 v^2 & Z_6 v^2 \\ Z_6 v^2 & Y_2^2 + \frac{1}{2} Z_{345} v^2 \end{pmatrix} \begin{pmatrix} h_1 \\ h_2 \end{pmatrix}, \tag{10.8}$$

and we need further rotation to obtain CP-even mass eigenstates h and H,

$$\begin{pmatrix} H \\ h \end{pmatrix} = \begin{pmatrix} \cos(\beta - \alpha) & -\sin(\beta - \alpha) \\ \sin(\beta - \alpha) & \cos(\beta - \alpha) \end{pmatrix} \begin{pmatrix} h_1 \\ h_2 \end{pmatrix}. \tag{10.9}$$

The squared masses of the CP-even Higgs bosons and the mixing angle $\beta - \alpha$ are given by

$$m_H^2 = \cos^2(\beta - \alpha)\mathcal{M}_{11}^2 + \sin^2(\beta - \alpha)\mathcal{M}_{22}^2 - \sin 2(\beta - \alpha)\mathcal{M}_{12}^2, \tag{10.10}$$

$$m_h^2 = \sin^2(\beta - \alpha)\mathcal{M}_{11}^2 + \cos^2(\beta - \alpha)\mathcal{M}_{22}^2 + \sin 2(\beta - \alpha)\mathcal{M}_{12}^2, \tag{10.11}$$

$$\tan 2(\beta - \alpha) = \frac{-2\mathcal{M}_{12}^2}{\mathcal{M}_{11}^2 - \mathcal{M}_{22}^2}. \tag{10.12}$$

We use the convention where $\sin(\beta - \alpha)$ is always positive, *i.e.*, $0 \le \beta - \alpha \le \pi$, and $\cos(\beta - \alpha)$ has the opposite sign from Z_6 [81]. In this paper, we identify h as the discovered Higgs boson $h(125)$, and all additional scalar bosons are assumed to be heavier than $h(125)$.

10.1.2 Alignment limit

In the mass eigenstate, the interaction terms among the gauge bosons and the CP-even scalars are given by,

$$\mathcal{L}_{int} = [\sin(\beta-\alpha)h + \cos(\beta-\alpha)H]\left(\frac{m_W^2}{v}W^{+\mu}W^-_\mu + \frac{m_Z^2}{2v}Z^\mu Z_\mu\right). \tag{10.13}$$

The Yukawa interaction terms among the fermions and the CP-even scalars are given by

$$\mathcal{L}_{int} = -\sum_{f=u,d,e}\frac{m_f}{v}\left(\xi_h^f \overline{f}fh + \xi_H^f \overline{f}fH\right), \tag{10.14}$$

where

$$\xi_h^f = \sin(\beta-\alpha) + \xi_f\cos(\beta-\alpha), \tag{10.15}$$

$$\xi_H^f = \cos(\beta-\alpha) - \xi_f\sin(\beta-\alpha), \tag{10.16}$$

and ξ_f is the Type dependent parameter given in Table 3.1. When $\sin(\beta-\alpha)=1$, the couplings of h with various SM particles become SM like. We call this SM-like limit, $\sin(\beta-\alpha)=1$, as the alignment limit in this paper.

The alignment limit can be achieved in different two ways [33, 156, 212]; (i) decoupling of additional Higgs bosons, and (ii) alignment without decoupling.

In the scenario (i), we take the decoupling limit: $M^2 \gg f(\lambda_i)v^2$. Then, we have

$$\tan 2(\beta-\alpha) \simeq \frac{-2Z_6v^2}{-M^2} \simeq 0, \tag{10.17}$$

where we have used that Z_6 does not depend on the M. Eq. (10.17) implies $\sin(\beta-\alpha)=1$, and the couplings of h become SM like. In this scenario, masses of the additional Higgs bosons are close to M, and they are decoupled from the electroweak physics.

In scenario (ii), the off-diagonal component of the mass matrix for CP-even state is equal to zero;

$$Z_6 = -\frac{1}{2}\sin 2\beta\left[\lambda_1\cos^2\beta - \lambda_2\sin^2\beta - \lambda_{345}\cos 2\beta\right] = 0, \tag{10.18}$$

where we have used abbreviation $\lambda_{345} = \lambda_3+\lambda_4+\lambda_5$. In this scenario, the additional Higgs bosons need not be decoupled, and masses of these particles can be taken around the electroweak scale. Therefore, this scenario is testable in current and future experiments [110, 200]. The simple realization of the condition in Eq. (10.18) is taking the natural alignment conditions [213],

$$\lambda_1 = \lambda_2 = \lambda_{345}, \tag{10.19}$$

where the alignment is realized independently of the value of $\tan\beta$. We will see that the conditions in Eq. (10.19) are derived from the twisted custodial symmetry [214].

10.1.3 The oblique parameters

The effect of new physics on the electroweak precision observables can be parameterized in terms of the oblique parameters, S, T and U [63,64]. In the 2HDM, the oblique parameters are modified from those in the SM due to the additional Higgs boson loop contritions and modified SM-like Higgs boson couplings.

Among these oblique parameters, the T parameter is related to the rho parameter as $\rho = 1 + \alpha_{em}T$, and it is sensitive for the mass squared differences of the Higgs bosons. When we decompose the T parameter into the SM contribution $T_{\rm SM}$ and the new physics effects ΔT, ΔT is given by [215–218]

$$\begin{aligned}\Delta T = \frac{1}{16\pi^2\alpha_{\rm em}v^2}\Big\{ & F(m_{H^\pm}^2, m_A^2) + s_{\beta-\alpha}^2\Big[F(m_{H^\pm}^2, m_H^2) - F(m_H^2, m_A^2)\Big] \\ & + c_{\beta-\alpha}^2\Big[F(m_h^2, m_{H^\pm}^2) - F(m_h^2, m_A^2)\Big] + 3c_{\beta-\alpha}^2\Big[F(m_H^2, m_Z^2) - F(m_H^2, m_W^2)\Big] \\ & + 3s_{\beta-\alpha}^2\Big[F(m_h^2, m_Z^2) - F(m_h^2, m_W^2)\Big] - 3\Big[F(m_{h_{ref}}^2, m_Z^2) - F(m_{h_{ref}}^2, m_W^2)\Big]\Big\}, \end{aligned} \tag{10.20}$$

where we have used abbreviation of $s_{\beta-\alpha} = \sin(\beta-\alpha)$ and $c_{\beta-\alpha} = \cos(\beta-\alpha)$. The function $F(x,y)$ is defined by

$$F(x,y) = \frac{x+y}{2} - \frac{xy}{x+y}\ln\frac{x}{y}, \tag{10.21}$$

and $F(x,x) = 0$. If one of the following relations (A, B or C) is satisfied, the loop corrections due to the additional Higgs bosons are canceled, and ΔT becomes small;

$$\text{(A)}: \quad m_A = m_{H^\pm}, \tag{10.22}$$

$$\text{(B)}: \quad m_H = m_{H^\pm} \text{ and } \sin(\beta-\alpha) = 1, \tag{10.23}$$

$$\text{(C)}: \quad m_h = m_{H^\pm} \text{ and } \cos(\beta-\alpha) = 1. \tag{10.24}$$

The possible value of ΔT is strictly constrained by the electroweak precision data [65, 219], and we expect that one of the above conditions is realized at the electroweak scale at least approximately. We will see that those conditions can be derived as a consequence of the custodial symmetry in the Higgs potential, and we can understand the smallness of ΔT in terms of the global symmetry structure of the Higgs potential.

10.1.4 Twisted custodial symmetry in the 2HDMs

We introduce bi-doublet fields [59] to study the structure of the Higgs potential especially for the $SU(2)_L \times SU(2)_R$ global symmetry.

$$M_i = (i\sigma_2 H_i^*, H_i), \quad (i = 1, 2), \tag{10.25}$$

where σ_2 is the second matrix of the Pauli matrices σ_a $(a = 1, 2, 3)$. These bi-doublet fields transform under the local gauge transformation as follows,

$$SU(2)_L: \ M_i \to \exp\{[ig\alpha_a(x)\tau_a]\}M_i, \quad U(1)_Y: \ M_i \to M_i \exp\{[-ig'Y\alpha_4(x)\sigma_3]\}, \tag{10.26}$$

where $\tau_a = \sigma_a/2$. We note that we may also use the following bi-doublets,

$$M_i P \equiv M_i \exp\{[-i\chi\sigma_3]\} = M_i \mathrm{diag}(e^{-i\chi}, e^{i\chi}), \quad \text{with } 0 \le \chi < 2\pi. \tag{10.27}$$

to construct the gauge-invariant Higgs potential since the $U(1)_Y$ transformation of bi-doublet fields commutes with P.

In the Higgs basis, we defined H_1 such that the VEV of this field is real and positive. Therefore we consider M_1 and $M_2' = M_2 P$ as building blocks of the Higgs potential. The $SU(2)_L \times SU(2)_R$ transformation of M_1 and M_2' is given by

$$M_1 \to L M_1 R^\dagger, \quad M_2' \to L M_2' R^\dagger, \tag{10.28}$$

where $L \in SU(2)_L, R \in SU(2)_R$. We can construct four $SU(2)_L \times U(1)_Y$ invariants as

$$\mathrm{Tr}(M_1^\dagger M_1) = 2|H_1|^2, \tag{10.29}$$

$$\mathrm{Tr}(M'^\dagger_2 M'_2) = 2|H_2|^2, \tag{10.30}$$

$$\mathrm{Tr}(M_1^\dagger M'_2) = e^{i\chi} H_1^\dagger H_2 + e^{-i\chi} H_2^\dagger H_1, \tag{10.31}$$

$$\mathrm{Tr}(M_1^\dagger M'_2 \sigma_3) = e^{i\chi} H_1^\dagger H_2 - e^{-i\chi} H_2^\dagger H_1, \tag{10.32}$$

where $\mathrm{Tr}(M_1^\dagger M_1), \mathrm{Tr}(M'^\dagger_2 M'_2)$ and $\mathrm{Tr}(M_1^\dagger M'_2)$ are hermitian and $SU(2)_L \times SU(2)_R$ invariant. On the other hand, $\mathrm{Tr}(M_1^\dagger M'_2 \sigma_3)$ is anti-hermitian and does not respect $SU(2)_L \times SU(2)_R$ symmetry.

The Higgs potential can be rewritten in terms of these invariants as

$$\begin{aligned}
V(M_1, M'_2) = {} & \frac{1}{2} Y_1^2 \mathrm{Tr}(M_1^\dagger M_1) + \frac{1}{2} Y_2^2 \mathrm{Tr}(M'^\dagger_2 M'_2) - \mathrm{Re}(Y_3^2 e^{-i\chi}) \mathrm{Tr}(M_1^\dagger M'_2) \\
& + \frac{1}{8} Z_1 \,\mathrm{Tr}^2(M_1^\dagger M_1) + \frac{1}{8} Z_2 \,\mathrm{Tr}^2(M'^\dagger_2 M'_2) + \frac{1}{4} Z_3 \,\mathrm{Tr}(M_1^\dagger M_1) \mathrm{Tr}(M'^\dagger_2 M'_2) \\
& + \frac{1}{4} [Z_4 + \mathrm{Re}(Z_5 e^{-2i\chi})] \mathrm{Tr}^2(M_1^\dagger M'_2) \\
& + \frac{1}{2} [\mathrm{Re}(Z_6 e^{-i\chi}) \,\mathrm{Tr}(M_1^\dagger M_1) + \mathrm{Re}(Z_7 e^{-i\chi}) \,\mathrm{Tr}(M'^\dagger_2 M'_2)] \mathrm{Tr}(M_1^\dagger M'_2) \\
& - i \,\mathrm{Im}(Y_3^2 e^{-i\chi}) \,\mathrm{Tr}(M_1^\dagger M'_2 \sigma_3) - \frac{1}{4} [Z_4 - \mathrm{Re}(Z_5 e^{-2i\chi})] \mathrm{Tr}^2(M_1^\dagger M'_2 \sigma_3) \\
& + \frac{i}{2} \mathrm{Im}(Z_5 e^{-2i\chi}) \,\mathrm{Tr}(M_1^\dagger M'_2) \mathrm{Tr}(M_1^\dagger M'_2 \sigma_3) \\
& + \frac{i}{2} [\mathrm{Im}(Z_6 e^{-i\chi}) \,\mathrm{Tr}(M_1^\dagger M_1) + \mathrm{Im}(Z_7 e^{-i\chi}) \,\mathrm{Tr}(M'^\dagger_2 M'_2)] \mathrm{Tr}(M_1^\dagger M'_2 \sigma_3).
\end{aligned} \tag{10.33}$$

As we mentioned, Z_6 and Z_7 are expressed in terms of the other Z_{1-5} and $\tan\beta$ in the softly-broken $\mathbb{Z}_2$ scenario.

If we assume the global $SU(2)_L \times SU(2)_R$ symmetry, we obtain

$$\mathrm{Im}(Y_3^2 e^{-i\chi}) = \mathrm{Im}(Z_5 e^{-2i\chi}) = \mathrm{Im}(Z_6 e^{-i\chi}) = \mathrm{Im}(Z_7 e^{-i\chi}) = 0, \tag{10.34}$$

$$Z_4 = \mathrm{Re}(Z_5 e^{-2i\chi}). \tag{10.35}$$

In order to satisfy Eqs. (10.34) and (10.35), CP invariance is required in the Higgs potential [220]. When the Higgs potential is CP invariant, Y_i^2 and Z_i are real, and we have

$$Z_4 = Z_5 \qquad \text{for} \quad \chi = 0,\, \pi, \tag{10.36}$$

or

$$Z_4 = -Z_5 \quad \text{and} \quad Y_3^2 = Z_6 = Z_7 = 0 \qquad \text{for} \quad \chi = \pi/2,\, 3\pi/2. \tag{10.37}$$

where we have used Eq. (10.34) to derive the second conditions of Eq. (10.37). These conditions can be expressed in terms of the parameters in Eq. (10.1), respectively,

$$\lambda_4 = \lambda_5, \qquad \text{for} \quad \chi = 0, \pi, \tag{10.38}$$

or

$$\lambda_4 = -\lambda_5,\ \lambda_1 = \lambda_2 = \lambda_3 \qquad \text{for} \quad \chi = \pi/2,\, 3\pi/2. \tag{10.39}$$

The former case shown in Eq. (10.38) corresponds to the usual realization of the custodial symmetry ($m_A = m_{H^\pm}$) introduced in Ref. [211], and the latter case in Eq. (10.39) is so-called the twisted custodial symmetry [214].

In the twisted-custodial symmetric scenario, the Higgs potential is given by

$$V(H_1, H_2) = Y_1^2 H_1^\dagger H_1 + Y_2^2 H_2^\dagger H_2 + \frac{1}{2} Z_S (H_1^\dagger H_1 + H_2^\dagger H_2)^2 - Z_{AS}(H_1^\dagger H_2 - H_2^\dagger H_1)^2, \quad (10.40)$$

where we have introduced $Z_S = Z_1 = Z_2 = Z_3$ and $Z_{AS} = Z_4 = -Z_5$. Masses of the physical Higgs bosons are expressed by

$$m_h^2 = Z_S v^2. \quad (10.41)$$

$$m_{H^\pm}^2 = m_H^2 = M^2 = Y_2 + \frac{1}{2} Z_S v^2. \quad (10.42)$$

$$m_A^2 = M^2 + Z_{AS} v^2. \quad (10.43)$$

We note that all scalars are simultaneously diagonalized in the Higgs basis, and we do not need additional rotation for the CP even states ($\sin(\beta - \alpha) = 1$). As we discussed in the previous subsection, ΔT becomes small when A is degenerate with $H^\pm$ or when H is degenerate with $H^\pm$ in the alignment limit. These conditions are naturally realized when the Higgs potential respects the custodial symmetry.

As it is pointed out in Ref. [220], the CP quantum numbers of H and A cannot be determined only from the Higgs potential when $Z_6 = Z_7 = 0$. If neutral Higgs-fermion interactions are CP conserving, as the case we are considering, we can determine such that H is the CP-even and A is the CP-odd. In the scenario of the twisted custodial symmetry defined in Eq. (10.37), $H^\pm$ is degenerated with the CP-even scalar H and this scenario is different from Case II in Ref. [211] where H should be regarded as the CP-odd state. Therefore, we can treat $\tan\beta$ as a free parameter differently from Case II where $\tan\beta = 1$ is required.

As it is well known that Yukawa coupling constants and the $U(1)_Y$ gauge coupling g' violate the custodial symmetry, so that this global symmetry is not the symmetry of the whole 2HDM Lagrangian. Therefore, the relations among the Higgs quartic couplings given in Eq. (10.39) are broken under the renormalization group evolution. Although we can explain the observed data of ΔT and aligned Higgs boson couplings by the twisted custodial symmetry in the Higgs potential, those violations indicate the peculiarity of the scenario where Higgs potential exactly respects twisted custodial symmetry at the electroweak scale. In the following section, we investigate the possibility of the approximate realization of the twisted-custodial symmetry at the electroweak scale, starting from a twisted-custodial symmetric theory at high scale Λ.

10.2 Boundary conditions and other setup for our scenario

In this section, we discuss constraints on S and T parameters and the Higgs boson couplings in the twisted-custodial symmetric scenario at a high energy scale Λ. We use the one-loop RG equations in the following analysis.

10.2.1 Boundary conditions at Λ

There are works in which several authors investigate the validity of the 2HDM up to higher energy scale and bounds of scalar masses thorough the RG evolution of the Higgs quartic couplings [91, 92, 221]. After the Higgs boson discovery, the possible cutoff scale is examined under the current experimental data [222–224]. In these works, experimental constraints on the oblique parameters and the SM like Higgs boson couplings are satisfied as the initial conditions

of the RG evolution at the electroweak scale. We can study the structure of the Higgs potential along this line by assuming a global symmetry is exactly realized at the electroweak scale. However, such a scenario is not plausible unless the global symmetry is the symmetry of the whole theory, because the Higgs potential no longer respects the global symmetry at any other scale.

In this paper, we investigate the possible explanation for the observed data at and below the electroweak scale in terms of the global symmetry of the Higgs potential at some higher scale Λ above which a fundamental theory should appear. Below Λ, the twisted-custodial symmetric 2HDM appears as the low energy effective theory. Following this scenario, we impose the condition of Eq. (10.39) at the scale Λ

$$\lambda_4(\Lambda) = -\lambda_5(\Lambda),\ \lambda_1(\Lambda) = \lambda_2(\Lambda) = \lambda_3(\Lambda). \tag{10.44}$$

As we discussed, the twisted custodial symmetry in the Higgs potential is broken under the RG evolution from Λ to the electroweak scale due to the correction of g' and y_i, so that we can expect that Eq. (10.44) are not satisfied at the electroweak scale.

10.2.2 Theoretical and experimental bounds

We numerically generate the parameter sets under the boundary condition in Eq. (10.44). We also impose the following theoretical conditions at and below Λ. First, we require (a) vacuum stability conditions [88–90,92,225]. Second, we require (b) perturbative unitarity bound [84–87]. Finally, we also require (c) absence of the Landau pole.

$$\lambda_i(\mu) < 8\pi,\ \overline{y}_f^2(\mu) < 4\pi. \tag{10.45}$$

To evaluate the $\lambda_i(\mu), (m_Z \leq \mu < \Lambda)$ from $\lambda_i(\Lambda)$, we need to know the value of the gauge couplings $g_i(\Lambda)$ and Yukawa couplings $y_i(\Lambda)$. At the one-loop level, the beta functions of g_i are independent of both λ_i and y_i, and $g_i(\Lambda)$ can be evaluated from the inputs $g_i(m_Z)$. Furthermore, the beta functions of y_i are independent of λ_i, so that we can evaluate $y_i(\Lambda)$ from the inputs values of m_f and $\tan\beta$ at the electroweak scale. For given values of $\lambda_i(\Lambda)$, $y_i(\Lambda)$ and $g_i(\Lambda)$, we calculate $\lambda_i(\mu), y_i(\mu)$ and $g_i(\mu)$ iteratively by using RG equations and confirm that the conditions (a), (b) and (c) are satisfied at each step until the electroweak scale.

To translate $\lambda_i(m_Z)$ into masses of the Higgs bosons and the mixing angle $\beta - \alpha$, we need to know the value of M. We scan M between $[0, 1000]$ GeV, and check if the parameter sets satisfy (d) the global minimum condition [93, 226];

$$D = m_{12}^2(m_{11}^2 - k^2 m_{22}^2)\left(\frac{v_2}{v_1} - k\right) > 0, \tag{10.46}$$

where $k = \sqrt[4]{\lambda_1/\lambda_2}$. We extract parameters that reproduce the mass of the discovered Higgs boson $m_h \simeq 125$ GeV. We allow the 5% error on the deduced value of m_h instead of imposing a more strict constraint because our numerical analysis is done at the one-loop order.

We evaluate S and T parameters and confirm whether the predicted values are satisfied by the current experimental data, *i.e.* $S = 0.02 \pm 0.10, T = 0.07 \pm 0.12$ and the 92% correlation among them [219]. We require the agreement between the prediction and observed data to be at the 2σ level [227].

The mixing between $h(125)$ and H, $\cos(\beta - \alpha)$, is evaluated from $\lambda_i(m_Z), M$ and $\tan\beta$. We check whether the predicted value of $\cos(\beta - \alpha)$ satisfies the current experimental bound at the 2σ level [20, 228].

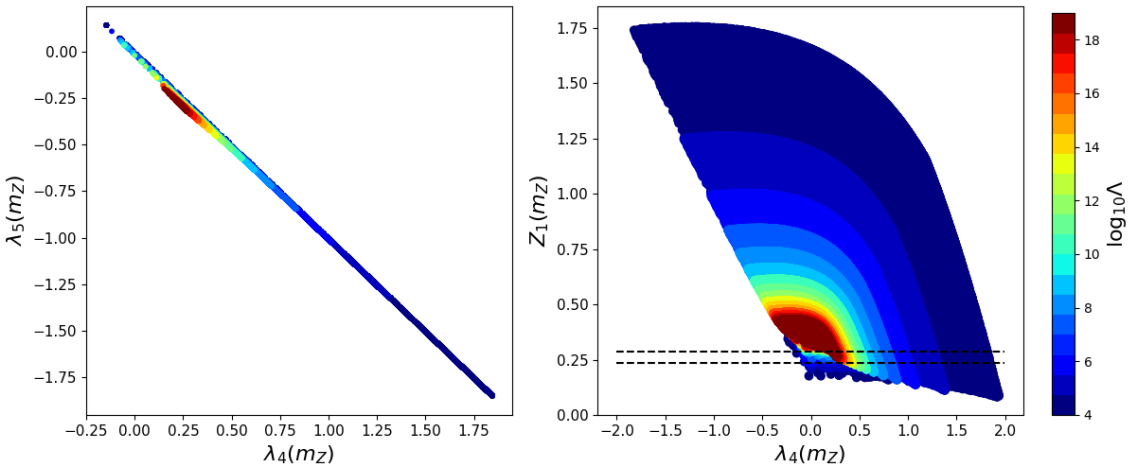

Figure 10.1: (Left) The values of λ_4 and λ_5 at electroweak scale for $\tan\beta = 5$ in Type I. (Right) The possible values of Z_1 and λ_4 at electroweak scale. The points in different color correspond to the different scale Λ. Dashed line shows the values of Z_1 which explains $m_h = 125 \pm 6$ GeV in the alignment limit.

10.2.3 Violation of the twisted custodial symmetry at the electroweak scale

In the twisted custodial scenario, the smallness of the ΔT parameter and the SM like Higgs boson couplings are realized by the condition of Eq. (10.39). However, this condition is violated at the electroweak scale even if the Higgs potential respects the twisted custodial symmetry at a higher scale Λ. In this subsection, we analyze the violation of the condition of Eq. (10.39) under the current experimental data.

In the following discussion, we show the results in the case of $\tan\beta = 5$ in Type-I as a representative. We have checked that the results for Type-X and Type-Y are similar for those for Type-I and Type-II, respectively. Furthermore, the major difference between Type-I and Type-II comes from the $b \to s\gamma$ constraint on the charged Higgs boson in Type-II: $m_{H^\pm} \gtrsim 580$ GeV [150]. As we will see later, $H^\pm$ and H are almost degenerate and they are lighter than A in our scenario. This implies that all of the additional Higgs bosons are heavier than 580 GeV, and it will be turned out that these are enough heavy to realize the alignment limit in the twisted-custodial symmetric scenario at a high energy scale. We have also checked that the behavior of λ_i couplings are almost same for various $\tan\beta$ except for the $\tan\beta \simeq 1$. We will discuss about the case of $\tan\beta \simeq 1$ later.

The left panel of Fig. 10.1 shows the possible values of $\lambda_4(m_Z)$ and $\lambda_5(m_Z)$. We can see that this scenario can be valid up to $\Lambda = 10^{19}$ GeV, and a part of the twisted-custodial condition in Eq. (10.39), $\lambda_4(m_Z) = -\lambda_5(m_Z)$, is approximately valid independently of the values of Λ. The sign of $\lambda_4(m_Z)$ tends to be positive, and it converges to be a finite value around 0.25 if we take Λ to a very high scale.

The stability of $\lambda_4 + \lambda_5 = 0$ can be understood by the form of the beta function,

$$\begin{aligned}\text{Type I}: 16\pi^2 \frac{d(\lambda_4+\lambda_5)}{d\ln\mu} &= 2(\lambda_1+\lambda_2+4\lambda_3+2\lambda_4+4\lambda_5)(\lambda_4+\lambda_5) - 3(3g^2+g'^2)(\lambda_4+\lambda_5) \\ &\quad + 2(3y_t^2+3y_b^2+y_\tau^2)(\lambda_4+\lambda_5) + 3g^2g'^2. \end{aligned} \tag{10.47}$$

As we have already mentioned, g' and y_i break the twisted custodial symmetry. Even if $\lambda_4+\lambda_5 = 0$ at initial point, $\lambda_4 + \lambda_5$ is generated via the $g^2g'^2$ term. However, this violating effect is

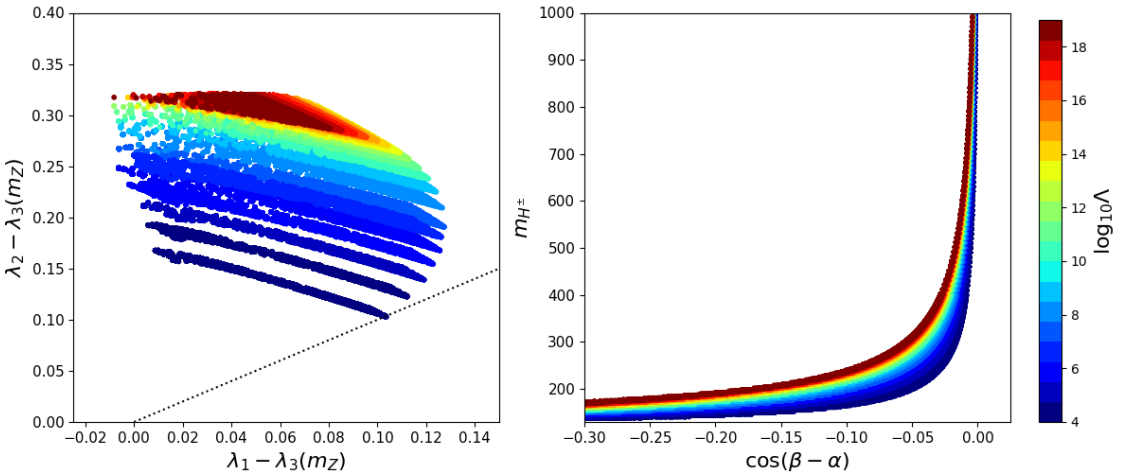

Figure 10.2: (Left) The values of $\lambda_2 - \lambda_1$ and $\lambda_2 - \lambda_3$ at electroweak scale for $\tan\beta = 5$ in Type I. The dashed line show the parameter points where $\lambda_1 = \lambda_2$. (Right) The decoupling behavior in the high scale twisted custodial symmetric scenario. The points in different color correspond to the different scale Λ and

negligible. In Type-II and Y, we also have the $y_t^2 y_b^2$ contribution to $\lambda_4 + \lambda_5$. However, this effect is also negligible, and $\lambda_4 + \lambda_5 = 0$ is approximately valid at the electroweak scale.

The right panel of Fig. 10.1 shows the predicted value of $Z_1(m_Z)$. As we have discussed, $\lambda_4(m_Z)$ tends to be positive and looks to converge to a small region. This behavior can be understood by looking at the predicted value of $Z_1(m_Z)$. In the alignment limit, the mass of $h(125)$ is given by

$$\begin{aligned} m_h^2 = Z_1 v^2 &= [\lambda_1 \cos^4\beta + \lambda_2 \sin^4\beta + 2\lambda_{345} \sin^2\beta \cos^2\beta]v^2 \\ &\simeq [\lambda_1 \cos^4\beta + \lambda_2 \sin^4\beta + 2\lambda_3 \sin^2\beta \cos^2\beta]v^2, \end{aligned} \tag{10.48}$$

where we have used $\lambda_4 + \lambda_5 \simeq 0$ in the last equality. To reproduce $m_h \simeq 125$ GeV, Z_1 should be $m_h^2/v^2 \simeq 0.26$ in the alignment limit. However, the vacuum stability condition

$$\sqrt{\lambda_1\lambda_2} + \lambda_3 + \lambda_4 - \lambda_5 \simeq \sqrt{\lambda_1\lambda_2} + \lambda_3 + 2\lambda_4 > 0, \tag{10.49}$$

sets the minimum value of Z_1 as

$$\begin{aligned} Z_1 &\simeq (\sqrt{\lambda_1}\cos^2\beta - \sqrt{\lambda_2}\sin^2\beta)^2 + 2(\sqrt{\lambda_1\lambda_2} + \lambda_3)\sin^2\beta\cos^2\beta \\ &> (\sqrt{\lambda_1}\cos^2\beta - \sqrt{\lambda_2}\sin^2\beta)^2 - 4\lambda_4 \sin^2\beta\cos^2\beta. \end{aligned} \tag{10.50}$$

This condition excludes $Z_1(m_Z) \simeq 0.26$ for almost all values of negative $\lambda_4(m_Z)$ in the alignment limit. Even positive λ_4, possible parameters with $Z_1 \simeq 0.26$ are limited when Λ is very high scale. This is why $\lambda_4(m_Z)$ takes some fixed values with $m_h \simeq 125$ GeV in the approximately alignment limit.

The left panel of Fig. 10.2 shows the possible values of $\lambda_1 - \lambda_3$ and $\lambda_2 - \lambda_3$ at the electroweak scale. As we can see both $\lambda_1 - \lambda_3$ and $\lambda_2 - \lambda_3$ take non-zero values, so that $\lambda_1 \neq \lambda_3$ and $\lambda_2 \neq \lambda_3$. Furthermore, most of the parameter points are away from the dotted line which indicates $\lambda_1 = \lambda_2$, so that the second condition $\lambda_1 = \lambda_2 = \lambda_3$ is violated at the electroweak scale. This violation generates the off-diagonal component of the mass matrix for the CP-even scalars, and it predicts deviations in the couplings of $h(125)$ with various SM particles from those in the SM.

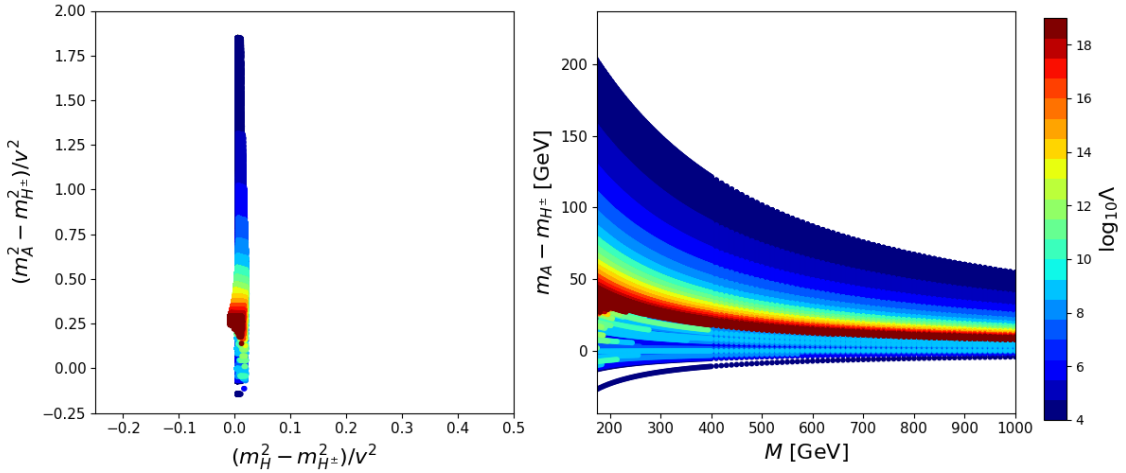

Figure 10.3: Possible mass differences among the additional Higgs bosons. Left figure shows M independent mass squared differences. Right figure shows mass differences among A and $H^\pm$.

The right panel of Fig. 10.2 shows the decoupling behavior in this scenario. We can see $m_{H^\pm} \gtrsim 300$ GeV is enough to achieve the alignment limit. Although Z_6 is generated via RG running, its value is not so large compared with the possible values which are allowed at the electroweak scale under the theoretical constraints.

As we have discussed in this section, we can explain the smallness of the ΔT parameter and the SM-like Higgs boson couplings without decoupling of the additional Higgs bosons by the twisted custodial symmetry of the Higgs potential at scale Λ. In the Type-II scenario, same argument is valid, however $m_{H^\pm} \lesssim 580$ GeV is excluded by the constraint of $b \to s\gamma$ [150].

10.3 Predictions from the boundary conditions

10.3.1 Mass spectrum of additional Higgs bosons

In this section, we analyze the prediction on the mass spectrum of additional Higgs bosons in the twisted-custodial symmetric scenario at a high energy scale. In the alignment limit, masses of the additional Higgs bosons are given in terms of the parameters in the $\mathbb{Z}_2$ basis,

$$m_H^2 = M^2 + \frac{1}{4}(\lambda_1 + \lambda_2 - 2\lambda_{345})v^2 \sin^2 2\beta, \tag{10.51}$$

$$m_{H^\pm}^2 = M^2 - \frac{1}{2}(\lambda_4 + \lambda_5)v^2, \tag{10.52}$$

$$m_A^2 = M^2 - \lambda_5 v^2. \tag{10.53}$$

Left panel of Fig. 10.3 shows the predicted mass squared differences in this scenario. We can see that A is heavier than $H^\pm$, while H is approximately degenerate with $H^\pm$ in the almost parameter spaces. To understand the prediction of the mass spectrum, we simplify the mass difference of the additional Higgs bosons using the condition $\lambda_4 + \lambda_5 \simeq 0$ which is valid even at the electroweak scale as shown in the left panel of Fig. 10.2,

$$\frac{m_A^2 - m_{H^\pm}^2}{v^2} = \lambda_4, \quad \frac{m_H^2 - m_{H^\pm}^2}{v^2} = (\lambda_1 + \lambda_2 - 2\lambda_3)\cot^2\beta \left(\frac{1}{1+\cot^2\beta}\right)^2. \tag{10.54}$$

The positivity and convergence behavior of the squared mass difference among A and $H^\pm$ are the consequence of the prediction on $\lambda_4(m_Z)$ which has been discussed in the previous section.

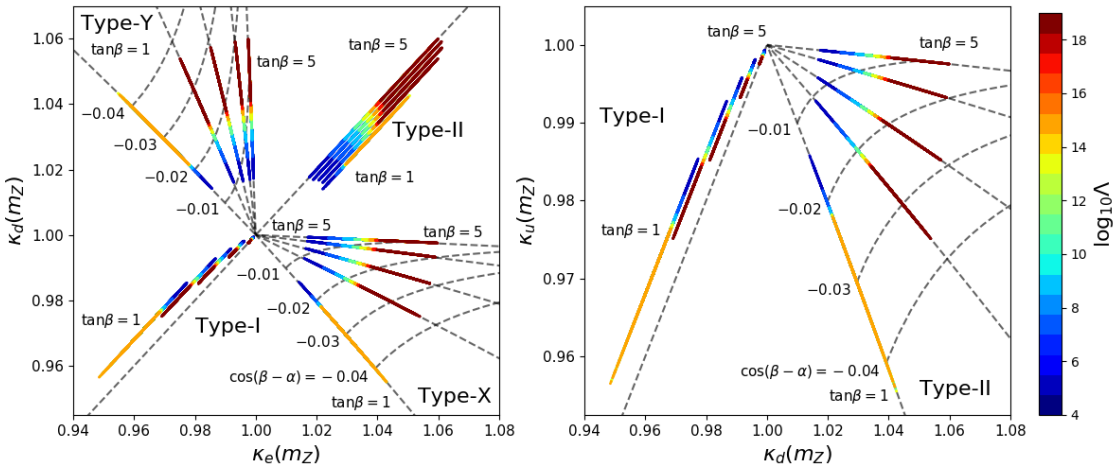

Figure 10.4: Predictions on the scaling factors of the SM-like Higgs boson in 2HDMs. The left figure shows the predicted values of κ_d and κ_e. The right figure shows those of κ_u and κ_d. $\tan\beta = 1, 1.5, 2, 3$ and 5 are chosen as representatives

Since $\lambda_1 - \lambda_3$ and $\lambda_2 - \lambda_3$ take non-zero values as shown in Fig. 10.2, the mass squared difference between H and $H^\pm$ is not zero. However, this difference becomes small if $\tan\beta$ is not close to unity because $\lambda_1 - \lambda_3$ and $\lambda_2 - \lambda_3$ are $\mathcal{O}(10^{-1})$ and $\cot^2\beta$ suppresses the possible mass squared difference. Therefore, the following mass spectrum is predicted in this scenario,

$$m_A \gtrsim m_H \simeq m_{H^\pm}. \tag{10.55}$$

The mass squared difference among A and $H^\pm$ converges to a definite value if Λ is as large as the Planck scale.

Right panel of Fig. 10.3 shows the behavior of the mass difference $\Delta m = m_A - m_{H^\pm}$, where Δm can be written as

$$\Delta m \simeq M\left[\sqrt{1 + \frac{\lambda_4 v^2}{M^2}} - 1\right]. \quad (\mu = m_Z) \tag{10.56}$$

If we take decoupling limit $M \to \infty$, Δm is close to zero as depicted in the right panel of Fig. 10.3. We note that mass squared differences Eq. (10.54) are M independent quantity, while Δm is M dependent quantity. If we determine Δm and masses of H and $H^\pm$, we can determine λ_4 and it imposes the upper bound of Λ.

We mention here the case of $\tan\beta \simeq 1$. In this parameter region, there is no $\cot^2\beta$ suppression, and $m_H - m_{H^\pm}$ can take about 50 GeV as the maximum value. However, these low $\tan\beta$ regions are constrained by the $b \to s\gamma$ experiments, and $m_{H^\pm} \gtrsim 600$GeV even in the Type-I and X [188].

10.3.2 The deviations in the Higgs boson couplings

In this subsection, we discuss the deviation in the SM-like Higgs boson couplings with gauge bosons, quarks and leptons. It is convenient to define the scaling factors by normalizing the coupling constant of the SM Higgs boson,

$$\mathcal{L}_{int} = \kappa_V h\left(\frac{m_W^2}{v} W^{+\mu} W^-_\mu + \frac{m_Z^2}{2v} Z^\mu Z_\mu\right) - \sum_{f=u,d,e} \kappa_f h \frac{m_f}{v} \overline{f} f. \tag{10.57}$$

From Eqs (10.13) and (10.14), κ factors are given at the tree level by

$$\kappa_V = \sin(\beta-\alpha), \quad \kappa_f = \xi_h^f = \sin(\beta-\alpha) + \xi_f \cos(\beta-\alpha). \tag{10.58}$$

As we have seen in Sec. 3, the alignment limit is approximately realized at the electroweak scale, and this implies that κ_V is necessarily close to the SM value in our scenario. For example, $|\cos(\beta-\alpha)| \leq 0.03$ when $\tan\beta = 10$ and $m_{H^\pm} \geq 300$ GeV in Type-I, and it corresponds to $\kappa_V \geq 0.9995$. It is difficult to measure this $\mathcal{O}(10^{-2})\%$ deviation even in the future precision measurement at the HL-LHC and the ILC. However, κ_f can be more deviated from SM values, because the deviations are enhanced by $\tan\beta$ except for Type-I. Furthermore, the direction of modifications for κ_d and κ_e are highly different in four types of Yukawa interactions, and we can discriminate the type of 2HDMs through the precise measurement of κ_f [110].

The left panel of Fig. 10.4 shows predicted values of κ_e and κ_d for each type of 2HDMs. We have plotted the predicted points for $\tan\beta = 1, 1.5, 2, 3, 5$ with 600GeV $\leq M \leq$ 700 GeV. For illustration purposes, we slightly shift lines along with $\kappa_x = \kappa_y$ in order to show $\tan\beta$ dependence in Type-I and II. As we can see, Λ can be taken to the Planck scale if $\tan\beta \geq 1.5$. When $\tan\beta = 1$, we cannot take Λ to be Planck scale and its maximal value is around 10^{14} GeV. This is because the square of the top Yukawa coupling becomes larger than 4π during RG evolution when $\tan\beta = 1$, and there is no solution above $\mu = 10^{14}$ GeV independently of the values of $\lambda_i(\Lambda)$. In Type-II, both of κ_d and κ_e deviates from SM values because $\xi_d = \xi_e = -\tan\beta$ enhances its deviation. In Type-X (Y), the modification of κ_e (κ_d) is enhanced respectively, while κ_d (κ_e) closes to SM value when we take larger $\tan\beta$ because its deviation proportional to $\cot\beta$. In Type-I, both of κ_d and κ_e close to SM values when we take large $\tan\beta$.

The right panel of Fig. 10.4 shows the predicted values of κ_u and κ_d. We slightly shift lines along with $\kappa_x = \kappa_y$ in order to show $\tan\beta$ dependence in Type-I as in the left panel. Although the predicted values of $\cos(\beta-\alpha)$ depend on the type of 2HDM, we only show the results in Type-I and II, because the scaling factors κ_u and κ_e are same in Type-I (II) and X (Y), and difference of predicted values between Type-I (II) and X (Y) which comes from τ Yukawa couplings in the beta functions are almost negligible. The modification of κ_u is proportional to $\cot\beta$ independently of the types of 2HDM, and it closes to the SM value when we take large $\tan\beta$. In Type-II and Y, the modification of κ_d is enhanced through $\tan\beta$, while κ_d also closes to SM value by $\cot\beta$ suppression in Type-I and X.

The possible deviations of κ_f are determined from the value of $\cos(\beta-\alpha)$ for fixed $\tan\beta$, and it is generated from the violating effect of the twisted custodial symmetry during RG evolution. Therefore modifications of the scaling factors become large when we take Λ to a higher scale, and we can expect about 5% deviations of κ_d and κ_e when Λ is Planck scale. We note that these several percent deviations in the scaling factors can be tested at the future HL-LHC and ILC experiments, and we can investigate not only the possible scale Λ but also the type of Yukawa interactions in 2HDMs through the precise measurement of κ_f.

Finally, we would like to mention the difference between our results and previous works. The discrimination of extended Higgs models thorough the precise measurement of SM-like Higgs boson couplings is studied at the tree level [110] and the one-loop level [97, 98]. In these works, the masses of additional Higgs bosons, M and mixing angles are free parameters, and they scanned parameters that satisfy the theoretical and experimental constraint. However, these values are predicted by the values of λ_i at Λ in our scenario, and the modifications of κ_f are related to the possible scale Λ. Therefore, we can utilize the precision measurement of the SM-like Higgs boson couplings not only to discriminate the types of the Yukawa interactions but also to investigate the new physics scale Λ, where global symmetry in the Higgs potential is restored and a fundamental theory should appear.

Chapter 11

Conclusion and discussion

In this thesis, we have comprehensively investigated the extended Higgs models. We have studied three main topics, the physics of the discovered Higgs boson, that of additional Higgs bosons and the global symmetry of the extended Higgs model.

In Chap. 6, we have discussed the physics of the discovered Higgs boson, especially its production cross section at electron-positron colliders. The discovery of the SM-like Higgs boson has opened a new window to indirectly explore a theory beyond the SM. The deviations from its SM predictions in the various Higgs observables such as the decay branching ratio, total width and production cross section tell us pieces of information of new physics models. After reviewing the renormalization procedure in the extended Higgs models and their applications to the SM-Higgs boson decay, we have discussed the production cross sections for the Higgs strahlung process at electron-proton colliders including the higher-order corrections. Most of the future lepton collider experiments are planned to operate at the center of beam energy around 250 GeV, where the production cross section of this process takes the maximal value. We have analyzed the deviation in the total cross section from its SM prediction in the various extended Higgs models. We have also examined the deviation in the cross section times branching ratio, and it is found that we can distinguish the various extended Higgs models by future precision measurements.

In Chaps. 7, 8 and 9, we have discussed the physics of additional Higgs bosons. The direct search of new particles is also the key program to study new physics models, and the LHC and HL-LHC will make remarkable progress in this direction. In Chaps. 7, we have pointed out that the indirect and direct studies play a complementary role. It is shown that the synergy between them enables us to explore the wide range of the parameter space of the 2HDM. Motivated by this investigation, we discuss the radiative corrections for the decays of additional Higgs bosons. We have found that the Higgs to Higgs decay process is sensitive to the radiative corrections, and including these effects are important to study the additional Higgs bosons.

In Chap. 10, we have discussed the structure of new physics, especially focusing on the global symmetry of the Higgs potential. The global symmetry whether it is exact or approximate is useful to understand the experimental data. We have proposed the scenario where the current experimental constraints are explained as a consequence of the global symmetry structure of the Higgs potential. In this scenario, the Higgs potential respects the global symmetry at a higher scale, but it is broken by the radiative corrections under the renormalization group running. While the Higgs potential respects the global symmetry no longer respects the global symmetry at the electroweak scale, we can explain the current experimental data without decoupling the additional Higgs bosons.

From the series of these studies, we have found that the nature of the Higgs sector can be

widely investigated by combining the precision measurement of the SM-like Higgs boson and the direct search of the additional Higgs bosons. In both of study, radiative corrections play an important role. Therefore, it is important to perform the theoretical calculation compatible with precision measurements in future collider experiments.

Appendix A

Input parameters

In this Appendix, we summarize the input parameters.

A.1 Lepton masses

The lepton masses are

$$m_e = 0.510998918 \times 10^{-3} \text{ GeV}, \tag{A.1}$$
$$m_\mu = 0.105658367 \text{ GeV}, \tag{A.2}$$
$$m_\tau = 1.77686 \text{ GeV}. \tag{A.3}$$

A.2 Electroweak parameters

The fine structure constant is

$$\alpha_{\text{em}}^{-1} = 137.035999139. \tag{A.4}$$

The Fermi constant is

$$G_F = 1.1663787 \times 10^{-5} \text{ GeV}^{-2}. \tag{A.5}$$

The mass of the Z boson is

$$m_Z = 91.1876 \text{ GeV}. \tag{A.6}$$

A.3 QCD parameters

A.3.1 Strong coupling constant

$$\alpha_s(m_Z) = 0.1181. \tag{A.7}$$

A.3.2 Quark masses

$$m_t = 173.1 \text{ GeV}, \tag{A.8}$$
$$m_b = 4.78 \text{ GeV}, \tag{A.9}$$
$$m_c = 1.27 \text{ GeV}. \tag{A.10}$$

A.4 Higgs boson mass

The mass of the discovered Higgs boson is

$$m_h = 125.1 \text{ GeV}. \tag{A.11}$$

Appendix B

Decay rates at the leading order

We present the analytic expressions of the decay rates of the Higgs boson at the LO. In order to specify the LO formula, the subscript 0 is put in the decay rate, Γ_0.

B.0.1 Decays of the neutral Higgs bosons

We define $\phi = h,\ H$ or A and $\mathcal{H} = h$ or H. The decay rates into a fermion pair are given by

$$\Gamma_0(\phi \to f\bar{f}) = \sqrt{2}G_F \frac{m_\phi m_f^2}{8\pi} |\kappa_f^\phi|^2 N_c^f \lambda_\phi \left(\frac{m_f^2}{m_\phi^2}, \frac{m_f^2}{m_\phi^2} \right), \tag{B.1}$$

where $N_c^f = 1$ (3) for f being a lepton (quark) and

$$\lambda_{h,H}(x,y) = \lambda^{3/2}(x,y), \quad \lambda_A(x,y) = \lambda^{1/2}(x,y), \tag{B.2}$$

with

$$\lambda(x,y) = (1-x-y)^2 - 2xy. \tag{B.3}$$

The decay rates into a pair of on-shell weak bosons ($V = W, Z$) are given by

$$\Gamma_0(\phi \to VV) = \sqrt{2}G_F \frac{m_\phi^3}{4\pi c_V} (\kappa_V^\phi)^2 \left(\frac{3m_V^4}{m_\phi^4} - \frac{m_V^2}{m_\phi^2} + \frac{1}{4} \right) \lambda^{1/2} \left(\frac{m_V^2}{m_\phi^2}, \frac{m_V^2}{m_\phi^2} \right), \tag{B.4}$$

where $c_V = 1$ (2) for $V = W$ (Z). When one of the weak bosons is off-shell, we obtain

$$\Gamma_0(\phi \to WW^*) = \frac{3m_W^4 G_F^2 m_\phi}{16\pi^3} (\kappa_V^\phi)^2 F\left(\frac{m_W}{m_\phi} \right), \tag{B.5}$$

$$\Gamma_0(\phi \to ZZ^*) = \frac{m_Z^4 G_F^2 m_\phi}{64\pi^3} (\kappa_V^\phi)^2 F\left(\frac{m_Z}{m_\phi} \right) \left(7 - \frac{40}{3} s_W^2 + \frac{160}{9} s_W^4 \right), \tag{B.6}$$

where

$$F(x) = -|1-x^2| \left(\frac{47}{2}x^2 - \frac{13}{2} + \frac{1}{x^2} \right) + 3(1 - 6x^2 + 4x^4) |\log x| + \frac{3(1 - 8x^2 + 20x^4)}{\sqrt{4x^2 - 1}} \cos^{-1}\left(\frac{3x^2 - 1}{2x^3} \right). \tag{B.7}$$

The loop induced decay rates are given by

$$\Gamma_0(\phi \to \gamma\gamma) = \frac{\sqrt{2}G_F\alpha_{\rm em}^2 m_\phi^3}{256\pi^3}\left|\kappa_V^\phi I_W^\phi + \sum_f \kappa_f^\phi Q_f^2 N_c^f I_F^\phi - \frac{\lambda_{H^+H^-\phi}}{v} I_S^\phi\right|^2, \tag{B.8}$$

$$\Gamma_0(\phi \to Z\gamma) = \frac{\sqrt{2}G_F\alpha_{\rm em}^2 m_\phi^3}{128\pi^3}\left(1-\frac{m_Z^2}{m_\phi^2}\right)^3\left|\kappa_V^\phi J_W^\phi + \sum_f \kappa_f^\phi Q_f N_c^f v_f J_F^\phi - \frac{\lambda_{H^+H^-\phi}}{v}\frac{g_Z c_{2W}}{2} J_S^\phi\right|^2, \tag{B.9}$$

$$\Gamma_0(\phi \to gg) = \frac{\sqrt{2}G_F\alpha_s^2 m_\phi^3}{128\pi^3}\left|\sum_q \kappa_q^\phi I_q^\phi\right|^2, \tag{B.10}$$

where

$$I_W^\phi = \frac{2m_W^2}{m_\phi^2}\left[6+\frac{m_\phi^2}{m_W^2}+(12m_W^2-6m_\phi^2)C_0(0,0,m_\phi^2;m_W,m_W,m_W)\right], \tag{B.11}$$

$$I_F^{\mathcal{H}} = -\frac{8m_f^2}{m_{\mathcal{H}}^2}\left[1+\left(2m_f^2-\frac{m_{\mathcal{H}}^2}{2}\right)C_0(0,0,m_{\mathcal{H}}^2;m_f,m_f,m_f)\right], \tag{B.12}$$

$$I_F^A = -4m_f^2 C_0(0,0,m_A^2;m_f,m_f,m_f), \tag{B.13}$$

$$I_S^\phi = \frac{2v^2}{m_\phi^2}[1+2m_{H^\pm}^2 C_0(0,0,m_\phi^2;m_{H^\pm},m_{H^\pm},m_{H^\pm})], \tag{B.14}$$

$$\begin{aligned} J_W^\phi = \frac{2m_W^2}{s_W c_W(m_\phi^2-m_Z^2)}\Bigg\{ & \left[c_W^2\left(5+\frac{m_\phi^2}{2m_W^2}\right)-s_W^2\left(1+\frac{m_\phi^2}{2m_W^2}\right)\right] \\ & \times\Bigg[1+2m_W^2 C_0(0,m_Z^2,m_\phi^2;m_f,m_f,m_f) \\ & +\frac{m_Z^2}{m_\phi^2-m_Z^2}[B_0(m_\phi^2;m_W,m_W)-B_0(m_Z^2;m_W,m_W)]\Bigg] \\ & -6c_W^2(m_\phi^2-m_Z^2)C_0(0,m_Z^2,m_\phi^2;m_f,m_f,m_f) \\ & +2s_W^2(m_\phi^2-m_Z^2)C_0(0,m_Z^2,m_\phi^2;m_f,m_f,m_f)\Bigg\}, \end{aligned} \tag{B.15}$$

$$\begin{aligned} J_F^{\mathcal{H}} = -\frac{8m_f^2}{s_W c_W(m_{\mathcal{H}}^2-m_Z^2)}\Big[1+\frac{1}{2}(4m_f^2-m_{\mathcal{H}}^2+m_Z^2)C_0(0,m_Z^2,m_{\mathcal{H}}^2;m_f,m_f,m_f) \\ +\frac{m_Z^2}{m_{\mathcal{H}}^2-m_Z^2}[B_0(m_{\mathcal{H}}^2;m_f,m_f)-B_0(m_Z^2;m_f,m_f)]\Big], \end{aligned} \tag{B.16}$$

$$J_F^A = -\frac{4m_f^2}{s_W c_W}C_0(0,m_Z^2,m_A^2;m_f,m_f,m_f), \tag{B.17}$$

$$\begin{aligned} J_S^\phi = \frac{2v^2}{e(m_\phi^2-m_Z^2)}\Bigg\{1+2m_{H^\pm}^2 C_0(0,m_Z^2,m_\phi^2;m_{H^\pm},m_{H^\pm},m_{H^\pm}) \\ +\frac{m_Z^2}{m_\phi^2-m_Z^2}\left[B_0(m_\phi^2;m_{H^\pm},m_{H^\pm})-B_0(m_Z^2;m_{H^\pm},m_{H^\pm})\right]\Bigg\}, \end{aligned} \tag{B.18}$$

where C_0 and B_0 are the Passarino-Veltman functions [229].

The decay rates into a scalar and an on-shell weak boson is given by

$$\Gamma_0(\phi \to \phi' V) = \frac{|g_{\phi\phi' V}|^2}{16\pi}\frac{m_\phi^3}{m_V^2}\lambda^{3/2}\left(\frac{m_V^2}{m_\phi^2}, \frac{m_{\phi'}^2}{m_\phi^2}\right), \tag{B.19}$$

where the scalar-scalar-gauge couplings are given in Appendix of Ref. [100]. When the weak boson is off-shell, the decay rate is given by

$$\Gamma_0(\phi \to \phi' W^*) = 9g^2|g_{\phi\phi' W}|^2\frac{m_\phi}{128\pi^3}G\left(\frac{m_{\phi'}^2}{m_\phi^2}, \frac{m_W^2}{m_\phi^2}\right), \tag{B.20}$$

$$\Gamma_0(\phi \to \phi' Z^*) = 3g_Z^2|g_{\phi\phi' Z}|^2\frac{m_\phi}{256\pi^3}G\left(\frac{m_{\phi'}^2}{m_\phi^2}, \frac{m_Z^2}{m_\phi^2}\right)\left(7 - \frac{40}{3}s_W^2 + \frac{160}{9}s_W^4\right), \tag{B.21}$$

where the function $G(x, y)$ is given as

$$\begin{aligned} G(x,y) = \frac{1}{12y}\Bigg\{ & 2(-1+x)^3 - 9\left(-1+x^2\right)y + 6(-1+x)y^2 \\ & + 6(1+x-y)y\sqrt{-\lambda(x,y)}\left[\tan^{-1}\left(\frac{-1+x-y}{\sqrt{-\lambda(x,y)}}\right) + \tan^{-1}\left(\frac{-1+x+y}{\sqrt{-\lambda(x,y)}}\right)\right] \\ & - 3\left[1 + (x-y)^2 - 2y\right]y\log x\Bigg\}. \end{aligned} \tag{B.22}$$

Finally, the decay rates into two lighter scalar bosons are given by

$$\Gamma_0(\phi \to \phi'\phi'') = (1+\delta_{\phi'\phi''})\frac{|\lambda_{\phi\phi'\phi''}|^2}{16\pi m_\phi}\lambda^{1/2}\left(\frac{m_{\phi'}^2}{m_\phi^2}, \frac{m_{\phi''}^2}{m_\phi^2}\right). \tag{B.23}$$

An example of this type of the decay is $H \to hh$.

B.0.2 Decays of the charged Higgs bosons

Decays of the charged Higgs bosons into two on-shell fermions are given by

$$\begin{aligned} \Gamma_0(H^\pm \to f f') = & \frac{G_F m_{H^\pm}}{4\sqrt{2}\pi}N_c^f C_f \lambda^{1/2}\left(\frac{m_f^2}{m_{H^\pm}^2}, \frac{m_{f'}^2}{m_{H^\pm}^2}\right) \\ & \times\left[\left(1 - \frac{m_f^2}{m_{H^\pm}^2} - \frac{m_{f'}^2}{m_{H^\pm}^2}\right)\left\{m_f^2\zeta_f^2 + m_{f'}^2\zeta_{f'}^2\right\} + 4\frac{m_f^2 m_{f'}^2}{m_{H^\pm}^2}\zeta_f\zeta_{f'}\right], \end{aligned} \tag{B.24}$$

where a factor C_f is $C_f = |V_{ud}|^2$ (1) for the decay into the up-type quark and the down-type quark (the lepton and the neutrino). The decay into an off-shell top quark and an on-shell down-type quark, $H^\pm \to t^* q_d \to W^\pm b q_d$ ($q_d = d, s, b$), is expressed by

$$\Gamma_0(H^\pm \to W^\pm b q_d) = \frac{3V_{tb}V_{tq_d}}{256\pi^3 m_{H^\pm}}g^2\frac{m_t^4}{v^2}\zeta_u^2 H\left(\frac{m_t^2}{m_{H^\pm}^2}, \frac{m_W^2}{m_{H^\pm}^2}\right), \tag{B.25}$$

with

$$H(x,y) = \frac{1}{4x^3y}\Big[2y^2\left\{4(x-1)y+3x\right\}\log y \\ + 2(x-1)\left\{(3x-1)x^3 - 3(x+1)xy^2 + 4y^3\right\}\log\frac{x-1}{x-y} \\ - x(y-1)\left\{(6x-5)x^2 - 4(x-2)y^2 + (3x-2)xy\right\}\Big], \tag{B.26}$$

where the mass of down-type quark is neglected.

The on-shell decays into a neutral Higgs boson and a W boson are expressed by

$$\Gamma_0(H^\pm \to \phi W^\pm) = \frac{m_{H^\pm}^3}{16\pi m_W^2}|g_{H^\pm\phi W}|^2\lambda^{\frac{3}{2}}\left(\frac{m_\phi^2}{m_{H^\pm}^2}, \frac{m_W^2}{m_{H^\pm}^2}\right), \tag{B.27}$$

where the coupling $g_{H^\pm\phi W}$ for each neutral Higgs boson is given in Appendix of Ref. [100]. The decays into a neutral Higgs boson and an off-shell W boson is given by

$$\Gamma_0(H^\pm \to \phi W^{\pm *}) = 9\frac{m_{H^\pm}}{128\pi^3}g^2|g_{H^\pm\phi W}|^2 G\left(\frac{m_\phi^2}{m_{H^\pm}^2}, \frac{m_W^2}{m_{H^\pm}^2}\right). \tag{B.28}$$

For the loop induced decay rates, $H^\pm \to W^\pm Z$ and $H^\pm \to W^\pm\gamma$, the concrete expressions of fermion loop contributions and boson loop contributions are given in Refs. [144, 146] and Refs. [145, 146], respectively.

Bibliography

[1] Chen-Ning Yang and Robert L. Mills. Conservation of Isotopic Spin and Isotopic Gauge Invariance. *Phys. Rev.*, Vol. 96, pp. 191–195, 1954.

[2] Ryoyu Utiyama. Invariant theoretical interpretation of interaction. *Phys. Rev.*, Vol. 101, pp. 1597–1607, 1956.

[3] H. Fritzsch, Murray Gell-Mann, and H. Leutwyler. Advantages of the Color Octet Gluon Picture. *Phys. Lett. B*, Vol. 47, pp. 365–368, 1973.

[4] D. J. Gross and Frank Wilczek. Asymptotically Free Gauge Theories - I. *Phys. Rev. D*, Vol. 8, pp. 3633–3652, 1973.

[5] D. J. Gross and Frank Wilczek. Asymptotically Free Gauge Theories - II. *Phys. Rev. D*, Vol. 9, pp. 980–993, 1974.

[6] H. David Politzer. Reliable Perturbative Results for Strong Interactions? *Phys. Rev. Lett.*, Vol. 30, pp. 1346–1349, 1973.

[7] S. L. Glashow. Partial Symmetries of Weak Interactions. *Nucl. Phys.*, Vol. 22, pp. 579–588, 1961.

[8] Steven Weinberg. A Model of Leptons. *Phys. Rev. Lett.*, Vol. 19, pp. 1264–1266, 1967.

[9] Abdus Salam. Weak and Electromagnetic Interactions. *Conf. Proc. C*, Vol. 680519, pp. 367–377, 1968.

[10] F. Englert and R. Brout. Broken Symmetry and the Mass of Gauge Vector Mesons. *Phys. Rev. Lett.*, Vol. 13, pp. 321–323, 1964.

[11] Peter W. Higgs. Broken Symmetries and the Masses of Gauge Bosons. *Phys. Rev. Lett.*, Vol. 13, pp. 508–509, 1964.

[12] Peter W. Higgs. Broken symmetries, massless particles and gauge fields. *Phys. Lett.*, Vol. 12, pp. 132–133, 1964.

[13] G. S. Guralnik, C. R. Hagen, and T. W. B. Kibble. Global Conservation Laws and Massless Particles. *Phys. Rev. Lett.*, Vol. 13, pp. 585–587, 1964.

[14] Peter W. Higgs. Spontaneous Symmetry Breakdown without Massless Bosons. *Phys. Rev.*, Vol. 145, pp. 1156–1163, 1966.

[15] S. Schael, et al. Precision electroweak measurements on the Z resonance. *Phys. Rept.*, Vol. 427, pp. 257–454, 2006.

[16] F. Abe, et al. Observation of top quark production in $\bar{p}p$ collisions. *Phys. Rev. Lett.*, Vol. 74, pp. 2626–2631, 1995.

[17] S. Abachi, et al. Observation of the top quark. *Phys. Rev. Lett.*, Vol. 74, pp. 2632–2637, 1995.

[18] Georges Aad, et al. Observation of a new particle in the search for the Standard Model Higgs boson with the ATLAS detector at the LHC. *Phys. Lett. B*, Vol. 716, pp. 1–29, 2012.

[19] Serguei Chatrchyan, et al. Observation of a New Boson at a Mass of 125 GeV with the CMS Experiment at the LHC. *Phys. Lett. B*, Vol. 716, pp. 30–61, 2012.

[20] Albert M Sirunyan, et al. Combined measurements of Higgs boson couplings in proton–proton collisions at $\sqrt{s} = 13\,\text{TeV}$. *Eur. Phys. J. C*, Vol. 79, No. 5, p. 421, 2019.

[21] Georges Aad, et al. Combined measurements of Higgs boson production and decay using up to 80 fb^{-1} of proton-proton collision data at $\sqrt{s} = 13$ TeV collected with the ATLAS experiment. *Phys. Rev. D*, Vol. 101, No. 1, p. 012002, 2020.

[22] N. Aghanim, et al. Planck 2018 results. VI. Cosmological parameters. *Astron. Astrophys.*, Vol. 641, p. A6, 2020. [Erratum: Astron.Astrophys. 652, C4 (2021)].

[23] Brian D. Fields, Keith A. Olive, Tsung-Han Yeh, and Charles Young. Big-Bang Nucleosynthesis after Planck. *JCAP*, Vol. 03, p. 010, 2020. [Erratum: JCAP 11, E02 (2020)].

[24] Y. Fukuda, et al. Evidence for oscillation of atmospheric neutrinos. *Phys. Rev. Lett.*, Vol. 81, pp. 1562–1567, 1998.

[25] Q. R. Ahmad, et al. Measurement of the rate of $\nu_e + d \to p + p + e^-$ interactions produced by ^{8}B solar neutrinos at the Sudbury Neutrino Observatory. *Phys. Rev. Lett.*, Vol. 87, p. 071301, 2001.

[26] Q. R. Ahmad, et al. Direct evidence for neutrino flavor transformation from neutral current interactions in the Sudbury Neutrino Observatory. *Phys. Rev. Lett.*, Vol. 89, p. 011301, 2002.

[27] Steven Weinberg. Implications of Dynamical Symmetry Breaking. *Phys. Rev. D*, Vol. 13, pp. 974–996, 1976. [Addendum: Phys.Rev.D 19, 1277–1280 (1979)].

[28] Eldad Gildener. Gauge Symmetry Hierarchies. *Phys. Rev. D*, Vol. 14, p. 1667, 1976.

[29] Leonard Susskind. Dynamics of Spontaneous Symmetry Breaking in the Weinberg-Salam Theory. *Phys. Rev. D*, Vol. 20, pp. 2619–2625, 1979.

[30] R. D. Peccei and Helen R. Quinn. CP Conservation in the Presence of Instantons. *Phys. Rev. Lett.*, Vol. 38, pp. 1440–1443, 1977.

[31] H. Georgi and S. L. Glashow. Unity of All Elementary Particle Forces. *Phys. Rev. Lett.*, Vol. 32, pp. 438–441, 1974.

[32] C. D. Froggatt and Holger Bech Nielsen. Hierarchy of Quark Masses, Cabibbo Angles and CP Violation. *Nucl. Phys. B*, Vol. 147, pp. 277–298, 1979.

[33] John F. Gunion and Howard E. Haber. The CP conserving two Higgs doublet model: The Approach to the decoupling limit. *Phys. Rev. D*, Vol. 67, p. 075019, 2003.

[34] Thomas Appelquist and J. Carazzone. Infrared Singularities and Massive Fields. *Phys. Rev. D*, Vol. 11, p. 2856, 1975.

[35] The International Linear Collider Technical Design Report - Volume 2: Physics. 6 2013.

[36] Keisuke Fujii, et al. Physics Case for the 250 GeV Stage of the International Linear Collider. 10 2017.

[37] Shoji Asai, Junichi Tanaka, Yutaka Ushiroda, Mikihiko Nakao, Junping Tian, Shinya Kanemura, Shigeki Matsumoto, Satoshi Shirai, Motoi Endo, and Mitsuru Kakizaki. Report by the Committee on the Scientific Case of the ILC Operating at 250 GeV as a Higgs Factory. 10 2017.

[38] Keisuke Fujii, et al. Tests of the Standard Model at the International Linear Collider. 8 2019.

[39] M. Bicer, et al. First Look at the Physics Case of TLEP. *JHEP*, Vol. 01, p. 164, 2014.

[40] Muhammd Ahmad, et al. CEPC-SPPC Preliminary Conceptual Design Report. 1. Physics and Detector. 3 2015.

[41] Masashi Aiko, Shinya Kanemura, and Kentarou Mawatari. Next-to-leading-order corrections to the Higgs strahlung process from electron–positron collisions in extended Higgs models. *Eur. Phys. J. C*, Vol. 81, No. 11, p. 1000, 2021.

[42] Masashi Aiko, Shinya Kanemura, Mariko Kikuchi, Kentarou Mawatari, Kodai Sakurai, and Kei Yagyu. Probing extended Higgs sectors by the synergy between direct searches at the LHC and precision tests at future lepton colliders. *Nucl. Phys. B*, Vol. 966, p. 115375, 2021.

[43] Masashi Aiko, Shinya Kanemura, and Kodai Sakurai. Radiative corrections to decays of charged Higgs bosons in two Higgs doublet models. *Nucl. Phys. B*, Vol. 973, p. 115581, 2021.

[44] Masashi Aiko and Shinya Kanemura. New scenario for aligned Higgs couplings originated from the twisted custodial symmetry at high energies. *JHEP*, Vol. 02, p. 046, 2021.

[45] Shinya Kanemura, Mariko Kikuchi, Kodai Sakurai, and Kei Yagyu. H-COUP: a program for one-loop corrected Higgs boson couplings in non-minimal Higgs sectors. *Comput. Phys. Commun.*, Vol. 233, pp. 134–144, 2018.

[46] Shinya Kanemura, Mariko Kikuchi, Kentarou Mawatari, Kodai Sakurai, and Kei Yagyu. H-COUP Version 2: a program for one-loop corrected Higgs boson decays in non-minimal Higgs sectors. *Comput. Phys. Commun.*, Vol. 257, p. 107512, 2020.

[47] Jorge C. Romao and Joao P. Silva. A resource for signs and Feynman diagrams of the Standard Model. *Int. J. Mod. Phys. A*, Vol. 27, p. 1230025, 2012.

[48] Yoichiro Nambu. Quasiparticles and Gauge Invariance in the Theory of Superconductivity. *Phys. Rev.*, Vol. 117, pp. 648–663, 1960.

[49] J. Goldstone. Field Theories with Superconductor Solutions. *Nuovo Cim.*, Vol. 19, pp. 154–164, 1961.

[50] T. Nakano and K. Nishijima. Charge Independence for V-particles. *Prog. Theor. Phys.*, Vol. 10, pp. 581–582, 1953.

[51] Kazuhiko Nishijima. Charge Independence Theory of V Particles. *Prog. Theor. Phys.*, Vol. 13, No. 3, pp. 285–304, 1955.

[52] M. Gell-Mann. Isotopic Spin and New Unstable Particles. *Phys. Rev.*, Vol. 92, pp. 833–834, 1953.

[53] Nicola Cabibbo. Unitary Symmetry and Leptonic Decays. *Phys. Rev. Lett.*, Vol. 10, pp. 531–533, 1963.

[54] Makoto Kobayashi and Toshihide Maskawa. CP Violation in the Renormalizable Theory of Weak Interaction. *Prog. Theor. Phys.*, Vol. 49, pp. 652–657, 1973.

[55] S. L. Glashow, J. Iliopoulos, and L. Maiani. Weak Interactions with Lepton-Hadron Symmetry. *Phys. Rev. D*, Vol. 2, pp. 1285–1292, 1970.

[56] L. D. Faddeev and V. N. Popov. Feynman Diagrams for the Yang-Mills Field. *Phys. Lett. B*, Vol. 25, pp. 29–30, 1967.

[57] K. Fujikawa, B. W. Lee, and A. I. Sanda. Generalized Renormalizable Gauge Formulation of Spontaneously Broken Gauge Theories. *Phys. Rev. D*, Vol. 6, pp. 2923–2943, 1972.

[58] Gerard 't Hooft. Renormalizable Lagrangians for Massive Yang-Mills Fields. *Nucl. Phys. B*, Vol. 35, pp. 167–188, 1971.

[59] P. Sikivie, Leonard Susskind, Mikhail B. Voloshin, and Valentin I. Zakharov. Isospin Breaking in Technicolor Models. *Nucl. Phys. B*, Vol. 173, pp. 189–207, 1980.

[60] Benjamin W. Lee, C. Quigg, and H. B. Thacker. The Strength of Weak Interactions at Very High-Energies and the Higgs Boson Mass. *Phys. Rev. Lett.*, Vol. 38, pp. 883–885, 1977.

[61] Benjamin W. Lee, C. Quigg, and H. B. Thacker. Weak Interactions at Very High-Energies: The Role of the Higgs Boson Mass. *Phys. Rev. D*, Vol. 16, p. 1519, 1977.

[62] Giuseppe Degrassi, Stefano Di Vita, Joan Elias-Miro, Jose R. Espinosa, Gian F. Giudice, Gino Isidori, and Alessandro Strumia. Higgs mass and vacuum stability in the Standard Model at NNLO. *JHEP*, Vol. 08, p. 098, 2012.

[63] Michael E. Peskin and Tatsu Takeuchi. A New constraint on a strongly interacting Higgs sector. *Phys. Rev. Lett.*, Vol. 65, pp. 964–967, 1990.

[64] Michael E. Peskin and Tatsu Takeuchi. Estimation of oblique electroweak corrections. *Phys. Rev. D*, Vol. 46, pp. 381–409, 1992.

[65] Johannes Haller, Andreas Hoecker, Roman Kogler, Klaus Mönig, Thomas Peiffer, and Jörg Stelzer. Update of the global electroweak fit and constraints on two-Higgs-doublet models. *Eur. Phys. J. C*, Vol. 78, No. 8, p. 675, 2018.

[66] D. de Florian, et al. Handbook of LHC Higgs Cross Sections: 4. Deciphering the Nature of the Higgs Sector. Vol. 2/2017, , 10 2016.

[67] A. Denner, S. Heinemeyer, I. Puljak, D. Rebuzzi, and M. Spira. Standard Model Higgs-Boson Branching Ratios with Uncertainties. *Eur. Phys. J. C*, Vol. 71, p. 1753, 2011.

[68] A. Djouadi, J. Kalinowski, and M. Spira. HDECAY: A Program for Higgs boson decays in the standard model and its supersymmetric extension. *Comput. Phys. Commun.*, Vol. 108, pp. 56–74, 1998.

[69] Abdelhak Djouadi, Jan Kalinowski, Margarete Muehlleitner, and Michael Spira. HDECAY: Twenty$_{++}$ years after. *Comput. Phys. Commun.*, Vol. 238, pp. 214–231, 2019.

[70] Ansgar Denner, Stefan Dittmaier, and Alexander Mück. PROPHECY4F 3.0: A Monte Carlo program for Higgs-boson decays into four-fermion final states in and beyond the Standard Model. *Comput. Phys. Commun.*, Vol. 254, p. 107336, 2020.

[71] Howard Georgi and Marie Machacek. DOUBLY CHARGED HIGGS BOSONS. *Nucl. Phys. B*, Vol. 262, pp. 463–477, 1985.

[72] Chien-Yi Chen, S. Dawson, and I. M. Lewis. Exploring resonant di-Higgs boson production in the Higgs singlet model. *Phys. Rev. D*, Vol. 91, No. 3, p. 035015, 2015.

[73] G. Cynolter, E. Lendvai, and G. Pocsik. Note on unitarity constraints in a model for a singlet scalar dark matter candidate. *Acta Phys. Polon. B*, Vol. 36, pp. 827–832, 2005.

[74] Shinya Kanemura, Mariko Kikuchi, and Kei Yagyu. One-loop corrections to the Higgs self-couplings in the singlet extension. *Nucl. Phys. B*, Vol. 917, pp. 154–177, 2017.

[75] Giovanni Marco Pruna and Tania Robens. Higgs singlet extension parameter space in the light of the LHC discovery. *Phys. Rev. D*, Vol. 88, No. 11, p. 115012, 2013.

[76] Jose R. Espinosa, Thomas Konstandin, and Francesco Riva. Strong Electroweak Phase Transitions in the Standard Model with a Singlet. *Nucl. Phys. B*, Vol. 854, pp. 592–630, 2012.

[77] Ian M. Lewis and Matthew Sullivan. Benchmarks for Double Higgs Production in the Singlet Extended Standard Model at the LHC. *Phys. Rev. D*, Vol. 96, No. 3, p. 035037, 2017.

[78] Sheldon L. Glashow and Steven Weinberg. Natural Conservation Laws for Neutral Currents. *Phys. Rev. D*, Vol. 15, p. 1958, 1977.

[79] E. A. Paschos. Diagonal Neutral Currents. *Phys. Rev. D*, Vol. 15, p. 1966, 1977.

[80] Sacha Davidson and Howard E. Haber. Basis-independent methods for the two-Higgs-doublet model. *Phys. Rev. D*, Vol. 72, p. 035004, 2005. [Erratum: Phys.Rev.D 72, 099902 (2005)].

[81] Jérémy Bernon, John F. Gunion, Howard E. Haber, Yun Jiang, and Sabine Kraml. Scrutinizing the alignment limit in two-Higgs-doublet models: m_h=125 GeV. *Phys. Rev. D*, Vol. 92, No. 7, p. 075004, 2015.

[82] Vernon D. Barger, J. L. Hewett, and R. J. N. Phillips. New Constraints on the Charged Higgs Sector in Two Higgs Doublet Models. *Phys. Rev. D*, Vol. 41, pp. 3421–3441, 1990.

[83] Mayumi Aoki, Shinya Kanemura, Koji Tsumura, and Kei Yagyu. Models of Yukawa interaction in the two Higgs doublet model, and their collider phenomenology. *Phys. Rev. D*, Vol. 80, p. 015017, 2009.

[84] Shinya Kanemura, Takahiro Kubota, and Eiichi Takasugi. Lee-Quigg-Thacker bounds for Higgs boson masses in a two doublet model. *Phys. Lett. B*, Vol. 313, pp. 155–160, 1993.

[85] Andrew G. Akeroyd, Abdesslam Arhrib, and El-Mokhtar Naimi. Note on tree level unitarity in the general two Higgs doublet model. *Phys. Lett. B*, Vol. 490, pp. 119–124, 2000.

[86] I. F. Ginzburg and I. P. Ivanov. Tree-level unitarity constraints in the most general 2HDM. *Phys. Rev. D*, Vol. 72, p. 115010, 2005.

[87] Shinya Kanemura and Kei Yagyu. Unitarity bound in the most general two Higgs doublet model. *Phys. Lett. B*, Vol. 751, pp. 289–296, 2015.

[88] Nilendra G. Deshpande and Ernest Ma. Pattern of Symmetry Breaking with Two Higgs Doublets. *Phys. Rev. D*, Vol. 18, p. 2574, 1978.

[89] K. G. Klimenko. On Necessary and Sufficient Conditions for Some Higgs Potentials to Be Bounded From Below. *Theor. Math. Phys.*, Vol. 62, pp. 58–65, 1985.

[90] Marc Sher. Electroweak Higgs Potentials and Vacuum Stability. *Phys. Rept.*, Vol. 179, pp. 273–418, 1989.

[91] Shuquan Nie and Marc Sher. Vacuum stability bounds in the two Higgs doublet model. *Phys. Lett. B*, Vol. 449, pp. 89–92, 1999.

[92] Shinya Kanemura, Takashi Kasai, and Yasuhiro Okada. Mass bounds of the lightest CP even Higgs boson in the two Higgs doublet model. *Phys. Lett. B*, Vol. 471, pp. 182–190, 1999.

[93] A. Barroso, P. M. Ferreira, I. P. Ivanov, and Rui Santos. Metastability bounds on the two Higgs doublet model. *JHEP*, Vol. 06, p. 045, 2013.

[94] I. F. Ginzburg, K. A. Kanishev, M. Krawczyk, and D. Sokolowska. Evolution of Universe to the present inert phase. *Phys. Rev. D*, Vol. 82, p. 123533, 2010.

[95] M. Bohm, H. Spiesberger, and W. Hollik. On the One Loop Renormalization of the Electroweak Standard Model and Its Application to Leptonic Processes. *Fortsch. Phys.*, Vol. 34, pp. 687–751, 1986.

[96] W. F. L. Hollik. Radiative Corrections in the Standard Model and their Role for Precision Tests of the Electroweak Theory. *Fortsch. Phys.*, Vol. 38, pp. 165–260, 1990.

[97] Shinya Kanemura, Mariko Kikuchi, Kentarou Mawatari, Kodai Sakurai, and Kei Yagyu. Loop effects on the Higgs decay widths in extended Higgs models. *Phys. Lett. B*, Vol. 783, pp. 140–149, 2018.

[98] Shinya Kanemura, Mariko Kikuchi, Kentarou Mawatari, Kodai Sakurai, and Kei Yagyu. Full next-to-leading-order calculations of Higgs boson decay rates in models with non-minimal scalar sectors. *Nucl. Phys. B*, Vol. 949, p. 114791, 2019.

[99] Shinya Kanemura, Mariko Kikuchi, and Kei Yagyu. Radiative corrections to the Yukawa coupling constants in two Higgs doublet models. *Phys. Lett. B*, Vol. 731, pp. 27–35, 2014.

[100] Shinya Kanemura, Mariko Kikuchi, and Kei Yagyu. Fingerprinting the extended Higgs sector using one-loop corrected Higgs boson couplings and future precision measurements. *Nucl. Phys. B*, Vol. 896, pp. 80–137, 2015.

[101] Shinya Kanemura, Mariko Kikuchi, and Kodai Sakurai. Testing the dark matter scenario in the inert doublet model by future precision measurements of the Higgs boson couplings. *Phys. Rev. D*, Vol. 94, No. 11, p. 115011, 2016.

[102] Shinya Kanemura, Kentarou Mawatari, and Kodai Sakurai. Single Higgs production in association with a photon at electron-positron colliders in extended Higgs models. *Phys. Rev. D*, Vol. 99, No. 3, p. 035023, 2019.

[103] Bernd A. Kniehl. Radiative corrections for $H \to$ f anti-f (γ) in the standard model. *Nucl. Phys. B*, Vol. 376, pp. 3–28, 1992.

[104] A. Dabelstein and W. Hollik. Electroweak corrections to the fermionic decay width of the standard Higgs boson. *Z. Phys. C*, Vol. 53, pp. 507–516, 1992.

[105] D. Yu. Bardin, B. M. Vilensky, and P. Kh. Khristova. Calculation of the Higgs boson decay width into fermion pairs. *Sov. J. Nucl. Phys.*, Vol. 53, pp. 152–158, 1991.

[106] Luminita Mihaila, Barbara Schmidt, and Matthias Steinhauser. $\Gamma(H \to b\bar{b})$ to order $\alpha\alpha_s$. *Phys. Lett. B*, Vol. 751, pp. 442–447, 2015.

[107] Bernd A. Kniehl. Higgs phenomenology at one loop in the standard model. *Phys. Rept.*, Vol. 240, pp. 211–300, 1994.

[108] Ansgar Denner. Techniques for calculation of electroweak radiative corrections at the one loop level and results for W physics at LEP-200. *Fortsch. Phys.*, Vol. 41, pp. 307–420, 1993.

[109] Abdelhak Djouadi. The Anatomy of electro-weak symmetry breaking. I: The Higgs boson in the standard model. *Phys. Rept.*, Vol. 457, pp. 1–216, 2008.

[110] Shinya Kanemura, Koji Tsumura, Kei Yagyu, and Hiroshi Yokoya. Fingerprinting non-minimal Higgs sectors. *Phys. Rev. D*, Vol. 90, p. 075001, 2014.

[111] Shinya Kanemura, Mariko Kikuchi, and Kei Yagyu. Radiative corrections to the Higgs boson couplings in the model with an additional real singlet scalar field. *Nucl. Phys. B*, Vol. 907, pp. 286–322, 2016.

[112] Shinya Kanemura, Mariko Kikuchi, Kodai Sakurai, and Kei Yagyu. Gauge invariant one-loop corrections to Higgs boson couplings in non-minimal Higgs models. *Phys. Rev. D*, Vol. 96, No. 3, p. 035014, 2017.

[113] Agnieszka Ilnicka, Tania Robens, and Tim Stefaniak. Constraining Extended Scalar Sectors at the LHC and beyond. *Mod. Phys. Lett. A*, Vol. 33, No. 10n11, p. 1830007, 2018.

[114] A. Belyaev, T. R. Fernandez Perez Tomei, P. G. Mercadante, C. S. Moon, S. Moretti, S. F. Novaes, L. Panizzi, F. Rojas, and M. Thomas. Advancing LHC probes of dark matter from the inert two-Higgs-doublet model with the monojet signal. *Phys. Rev. D*, Vol. 99, No. 1, p. 015011, 2019.

[115] Ansgar Denner, J. Kublbeck, R. Mertig, and M. Bohm. Electroweak radiative corrections to e+ e- —> H Z. *Z. Phys. C*, Vol. 56, pp. 261–272, 1992.

[116] Keisuke Fujii, et al. The role of positron polarization for the inital 250 GeV stage of the International Linear Collider. 1 2018.

[117] Bernd A. Kniehl. Radiative corrections for associated ZH production at future e^+e^- colliders. *Z. Phys. C*, Vol. 55, pp. 605–618, 1992.

[118] F. Bojarski, G. Chalons, D. Lopez-Val, and T. Robens. Heavy to light Higgs boson decays at NLO in the Singlet Extension of the Standard Model. *JHEP*, Vol. 02, p. 147, 2016.

[119] Marcel Krause, Robin Lorenz, Margarete Muhlleitner, Rui Santos, and Hanna Ziesche. Gauge-independent Renormalization of the 2-Higgs-Doublet Model. *JHEP*, Vol. 09, p. 143, 2016.

[120] J. Fleischer and F. Jegerlehner. Radiative Corrections to Higgs Production by $e^+e^- \to ZH$ in the {Weinberg-Salam} Model. *Nucl. Phys. B*, Vol. 216, pp. 469–492, 1983.

[121] Wenhai Xie, R. Benbrik, Abdeljalil Habjia, Souad Taj, Bin Gong, and Qi-Shu Yan. Signature of 2HDM at Higgs Factories. *Phys. Rev. D*, Vol. 103, No. 9, p. 095030, 2021.

[122] G. Belanger, F. Boudjema, J. Fujimoto, T. Ishikawa, T. Kaneko, K. Kato, and Y. Shimizu. Automatic calculations in high energy physics and Grace at one-loop. *Phys. Rept.*, Vol. 430, pp. 117–209, 2006.

[123] Qing-Feng Sun, Feng Feng, Yu Jia, and Wen-Long Sang. Mixed electroweak-QCD corrections to e+e-→HZ at Higgs factories. *Phys. Rev. D*, Vol. 96, No. 5, p. 051301, 2017.

[124] Yinqiang Gong, Zhao Li, Xiaofeng Xu, Li Lin Yang, and Xiaoran Zhao. Mixed QCD-EW corrections for Higgs boson production at e^+e^- colliders. *Phys. Rev. D*, Vol. 95, No. 9, p. 093003, 2017.

[125] Jacqueline Yan, Shun Watanuki, Keisuke Fujii, Akimasa Ishikawa, Daniel Jeans, Jan Strube, Junping Tian, and Hitoshi Yamamoto. Measurement of the Higgs boson mass and $e^+e^- \to ZH$ cross section using $Z \to \mu^+\mu^-$ and $Z \to e^+e^-$ at the ILC. *Phys. Rev. D*, Vol. 94, No. 11, p. 113002, 2016. [Erratum: Phys.Rev.D 103, 099903 (2021)].

[126] M. Misiak, Abdur Rehman, and Matthias Steinhauser. Towards $\overline{B} \to X_s\gamma$ at the NNLO in QCD without interpolation in m_c. *JHEP*, Vol. 06, p. 175, 2020.

[127] Georges Aad, et al. Combined measurements of Higgs boson production and decay using up to 80 fb^{-1} of proton-proton collision data at $\sqrt{s} = 13$ TeV collected with the ATLAS experiment. *Phys. Rev. D*, Vol. 101, No. 1, p. 012002, 2020.

[128] J. de Blas, et al. Higgs Boson Studies at Future Particle Colliders. *JHEP*, Vol. 01, p. 139, 2020.

[129] S. G. Gorishnii, A. L. Kataev, S. A. Larin, and L. R. Surguladze. Corrected Three Loop QCD Correction to the Correlator of the Quark Scalar Currents and $\Gamma_{\rm tot}(H^0 \to \text{Hadrons})$. *Mod. Phys. Lett. A*, Vol. 5, pp. 2703–2712, 1990.

[130] S. G. Gorishnii, A. L. Kataev, S. A. Larin, and L. R. Surguladze. Scheme dependence of the next to next-to-leading QCD corrections to Gamma(tot) (H0 —> hadrons) and the spurious QCD infrared fixed point. *Phys. Rev. D*, Vol. 43, pp. 1633–1640, 1991.

[131] K. G. Chetyrkin and A. Kwiatkowski. Second order QCD corrections to scalar and pseudoscalar Higgs decays into massive bottom quarks. *Nucl. Phys. B*, Vol. 461, pp. 3–18, 1996.

[132] S. A. Larin, T. van Ritbergen, and J. A. M. Vermaseren. The Large top quark mass expansion for Higgs boson decays into bottom quarks and into gluons. *Phys. Lett. B*, Vol. 362, pp. 134–140, 1995.

[133] E. Braaten and J. P. Leveille. Higgs Boson Decay and the Running Mass. *Phys. Rev. D*, Vol. 22, p. 715, 1980.

[134] Manuel Drees and Ken-ichi Hikasa. Heavy Quark Thresholds in Higgs Physics. *Phys. Rev. D*, Vol. 41, p. 1547, 1990.

[135] Abdelhak Djouadi. The Anatomy of electro-weak symmetry breaking. II. The Higgs bosons in the minimal supersymmetric model. *Phys. Rept.*, Vol. 459, pp. 1–241, 2008.

[136] David Albert, William J. Marciano, Daniel Wyler, and Zohreh Parsa. Decays of Intermediate Vector Bosons, Radiative Corrections and QCD Jets. *Nucl. Phys. B*, Vol. 166, pp. 460–492, 1980.

[137] S. Dawson and R. Kauffman. QCD corrections to Higgs boson production: nonleading terms in the heavy quark limit. *Phys. Rev. D*, Vol. 49, pp. 2298–2309, 1994.

[138] M. Spira, A. Djouadi, D. Graudenz, and P. M. Zerwas. Higgs boson production at the LHC. *Nucl. Phys. B*, Vol. 453, pp. 17–82, 1995.

[139] Robert Harlander and Philipp Kant. Higgs production and decay: Analytic results at next-to-leading order QCD. *JHEP*, Vol. 12, p. 015, 2005.

[140] Matthias Steinhauser. Corrections of O ($\alpha_s^{2)}$ to the decay of an intermediate mass Higgs boson into two photons. In *Ringberg Workshop: The Higgs Puzzle - What can We Learn from LEP2, LHC, NLC, and FMC?*, pp. 177–185, 12 1996.

[141] K. G. Chetyrkin, Bernd A. Kniehl, and M. Steinhauser. Hadronic Higgs decay to order α_s^4. *Phys. Rev. Lett.*, Vol. 79, pp. 353–356, 1997.

[142] K. G. Chetyrkin, Bernd A. Kniehl, M. Steinhauser, and William A. Bardeen. Effective QCD interactions of CP odd Higgs bosons at three loops. *Nucl. Phys. B*, Vol. 535, pp. 3–18, 1998.

[143] A. Djouadi and P. Gambino. QCD corrections to Higgs boson selfenergies and fermionic decay widths. *Phys. Rev. D*, Vol. 51, pp. 218–228, 1995. [Erratum: Phys.Rev.D 53, 4111 (1996)].

[144] Michel Capdequi Peyranere, Howard E. Haber, and Paulo Irulegui. H+- —> W+- gamma and H+- —> W+- Z in two Higgs doublet models. 1. The Large fermion mass limit. *Phys. Rev. D*, Vol. 44, pp. 191–201, 1991.

[145] Shinya Kanemura. Enhancement of loop induced $H^{\pm}W^{\mp}Z^0$ vertex in two Higgs doublet model. *Phys. Rev. D*, Vol. 61, p. 095001, 2000.

[146] Shinya Kanemura. Possible enhancement of the e+ e- —> H+- W-+ cross-section in the two Higgs doublet model. *Eur. Phys. J. C*, Vol. 17, pp. 473–486, 2000.

[147] Abdesslam Arhrib, Rachid Benbrik, and Mohamed Chabab. Charged Higgs bosons decays $H^{\pm} \to W^{\pm}$ (γ, Z) revisited. *J. Phys. G*, Vol. 34, pp. 907–928, 2007.

[148] Stephan Buehler and Claude Duhr. CHAPLIN - Complex Harmonic Polylogarithms in Fortran. *Comput. Phys. Commun.*, Vol. 185, pp. 2703–2713, 2014.

[149] David Eriksson, Johan Rathsman, and Oscar Stal. 2HDMC: Two-Higgs-Doublet Model Calculator Physics and Manual. *Comput. Phys. Commun.*, Vol. 181, pp. 189–205, 2010.

[150] Mikolaj Misiak and Matthias Steinhauser. Weak radiative decays of the B meson and bounds on $M_{H^{\pm}}$ in the Two-Higgs-Doublet Model. *Eur. Phys. J. C*, Vol. 77, No. 3, p. 201, 2017.

[151] P. A. Zyla, et al. Review of Particle Physics. *PTEP*, Vol. 2020, No. 8, p. 083C01, 2020.

[152] S. Alekhin, J. Blumlein, and S. Moch. The ABM parton distributions tuned to LHC data. *Phys. Rev. D*, Vol. 89, No. 5, p. 054028, 2014.

[153] Joyce Garden, Jochen Heitger, Rainer Sommer, and Hartmut Wittig. Precision computation of the strange quark's mass in quenched QCD. *Nucl. Phys. B*, Vol. 571, pp. 237–256, 2000.

[154] A. Arhrib, M. Capdequi Peyranere, W. Hollik, and S. Penaranda. Higgs decays in the two Higgs doublet model: Large quantum effects in the decoupling regime. *Phys. Lett. B*, Vol. 579, pp. 361–370, 2004.

[155] A. Arhrib, R. Benbrik, J. El Falaki, and W. Hollik. Triple Higgs coupling effect on $h^0 \to b\bar{b}$ and $h^0 \to \tau^+\tau^-$ in the 2HDM. *Phys. Lett. B*, Vol. 774, pp. 195–204, 2017.

[156] Shinya Kanemura, Yasuhiro Okada, Eibun Senaha, and C. P. Yuan. Higgs coupling constants as a probe of new physics. *Phys. Rev. D*, Vol. 70, p. 115002, 2004.

[157] Ning Chen, Tao Han, Shufang Su, Wei Su, and Yongcheng Wu. Type-II 2HDM under the Precision Measurements at the Z-pole and a Higgs Factory. *JHEP*, Vol. 03, p. 023, 2019.

[158] Jiayin Gu, Honglei Li, Zhen Liu, Shufang Su, and Wei Su. Learning from Higgs Physics at Future Higgs Factories. *JHEP*, Vol. 12, p. 153, 2017.

[159] H. Castilla-Valdez, A. Moyotl, M. A. Perez, and C. G. Honorato. Sensitivity of the decay $h \to ZZ^* \to Zl + l-$ to the Higgs self-coupling through radiative corrections. *Phys. Rev. D*, Vol. 93, No. 5, p. 055001, 2016.

[160] Lukas Altenkamp, Stefan Dittmaier, and Heidi Rzehak. Renormalization schemes for the Two-Higgs-Doublet Model and applications to h $\to$ WW/ZZ $\to$ 4 fermions. *JHEP*, Vol. 09, p. 134, 2017.

[161] Lukas Altenkamp, Stefan Dittmaier, and Heidi Rzehak. Precision calculations for $h \to WW/ZZ \to 4$ fermions in the Two-Higgs-Doublet Model with Prophecy4f. *JHEP*, Vol. 03, p. 110, 2018.

[162] Marcel Krause, Margarete Muhlleitner, Rui Santos, and Hanna Ziesche. Higgs-to-Higgs boson decays in a 2HDM at next-to-leading order. *Phys. Rev. D*, Vol. 95, No. 7, p. 075019, 2017.

[163] Marcel Krause and Margarete Mühlleitner. Impact of Electroweak Corrections on Neutral Higgs Boson Decays in Extended Higgs Sectors. *JHEP*, Vol. 04, p. 083, 2020.

[164] Ansgar Denner, Stefan Dittmaier, and Jean-Nicolas Lang. Renormalization of mixing angles. *JHEP*, Vol. 11, p. 104, 2018.

[165] Marcel Krause, Margarete Mühlleitner, and Michael Spira. 2HDECAY —A program for the calculation of electroweak one-loop corrections to Higgs decays in the Two-Higgs-Doublet Model including state-of-the-art QCD corrections. *Comput. Phys. Commun.*, Vol. 246, p. 106852, 2020.

[166] Robert V. Harlander, Stefan Liebler, and Hendrik Mantler. SusHi: A program for the calculation of Higgs production in gluon fusion and bottom-quark annihilation in the Standard Model and the MSSM. *Comput. Phys. Commun.*, Vol. 184, pp. 1605–1617, 2013.

[167] Robert V. Harlander, Stefan Liebler, and Hendrik Mantler. SusHi Bento: Beyond NNLO and the heavy-top limit. *Comput. Phys. Commun.*, Vol. 212, pp. 239–257, 2017.

[168] Edmond L. Berger, Tao Han, Jing Jiang, and Tilman Plehn. Associated production of a top quark and a charged Higgs boson. *Phys. Rev. D*, Vol. 71, p. 115012, 2005.

[169] Stefan Dittmaier, Michael Kramer, Michael Spira, and Manuel Walser. Charged-Higgs-boson production at the LHC: NLO supersymmetric QCD corrections. *Phys. Rev. D*, Vol. 83, p. 055005, 2011.

[170] Martin Flechl, Richard Klees, Michael Kramer, Michael Spira, and Maria Ubiali. Improved cross-section predictions for heavy charged Higgs boson production at the LHC. *Phys. Rev. D*, Vol. 91, No. 7, p. 075015, 2015.

[171] Celine Degrande, Maria Ubiali, Marius Wiesemann, and Marco Zaro. Heavy charged Higgs boson production at the LHC. *JHEP*, Vol. 10, p. 145, 2015.

[172] Morad Aaboud, et al. Search for additional heavy neutral Higgs and gauge bosons in the ditau final state produced in 36 fb^{-1} of pp collisions at $\sqrt{s} = 13$ TeV with the ATLAS detector. *JHEP*, Vol. 01, p. 055, 2018.

[173] Georges Aad, et al. Search for heavy neutral Higgs bosons produced in association with b-quarks and decaying into b-quarks at $\sqrt{s} = 13$ TeV with the ATLAS detector. *Phys. Rev. D*, Vol. 102, No. 3, p. 032004, 2020.

[174] Morad Aaboud, et al. Search for heavy particles decaying into top-quark pairs using lepton-plus-jets events in proton–proton collisions at $\sqrt{s} = 13$ TeV with the ATLAS detector. *Eur. Phys. J. C*, Vol. 78, No. 7, p. 565, 2018.

[175] Morad Aaboud, et al. Search for pair production of Higgs bosons in the $b\bar{b}b\bar{b}$ final state using proton-proton collisions at $\sqrt{s} = 13$ TeV with the ATLAS detector. *JHEP*, Vol. 01, p. 030, 2019.

[176] Morad Aaboud, et al. Search for heavy resonances decaying into WW in the $e\nu\mu\nu$ final state in pp collisions at $\sqrt{s} = 13$ TeV with the ATLAS detector. *Eur. Phys. J. C*, Vol. 78, No. 1, p. 24, 2018.

[177] M. Aaboud, et al. Search for heavy ZZ resonances in the $\ell^+\ell^-\ell^+\ell^-$ and $\ell^+\ell^-\nu\bar{\nu}$ final states using proton–proton collisions at $\sqrt{s} = 13$ TeV with the ATLAS detector. *Eur. Phys. J. C*, Vol. 78, No. 4, p. 293, 2018.

[178] Morad Aaboud, et al. Search for heavy resonances decaying into a W or Z boson and a Higgs boson in final states with leptons and b-jets in 36 fb^{-1} of $\sqrt{s} = 13$ TeV pp collisions with the ATLAS detector. *JHEP*, Vol. 03, p. 174, 2018. [Erratum: JHEP 11, 051 (2018)].

[179] Morad Aaboud, et al. Search for charged Higgs bosons decaying into top and bottom quarks at $\sqrt{s} = 13$ TeV with the ATLAS detector. *JHEP*, Vol. 11, p. 085, 2018.

[180] Morad Aaboud, et al. Search for charged Higgs bosons decaying via $H^\pm \to \tau^\pm\nu_\tau$ in the τ+jets and τ+lepton final states with 36 fb^{-1} of pp collision data recorded at $\sqrt{s} = 13$ TeV with the ATLAS experiment. *JHEP*, Vol. 09, p. 139, 2018.

[181] Vardan Khachatryan, et al. Search for heavy resonances decaying to tau lepton pairs in proton-proton collisions at $\sqrt{s} = 13$ TeV. *JHEP*, Vol. 02, p. 048, 2017.

[182] Albert M Sirunyan, et al. Search for beyond the standard model Higgs bosons decaying into a $\mathrm{b\bar{b}}$ pair in pp collisions at $\sqrt{s} = 13$ TeV. *JHEP*, Vol. 08, p. 113, 2018.

[183] Albert M Sirunyan, et al. Search for $\mathrm{t\bar{t}}$ resonances in highly boosted lepton+jets and fully hadronic final states in proton-proton collisions at $\sqrt{s} = 13$ TeV. *JHEP*, Vol. 07, p. 001, 2017.

[184] A. M. Sirunyan, et al. Search for a massive resonance decaying to a pair of Higgs bosons in the four b quark final state in proton-proton collisions at $\sqrt{s} = 13$ TeV. *Phys. Lett. B*, Vol. 781, pp. 244–269, 2018.

[185] Vardan Khachatryan, et al. Search for heavy resonances decaying into a vector boson and a Higgs boson in final states with charged leptons, neutrinos, and b quarks. *Phys. Lett. B*, Vol. 768, pp. 137–162, 2017.

[186] Albert M Sirunyan, et al. Search for a heavy pseudoscalar boson decaying to a Z and a Higgs boson at $\sqrt{s} = 13$ TeV. *Eur. Phys. J. C*, Vol. 79, No. 7, p. 564, 2019.

[187] Georges Aad, et al. Search for heavy Higgs bosons decaying into two tau leptons with the ATLAS detector using pp collisions at $\sqrt{s} = 13$ TeV. *Phys. Rev. Lett.*, Vol. 125, No. 5, p. 051801, 2020.

[188] A. Arbey, F. Mahmoudi, O. Stal, and T. Stefaniak. Status of the Charged Higgs Boson in Two Higgs Doublet Models. *Eur. Phys. J. C*, Vol. 78, No. 3, p. 182, 2018.

[189] Abdesslam Arhrib, Rachid Benbrik, Hicham Harouiz, Stefano Moretti, and Abdessamad Rouchad. A Guidebook to Hunting Charged Higgs Bosons at the LHC. *Front. in Phys.*, Vol. 8, p. 39, 2020.

[190] D. A. Dicus, J. L. Hewett, C. Kao, and T. G. Rizzo. W+- H-+ PRODUCTION AT HADRON COLLIDERS. *Phys. Rev. D*, Vol. 40, p. 787, 1989.

[191] A. A. Barrientos Bendezu and Bernd A. Kniehl. W+- H-+ associated production at the large hadron collider. *Phys. Rev. D*, Vol. 59, p. 015009, 1999.

[192] Stefano Moretti and Kosuke Odagiri. The Phenomenology of W+- H-+ production at the large hadron collider. *Phys. Rev. D*, Vol. 59, p. 055008, 1999.

[193] A. G. Akeroyd, et al. Prospects for charged Higgs searches at the LHC. *Eur. Phys. J. C*, Vol. 77, No. 5, p. 276, 2017.

[194] S. Moretti. Pair production of charged Higgs scalars from electroweak gauge boson fusion. *J. Phys. G*, Vol. 28, pp. 2567–2582, 2002.

[195] Alexandre Alves and Tilman Plehn. Charged Higgs boson pairs at the CERN LHC. *Phys. Rev. D*, Vol. 71, p. 115014, 2005.

[196] Oliver Brein, Wolfgang Hollik, and Shinya Kanemura. The MSSM prediction for W+- H-+ production by gluon fusion. *Phys. Rev. D*, Vol. 63, p. 095001, 2001.

[197] O. Brein and W. Hollik. Pair production of charged MSSM Higgs bosons by gluon fusion. *Eur. Phys. J. C*, Vol. 13, pp. 175–184, 2000.

[198] Shinya Kanemura, Koji Tsumura, and Hiroshi Yokoya. Multi-tau-lepton signatures at the LHC in the two Higgs doublet model. *Phys. Rev. D*, Vol. 85, p. 095001, 2012.

[199] Georges Aad, et al. A search for $t\bar{t}$ resonances using lepton-plus-jets events in proton-proton collisions at $\sqrt{s} = 8$ TeV with the ATLAS detector. *JHEP*, Vol. 08, p. 148, 2015.

[200] Shinya Kanemura, Hiroshi Yokoya, and Ya-Juan Zheng. Complementarity in direct searches for additional Higgs bosons at the LHC and the International Linear Collider. *Nucl. Phys. B*, Vol. 886, pp. 524–553, 2014.

[201] M. Cepeda, et al. Report from Working Group 2: Higgs Physics at the HL-LHC and HE-LHC. *CERN Yellow Rep. Monogr.*, Vol. 7, pp. 221–584, 2019.

[202] Youichi Yamada. Gauge dependence of the on-shell renormalized mixing matrices. *Phys. Rev. D*, Vol. 64, p. 036008, 2001.

[203] A. Sirlin. Radiative Corrections in the SU(2)-L x U(1) Theory: A Simple Renormalization Framework. *Phys. Rev. D*, Vol. 22, pp. 971–981, 1980.

[204] Karina E. Williams, Heidi Rzehak, and Georg Weiglein. Higher order corrections to Higgs boson decays in the MSSM with complex parameters. *Eur. Phys. J. C*, Vol. 71, p. 1669, 2011.

[205] N. Sakai. Perturbative QCD Corrections to the Hadronic Decay Width of the Higgs Boson. *Phys. Rev. D*, Vol. 22, p. 2220, 1980.

[206] Takeo Inami and Takahiro Kubota. Renormalization Group Estimate of the Hadronic Decay Width of the Higgs Boson. *Nucl. Phys. B*, Vol. 179, pp. 171–188, 1981.

[207] Manuel Drees and Ken-ichi Hikasa. NOTE ON QCD CORRECTIONS TO HADRONIC HIGGS DECAY. *Phys. Lett. B*, Vol. 240, p. 455, 1990. [Erratum: Phys.Lett.B 262, 497 (1991)].

[208] Andrew G. Akeroyd, Abdesslam Arhrib, and El-Mokhtar Naimi. Yukawa coupling corrections to the decay $H^+ \to W^+$ A0. *Eur. Phys. J. C*, Vol. 12, pp. 451–460, 2000. [Erratum: Eur.Phys.J.C 14, 371 (2000)].

[209] A. G. Akeroyd, A. Arhrib, and E. Naimi. Radiative corrections to the decay $H^+ \to W^+$ A0. *Eur. Phys. J. C*, Vol. 20, pp. 51–62, 2001.

[210] R. Santos, A. Barroso, and L. Brucher. Top quark loop corrections to the decay H+ —> h0 W+ in the two Higgs doublet model. *Phys. Lett. B*, Vol. 391, pp. 429–433, 1997.

[211] Alex Pomarol and Roberto Vega. Constraints on CP violation in the Higgs sector from the rho parameter. *Nucl. Phys. B*, Vol. 413, pp. 3–15, 1994.

[212] Shinya Kanemura and Hide-Aki Tohyama. Nondecoupling effects of Higgs bosons on e+ e- —> W(L)+ W(L)- in the two doublet model. *Phys. Rev. D*, Vol. 57, pp. 2949–2956, 1998.

[213] P. S. Bhupal Dev and Apostolos Pilaftsis. Maximally Symmetric Two Higgs Doublet Model with Natural Standard Model Alignment. *JHEP*, Vol. 12, p. 024, 2014. [Erratum: JHEP 11, 147 (2015)].

[214] J. M. Gerard and M. Herquet. A Twisted custodial symmetry in the two-Higgs-doublet model. *Phys. Rev. Lett.*, Vol. 98, p. 251802, 2007.

[215] D. Toussaint. Renormalization Effects From Superheavy Higgs Particles. *Phys. Rev. D*, Vol. 18, p. 1626, 1978.

[216] Stefano Bertolini. Quantum Effects in a Two Higgs Doublet Model of the Electroweak Interactions. *Nucl. Phys. B*, Vol. 272, pp. 77–98, 1986.

[217] W. Grimus, L. Lavoura, O. M. Ogreid, and P. Osland. The Oblique parameters in multi-Higgs-doublet models. *Nucl. Phys. B*, Vol. 801, pp. 81–96, 2008.

[218] Shinya Kanemura, Yasuhiro Okada, Hiroyuki Taniguchi, and Koji Tsumura. Indirect bounds on heavy scalar masses of the two-Higgs-doublet model in light of recent Higgs boson searches. *Phys. Lett. B*, Vol. 704, pp. 303–307, 2011.

[219] M. Tanabashi, et al. Review of Particle Physics. *Phys. Rev. D*, Vol. 98, No. 3, p. 030001, 2018.

[220] Howard E. Haber and Deva O'Neil. Basis-independent methods for the two-Higgs-doublet model III: The CP-conserving limit, custodial symmetry, and the oblique parameters S, T, U. *Phys. Rev. D*, Vol. 83, p. 055017, 2011.

[221] P. M. Ferreira and D. R. T. Jones. Bounds on scalar masses in two Higgs doublet models. *JHEP*, Vol. 08, p. 069, 2009.

[222] Nabarun Chakrabarty, Ujjal Kumar Dey, and Biswarup Mukhopadhyaya. High-scale validity of a two-Higgs doublet scenario: a study including LHC data. *JHEP*, Vol. 12, p. 166, 2014.

[223] Dipankar Das and Ipsita Saha. Search for a stable alignment limit in two-Higgs-doublet models. *Phys. Rev. D*, Vol. 91, No. 9, p. 095024, 2015.

[224] Phillipp Basler, Pedro M. Ferreira, Margarete Mühlleitner, and Rui Santos. High scale impact in alignment and decoupling in two-Higgs doublet models. *Phys. Rev. D*, Vol. 97, No. 9, p. 095024, 2018.

[225] I. P. Ivanov. Minkowski space structure of the Higgs potential in 2HDM. *Phys. Rev. D*, Vol. 75, p. 035001, 2007. [Erratum: Phys.Rev.D 76, 039902 (2007)].

[226] A. Barroso, P. M. Ferreira, I. P. Ivanov, Rui Santos, and Joao P. Silva. Evading death by vacuum. *Eur. Phys. J. C*, Vol. 73, p. 2537, 2013.

[227] Pier Paolo Giardino, Kristjan Kannike, Isabella Masina, Martti Raidal, and Alessandro Strumia. The universal Higgs fit. *JHEP*, Vol. 05, p. 046, 2014.

[228] Combined measurements of Higgs boson production and decay using up to 80 fb^{-1} of proton-proton collision data at $\sqrt{s} = 13$ TeV collected with the ATLAS experiment. 3 2019.

[229] G. Passarino and M. J. G. Veltman. One Loop Corrections for e+ e- Annihilation Into mu+ mu- in the Weinberg Model. *Nucl. Phys. B*, Vol. 160, pp. 151–207, 1979.